METALLURGICAL, OPTICAL, AND ELECTRICAL PROPERTIES OF LEAD-TIN-TELLURIDE SEMICONDUCTING ALLOYS

by

GASTON DIONNE

Dissertation submitted to the Faculty of the Graduate School
of the University of Ottawa in partial fulfillment
of the requirements for the degree
Doctor of Philosophy

1971

ACKNOWLEDGMENTS

I would like to thank Dr. J.C. Woolley, who was the chairman of the Physics Department and also my research director for giving me the opportunity to use the facilities of his laboratory and for his guidance and discussions throughout the course of this work.

The several discussions on the different aspects of the work with other professors of the Physics Department and all the graduate students of the group are also gratefully acknowledged; in particular, I am very grateful to Professor K.S. Song, R.R. Senechal and D. Demars for their help and comments.

I would like to thank the members of the staff of the Physics Department for their assistance and, in particular, all members of the workshop for their careful and expert work in making some experimental apparatus. Also, many thanks to Mrs. E. Storto and Mr. R. Lavallée for typing the thesis and making the drawings respectively.

I also would like to thank my wife Juliette and my daughter Sophie for their inestimable cooperation.

Finally I thank the National Research Council of Canada for a Post Industrial Experience Research Fellowship, and the Ontario Government for its general financial support.

TABLE OF CONTENTS

LIST OF FIGURES

LIST OF TABLES

CHAPTER I

INTRODUCTION

The lead telluride (PbTe) compound and the alloys of PbTe with tin telluride (SnTe) are among the semiconductors that have generated most interest recently. The increased activity on $Pb_{1-x}Sn_xTe$ semiconducting compounds and alloys arises from an exceptional combination of academic and practical interests. This has stimulated fundamental studies in several areas simultaneously and led to several device applications.

The properties that have received most attention in $Pb_{1-x}Sn_xTe$ are those which relate to the stoichiometry, the band structure, and conductivity mechanisms. Perhaps, the close interaction between fundamental and practical studies is best exemplified in the work associated with the stoichiometry of $Pb_{1-x}Sn_xTe$. Because the electrical properties are mainly determined by deviations from stoichiometry, fundamental studies on the physical chemistry of the compounds and alloys can be performed to a high degree of accuracy (68 S1). In turn, the knowledge of the functional relationships between composition, vapor pressure, and temperature, obtained in these fundamental studies, permits the preparation of materials with controlled electrical properties for other scientific studies as well as for device fabrication. A unique feature of the energy bands in $Pb_{1-x}Sn_xTe$ is its valence-conduction band gap. By varying the alloy composition, the pressure,

and the temperature, the energy gap can be controlled down to zero energy (66 D1). This property of the energy bands led to the fabrication of infrared detectors and lasers which operate at longer wavelengths than otherwise obtained with semiconductors (68 B1, 68 M2). Also, the transport properties of $Pb_{1-x}Sn_xTe$ compounds and alloys make them the most efficient materials for thermoelectric generators working between room temperature and 600-650°C (70 R3). Several power sources in which $Pb_{1-x}Sn_xTe$ thermoelements convert heat energy directly into electrical energy have been built for space and military applications.

In spite of the activities around $Pb_{1-x}Sn_xTe$ compounds and alloys, the band structure is still not adequately known with sufficient detail to permit quantitative explanation of the transport and optical properties. It is well established that in PbTe both valence and conduction bands are situated at the L point and that the constant energy surfaces consist of four equivalent prolate ellipsoids at low carrier concentrations (64 C1, 60 A1). The same conclusions were reached recently for $Pb_{1-x}Sn_xTe$ with $0 < x < .32$ (71 M1). However, little is known about the change in these energy surfaces and in the density of states (or effective masses) with increasing carrier concentrations. Several models of energy surfaces have been proposed for the conduction and valence bands at the L point, but they have had only limited success in explaining the optical and transport properties. Moreover, with increased carrier concentrations in p-type $Pb_{1-x}Sn_xTe$ there is evidence that the carriers are not only in the <111> maxima

at the L point but occupy another energy band*as well (66 Al). This extra heavy mass band is not yet positioned in k-space and its energy position is still imprecisely known. Thus in p-type $Pb_{1-x}Sn_xTe$ with increased carrier concentrations not only the main <111> valence band is not well described but there is another contributing heavy mass valence band for which little is known. The motivation of the present work has been to contribute some further information about the valence bands in p-type $Pb_{1-x}Sn_xTe$ alloys.

This work is the first study of $Pb_{1-x}Sn_xTe$ alloys in this laboratory. For this reason, an extensive program was undertaken to grow single crystal ingots over the whole alloy range and to prepare homogeneous samples of given carrier concentrations as well as given alloy compositions. This program originated in 1967 and was done by the author alone, using his own techniques and independently of related work at other laboratories after 1967. All $Pb_{1-x}Sn_xTe$ single crystal alloys studied in this work were prepared by the author in this laboratory as described in Chapter 2 entitled: Metallurgical properties of $Pb_{1-x}Sn_xTe$ alloys. Chapter 3 deals with the optical properties of p-type $Pb_{1-x}Sn_xTe$ alloys and in particular with measurements of susceptibility effective masses which were done to test different energy band models. Also included in Chapter 3 is a much needed systematic and critical study of the different methods of analysis to obtain susceptibility effective masses from infrared reflectivity data.

*The "heavy mass band" is not a second valence band strickly speaking but a subsidiary maxima of the same valence band as the main one at the L point.

Chapter 4 is mainly concerned with measurements of Hall coefficient, resistivity and magnetoresistance in p-type $Pb_{1-x}Sn_xTe$ alloys. A detailed quantitative analysis of the electrical properties in p-type $Pb_{1-x}Sn_xTe$ still awaits an adequate model for the energy surfaces of the <111> minima. In spite of this, several new results related to mobility ratios, energy gaps, and energy surfaces have been obtained from the electrical measurements and will be reported in Chapter 4.

CHAPTER II

METALLURGICAL PROPERTIES OF $Pb_{1-x}Sn_xTe$

2.1 Introduction

The group IV elements germanium, tin, and lead form nine 1:1 compounds with the group VI elements sulfur, selenium, and tellurium. Of these compounds, the lead chalcogenides (i.e. the compounds of lead with sulfur, selenium, and tellurium) and SnTe have much in common. They all have the same cubic rocksalt structure, have similar phase diagrams, can be grown by similar methods, and their carrier concentrations can be controlled in a similar manner. In addition, in systems so far investigated,* these compounds are completely soluble in one another to form alloys with the above common characteristics. In this chapter, we will study the alloy $Pb_{1-x}Sn_xTe$ which will often be represented by the symbole MN to generalize the discussion to all the above systems. In this notation, M represents the element(s) of the group IV and N represents the element(s) of the group VI.

The use of stoichiometric formulae such as MN (i.e. the number of atoms M is exactly equal to the number of atoms N) to represent the compounds is only approximate. At finite temperatures, the free energy of the crystal is lowered by the introduction of atomic point defects (such as vacancies) and in general the compound

*PbS-PbTe are not completely soluble

is stable over a range of compositions (homogeneity range) which sometimes does not include the stoichiometric composition implied by the formula. These deviations from stoichiometry are too small to be detected by conventional analytical techniques. However, for the above MN systems, the carrier concentration is a direct measure of the deviation from stoichiometry because the point defects, responsible for this deviation, supply all extrinsic carriers in undoped specimens. This is the reason for the considerable interest in deviations from stoichiometry in the IV-VI compounds (see 68 S1 for extensive references). Our interest here is not directed towards fundamental investigations, but is practical. Rather than using carrier concentration measurements to find the different phase diagrams near the stoichiometric composition, we will invert the procedure to obtain samples of different carrier concentrations.

This chapter will be concerned with the growth and the control of carrier concentration by heat treatment in $Pb_{1-x}Sn_xTe$. The purpose of this study is twofold. Firstly, it is to provide crystals of good quality for general use in our laboratory. Secondly, it is to obtain crystals with given alloy compositions and carrier concentrations for the experiments to be described in the next two chapters.

2.2 Apparatus Design

2.2.1 The Growth Furnace

The furnace used to grow all our crystals is shown schematically in Figure 2.1. A typical temperature profile is also shown. The furnace consists of a high and a low temperature section which are independently controlled. The two sections are separated by a water cooled jacket which permits the establishment of a steep temperature gradient. The quartz ampoule, containing the melt, was held in a mullite tube which was driven slowly in the direction of the low temperature zone. The driving mechanism was built to provide three speeds: 1.1, 3.4, and 10.4 cm/day. In addition, the furnace could be tilted as shown in Figure 2.1. The temperature gradient, at the temperature of freezing, was always greater than 50°C/cm.

2.2.2 The Annealing Furnace

For the heat treatments to be described in Section 2.4, a constant temperature furnace was needed. In order to satisfy this requirement for several temperatures, it was necessary to build a furnace with two concentric furnace tubes, each with a particular type of winding. The outer heater consisted of a wire element very closely wound near both ends of the furnace, and gradually more spaced in going toward the center of the furnace. The temperature profile of the outer heater alone is shown schematically in Figure 2.2. The inner

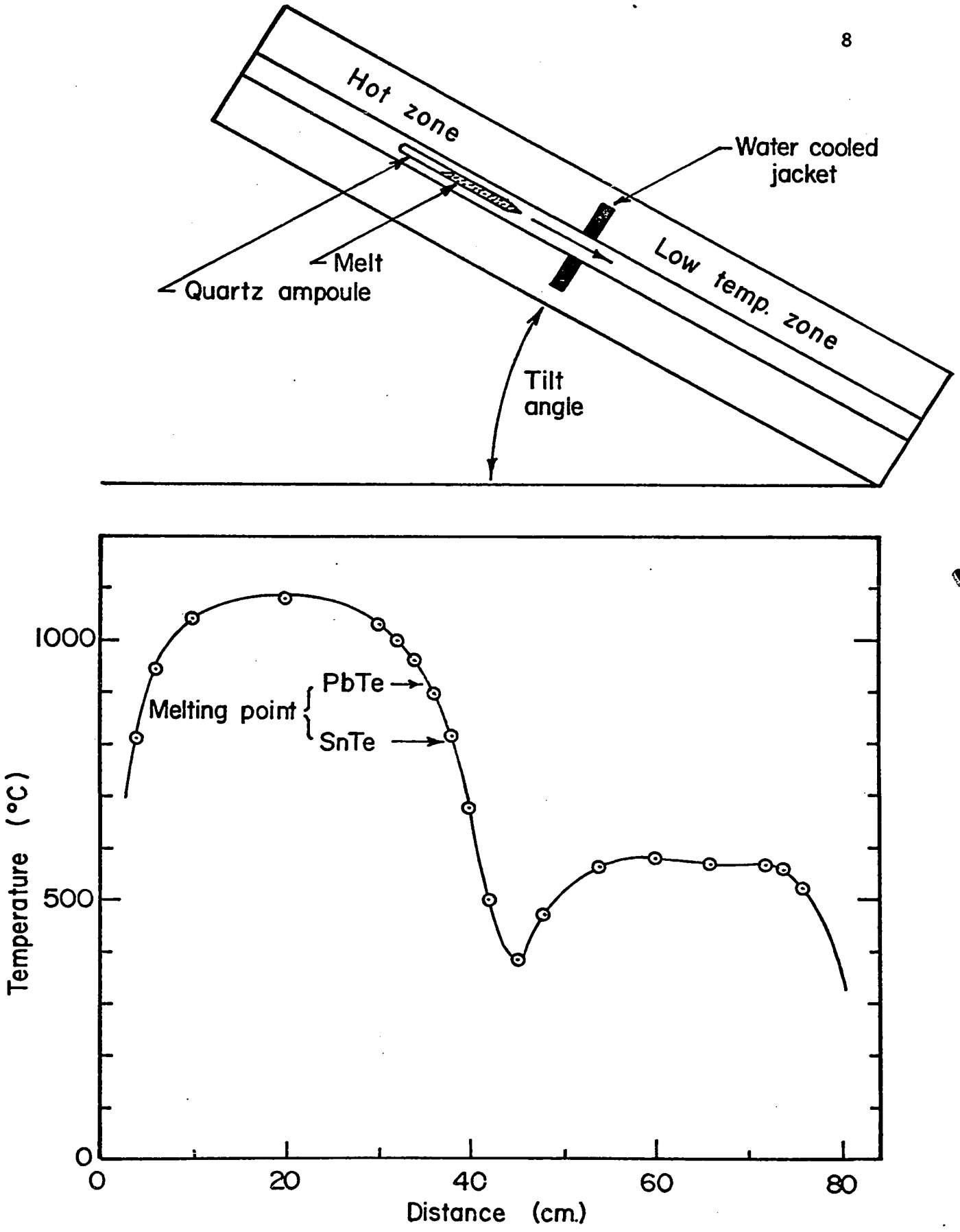

Figure 2.1 Schematic of step-freeze furnace and its temperature profile.

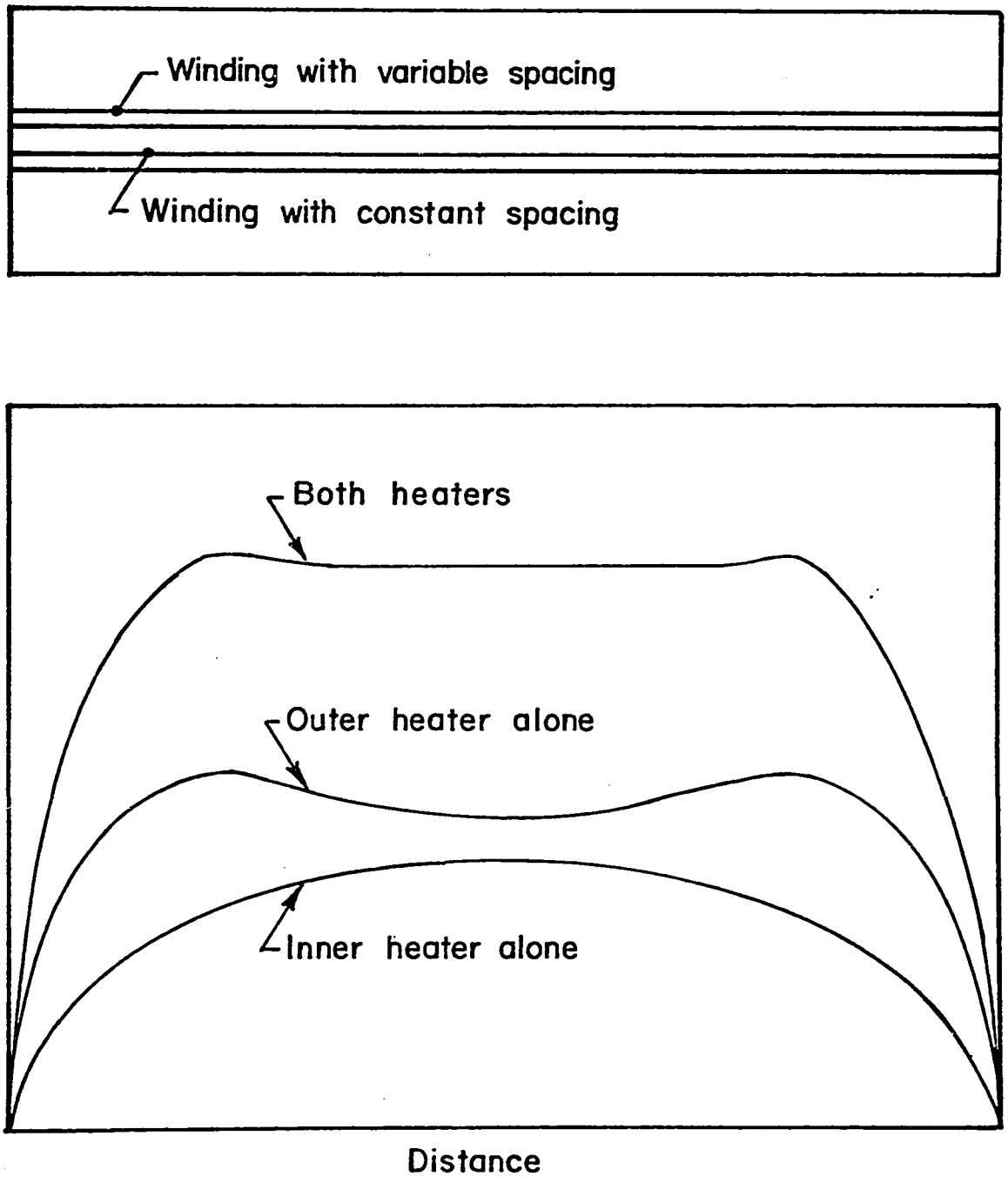

Figure 2.2 Schematic of annealing furnace and temperature profiles.

heater was wound with a constant spacing between the turns and gave a temperature profile as shown in Figure 2.2. For all temperatures, at which the furnace was used, it was possible to find current settings on both heaters that gave a constant temperature (± 1°C), over at least 15 cm, as illustrated in Figure 2.2. The furnace temperature was maintained constant by a proportional comptroller acting on the outer heater. The value of the correct current in the inner heater was found by trial and error for each annealing temperature and kept fixed.

2.3 Growth and Characterization

2.3.1 Growth Procedures

The melts were prepared by mixing the elements in stoichiometric proportion. Lead, tin, and tellurium, all 69s grade, were obtained from Cominco Ltd., Montreal. Lead and tin were available in the form of rods, approximately 12 mm in. diameter, from which sections were cut and the oxide skin removed, with a steel blade, just before usage. The elements were sealed under vacuum in a 13 mm inside diameter quartz ampoule, one end of which was made conical. The ampoule was then introduced in the hot zone of the step-freeze furnace and left there, at a temperature higher than 1000°C, for at least 1 day for complete mixing. The melt was driven through the steep temperature gradient (> 50°/cm), the conical tip being the first to freeze, at a speed of 3.4 cm/day.

Table 2.1 lists the $Pb_{1-x}Sn_xTe$ ingots grown using the above procedure. Ingots 2 to 4 were grown with the furnace in the horizontal position, while ingots 5 to 8 were grown with a tilt angle of 45°(see Figure 2.1). The main advantages of the tilted position are the following: 1) Since the melt completely fills the ampoule, as shown in Figure 2.1, large cross sections of crystal are obtained. 2) There is no transport of material, through the vapor phase, over already grown material as there is in the horizontal set-up. 3) There is no need to seal the quartz ampoules close to the material thus avoiding oxidation during this operation.

Ingot #	Starting x	Weight grs.	1st to Freeze x	$p=(1/R_o e)_{77^oK}$ cm^{-3}
2	.2	50	.12	2-4 x 10^{19}
3	.4	50	.27	.7-1.5 x 10^{20}
4	.6	50	.45	2-4 x 10^{20}
5	.8	75		5 x 10^{20}
6	.1	100	.05	1.2 x 10^{19}
7	0	67	0	7. x 10^{18}
8	.3	100	.18	4. x 10^{19}

TABLE 2.1 $Pb_{1-x}Sn_xTe$ INGOTS GROWN BY THE STEP-FREEZE TECHNIQUE IN OUR LABORATORY

The starting compositions and the first-to-freeze compositions, listed in Table 2.1, are consistent with the phase diagram for $Pb_{1-x}Sn_xTe$ determined by Wagner and Woolley (67 W1) and shown in Figure 2.3. The compositions were determined as described in Section 2.3.2. As seen from the phase diagram 2.3, the grown material is always richer in PbTe than the melt. As growth slowly proceeds, the melt becomes more and more depleted of PbTe and a composition gradient exists along the length of the ingot. However, the composition gradient is very small in the first quarter to freeze due to the relatively small separation between the liquidus and the solidus curves at a given temperature. In ingot #2, for example, the composition varies by less than 2% in the first quarter of the ingot to freeze.

Table 2.1 also lists the range of carrier concentrations measured in these ingots. The higher the SnTe content of the alloys, the higher the carrier concentrations are. This is due to an increasing deviation from stoichiometry as we go from PbTe to SnTe. When grown from stoichiometric melts, $Pb_{1-x}Sn_xTe$ alloys are always tellurium rich and this excess tellurium is accommodated in the lattice by lead and/or tin vacancies which ionize to produce p-type carriers. That the alloys grown from stoichiometric melt are tellurium rich is clearly seen in SnTe rich ingots for which the last to freeze is always a small amount of pure tin. Also, Brebrick (63 B2) showed that the point defects in SnTe were tin vacancies and that the carrier-to-vacancy ratio was approximately 3. But, Brebrick calculated the carrier concentration

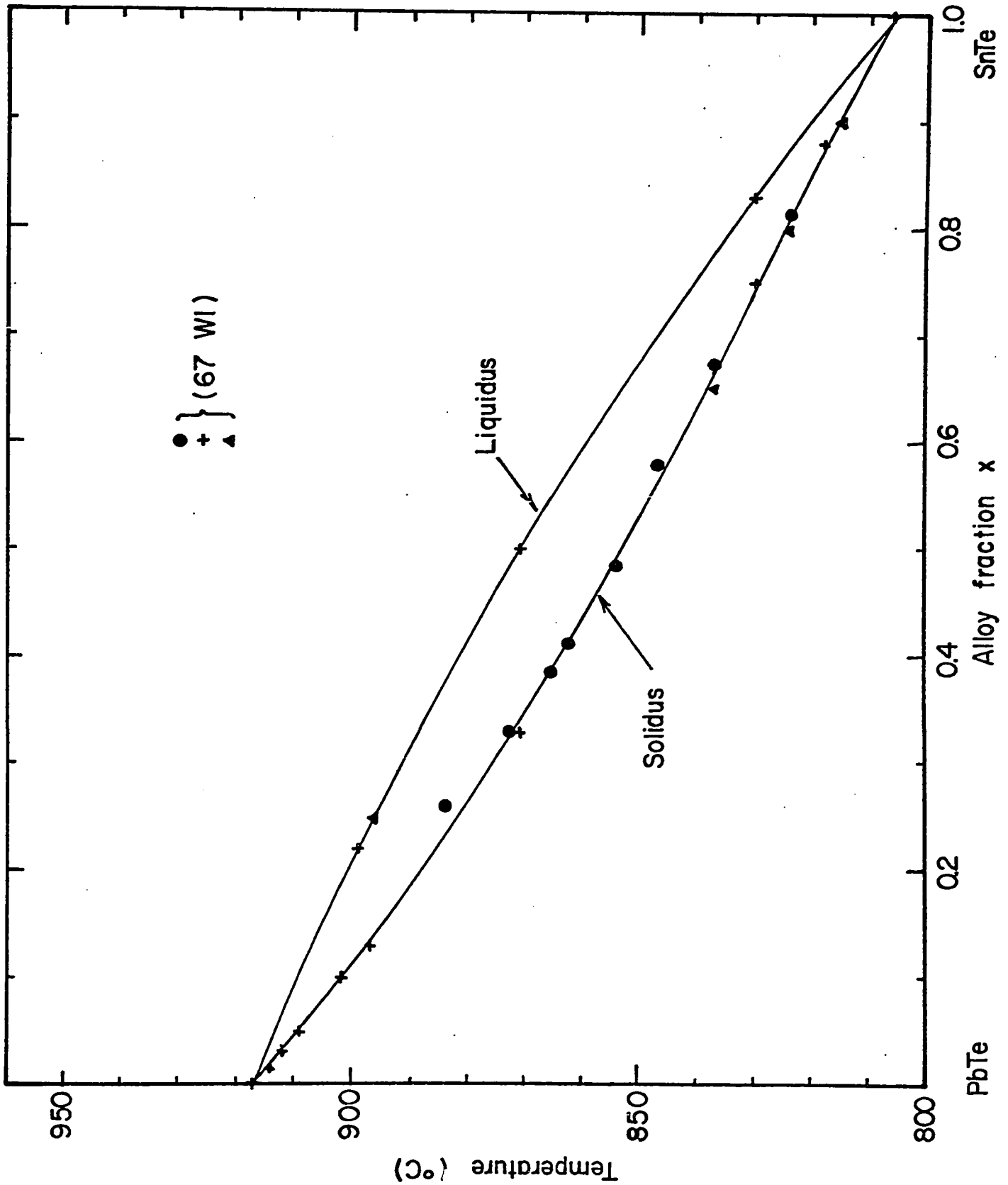

Figure 2.3 Temperature-composition equilibrium diagram of $Pb_{1-x}Sn_xTe$ alloys.

using $p = 1/R_o e$ in which R_o is the low field Hall constant and e is the electronic charge. When using the correct expression for the carrier concentration $p = r/R_o e$, with the values for r given by Tsu et al. (68 T1), the carrier-to-vacancy ratio becomes 2. This agrees with the intuitive notion that an ionized divalent (Sn^{++}) vacancy produces exactly 2 carriers. The increase of carriers from PbTe to SnTe is almost 100 fold for ingots grown from stoichiometric melts (see Table 2.1) suggesting that tin vacancies are more easily generated than lead vacancies.

2.3.2 Determination of Alloy Compositions

The largest deviation from stoichiometry is around 1% in $Pb_{1-x}Sn_xTe$. This nevertheless makes the system slightly ternary with the correct formula given by $M_{\frac{1}{2}-\delta}\ N_{\frac{1}{2}+\delta}$, where δ is the deviation from stoichiometry. Thus, to specify the alloy, both x and δ need to be known. If δ is constant across the alloy range, then the system may be considered as a binary system and be specified by the composition x.

a) Lattice Constant versus Composition-Vegard's Law

Bis and Dixon (69 B1) have shown that in $Pb_{1-x}Sn_xTe$, Vegard's law is valid provided all alloys deviate from stoichiometry by a fixed amount δ. Vegard's law says that the variation of the lattice constant with alloy composition is linear; hence, a single lattice constant

measurement is necessary to determine any alloy compositions x if the lattice constant of PbTe and SnTe are known.

The results of Bis and Dixon are shown in Figure 2.4. The points are from Wagner and Woolley (67 W1) and are for samples which deviated more and more from stoichiometry with increasing SnTe content. These deviations are estimated to be comparable to those of the as-grown alloys of Table 2.1. The crosses are from Bis and Dixon (69 B1) and were obtained from samples of relatively low carrier concentrations ($< 7 \times 10^{19}$ cm^{-3}). As seen, Vegard's law is verified for the latter samples with small deviations from stoichiometry. The insert shows the variation of the lattice constant with carrier concentration in SnTe. By assuming the same variation throughout the alloy range, Bis and Dixon gave a set of lines for constant p (or δ). For p less than 10^{20} holes cm^{-3} the deviation from stoichiometry may be disregarded in determining the composition. The apparent deviation from Vegard's law in Wagner and Woolley data are thus explained (69 B1) by deviations from stoichiometry which are negligible in PbTe rich alloys but becomes larger in SnTe rich alloys. All alloy compositions in this work were determined by finding the carrier concentration and the lattice constant, and subsequently using Figure 2.4. Composition determined in this way were accurate to better than 1%. The lattice constant was determined from standard analysis of the x-ray powder photographs. To remove the internal stress, produced during the grinding operation, the alloy powders were annealed for about 10 hrs. at a temperature no higher

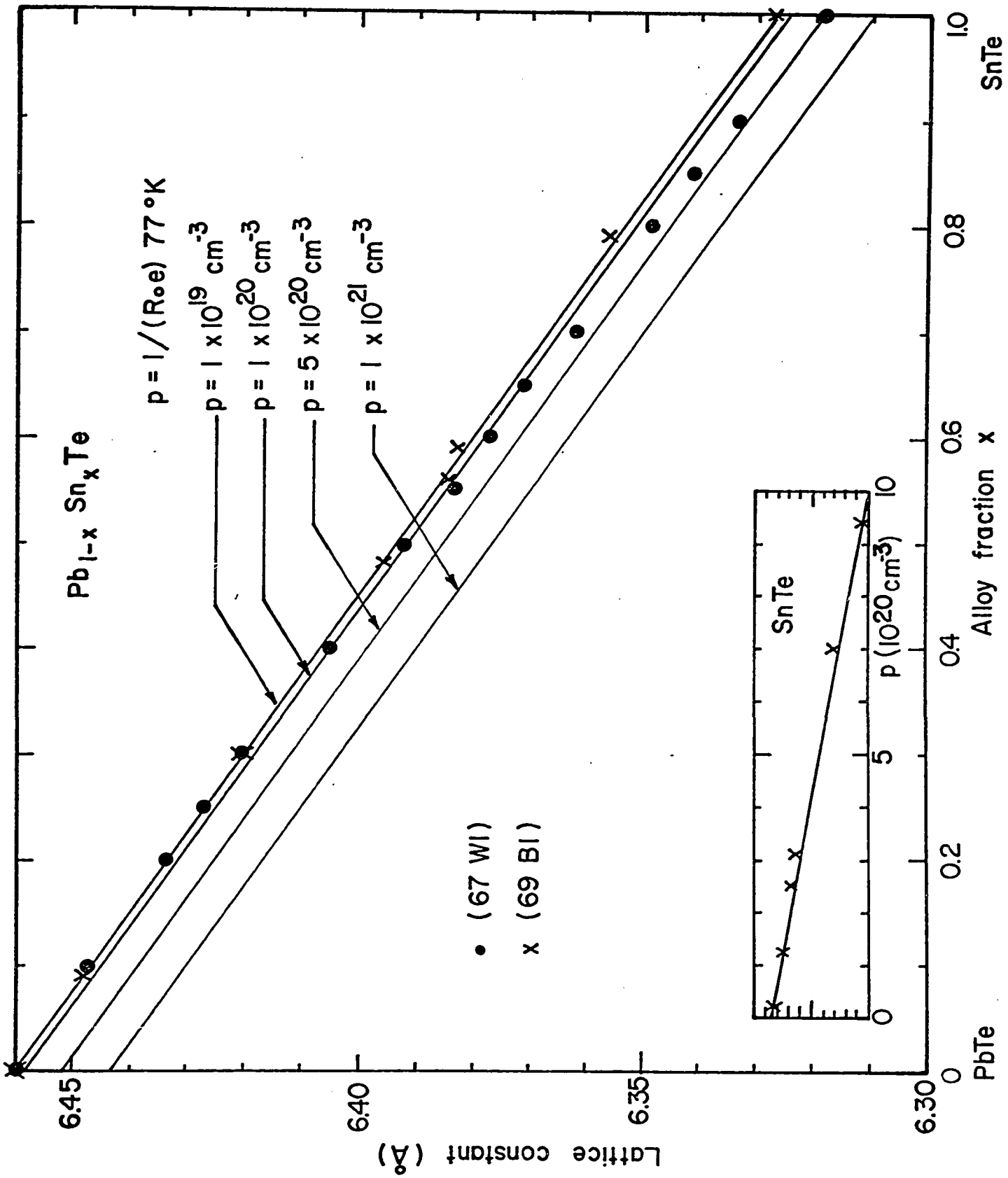

Figure 2.4 Lattice constant vs. alloy composition in $Pb_{1-x}Sn_xTe$ alloys with different carrier concentrations.

than 250°C. The accuracy of the lattice constant determined was ± .0005 Å.

b) Diffracted Intensities versus Alloy Composition

We would like to propose here a new method that permits a rough determination of the alloy composition by visual examination of the x-ray powder photograph or an accurate determination when measuring the integrated intensities of only two lines. This method is particularly useful in systems of the type $A_{1-x}B_xC$ for which atoms B and C have appreciably lower atomic numbers than atoms A. $Pb_{1-x}Sn_xTe$ is such a system. For simplicity, let us assume that the deviations from stoichiometry are negligible (i.e., $p < 10^{20}$ cm^{-3}).

$Pb_{1-x}Sn_xTe$ alloys have the cubic sodium chloride structure with the lead and tin atoms located on a face-centered lattice with origin at (0,0,0), and the tellurium atoms located on another face-centered lattice with origin at (1/2, 1/2, 1/2). The integrated intensities of the different x-ray lines for fine powders are proportional to the structure factors squared (F^2). It is given (59 C1) for $Pb_{1-x}Sn_xTe$ by:

$$F^2 = 0 \quad \text{for mixed indices (even and odd)}$$
$$F^2 = 16\left((1-x)\, f_{Pb} + x\, f_{sn} + f_{Te}\right)^2 \quad \text{if } (h+k+1) \text{ is even} \qquad (2\text{-}1)$$
$$F^2 = 16\left((1-x)\, f_{Pb} + x\, f_{sn} - f_{Te}\right)^2 \quad \text{if } (h+k+1) \text{ is odd}$$

in which f represents the atomic scattering factor for the element in

subscript, and (h,k,l) are the Miller indices. Since the atomic scattering factor increases with increasing atomic number, F^2 will be relatively large (if (h+k+l) is odd) for x = 0 and close to zero for x = 1.

Let us consider the (311) and the (222) lines (the sum of their indices is odd and even, respectively) and let us calculate the ratio of their integrated intensities. It is given for the Debye-Sherrer method (59 C1) by:

$$\frac{I_{311}}{I_{222}} = \frac{|F_{311}|^2}{|F_{222}|^2} \; p \; C(\theta) \qquad (2\text{-}2)$$

in which F is the structure factor, p is the ratio of the multiplicity factors and is equal to 3 for the above reflections, and $C(\theta)$ is the ratio of the Lorentz factors (59 C1). The above formula is expected to be quite accurately obeyed in the present case because all other factors influencing the integrated intensity are the same for both reflections and cancel one another in the ratio. The intensity of the incident beam, the irradiated volume of the specimen, the camera radius are such constant factors. Other factors, such as the temperature and the absorption factors (59 C1), cancel out because the Bragg angles for the two reflections differ by only 1^o in the present case.

The Bragg angle for the (311) and (222) lines vary by approximately $1/2^o$ across the alloy range and a negligible error is introduced,

by taking the Bragg angle corresponding to the middle of the alloy range, in finding $C(\theta)$ and the atomic structure factors. Using the value of structure factors and $C(\theta)$ given in Tables (52 T1) equation (2-2) becomes for CuK_α radiation and $Pb_{1-x}Sn_xTe$ alloys:

$$\frac{I_{311}}{I_{222}} = 3.332 \left[\frac{.933 - x}{3.713 - x} \right]^2 \qquad (2\text{-}3)$$

A plot of equation (2-3) is shown in Figure 2.5. Accurate intensity measurements using a diffractometer were not performed. However, approximate intensity ratios were determined using a photometer and are shown in Figure 2.5. The corresponding composition x were known from the lattice constants. The agreement is rather good in view of the inaccuracy of the method used to determine the integrated intensities (59 C1, p.173). The variation of integrated intensity of the (311) and (222) lines with alloy composition is illustrated in Figure 2.6b, which shows sections of the Debye-Sherrer powder photographs for different alloy compositions. The adjacent (311) and (222) lines are indicated by an arrow.

2.3.3 Characterization of the "As-grown" Alloys

Visual and metallographic examination revealed that the "as-grown" ingots were single crystals. In ingot #8, for example, the first to freeze material was single crystal with small angle grain boundaries ($\sim 2^\circ - 3^\circ$) which disappeared rapidly with increasing distance

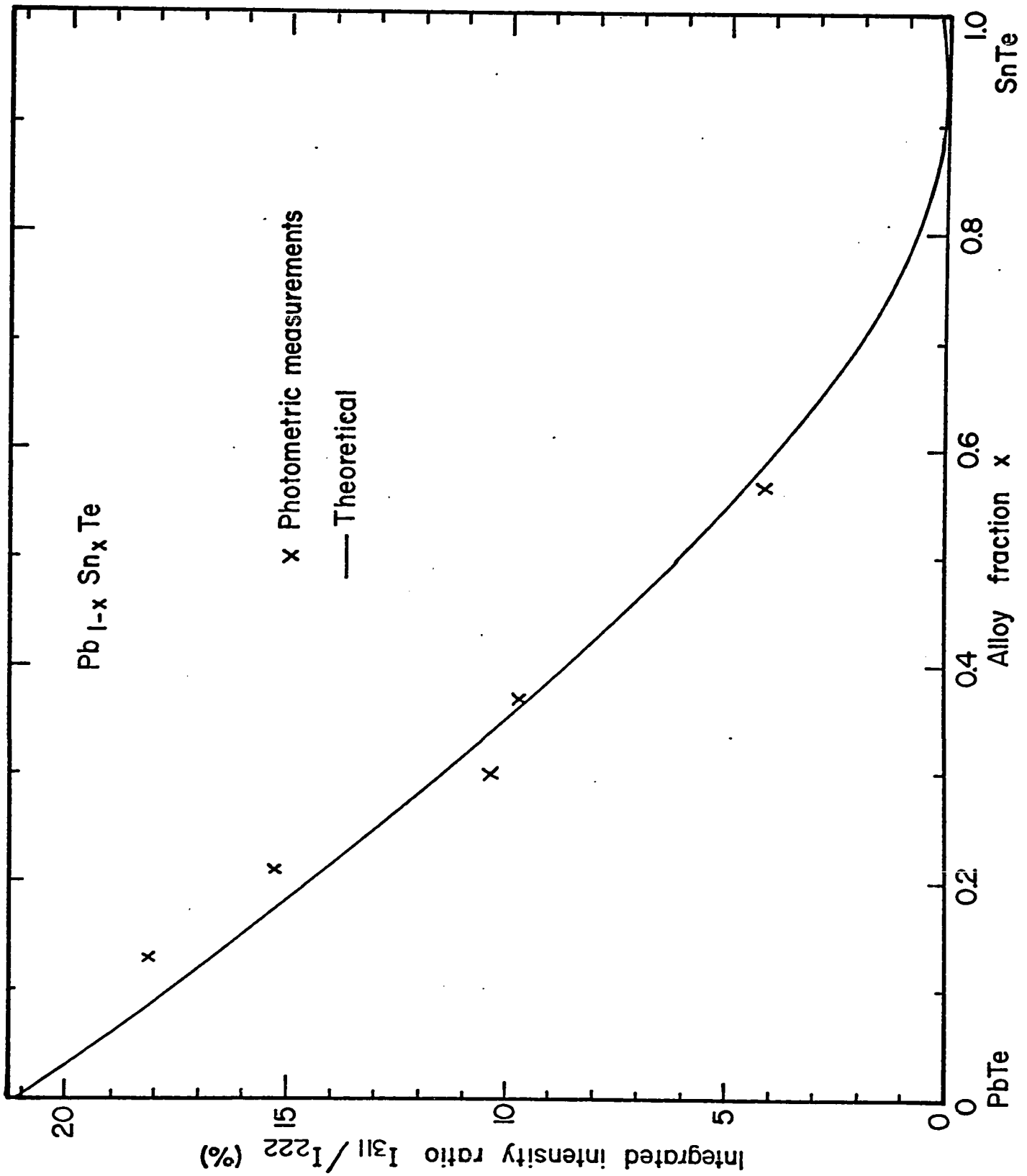

Figure 2.5 Diffracted intensity ratio vs. alloy fraction

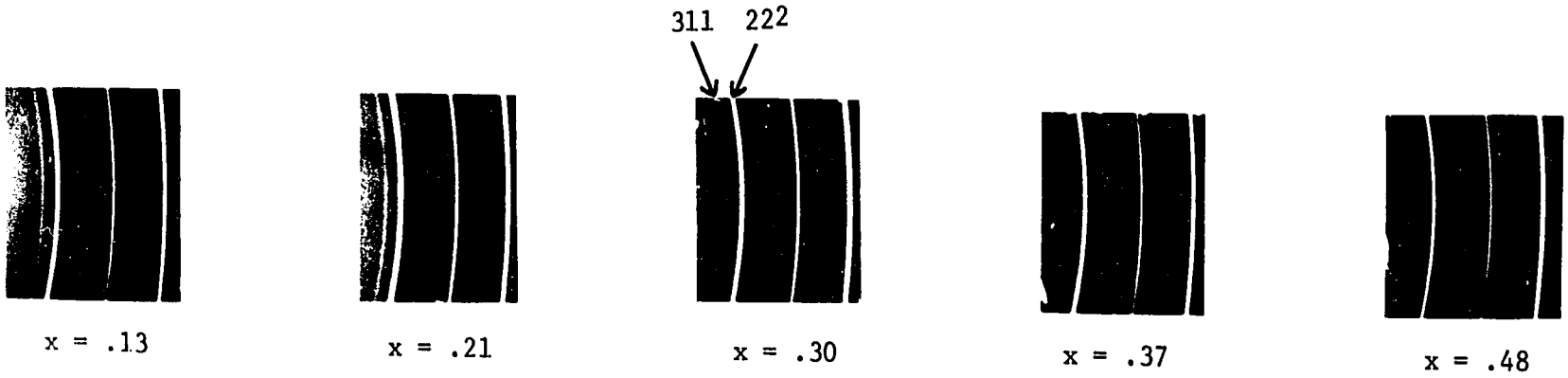

(b)

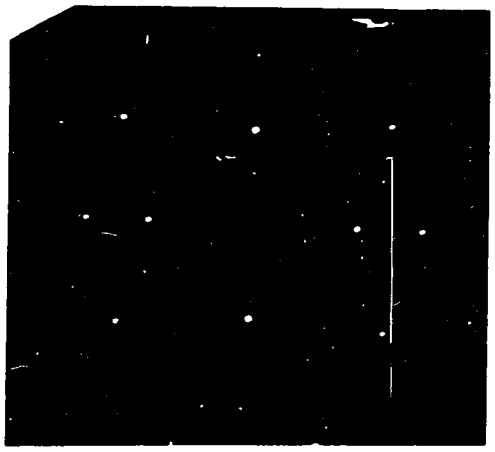

(a)

Figure 2.6 X-ray photographs of $Pb_{1-x}Sn_xTe$ alloys a) back-reflection Laue photograph b) sections of Debye-Scherrer photographs.

away from the first to freeze. X-ray back reflection photographs, taken every 3 mm across a diameter of the cylindrical ingot on a face parallel to the long axis of the ingot, showed identical pattern for normal incidence of the x-ray beam. One of the x-ray photographs is shown in Figure 2.6a. The single crystal character of the material is confirmed and the small size of the x-ray spots indicates a highly perfect crystal. Similar results were obtained from ingot #6.

Mechanically, the material is fragile and often difficult to cut and lap. It cleaves along {100} planes. This operation is difficult to perform at room temperature but becomes easier at lower temperatures. For example, good cleavage could be obtained in cold water with much greater facility than at room temperature. The cutting and lapping were found to be relatively easy along {100} planes. But difficulties were often experienced when the {100} planes were at an angle with the face to be lapped. Micro-cleavage was often observed on the lapped surface when the lapping direction formed an obtuse angle with {100} planes. By avoiding such undesirable situations good surfaces were always obtained.

The "as-grown" material was homogeneous. Firstly, metallographic examination showed no voids, no cracks, and no sign of metal precipitation. We believe that the small growth rate (3.4 cm/day) and the steep temperature gradient at the freezing interface (> 50°C/cm) were responsible for the absence of metal precipitation and cellular substructure frequently observed in $Pb_{1-x}Sn_xTe$ ingots (68 B1).

Secondly, x-ray diffraction (Debye-Sherrer powder photographs) indicated that the alloys were single phase and of good alloy homogeneity. Figure 2.7 illustrates this by showing the high angle diffraction lines which are well resolved for all alloy compositions shown. Thirdly, resistivity measurements taken at two different positions along the samples, indicated that the "as-grown" material was homogeneous in carrier concentration. Several samples were measured this way between 4.2°K and room temperature and, in all cases, the two measurements agreed to better than 1% at all temperatures.

The carrier concentration and the Hall mobility also reflected the high quality of the material grown in our laboratory. The Hall constant and the Hall mobility are plotted in Figures 2.8 and 2.9. For comparison, the results for Czochralski grown (68 W1) single crystals are also shown. It is seen that the alloys grown by the step-freeze method in our laboratory have fewer carriers and higher mobilities.

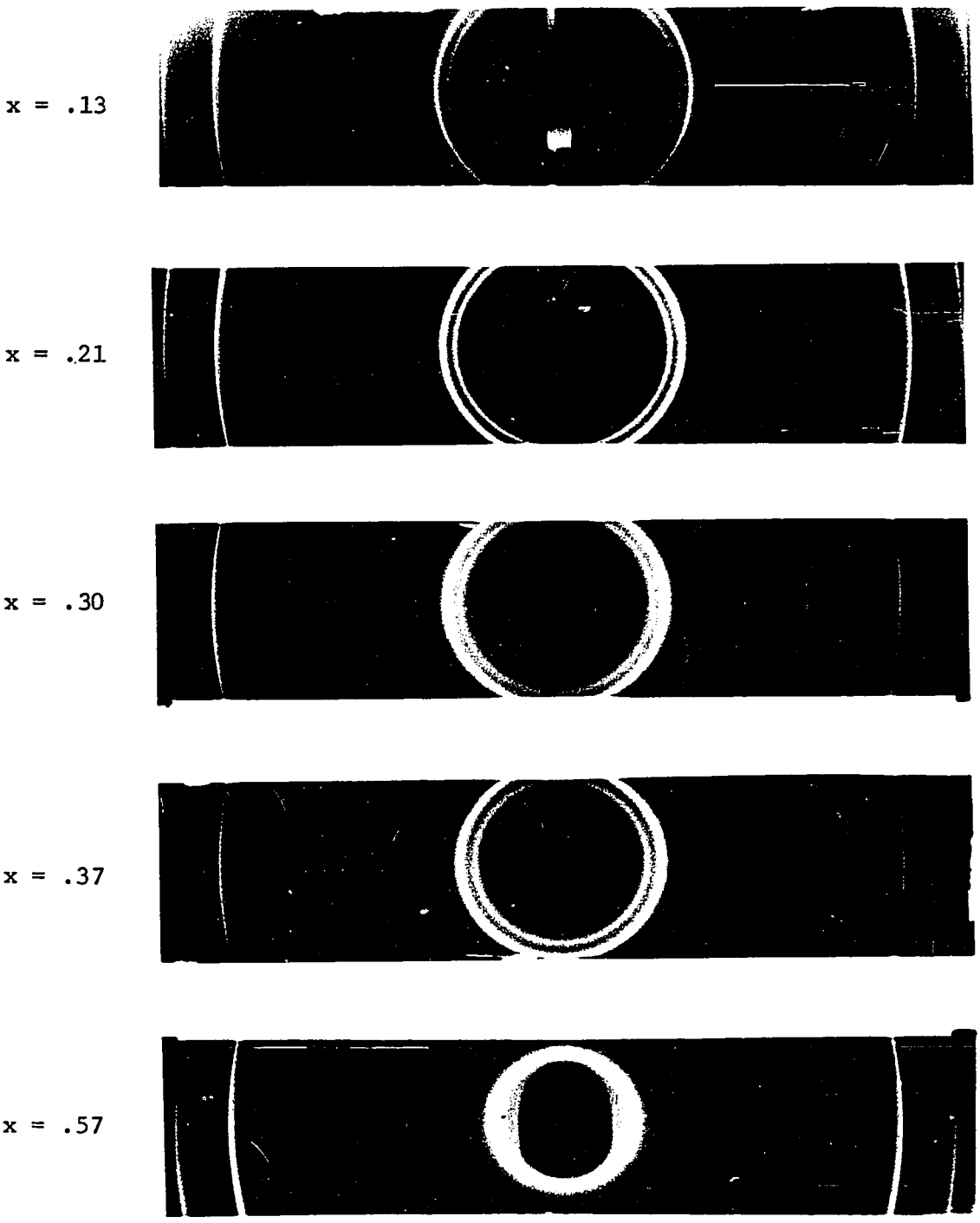

Figure 2.7 Debye-Scherrer photographs of $Pb_{1-x}Sn_xTe$ alloys

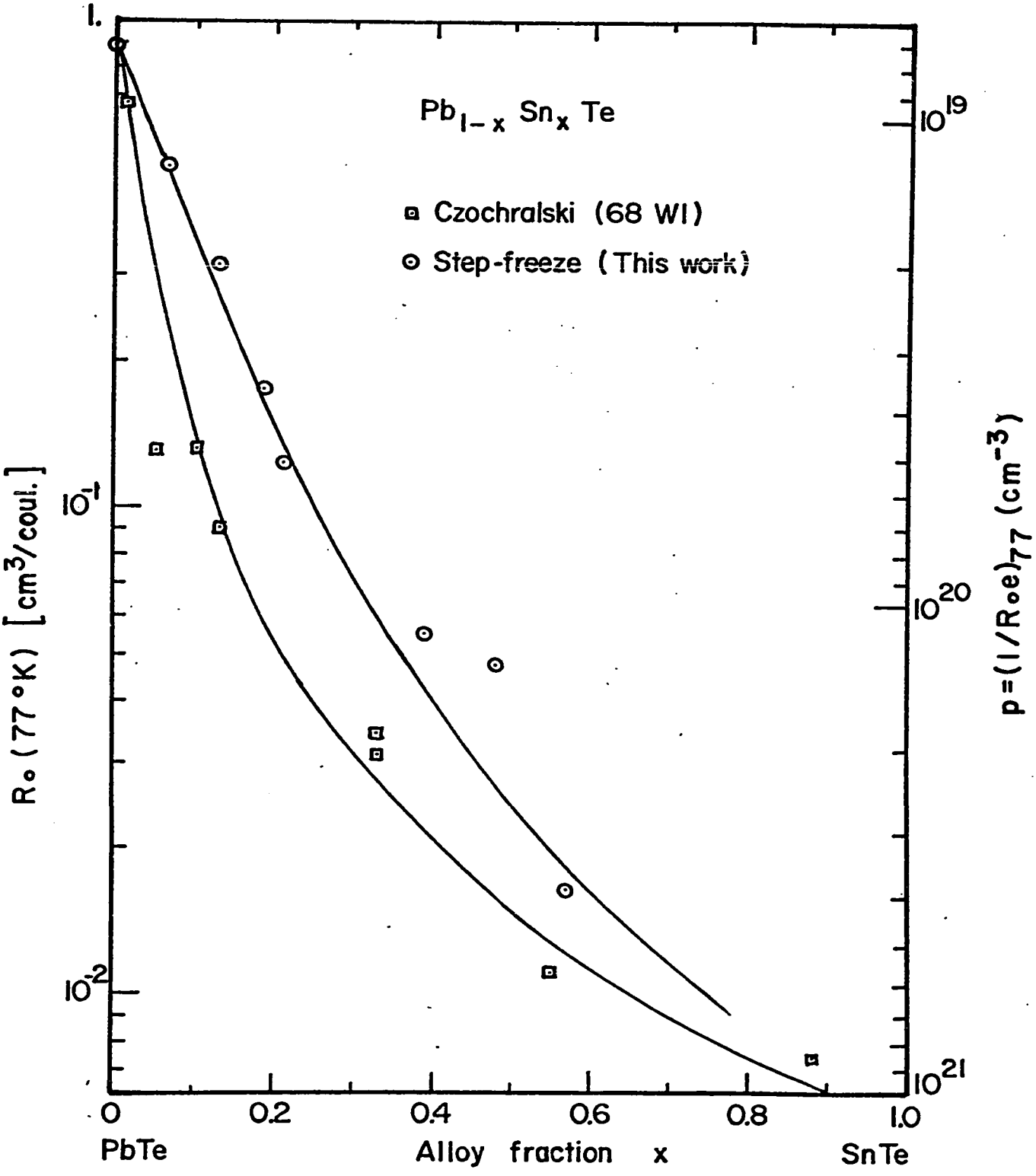

Figure 2.8 Hall coefficient vs. alloy fraction in as-grown $Pb_{1-x}Sn_xTe$ alloys.

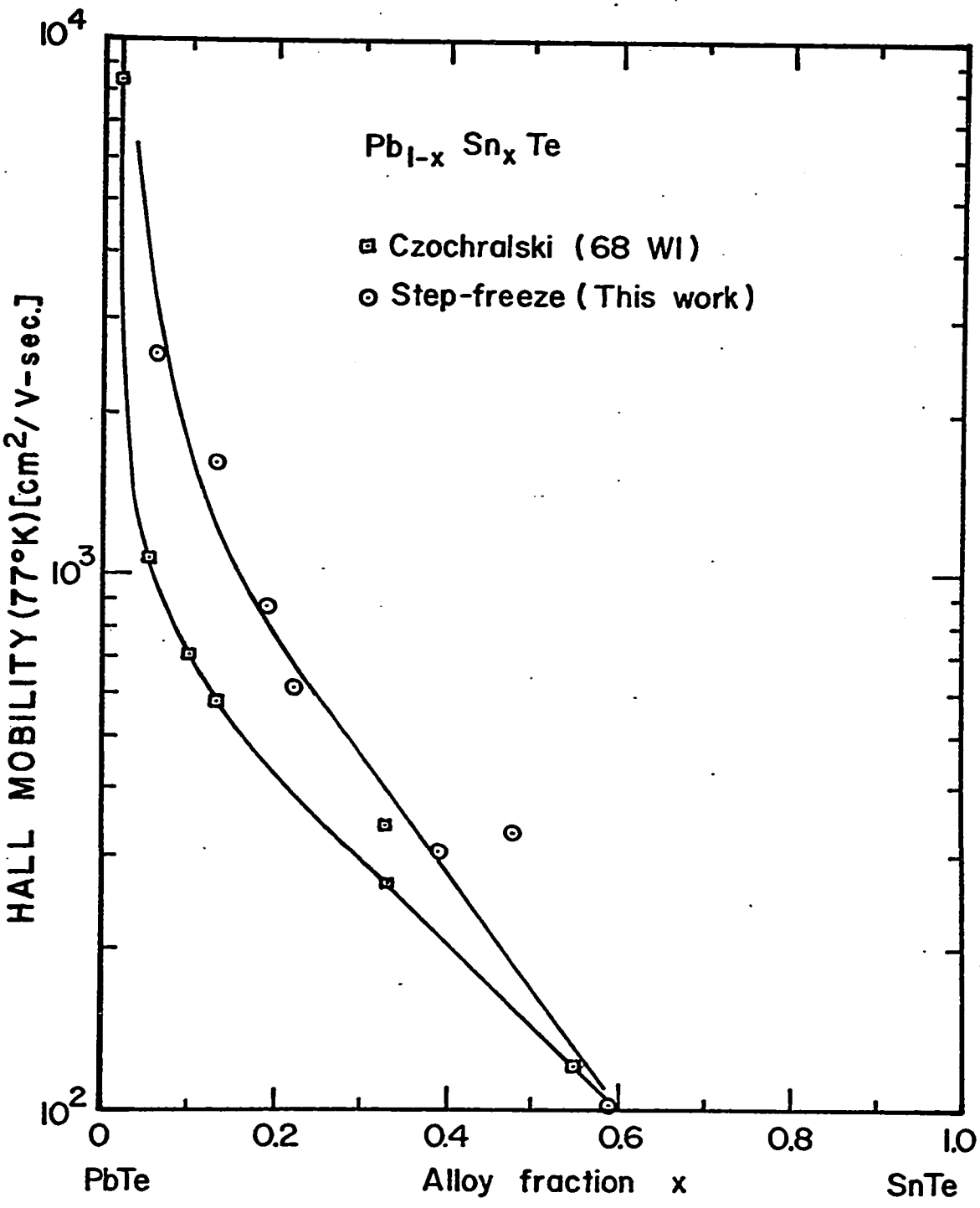

Figure 2.9 Hall mobility vs. alloy fraction in as-grown $Pb_{1-x}Sn_xTe$ alloys.

2.4 Isothermal Annealing

As pointed out in Section 2.3.1, the carrier concentration can be used to measure the deviation for stoichiometry in MN systems. This is because the non-stoichiometry is due to vacancies which ionize to produce carriers. It should be pointed out that, in addition to carriers due to the non-stoichiometry, intrinsic carriers and carriers due to ionized impurities may contribute to the total carrier concentration. In the present work, the lowest carrier concentration investigated in $Pb_{1-x}Sn_xTe$ is about 10^{17} cm^{-3}. At the temperature of the measurements (77^oK), the intrinsic carrier concentration is negligible and the doping is believed* to be much less than 10^{17} cm^{-3}. Thus, the total carrier concentration is a direct measure of the non-stoichiometry. In fact, in SnTe each tin vacancy produces 2 holes (63 B2, 64 B1). We will assume 2 holes/vacancy for the whole alloy range in $Pb_{1-x}Sn_xTe$.

The purpose here is to prepare $Pb_{1-x}Sn_xTe$ samples of different carrier concentrations by controlling the deviation from stoichiometry. Before we describe the methods of achieving this, a knowledge of the various phase diagrams, describing the non-stoichiometry, is required. A general review of this information is given by Strauss and Brebrick (68 S1). Here we will summarize briefly the main features of these phase diagrams.

*This belief is based on the fact that the starting elements were 6-9's grade and that the material was cleanly encapsulated in a closed quartz tube for growth. However, no impurity analysis was done to see if the quartz container contributed impurities to the grown material.

2.4.1 Non-Stoichiometry-Phase Diagrams.

Let us consider generally the binary system of elements M and N. The phase relation can be completely specified by a three-dimensional pressure temperature composition (P-T-n) diagram, where n is used to represent the atomic fraction of element N. It is conventional to present this information in the form of two-dimensional projections called: T-n, P-n, and P-T projections.

Figure 2.10a is a schematic representation of the T-n projection. The deviation from stoichiometry is so small that, on the scale shown, it is a line phase with n = 0.5. Expansion of the abscissa around n = 0.5 reveals the homogeneity range as shown schematically in Figure 2.10b. The compositions of the maximum melting point are larger than n = 0.5 in all three projections. They are approximately the "as-grown" compositions in the step-freeze technique. The "as-grown" material is thus more and more N-rich (or p-type) for the T-n projections from left to right. This corresponds to the situation in $Pb_{1-x}Sn_xTe$ with increasing SnTe content as shown earlier (Section 2.3.1) and as indicated above the individual projections. Below the maximum melting point, the M-saturated and N-saturated solidus lines define the boundary of the homogeneity range. For the rightmost T-n projection (that corresponding to SnTe) the homogeneity range is entirely on the N-rich side, and does not contain the stoichiometric composition. Thus, it is not possible to obtain undoped SnTe which is

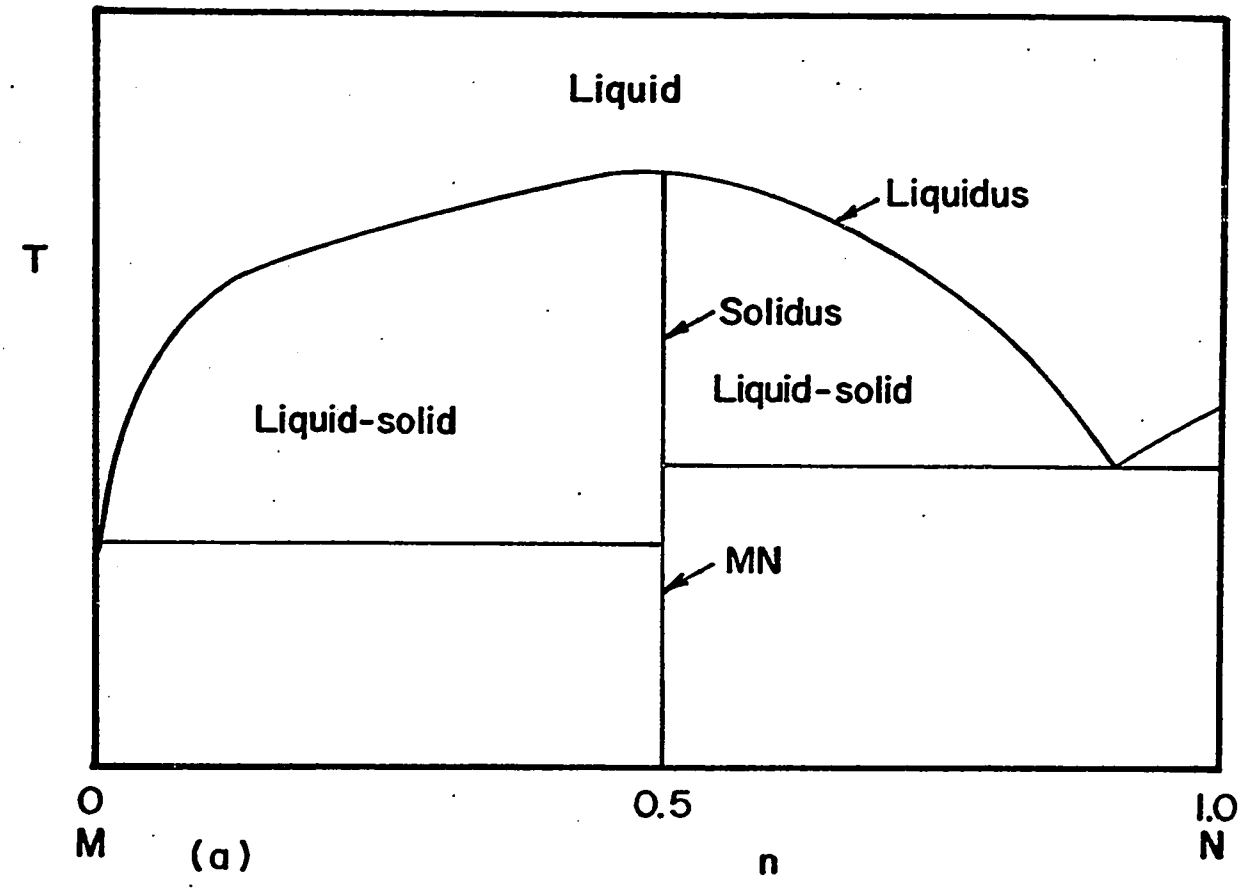

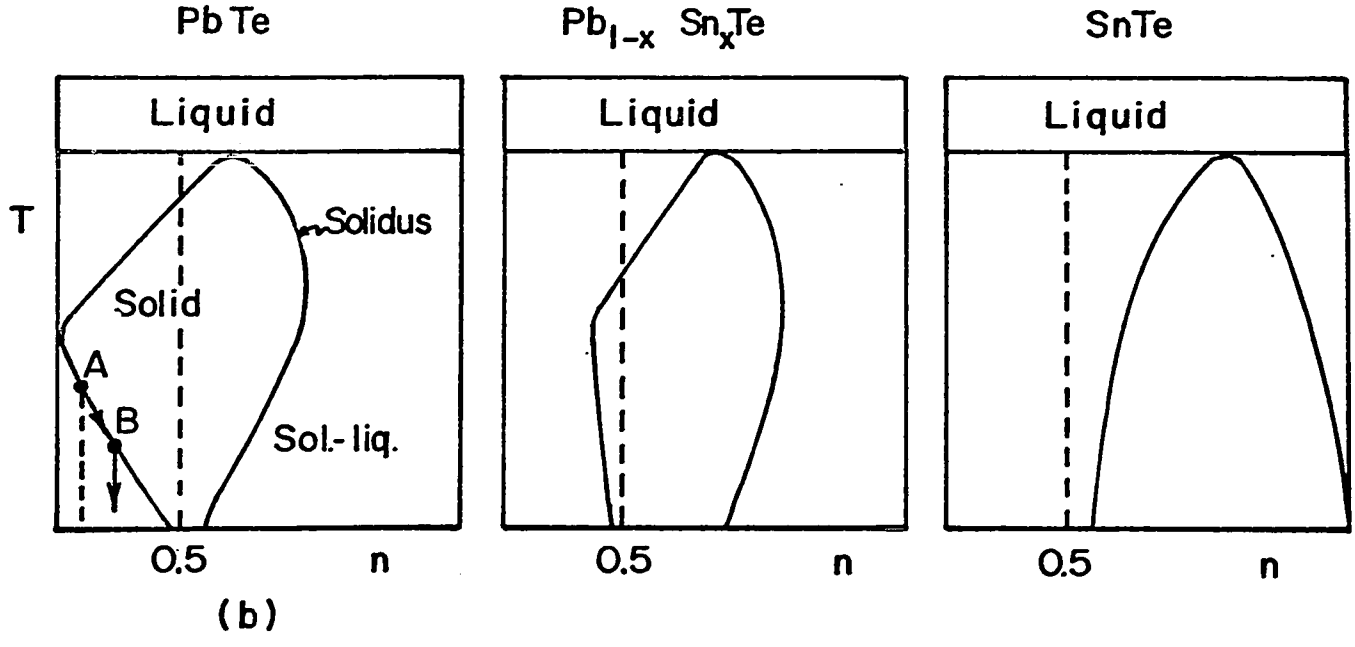

Figure 2.10 Schematic T-n projections. T is the temperature and n is the atomic fraction of the element N in the binary system MN. In b) the abscissa has been expanded around 0.5 n.

M-rich or n-type. However, the homogeneity range for undoped $Pb_{1-x}Sn_xTe$ contains the stoichiometric composition (at least up to $x \sim .3$) for some range of temperature making it possible to obtain both n- and p-type specimens without doping.

It is important to note here that the T-n projection shows a retrograde solubility below a certain temperature in the PbTe rich alloys. If, for example, a solid PbTe sample is made Pb-rich at a temperature corresponding to point A in Figure 2.10a, an extremely fast quenching rate would be required to quench this phase to room temperature as indicated by the dotted line. At room temperature, the phase would then be preserved since diffusion at room temperature is negligible (see Section 3.5.3). In practice, however, quenching rates, fast enough to prevent precipitation in the first instant of cooling, may not be attainable, and the cooling curve may coincide with the solidus down to an effective quenching temperature corresponding to point B. The precipitation process is the only one fast enough to be significant here (the loss of excess Pb to the vapor phase is negligible during quenching); it requires diffusion over small distances only. The same situation exists on the N-saturated portion of the solidus line where micro-precipitates of N may form during cooling. The extent of this precipitation will depend on the temperature at which the retrograde solidus line is crossed. The lower this temperature the less precipitation will occur, and, at a temperature below which diffusion over short distances is slow, precipitation does not occur.

Figure 2.11a illustrates schematically the P-n projection. The abscissa scale is distorted to show liquid, solid-liquid, and solid regions. The partial pressure of the N_2 molecules (P_{N_2}) at a constant temperature is shown. It is to be noted that, in the region where the liquid, the solid, and the vapor co-exist, the partial pressure is independent of n and is entirely determined by the temperature. Also, there is a large change in N_2 partial pressure across the narrow homogeneity range. This is also illustrated in the P-T projection.

Figure 2.11b shows the P-T projection in the vicinity of the homogeneity range. Log P versus 1/T are the standard coordinates for this projection because in many cases log P and 1/T are linearly related. As in Figure 2.11a, only the P_{N_2} partial pressure is shown since it is in general much larger than the partial vapor pressure of M. The loop is called the three-phase line since solid, liquid, and vapor co-exist on it. Inside the loop, only solid and vapor co-exist while, outside the loop, there is only liquid and vapor. The upper branch gives the partial vapor pressure P_{N_2} for solid MN in equilibrium with N-rich liquid; the lower branch gives P_{N_2} for solid MN in equilibrium with N-rich liquid. At relatively low temperatures, the upper and lower branches meet the partial vapor pressure for pure N and pure M, respectively. By fixing the temperature and the partial vapor pressure P_{N_2}, one can obtain equilibrated MN solids of a given composition within the homogeneity range. Since composition data can be obtained from carrier concentration measurements, as explained earlier,

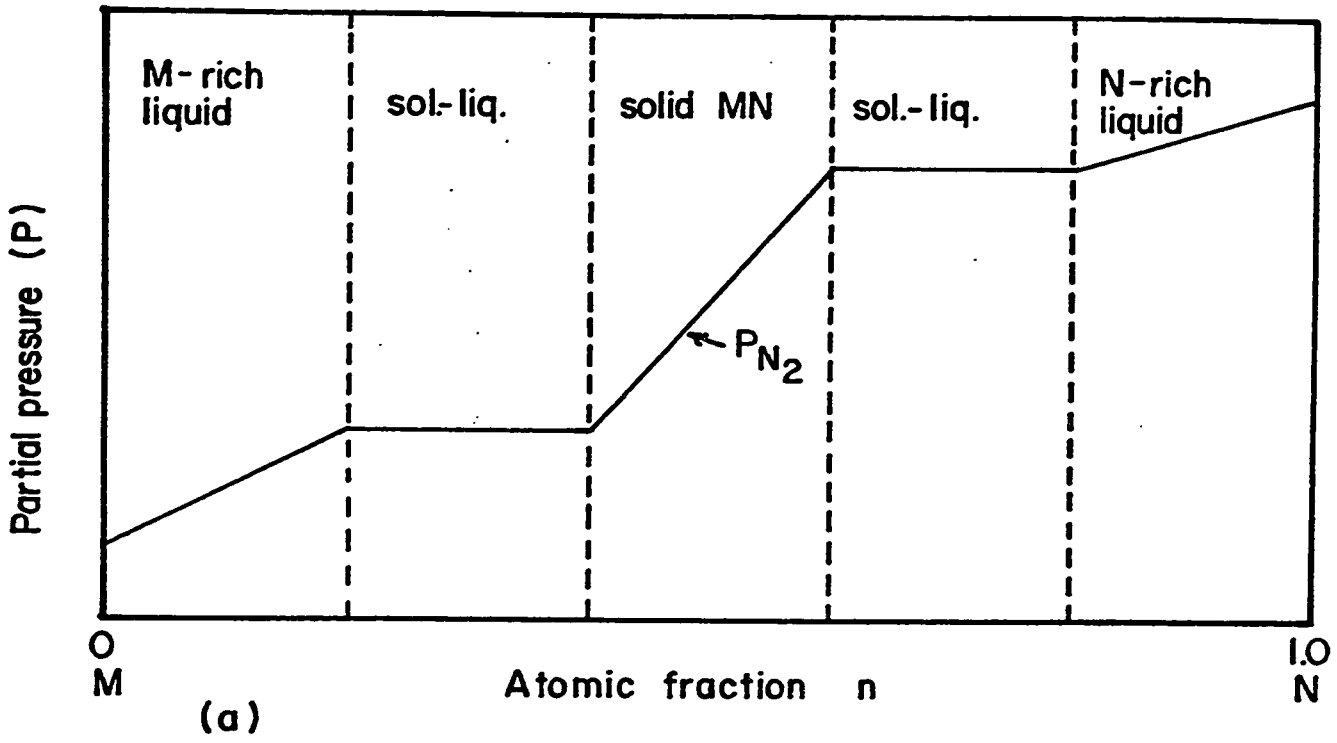

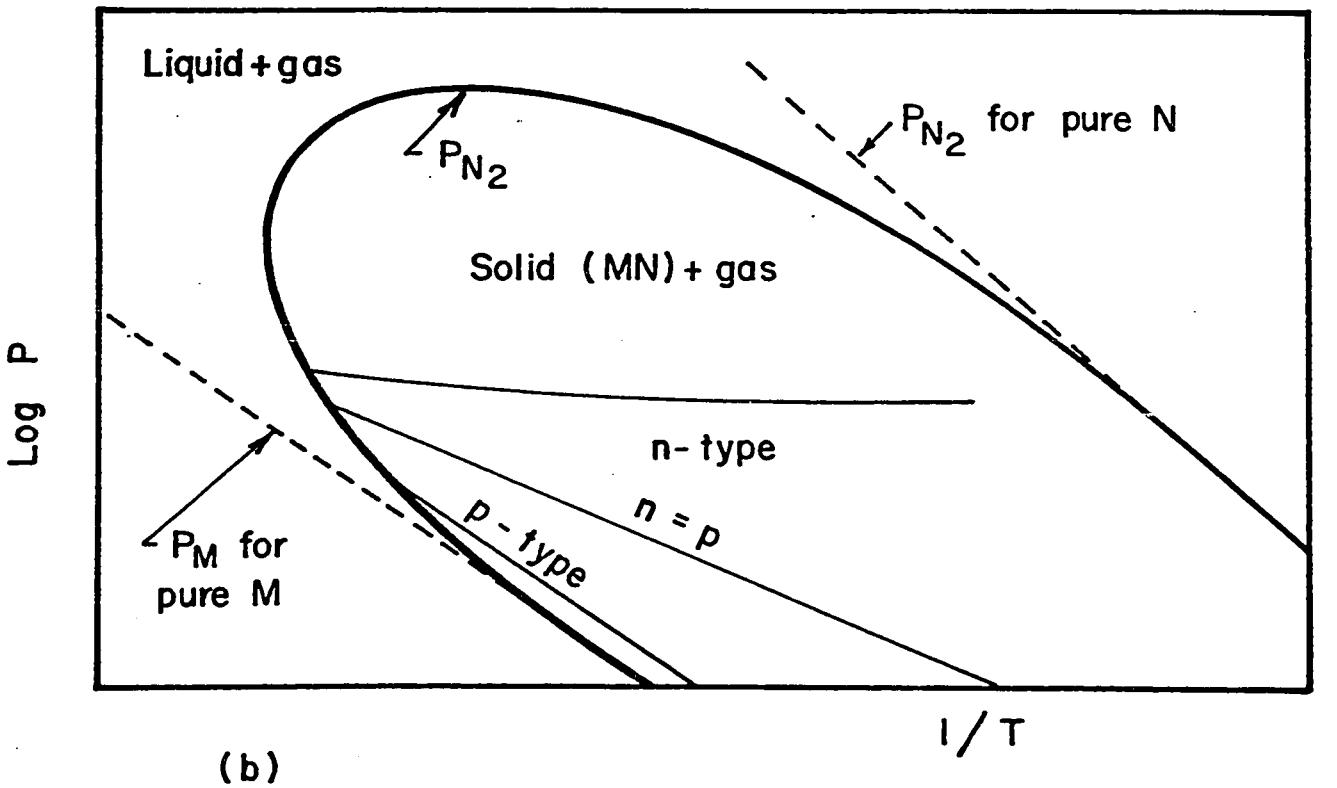

Figure 2.11 Schematic projections a) P-n projection b) P-T projection with lines of constant carrier concentrations inside the loop.

lines of constant composition inside the homogeneity region are often shown as lines of constant carrier concentration. This is illustrated schematically in Figure 2.11b which shows a few lines of constant carrier concentrations inside the homogeneity range.

2.4.2 Methods of Controlling Carrier Concentration

The above phase diagrams suggest several methods by which the non-stoichiometry (or carrier concentration) can be controlled. For example, the carrier concentration can be controlled by fixing the temperature and the partial vapor pressure P_{N_2} over the solid MN. However, this is a technique that requires special furnaces to control the two variables P_{N_2} and T. Another more practical method was first used by Brebrick and Allgaier in PbTe (60 B1). The technique involved the equilibration under isothermal conditions of a Pb-rich PbTe charge with a small sample of PbTe. The charge and the sample are enclosed in a sealed quartz ampoule the volume of which is made small enough to prevent any change of composition of the condensed phase by volatilization. At equilibrium, the PbTe sample lies on the Pb-rich solidus line and is made to retain that phase by fast quenching to room temperature. For the alloys system $Pb_{1-x}Sn_xTe$, this technique requires the preparation of metal rich charges having the same Pb-Sn ratios as those of the samples to be annealed. We will now describe the simplified annealing techniques used here.

a) Equilibration with Small Charges

The annealing technique, used in the present experiment, is based on the same principle as that of Brebrick and Allgaier (60 B1). As seen earlier, if the MN system is closed and contains all three phases (liquid, solid, and vapor) it has only one degree of freedom and fixing the temperature fixes the equilibrium composition of each phase. Thus, if the composition of the charge and the sample together lie in the liquid-solid region (between the liquidus and the solidus line in Figure 2.10a), the solid composition and the liquid composition are fixed by that of the solidus and the liquidus line at the annealing temperature, and the partial pressure P_{N_2} in equilibrium with the system is fixed by the annealing temperature as seen in Figure 2.11a. When the above condition is satisfied, the composition of the sample changes by solid state diffusion until, at equilibrium, it reaches the M-satureated or N-saturated solidus line depending on whether the charge is M-rich or N-rich. By varying the annealing temperature, solid specimens can be equilibrated to various non-stoichiometry represented by the solidus line in Figure 2.10b and corresponding to various carrier concentrations.

The simplification of the present annealing technique over those used elsewhere (see, for example, 60 B1 and 68 C2) is in the use of minute charges of pure N or pure M only. Since the only requirement is that the composition of the sample and the charge together lie

between the solidus and the liquidus curve at the annealing temperature, the amount of M or N needed is given by:

$$\text{atoms of M or N} > \left(p(\text{sample}) - p\ (\text{at the solidus line})\right)/2 \qquad (2\text{-}4)$$

in which p represents carrier concentration and 2 carriers per vacancy has been assumed. For example, let us consider a PbTe sample, with 2×10^{19} holes cm^{-3} and of dimensions .1 x .3 x 1. cm^3, which is to be equilibrated at a temperature for which the Pb-saturated solidus line is at the stoichiometric composition. The number of atoms of pure Pb required is given by equation (2-4) and is $> 3 \times 10^{17}$ cm^{-3}. Thus only a little over .1 mg of pure lead, introduced in the quartz ampoule with the PbTe sample, is necessary to equilibrate the sample to the stoichiometric composition. The exact amount is not critical and in general 2 to 3 times the amount calculated using equation (2-4) can be used to ensure that the composition of the charge and the sample together is well in the liquid-solid region. At the start of the annealing, the Pb charge is liquid. The excess tellurium in the sample is transferred (via vapor phase) to the charge until the charge has collected enough Te to cross the liquidus line. Then, the charge will be partly liquid and partly solid until equilibrium is reached. At equilibrium, the sample is lead saturated and lies on the solidus line. If the amount of pure lead used is so large as to prevent the charge from reaching the liquidus line before the samples reach the solidus line, then

surface melting of the specimen will occur to provide the extra Te needed by the charge to reach the liquidus line. Thus, the upper limit to the amount of pure Pb needed to prevent melting of the specimen depends on the position of the liquidus line in the T-n projection. It is given by

$$\text{atoms of M} < \frac{\Delta p}{2}\left(\frac{1-n}{n}\right) \tag{2-5}$$

$$\text{atoms of N} < \frac{\Delta p}{2}\left(\frac{n}{1-n}\right) \tag{2-6}$$

in which $\Delta p/2$ is the right handed side of equation (2-4) and n is the composition of the appropriate liquidus at the annealing temperature. For example, in PbTe n = .1 at 700°C for the Pb-rich liquidus. From equation (2-5) we find $9(\Delta p/2)$ as the upper limit to the number of atoms in the Pb charge.

For $Pb_{1-x}Sn_xTe$ alloy samples, the charges used were pure tellurium and mixture of lead with tin for N- and M-saturation, respectively. The mixtures of lead with tin were prepared for every 5 atomic percent by melting at high temperatures followed by hard quenching. For M-saturation the mixture having the closest Pb-Sn ratio to that of the $Pb_{1-x}Sn_xTe$ sample to be equilibrated was used. It was not necessary to have exactly the same Pb-Sn ratio in both the charge and the specimen because the charge was minute and could not produce an appreciable change in composition x of the much larger $Pb_{1-x}Sn_xTe$ sample. The charges were weighed using a precision balance.

For the samples to be annealed, the weight of the charges ranged from .1 to 1.3 mg. After the annealing treatment was over, the small quartz ampoule containing the sample was quenched in water.

The main advantages of the present annealing technique are:

-The preparation of the charge is simple and exactly the same Pb-Sn ratio as the one in the sample is not required as it was in previous techniques (60 B1, 68 C2). Thus, it is not necessary to prepare a charge for every composition x of the $Pb_{1-x}Sn_xTe$ samples to be annealed.

-The specimen and the small charge can be easily separated inside the quartz ampoule and no complications such as "tube within a tube" (68 C2) is necessary to separate them.

-Owing to smaller size quartz ampoules, it is easier to have the whole ampoule in a region of constant temperature in the furnace. This is desirable to prevent transport of the sample, through the vapor phase, toward colder regions of the ampoule.

-The small size of the quartz ampoule permits higher quenching rates. Fast quenching is desirable, as seen earlier, to prevent internal precipitation.

The results of the annealing experiments using the above technique are given in Table 2.2 for several composition x of $Pb_{1-x}Sn_xTe$ alloys. The first column gives the sample number. The

Sample #	Charge	Thickness (mm)	Temp. (°C)	Annealing Time (days)	Carrier Concentration $p = \left(\frac{1}{R_o e}\right)_{77°K}$ (cm^{-3})	Mobility $\mu_H = (R_o \sigma)_{77°K}$ $cm^2/v.sec$
			a) Composition: 6% SnTe			
6-0	none	as-grown			1.25×10^{19}	2,560
6-1	Te	1.02	771	4	3.20×10^{19}	860
6-6	M	1.56	869	4	6.41×10^{18}	4,670
6-5	M	1.3	845	8	3.33×10^{18}	7,370
6-4	M	1.1	810	4	9.00×10^{17}	12,870
6-3	M	1.4	800	6	5.06×10^{17}	14,300
6-2	M	1.42	771	4	1.56×10^{17}	14,920
6-8	M	1.5	680	30		
			b) Composition: 21% SnTe			
8-1	none	as-grown			5.10×10^{19}	612
8-3	Te	1.6	842	2 3/4	1.32×10^{20}	164
8-5	Te	1.34	771	4	1.17×10^{20}	188
8-6	Te	1.34	800	6	1.10×10^{20}	211
8-2	M	1.76	842	2 3/4	2.14×10^{19}	1,660
8-7	M	1.43	800	6	1.08×10^{19}	3,270
8-4	M	1.68	771	4	7.11×10^{18}	4,750
8-8	M	1.5	680	30	2.88×10^{18}	9,550

TABLE 2.2 RESULTS OF ISOTHERMAL SATURATION ANNEALING EXPERIMENTS IN $Pb_{1-x}Sn_xTe$ ALLOYS GROWN BY THE STEP-FREEZE TECHNIQUE

Sample #	Charge	Thickness (mm)	Temp. (°C)	Annealing Time (days)	Carrier Concentration $p = \left(\frac{i}{R_o e}\right)_{77°K}$ (cm^{-3})	$\mu_H = (R_o \sigma)_{77°K}$ $cm^2/v.sec$
				c) Composition: 13%		
2-2	none	as-grown			2.00×10^{19}	1,600
2-2.1	M	1.	734	2	5.65×10^{17}	15,000
2-2.4	M	1.	712	3	7.9×10^{16}	16,000
2-2.3	M	1.	667	7	3.9×10^{17} (n)	40,600
				d) Composition: 48% SnTe		
3-8.5	none	as-grown			1.34×10^{20}	325
3-8.4	M	1.	570	21	1.13×10^{19}	4,450
				e) Composition: 30% SnTe		
3-1.8	M	1.3	570	21	4.45×10^{18} (at R.T.)	

TABLE 2.2

second column indicates the nature of the charge (M for Pb-Sn mixture, and Te for tellurium) the amount of which was determined using equation (2-4), (2-5), and (2-6) and varied from .1 to 1.3 mg for typical sample volume of .15 x 1. x .3 cm^3. The third, fourth, and fifth columns gives the thickness in mm, the annealing temperature in degree centigrade, and the annealing time in days, respectively. The annealing times were chosen to satisfy Henry's diffusion result that for $Dt/l^2 > 1$ (where D is the diffusion coefficient, t is the time, and l is the thickness of the sample) equilibration is predicted (68 C2). It should be noted here that D is the inter-diffusion coefficient, also designated the chemical diffusion coefficient, which describes the rate at which changes in composition are propagated through the crystal (59 S1). In PbTe, it has been found to be 5×10^{-8} cm^2/sec at 500°C (59 S1). Assuming this value for $Pb_{1-x}Sn_xTe$, Henry's diffusion result is satisfied for annealing time a little over 2 days for a sample 1 mm thick at 500°C. In view of the fact that the diffusion increases exponentially with increasing temperature, it is seen that $Dt/l^2 >> 1$ is satisfied in all cases listed and that equilibrium is more than reached in all cases. The sixth and seventh columns gives the carrier concentration and the Hall mobility respectively.

The results of annealing are also plotted in Figure 2.12. It could easily be converted to a T-n projection, as in Figure 2.10b, by assuming 2 carriers per vacancies, but it is more readily usable

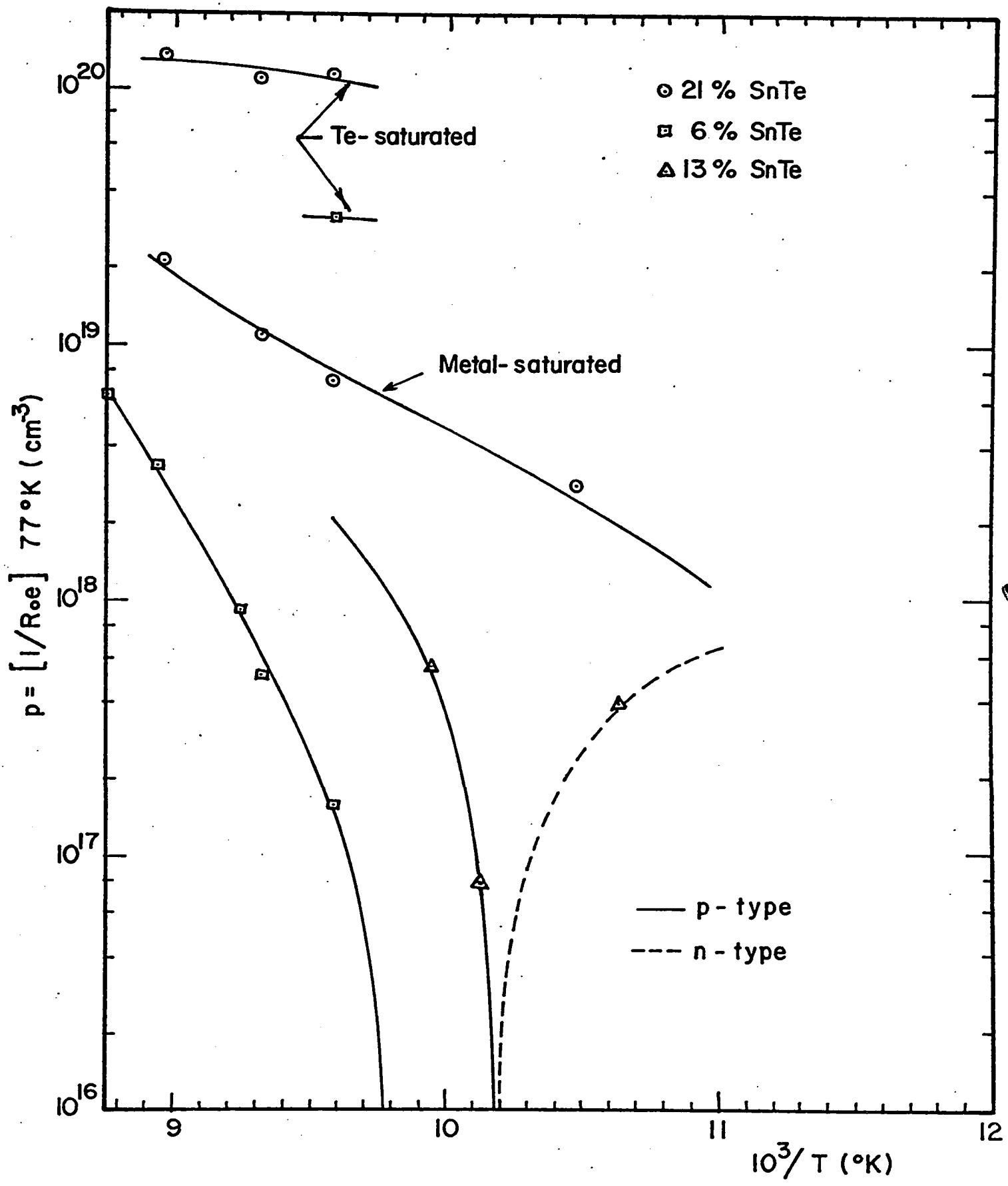

Figure 2.12 Carrier concentration (p) vs. isothermal annealing temperature in $Pb_{1-x}Sn_xTe$ alloys.

as shown. Similar curves were obtained independently by Calawa et al. (68 C2) in $Pb_{1-x}Sn_xTe$ for different compositions. The general agreement is good. However, our 13% SnTe curve shows a crossover temperature (from p-type to n-type) significantly higher than that reported by Calawa et al. (68 C2) for the same composition. This difference could be due to the presence of ionized impurities, in addition to ionized vacancies, which would be n-type in our material or p-type in Calawa et al. material.

The present technique, can also be used to obtain equilibrated solids inside the homogeneity region if a smaller charge than that required by equation (2-4) is used. At equilibrium, the charge and the sample are both solid and have identical composition determined by the temperature and the partial vapor pressure in equilibrium over both the sample and the charge. A few samples were annealed this way and were found to be in the homogeneity region as expected. We believe that it may be possible, by careful weighing of the charges, to check experimentally* the assumption that there are 2 holes/vacancy in highly doped alloys. All that would be required are the weight of the charge, and the carrier concentration before and after the equilibration.

b) Equilibration without Charges

A technique that may turn out to be practical to obtain nearly stoichiometric samples is the equilibration of a solid sample in an empty quartz ampoule of volume V_a. In PbTe, for example, the

*Houston et al. (Bull. Am. Phys. Soc., 9, 60, 1964) carried out such an experiment in SnTe and reported that the results were consistent with the assumption that there are 2 holes/vacancy.

partial vapor pressure of Te_2 in equilibrium with stoichiometric solid is much larger than that of Pb (68 S1) and hence, a net loss of Te from the specimen occurs to make up the partial vapor pressure P_{Te} in the volume V_a. Neglecting the loss of Pb vapor, the size of ampoule, V_a, required to make a p-type sample stoichiometric is given by:

$$V_a = \frac{n}{N} \frac{RT}{Ps} \qquad (2\text{-}7)$$

in which V_a is the volume of the ampoule, T is the temperature, N is the Avogadro number, R is the gas constant, Ps is the partial pressure of Te_2 in equilibrium with stoichiometric PbTe at temperature T, and n is the number of Te_2 molecules. For a p-type PbTe sample with 4×10^{17} holes cm^{-3}, it is necessary to remove $n = 10^{17}$ Te_2 molecules cm^{-3} from the sample to make it stoichiometric. Since at 800°C Ps $\approx 10^{-5}$ atmosphere (69 D1), the volume required to accommodate the molecules of Te_2, evaporating from a 1 x .1 x .1 cm^3 sample, is from equation (2-7) about 14 cm^3. The above technique was not used here since very low carrier concentrations were not wanted. But if very low carrier concentration are aimed at it may prove to be an accurate technique.

Another technique that requires very short equilibration time may be used on material grown fast or in small temperature gradients. As seen earlier, in ingots grown this way, there is metal precipitation and cellular structure (68 B1). Thus the metal charge required for M-saturation (see Section 2.4.2b) is already present in the sample

itself in the form of metal precipitates distributed in the volume of the sample. Vacuum annealing in small quartz ampoule will therefore dissolve the microprecipitates of metal and bring the sample composition towards the metal saturated solidus line (see Figure 2.10b). The time required for equilibration is very short since diffusion over short distances only is required. Therefore, very low annealing temperature can be used and lower carrier concentration may be achieved (in $Pb_{1-x}Sn_xTe$ with large SnTe content) than with any other techniques. Some of our "as-grown" material was vacuum annealed in small quartz ampoule; as expected, the carrier concentration before and after the annealing did not differ significantly. This supports our earlier conclusion that no metal precipitates were present.

2.5 Discussion

The temperature of the annealing furnace was maintained constant (± 2°C) over long periods of time and there was a negligible gradient (± 1°C) across the quartz ampoules. After the specimen had been equilibrated, the quartz ampoules, containing the samples, were quenched in water. In addition, the annealed samples were lapped, on all 6 faces, to remove about 100 μ of material before any measurements were performed. Because this procedure was scrupulously followed, we believe that our annealed samples were homogeneous in their alloy composition as well as in their carrier concentration. The homogeneity in carrier concentration was checked by measuring the resistivity at two positions along the specimens. At least 20 specimens were measured this way from 4.2°K to room temperature. For the range of temperature from 77°K to room temperature the agreement was better than 1% between the two measurements. However, in the lowest carrier concentration samples ($< 5 \times 10^{17}$) drastic changes occurred at temperatures lower than 77°K. We believe that these changes are not due to a spatial variation of the carrier concentration in the bulk of the sample, but are due to surface effects and rectifying current contacts. In support of this we noted that the higher resistivity portion of the sample reverted to the lower resistivity portion when the current was reversed. We nevertheless rejected any measurements made on these samples in the temperature range where this effect was noticeable.

For the annealed $Pb_{1-x}Sn_xTe$ samples, no sign of precipitation was detected. We believe that during the quenching the solidus curve was not crossed, or was crossed at too low temperature for precipitation to occur. This would be expected for a T-n projection of the type shown in the center of Figure 2.10b. Figure 2.12 also shows that precipitation did not occur since, for high equilibration temperatures, the carrier concentration increased with increasing temperatures. If the N-rich solidus line had been crossed during quenching the carrier concentration would have reached a constant plateau at high temperatures.

CHAPTER III

OPTICAL PROPERTIES OF $Pb_{1-x}Sn_xTe$

3.1 Introduction

The L-symmetry of the valence and conduction band extrema appears to be well established in PbTe. Because of the small energy gap, both conduction and valence bands are non-parabolic and their non-parabolicity is mainly due to the interaction of these two bands (64 C1). In fact, the two-band models of the non-parabolicity, such as the Cohen model and the Kane model, have been used with some success to explain experimental data in PbTe (65 D1, 68 C1, etc.). However, theoretical band structure investigations (66 L1, 70 O1, etc.) show that there are six relatively closely space <111> bands near the Fermi level, the interaction of which needs to be considered to determine the non-parabolicity of the valence and conduction bands. As pointed out by Dubrovskaya (70 D1), the success of the two-band models is surprising, but it can be explained because of the considerable compensation of the effects of the two higher and the two lower bands.

In p-type PbTe, the holes are mainly in the above mentioned <111> extrema at low carrier concentration. There exists evidence for extra bands contributing to conduction. Allgaier and Houston (66 A1) report, from measurements of the temperature dependence of the

Hall coefficient, that there is a heavy mass band situated .14 e.v. below the <111> extrema at 0°K. From the minimum in the curve of thermoelectric power versus carrier concentration, and the Kane model, Chernik (68 C1) reports a value as high as .28 e.v. below the <111> extrema at 120°K. To resolve such discrepancies between different types of experiments, two heavy mass bands may be necessary besides the <111> extrema. If such a situation was to exist in PbTe, non-parabolicity effects and heavy mass band effects could be difficult to distinguish. In the present experiments, we choose to investigate the p-type Pb_{1-x} Sn_xTe alloys with x = .06 and x = .2 because their band structure is similar to that of PbTe. Also it was hoped, since the main gap changes appreciably with alloying, that the relative position of all the bands participating in conduction would change enough to give new manifestation of their presence.

One of the best tools to investigate the non-parabolicity and the presence of extra bands participating in conduction is the determination of susceptibility effective masses from measurements of infrared reflectivity. Such measurements can be made over a large range of carrier concentration and temperature. To quote Dixon and Riedl (65 D1) "They serve as a stringent consistency test of proposed band models and their parameters".

In this chapter, after a brief description of the experimental arrangement, we will review briefly the theory that permits us to relate the susceptibility effective mass to the energy bands. Then, the different methods of analysis will be studied in detail. We will emphasize that section because the use of different methods often give different results and also because there are cases in the literature for which improper analysis has led to large errors. We will proceed with the results concerning the high frequency dielectric constant, the carrier concentration, and the effects of surface preparation. Finally, the optical mobility and effective mass results will be given versus carrier concentration and temperature. The prediction of the different band models will be compared with the experimental results and their consistency will be discussed.

3.2 Experimental

3.2.1 Samples

The samples were obtained from two 100 grams ingots grown from stoichiometric $Pb_{1-x}Sn_xTe$ melt containing 10% and 30% SnTe respectively. The samples were cut from circular disks, 1¼ centimeters in diameter and 3 mm thick, taken from the first quarter to freeze. Eight samples were cut from each single crystal disk using a spark cutter. The compositions of the sets of samples were 6% and 20.8% SnTe and the as-grown composition gradients across the thickness of the disks were about 0.1% and 0.3% respectively.* The different carrier concentrations were obtained through heat treatments following which about 100 microns of material was removed, from all 6 faces of the samples, to eliminate the concentration gradient present near the surface after the heat treatment. The heat treatment procedures and growth techniques are described in Chapter 2. The final dimensions of the samples were approximately 9 mm long, 2 mm wide, and 1 mm thick. After the measurements of the Hall effect, resistivity, and thermoelectric power had been performed, the samples were prepared for the reflectivity measurements.

Two polishing procedures have been used. The first one consisted of chemical etching to remove all the surface damage followed by a light mechanical polish using .05 μ powder to improve to maximum the reflectivity which deteriorated during the etching. It was thought

*As determined from the measured variation in alloy composition versus distance around the chosen disks.

that the light mechanical polish would cause negligible damage in a thickness small compared to the penetration depth of the infrared light. This assumption proved to be wrong as we shall see later (Section 3.5) and the measurements had to be rejected because of improper surface preparation. A good etching technique was subsequently found which produced a smooth mirror-like surface. The second and correct polishing procedure consisted of a mechanical polish, using no more than 0.1 μ powder, followed by a 2-5 min chemical etching that eliminated the thin damaged layer and produced a smooth mirror-like surface. The etching solution used consisted of 10 volume of ethylene glycol, 2-3 volume of H_2O_2 and 10 volume of KOH. The etching procedure was that described for similar etches by Coates et al. (61 C1). The samples were held using bare stainless steel tweezers. The sensitive variables were the proportion of H_2O_2 and the degree of agitation. Occasionally, the surface quality deteriorated during the etching, and the whole procedure, starting with mechanical polishing, was repeated until the smooth mirror-like surface was obtained. The etching rate was estimated to be 5 μ/min.

3.2.2. Reflectivity Arrangements

The source of monochromatic radiation was a Baird Associate double beam infrared spectrometer modified for single beam use. A wavelength range from 2 to 23 μ was available using NaCl and KBr prisms for the shorter (2-16 μ) and the longer wavelengths (12-23 μ) respectively.

The reflectometer is shown in Figure 3.1. A first spherical mirror is collecting all the light from the exit slit of the monochromator and focuses its image on the sample. The reflected light is then focused onto the detector using a short focal length ellipsoidal mirror. The signal from the bolometer detector is amplified using a preamplified and a lock-in-amplifier tuned to the chopping frequency of the light. The reflected intensity is read on a digital voltmeter or recorder.

A cryostat similar to that described by Fortin (70 F1) was mounted on a table that provided movement in three perpendicular directions. In addition, rotation about the axis of the cold finger was possible for both the cold finger and the windows independently. Three samples could be mounted on the cold finger together with an aluminium mirror. The sample and the window were adjusted so that only the light reflected from the sample could be collected; the light reflected from the window being eliminated in a systematic way, as shown in Figure 3.1.

The reflectivity was measured by a comparison of the intensity reflected from the sample with that reflected from the mirror both measurements being performed in identical conditions. In particular, the light was focussed on the bolometer sensitive area so that the image of the exit slit was always centered on the sensitive area and contained within it. Also, the stability of the light source (globar) was checked by measuring the intensity reflected

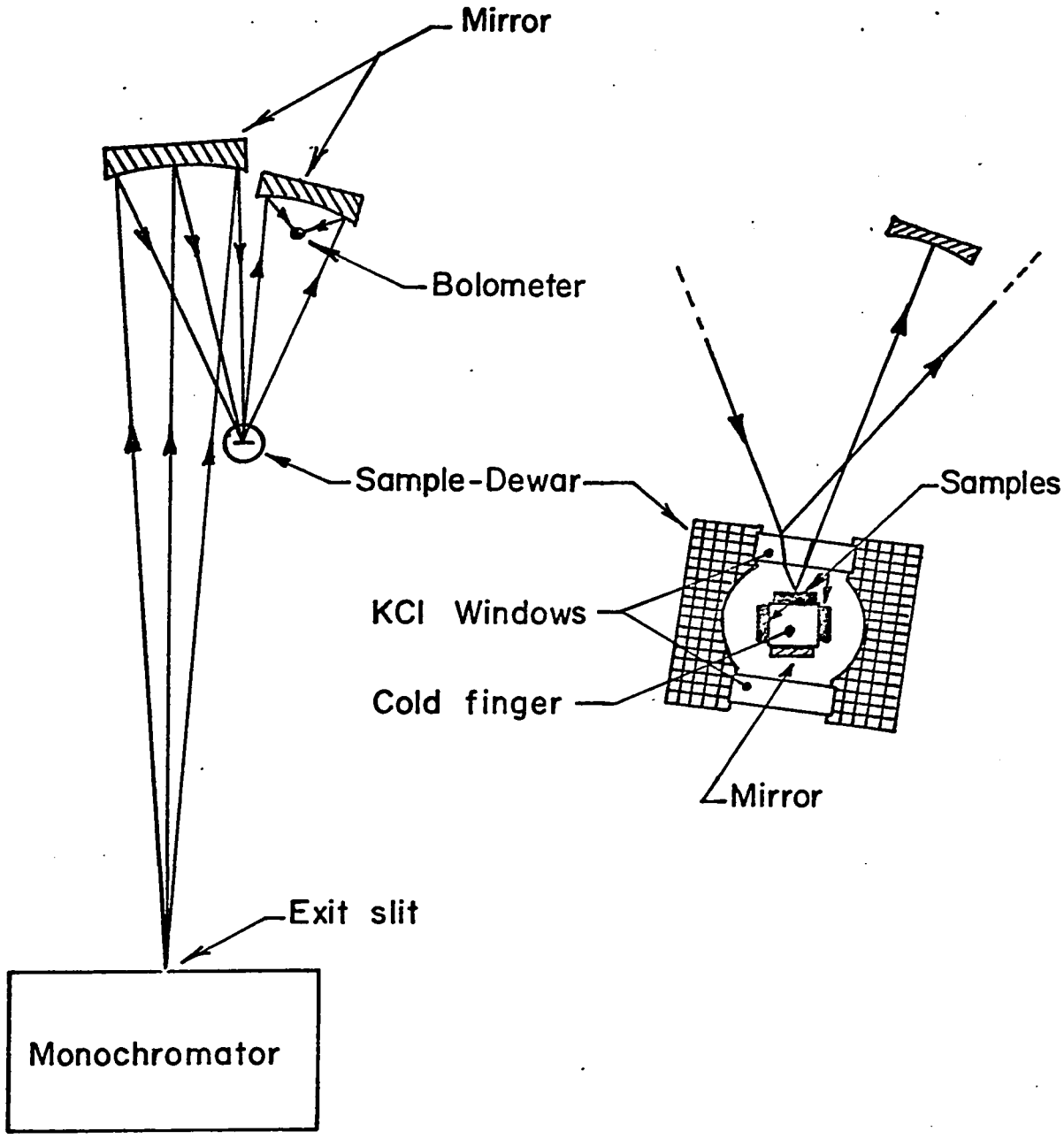

Figure 3.1 Schematic of reflectometer.

from the mirror both before and after that reflected from the sample. The measurements were rejected when the difference between the two mirror measurements was greater than 2%.

The samples were mounted on the cold finger using Silastic. The temperature was measured using a copper-constantan thermocouple soldered to the copper cold finger. The angle of incidence of the light on the sample was about 10^{o} from normal for the central rays and 15^{o} from normal for the extreme rays.

3.3 Theory

In this section, we intend to describe the phenomenon of reflection from a classical view point. The quantum mechanical treatment provides a more detailed picture, but leads to equations similar in form to those of the classical treatment in all cases of interest here (60 M1, p.29).

We will start with the Maxwell's equations to describe the phenomenon on the macroscopic scale through quantities such as dielectric constants. Then, these optical constants will be expressed in terms of the details of the interaction of light with matter to extract quantities such as the effective mass. Finally, the effective mass will be related to the band structure of the material.

3.3.1 Macroscopic Description-Optical Constant

For a non-magnetic material, the Maxwell's equations which describe the macroscopic behavior of electromagnetic waves in an uncharged polarizable medium may be written in M.K.S. units:

$$\text{div. } (\varepsilon_o \overline{E} + \overline{P}) = 0 \qquad \text{curl. } \overline{E} = -\frac{\partial}{\partial t} \mu_o \overline{H} \tag{3-1}$$

$$\text{div. } \overline{H} = 0 \qquad \text{curl. } \overline{H} = \sigma \overline{E} + \frac{\partial}{\partial t}(\varepsilon_o \overline{E} + \overline{P})$$

in which ε_o and μ_o are the dielectric constants and permeability of free space, and the other symbols have their usual meaning. In the particular case of cubic crystals the polarization $\overline{P}$ is proportional

to the field and can be expressed by:

$$\overline{P} = \varepsilon_o \chi \overline{E} \tag{3-2}$$

where χ, a scalar quantity, is called the electric susceptibility. The electric displacement thus becomes:

$$\varepsilon_o \overline{E} + \overline{P} = \varepsilon_o (1 + \chi)\overline{E} = \varepsilon_o \varepsilon \overline{E} \tag{3-3}$$

which defines the specific dielectric constant ε of the medium. Substitution of equations (3-3) in equations (3-1) leads to the wave equation for $\overline{E}$:

$$\nabla^2 \overline{E} - \mu_o \sigma \frac{\partial \overline{E}}{\partial t} - \mu_o \varepsilon \varepsilon_o \frac{\partial^2 \overline{E}}{\partial t} = 0 \tag{3-4}$$

a solution of this equation for waves propagating in the x direction is:

$$E = E_o \text{ exp. } i\omega(t - x/v) \tag{3-5}$$

which is a plane wave of amplitude E_o, frequency ω, and phase velocity v. The solution (3-5) satisfies equation (3-4) provided:

$$\frac{c^2}{v^2} = \varepsilon - i\sigma/\omega\varepsilon_o \tag{3-6}$$

Thus, if σ and ε are known for a material, equations (3-6) and (3-5) specify the nature of the wave in that material. However, it is more convenient to define other pairs in terms of a complex refractive

index $\tilde{N}$, and a complex dielectric constant $\tilde{\varepsilon}$:

$$\tilde{\varepsilon} \equiv \varepsilon_1 + i\varepsilon_2 \equiv \frac{c^2}{v^2} \tag{3-7}$$

$$\tilde{N} \equiv \eta + i\kappa \equiv \frac{c}{v} \tag{3-8}$$

where η is the index of refraction, κ is the extinction coefficient, ε_1 and ε_2 are the real and imaginary parts of the dielectric constants. Equations (3-6), (3-7) and (3-8) lead to the following relations:

$$\begin{aligned} \eta^2 - \kappa^2 &= \varepsilon_1 = \varepsilon \\ 2\eta\kappa &= \varepsilon_2 = \sigma/\omega\varepsilon_o \end{aligned} \tag{3-9}$$

In what follows, we will be concerned with the measurement of the reflectivity R at normal incidence on thick specimens in air. It is given in Moss (60 M1, p.6):

$$R = \frac{(\eta - 1)^2 + \kappa^2}{(\eta + 1)^2 + \kappa^2} \tag{3-10}$$

Such measurements and any measurements yielding knowledge of the pairs (ε,σ), $(\varepsilon_1,\varepsilon_2)$ or (η,κ) fully describe the situation macroscopically. On the atomic scale, the alternating electric field of the incident light causes the electrons or ions to oscillate which in turn reradiate to produce the reflected beam. Consequently, the reflected beam contains information about the mass, the concentration,

and the interaction of these electrons or ions in the solid. The determination of any of the above pairs cannot yield this microscopic information unless they are related to models that describe the physical processes on the atomic scale. The different dispersion mechanisms will now be reviewed for the range of frequencies of interest.

3.3.2 Microscopic Description-Dispersion Mechanisms

The macroscopic parameter $\tilde{\varepsilon}$, the complex dielectric constant, varies widely with temperature and frequency within the same cubic material. To explain these variations, a model based on the atomic structure of the material is needed. A basic concept from the atomic viewpoint is that of the electric dipole moment $\bar{p}$. It is related to the macroscopic electric polarization $\bar{P}$ which appears in the equations (3-1) by:

$$P = Np = N\,e\,x \qquad (3\text{-}11)$$

Where N is the concentration of particles each of charge e and displacement x from the equilibrium position.

In Figure 3.2, a reproduction from Kittel (56 K1, p.165), illustrates the different contributions to polarization in solids. The division of polarization into three types: electronic, ionic, and orientational, is quite general. As the frequency increases the different components disappear as they no longer respond to fast

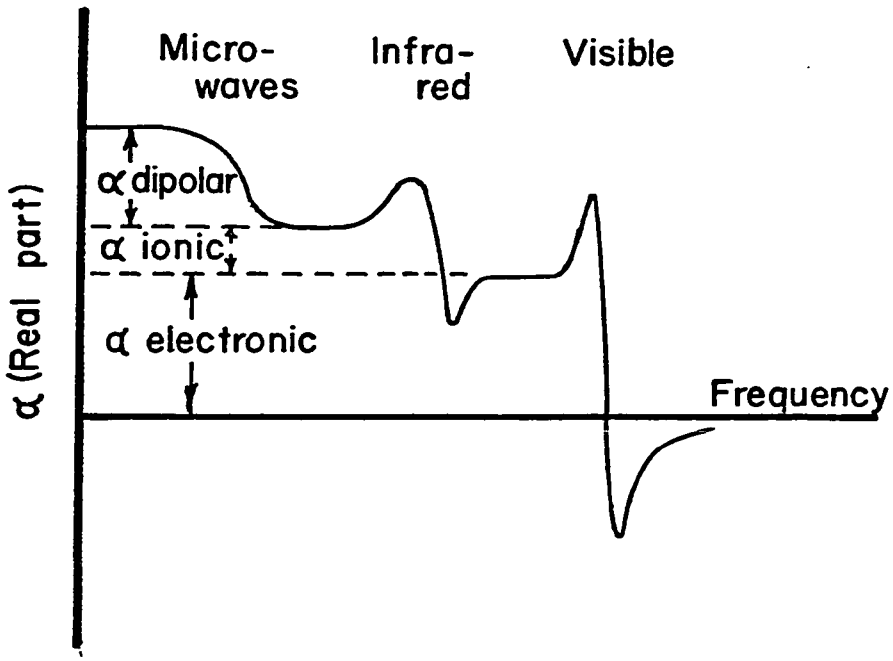

Figure 3.2 Frequency dependence of the polarizability $\alpha_i = p_i/E$.

changes in the applied field. These changes usually occur at radio or microwave frequencies for the orientational polarization, in the infrared region for the ionic polarization, and in the visible or ultraviolet region for the electronic polarization. Our attention will be focused here on the range 4-25 μ of infrared radiation for which the total contribution to polarization, in the material studied, is electronic with perhaps a small contribution from ionic polarization at the longest wavelengths considered.

The electronic contribution to polarization in semiconductors is further characterized in terms of the electronic energy bands. The effects of the electrons or holes may be intraband or interband in nature.

In Figure 3.2, a single resonance is shown at high frequencies. There are in fact several resonances for frequencies equal or higher than the main gap between the valence and the conduction bands. They correspond to interband transitions in which light has sufficient energy to excite the carriers from one band to another. In all cases studied here, the frequencies used are lower than those corresponding to valence-conduction band transitions. However, for p-type materials, intervalence band transitions may contribute a small polarization when the holes are present in two or more valence bands closely spaced in energy. The main contribution to polarization, for the range of wavelength used here, is electronic intraband.

It is also convenient to distinguish between the polarization arising from free carriers and bound carriers. The bound electrons in a semiconductor are all those not contributing to electronic conduction. Their contribution to the dielectric constant is constant over the range of wavelength 4-25 μ except at the smaller wavelengths where the energy of the photons is close to that corresponding to valence-conduction band transitions.

To summarize, of the different dispersion mechanisms to be considered in the present experiment, the main one is the free-carrier dispersion. All other contributions to polarization, mentioned above, are constant or small, and the corresponding dispersion mechanisms will be briefly reviewed and called corrections.

a) Free-Carrier Dispersion

The theory of the free-carrier dispersion is developed in detail by Moss (60 M1). The classical and quantum mechanical treatments lead to similar results. According to the classical model, the free carriers with effective mass m*, and charge e are displaced by an amount x under the influence of the total field E and are subject to a retarding force $m^*\gamma \frac{dx}{dt}$. The equation of motion is:

$$m^* \frac{d^2x}{dt^2} + m^*\gamma \frac{dx}{dt} = eE e^{i\omega t} \qquad (3\text{-}13)$$

in which the applied field of the incident radiation has been written for the effective field acting on the electron. The effective

field includes the field due to the other electrons as well and is in general different from the externally applied field. Darwin (43 D1) found that the effective field, if the carriers are free, is the applied electric field E. For bound charges, the assumption that the effective field equals the applied field has been discussed by Stern (63 S1, p.343) and Moss (60 M1, p.17). It is mentioned there that the assumption is valid in highly polarizable medium such as the one under study. With this assumption the passage from a microscopic description to a macroscopic description is greatly simplified and equations (3-11) and (3-2) can readily be used. If γ is assumed to be independent of frequency, equation (3-13) can be solved for the amplitude x which is:

$$x = \frac{e\,E}{m^*\omega(\omega + i\gamma)} \tag{3-14}$$

For a system of N electrons or holes, each of charge q and mass m^*, one passes to a macroscopic description and dielectric constant using equations (3-11) and (3-2)

$$\tilde{\chi}_{FC} = \frac{P}{\varepsilon_o E} = \frac{Ne^2}{\varepsilon_o m^*\omega(\omega+i\gamma)} \tag{3-15}$$

As mentioned earlier, the bound carrier contribution is constant over the wavelength range of interest. The susceptibility $\tilde{\chi}_{BC}$ is obtained by adding a restoring force βx to equation (3-13) and by making the same assumption that the total field is identical

to the applied field. It thus follows that the susceptibility due to free carriers and the susceptibility due to bound carriers are additive:

$$\tilde{\varepsilon} = 1 + \tilde{\chi}_{FC} + \tilde{\chi}_{BC} = \varepsilon_{\infty} + \tilde{\chi}_{FC} \tag{3-16}$$

in which $\varepsilon_{\infty} \equiv 1 + \tilde{\chi}_{BC}$ is real and is usually called the high frequency dielectric constant. Using equations (3-9) to obtain the real and imaginary part of ε, we have:

$$\eta^2 - \kappa^2 - \varepsilon_{\infty} = \frac{-Ne^2}{m^* \varepsilon_o} \left[\frac{1}{\omega^2 + \gamma^2} \right] \tag{3-17a}$$

$$2\eta\kappa = \frac{Ne^2}{m^* \varepsilon_o \omega} \left[\frac{\gamma}{(\omega^2 + \gamma^2)} \right] \tag{3-17b}$$

The quantity γ is given its full meaning when the steady field solution of equation (3-13) is considered. For a steady field, we have $m^*\gamma \, dx/dt = eE$, but in a steady field $\frac{dx}{dt} = \mu E$ where μ is the mobility. Thus:

$$\gamma = \frac{e}{\mu m^*} = \frac{1}{\tau} \tag{3-18}$$

The scattering time τ is expected to be the same at optical frequencies as in the steady state since τ is dependent on the velocity of the carriers (thermal velocity) which is hardly modified by the application of the alternating electric field of the incident light.

Equations (3-17) are directly applicable to semiconductors provided γ is independent of frequency and there is total degeneracy. In this case, no average is necessary to arrive at equations (3-17).* As pointed out by Lyden (64 L1), the assumption that γ is independent of frequency is not restrictive since it is determined by the temperature, the energy-band structure, and imperfections of the crystal. The degeneracy condition is often satisfied, in particular, for measurements performed at low temperatures. For example, for the lowest carrier concentration that will be investigated in the range 4-25 μ, the Fermi energy in the samples studied was about 0.1 e.v. (Section 3.5) corresponding to high degeneracy at liquid nitrogen temperature ($E_F/kT \sim 10$).

If the condition of high degeneracy is not met, as for measurements at high temperatures, then equations (3-17) must be averaged with respect to the distribution function. In the case of parabolic bands the effective mass is a constant independent of energy and the average over the distribution function is performed on the bracketed terms only. When this is done, the ω and τ dependences are no longer explicit and the equations are not readily usable. Lyden (64 L1) has proposed the following approximations:

$$\left\langle \frac{\tau^2}{1 + \omega^2\tau^2} \right\rangle \simeq \frac{\langle\tau\rangle^2}{1 + \omega^2\langle\tau\rangle^2} \qquad (3\text{-}19)$$

$$\left\langle \frac{\tau}{1 + \omega^2\tau^2} \right\rangle \simeq \frac{\langle\tau\rangle}{1 + \omega^2\langle\tau\rangle^2}$$

*For anisotropic energy surface an average over direction is required.

where $\gamma = 1/\tau$ has been used and the average is performed over the Fermi-Dirac distribution function f_o, according to the standard formula (63 B1, p.94)

$$\langle A \rangle \equiv \frac{\int_o^\infty \frac{-\partial f_o}{\partial E} A(E)\, E^{3/2}\, dE}{\int_o^\infty \frac{-\partial f_o}{\partial E} E^{3/2}\, dE} \tag{3-20}$$

Lyden has discussed in detail the effect of this approximation. It is found to introduce no error when τ is independent of energy E and in the case of high degeneracy as stated earlier. Assuming that $\tau = \tau_o E^s$ the ratio of the correct average over the approximated average in equations (3-19) has been calculated by Lyden for acoustical (s = -1/2), dislocation (s = -1/2), optical (s = 1/2), and ionized impurity (s = 3/2) scattering for different degrees of degeneracy and values of $\omega\tau$. Figure 4 of Lyden (64 L1) summarizes these results. In most practical cases, the error involved in this approximation is small. The error due to the degree of degeneracy in Lyden's approximation can be greatly diminished by using, after Rheinlander (70 R1); the following approximations:

$$\left\langle \frac{\tau^2}{1+\omega^2\tau^2} \right\rangle \simeq \frac{\langle\tau^2\rangle}{1+\omega^2\langle\tau^2\rangle} = \frac{r^2\langle\tau\rangle^2}{1+\omega^2 r^2\langle\tau\rangle^2}$$

$$\left\langle \frac{\tau}{1+\omega^2\tau^2} \right\rangle \simeq \frac{\langle\tau\rangle}{1+\omega^2\langle\tau^2\rangle} = \frac{\langle\tau\rangle}{1+\omega^2 r^2\langle\tau\rangle^2} \tag{3-21}$$

which differs from the Lyden's approximation by the added factor $r^2 = \langle\tau^2\rangle/\langle\tau\rangle^2$. For acoustical scattering $1 < r^2 < 1.18$. For ionized impurity scattering $1 < r^2 < 1.93$ and is given by $r^2 = 0.75\, F_{1/2}(\zeta)\, F_{7/2}(\zeta)\, [F_2(\zeta)]^{-2}$ where $\zeta = E_F/kT$ and $F_n(\zeta)$ are standard Fermi integrals. It should be pointed out here that the low field Hall constant for spherical bands is given by $R_o = \frac{r^2}{Ne}$, in which r^2 is the same as above. Thus, the low field Hall constant can be used in the determination of the effective mass using equation (3-17a) and (3-19) which become: $\eta^2 - \kappa^2 - \varepsilon_\infty = \frac{-e}{R_o m^* \varepsilon_o} \frac{r^4\langle\tau\rangle^2}{1 + \omega^2 r^2 \langle\tau\rangle^2}$.

Because the above equations are often used to determine the effective mass variation due to the non-parabolicity of the energy bands, a question arises: what is the meaning of the experimental value of the effective mass determined? For parabolic bands, the effective mass determined is the conductivity effective mass (57 S1). For non-parabolic bands however an effective mass must be defined for each phenomenon studied and it depends on the energy according to the particular energy dispersion relation for that band. Let us call this mass the susceptibility effective mass m_s.

When $\omega\tau >> 1$, equation (3-15) is independent of the scattering time and becomes:

$$\chi_{FC} = \frac{-Ne^2}{\varepsilon_o \omega^2 m_s} \tag{3-22}$$

in which m_s, the susceptibility effective mass is some reciprocal average over energy to be specified later. For the case of high

degeneracy, the susceptibility effective mass and the conductivity effective mass are identical even for non-parabolic bands (see Section 3.3.3).

For the general case, when both the effective mass and the scattering time vary with energy, we have to assume that the bracketed terms in equation (3-17) can be averaged separately. This assumption is not restrictive for equation (3-17a) since in all cases studied $\omega\tau$ is sufficiently large and the bracketed term does not depend much on the energy. However, this is clearly not a good approximation for equation (3-17b). We nevertheless make the assumption for both equations (3-17) in order to bring out explicitly the dependence of all variables. We will discuss later the effect of this assumption in equation (3-17b) on the measurement of scattering time. As far as the measurement of susceptibility effective mass is concerned, the assumption is quite valid since the susceptibility mass is determined almost exclusively by equation (3.17a). It is to be noted that, for finite temperatures, the susceptibility effective mass is well defined while the conductivity effective mass cannot be defined due to the inseparability of τ and m for non-parabolic bands.

The above assumption allows us to use the approximation (3-21) with the understanding that m_s is the quantity measured and that for non-parabolic band $r^2 = \langle\tau^2\rangle/\langle\tau\rangle^2$ is calculated using (64 K1):

$$\langle A\rangle \equiv \frac{\int_0^\infty -\frac{\partial f_o}{\partial E}\, A(E)\, \gamma^{3/2}(E)\, dE}{\int_0^\infty \frac{-\partial f_o}{\partial E}\, \gamma^{3/2}(E)\, dE} \qquad (3\text{-}23)$$

which is more general than equation (3-20) and is valid for energy surfaces described in tensor notation by:

$$1/2\ A_{\alpha\beta}\ k_\alpha k_\beta = \gamma(E) \tag{3-24}$$

in which the components $A_{\alpha\beta}$ are constants independent of energy, and $\gamma(E)$ is an arbitrary function of energy. For parabolic bands $\gamma(E) = E$ and equation (3-23) reduces to equation (3-20). For a simplified Kane band, $\gamma(E) = E + E^2/E_G$. The expression for τ is given by (64 K1):

$$\tau = \tau_o\ \gamma^s\ (d\gamma/dE)^{-1} \tag{3-25}$$

which reduces to $\tau = \tau_o E^s$ for parabolic bands.

Values of $r^2 = \langle\tau^2\rangle/\langle\tau\rangle^2$ have been calculated using equations (3-23) and (3-25) for $\gamma(E) = E + E^2/E_G$. The integrations were performed numerically on a computer for several values of the energy gap (E_G), temperature and Fermi energy (E_F). Figure 3.3 shows selected results for acoustical scattering (s = -1/2) and ionized impurity scattering (s = 3/2). The corresponding curves for optical scattering (s = 1/2) are not shown since r^2 does not deviate appreciably from $r^2 = 1$.

To summarize, for all cases of interest here, the electronic contribution to susceptibility or dielectric constant may be written

$$\eta^2 - \kappa^2 - \varepsilon_\infty = \frac{-Ne^2}{m_s \varepsilon_o} \quad \frac{r^2\langle\tau\rangle^2}{1 + \omega^2 r^2 \langle\tau\rangle^2} \tag{3-26a}$$

$$2\eta\kappa = \frac{Ne^2}{m_s \varepsilon_o \omega} \quad \frac{\langle\tau\rangle}{1 + \omega^2 r^2 \langle\tau\rangle^2} \tag{3-26b}$$

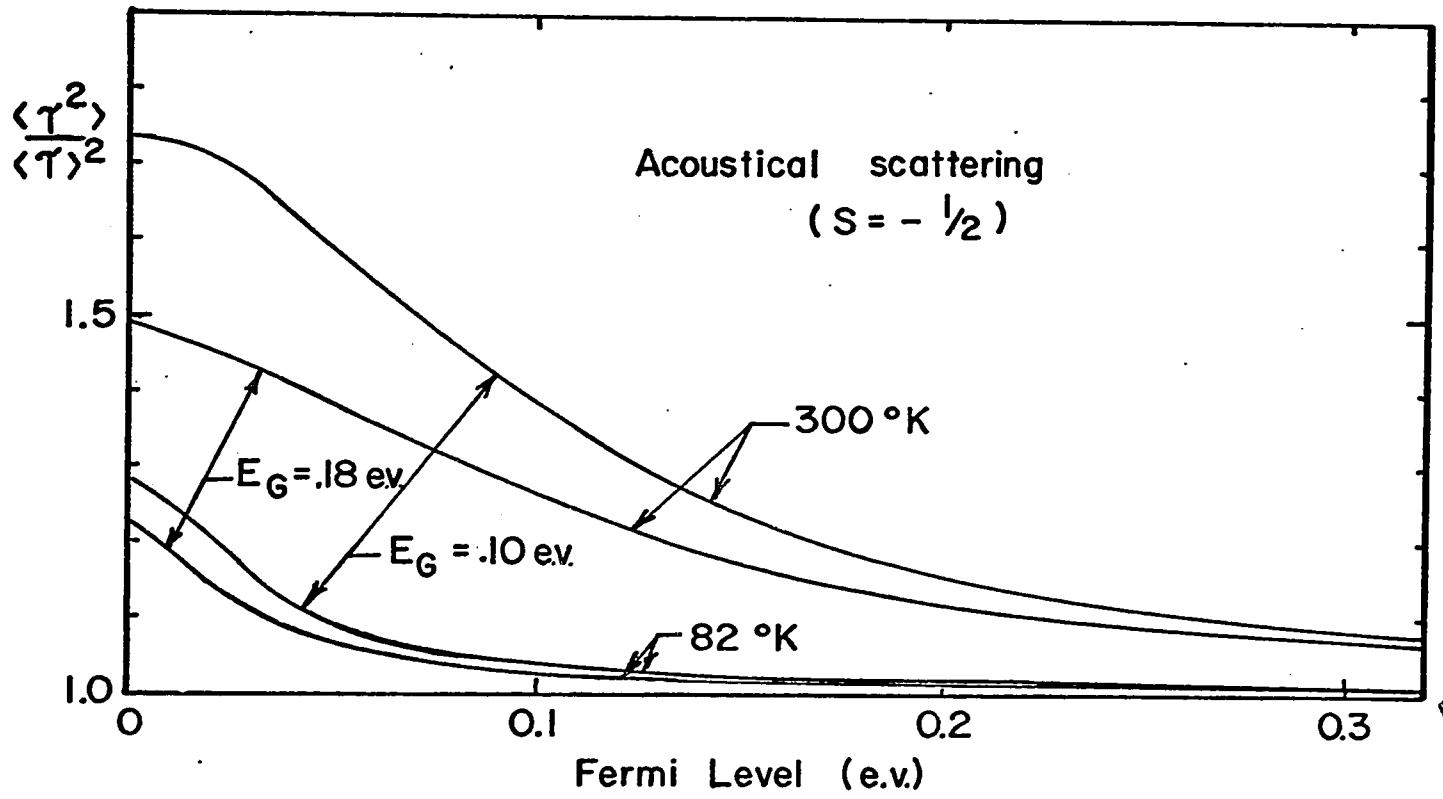

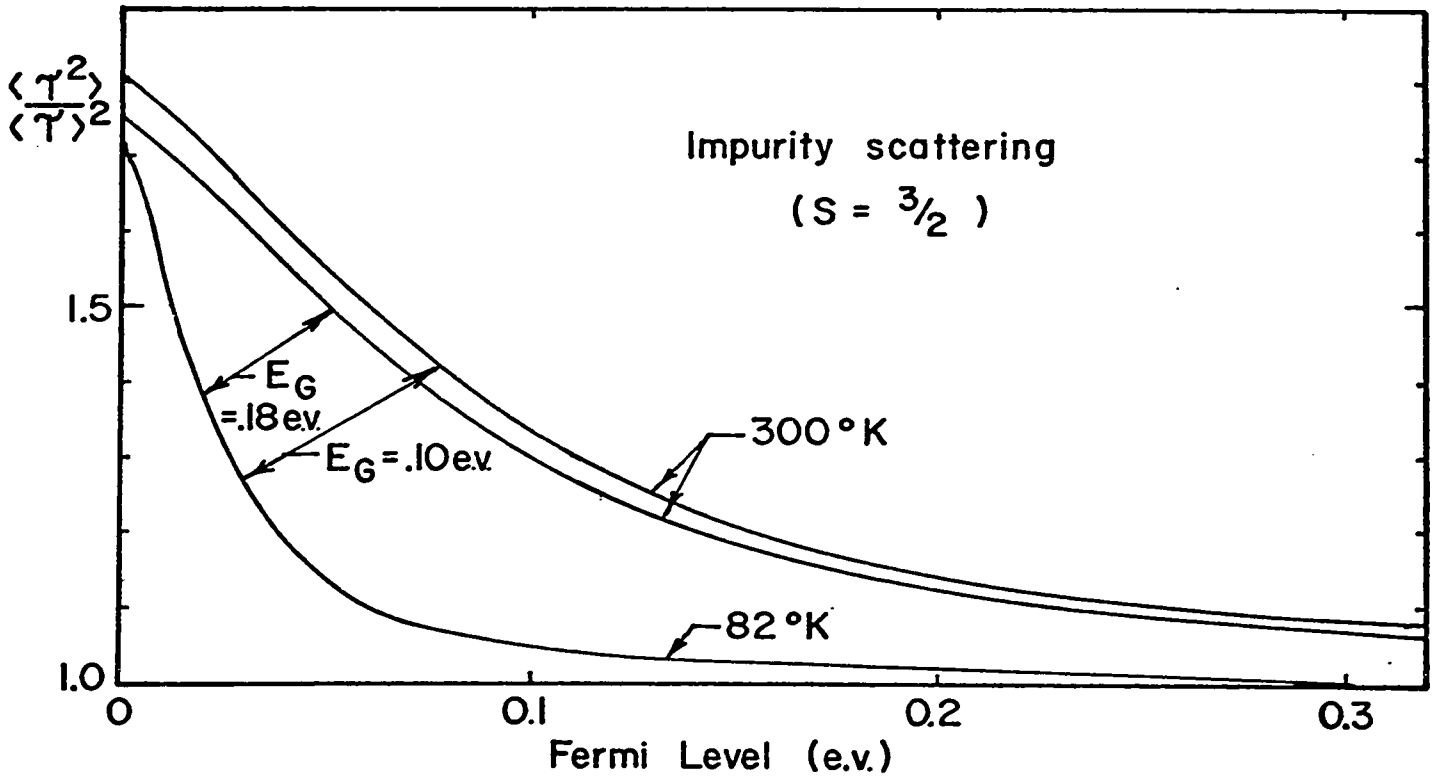

Figure 3.3 $\langle\tau^2\rangle/\langle\tau\rangle^2$ vs. Fermi level.

in which $r^2 = \langle\tau^2\rangle/\langle\tau\rangle^2$ and the brackets indicate the proper average with respect to energy.

b) Corrections for Other Dispersion Mechanisms

As mentioned earlier, there may be other contributions to susceptibility namely: deviation of bound carrier dispersion from a constant ε_∞, lattice (or ionic) dispersion, and inter-band dispersion. Their susceptibilities add, as discussed previously, and we have:

$$\tilde{\varepsilon} = (1 + \tilde{\chi}_{BC}) + \tilde{\chi}_{FC} + \tilde{\chi}_{LV} + \tilde{\chi}_{I-B} \qquad (3\text{-}27)$$

The use of equation (3-26) implies that the bracketed term in equation (3-27) is a constant equal to ε_∞ and that the last two terms are negligible. Let us now consider the necessary corrections when these conditions are not met.

1) Bound Carrier Dispersion

The bound carriers are localized and attached to the atoms by a force equal to βx. The natural angular frequency of the system is $\omega_o = \sqrt{\beta/m}$. Thus, the restoring force may be written as $m\,\omega_o^2 x$. Adding this extra term in equation (3-13) and solving for x leads to:

$$x = \frac{eE}{m(\omega_o^2 - \omega^2 + i\omega\gamma)} \qquad (3\text{-}28)$$

When assuming that the effective field equals the applied field equation (3-28) gives for N bound electrons of mass m:

$$\tilde{\varepsilon}_{BC} = 1 + \tilde{\chi}_{BC} = 1 + \frac{e^2}{\varepsilon_o} \frac{N}{m} \frac{1}{(\omega_o^2 - \omega^2 + i\omega\gamma)} \qquad (3\text{-}29)$$

As ω decreases, for wavelengths longer than those corresponding to valence-conduction band transitions, $\kappa << \eta$ and equation (3-29) may be approximated by:

$$\eta^2 - 1 = \frac{Ne^2}{m\varepsilon_o} (\omega_o^2 - \omega^2)^{-1} \qquad (3\text{-}30)$$

The deviation of ε_∞ from a constant in that range of wavelengths is thus given by:

$$\Delta\varepsilon_\infty = \varepsilon_\infty \frac{\omega^2}{(\omega_o^2 - \omega^2)} = \varepsilon_\infty \frac{\lambda_o^2}{\lambda^2 - \lambda_o^2} \qquad (3\text{-}31)$$

A quantum mechanical treatment gives similar results. The only difference is that equation (3-29) is summed over a set of linear oscillators each with a resonance frequency corresponding to an allowed transition of oscillator strength f. As $\omega \to 0$, $\tilde{\varepsilon} = \varepsilon_1$ and $\kappa = 0$ giving:

$$\varepsilon_\infty = \eta^2 - 1 = \frac{Ne^2 f}{m\varepsilon_o \omega_o^2} \qquad (3\text{-}32)$$

in which it is assumed that the material can be well described by a single oscillator of frequency ω_o and of oscillator strength f.

According to Moss (60 M1, p.190), PbTe can be roughly represented by two oscillators: one of oscillator strength f = 4 at .68 μ and one of oscillator strength f = .1 at 2 μ. For n oscillators we have:

$$\Delta\varepsilon_\infty = \varepsilon_\infty \sum_n \sum_{m=1}^{n} \frac{f_n \lambda_{on}^2}{f_m \lambda_{om}^2} \cdot \frac{\lambda_{on}^2}{\lambda^2 - \lambda_{on}^2} \qquad (3\text{-}33)$$

which gives for PbTe : $\Delta\varepsilon_\infty = .82\ \{.46/(\lambda^2 - .46)\} + .18\ \{4/(\lambda^2 - 4)\}$. For $\lambda = 5\ \mu$ and $\lambda = 10\ \mu$, the increase of ε_∞ with respect to its constant long wavelength value is equal to 5% and 1% respectively. This rough calculation indicates that small changes of ε_∞ are expected for pure PbTe only at the lowest wavelengths in the range of interest (4 - 25μ).

In practice, equation (3-33) is not immediately usable in estimating the corrections since values for oscillator frequencies and strength are not directly accessible. On the other hand, values for η and κ are often available. Since the real $(\eta^2 - \kappa^2)$ and imaginary part $(2\eta\kappa)$ of equation (3-29) depends on the same quantities, it is possible to express them in terms of one another. Useful interrelations are given by Moss (60 M1, p.24) for zero frequency. They are:

$$\varepsilon_\infty - 1 = \frac{2}{\pi} \int_0^\infty (2\eta\kappa)\, \frac{d\lambda}{\lambda}$$

$$\sqrt{\varepsilon_\infty} - 1 = \frac{1}{2\pi^2} \int_0^\infty K d\lambda \qquad (3\text{-}34)$$

in which $K = 4\pi\kappa/\lambda$. Thus, if ηκ or simply K is known as a function of wavelength, ε_∞ can be calculated from the area under the curve. The two equations (3-34) are very useful in estimating the changes in ε_∞ as a function of carrier concentration or temperature since changes in the integrant occur only near the absorption edge which may change

its position as a function of temperature or be Burstein shifted as a function of carrier concentration. Thus if these changes are known in terms of η and κ, we have:

$$\Delta\varepsilon_\infty = \frac{2}{\pi}\int_0^\infty \Delta(2\eta\kappa)\,\frac{d\lambda}{\lambda}$$

$$\Delta\eta_\infty = \frac{1}{2\pi^2}\int_0^\infty \Delta K\, d\lambda \qquad (3\text{-}35)$$

The second of equations (3-35) has been used by Riedl et al. (67 R1) to explain the variation of ε_∞ with carrier concentration in SnTe.

2) Lattice Dispersion

The contribution to the dielectric constant arising from the oscillating charged atoms is given by Stern (63 S1) as:

$$\tilde{\varepsilon}_{LV} = \varepsilon_\infty\,(\omega_L^2 - \omega_T^2)/(\omega_T^2 - \omega^2 - i\gamma_{LV}\omega) \qquad (3\text{-}36)$$

in which ω_T and ω_L are the transverse and longitudinal modes of lattice oscillation and γ_{LV} is the damping constant. For the wavelength range of interest, $\omega^2 >> \omega_T >> \gamma_{LV}\,\omega$ and we have:

$$\eta_{LV}^2 = -\varepsilon_\infty\,(\omega_L^2 - \omega_T^2)/\omega^2 = -\frac{(\varepsilon_s - \varepsilon_\infty)}{\lambda_T^2}\,\lambda^2 \qquad (3\text{-}37)$$

in which the relation $\omega_L^2/\omega_T^2 = \varepsilon_s/\varepsilon_\infty$ (63 S1, p.353) has been used, where ε_s is the static dielectric constant. For PbTe at room temperature (69 D1) $\varepsilon_\infty = 32.8$, $\varepsilon_s = 380$, $\lambda_T = 310\ \mu$ giving η_{LV}^2 equal to -.09

and -1.44 for λ = 5 μ and 20 μ respectively. The contribution from the lattice at 20 μ is therefore less than 4% of the contribution from the bound carriers.

3) Dispersion Due to Inter-band Transitions

An additional contribution to the dielectric constant may arise for wavelengths longer than the fundamental absorption edge if carriers are distributed in two bands. If the extinction coefficient κ, associated with the extra absorption then present is known, this contribution is simply calculated using equations (3-34). Such a calculation has been performed by Dixon and Riedl (65 D1) for a p-type PbTe sample. ε_1 was found to be less than .15 for all wavelengths. This is negligible compared to ε_∞ = 32.8 and inter-valence band contribution will be disregarded in this work.

To summarize, the above corrections can all be taken into account if one replaces ε_∞ in equation (3-26) by:

$$\varepsilon_c = \varepsilon_\infty + \left[\begin{array}{c} \dfrac{\varepsilon_\infty \lambda_o^2}{\lambda^2 - \lambda_o^2} \\ \text{or} \\ \dfrac{2}{\pi} \displaystyle\int_0^\infty \Delta(2n\kappa) \, \frac{d\lambda}{\lambda} \end{array} \right] - \frac{(\varepsilon_s - \varepsilon_\infty)}{\lambda_T^2} \lambda^2 \qquad (3\text{-}38)$$

It should be pointed out here that there is partial cancellation at a given wavelength, the last two terms being of opposite signs.

Equations (3-26) and (3-38) allow us to determine experimentally the susceptibility effective mass m_s. The average value of

the mass near the Fermi level does not provide direct information about the band structure. However, it is possible to obtain this information indirectly by comparing the measured susceptibility mass with that calculated for particular energy bands. It is the purpose of the next section to give an expression for m_s in terms of the details of the energy-band structure.

3.3.3 Statistical Description and Relationship to Band Structure

The Boltzman equation, in steady state, in the presence of an electric field only ($\bar{\mathcal{E}}$) is:

$$\left.\frac{e}{\hbar}\bar{\mathcal{E}} \cdot \overline{\nabla_k f}(k) = \frac{\partial f(k)}{\partial t}\right\rangle_{\text{collision}} \tag{3-39}$$

where $f(k)$ is the distribution function giving the probability of occupation. If the equilibrium distribution is $f_o(k)$ and the deviation from that equilibrium is small, we may replace on the left $f(k)$ by $f_o(k)$. Also since $f_o(k)$ depends only on the energy (E) we have:

$$\overline{\nabla_k f_o}(k) = \overline{\nabla_k E_k}\ \frac{\partial f_o(k)}{\partial E(k)} \tag{3-40}$$

If we further assume that the collision term can be expressed in the form :

$$\left.\frac{\partial f(k)}{\partial t}\right\rangle_{\text{collision}} = -\frac{(f(k) - f_o(k))}{\tau(k)} = -\frac{\Delta f(k)}{\tau(k)} \tag{3-41}$$

then from (3-39), (3-40) and (3-41) we have:

$$\Delta f(k) = -\frac{e}{\hbar}\frac{\partial f_o}{\partial E}\,\tau\bar{\mathcal{E}}\cdot\overline{\mathrm{Grad}_k E} \tag{3-42}$$

When the applied field varies with time according to:

$$\mathcal{E}_x = \mathcal{E}_o\, e^{i\omega t} \tag{3-43}$$

then (36 W1) we have:

$$\Delta f = \frac{1}{1+i\omega\tau}\,\Delta f_1 = \frac{(1-i\omega\tau)}{1+(\omega\tau)^2}\,\Delta f_1 \tag{3-44}$$

where Δf_1 is the solution for steady state given by equation (3-42) and τ is the carrier relaxation time.

The current density in the x direction due to electrons (or holes) is:

$$J_x = \frac{-2}{(2\pi)^3}\int e\, v_x f(k)\, d\Omega_k = \frac{-2}{(2\pi)^3}\int e\, v_x \Delta f\, d\Omega_k, \tag{3-45}$$

in which $d\Omega_k = dk_x dk_y dk_z$ is the volume element in wave number space and v_x is the electron velocity in the x direction. The occupation probability $f(k) = f_o + \Delta f$ can be replaced by Δf since the normal distribution f_o produces no current. Substituting equation (3-44) in (3-45), writing $\frac{\partial \mathcal{E}_x}{\partial t} = i\omega\mathcal{E}_x$ and $v_x = \frac{1}{\hbar}\frac{\partial E}{\partial k_x}$ we have:

$$J_x = \frac{-2e^2}{(2\pi)^3}\left[\mathcal{E}_x\int\frac{\tau\, v_x^2}{1+(\omega\tau)^2}\frac{\partial f_o}{\partial E}\,d\Omega_k - \frac{\partial \mathcal{E}_x}{\partial t}\int\frac{\tau^2 v_x^2}{1+(\omega\tau)^2}\frac{\partial f_o}{\partial E}\,d\Omega_k\right] \tag{3-46}$$

Equation (3-1) gives $J_x = \sigma\mathcal{E}_x + \varepsilon_o\chi\,\partial\mathcal{E}_x/\partial t$ which compared to equation (3-46) leads to:

$$\sigma = -\frac{2e^2}{(2\pi)^3} \int \frac{\tau v_x^2}{1+(\omega\tau)^2} \frac{\partial f_o}{\partial E} d\Omega_k \qquad (3\text{-}47)$$

$$\varepsilon_o \chi = \frac{2e^2}{(2\pi)^3} \int \frac{\tau^2 v_x^2}{1+(\omega\tau)^2} \frac{\partial f_o}{\partial E} d\Omega_k \qquad (3\text{-}48)$$

For cubic symmetry, the conductivity σ and the susceptibility χ are independent of direction and v_x^2 may be replaced by $v^2/3$. Also, for cubic multivalley semiconductors, the susceptibility for the crystal is obtained by multiplying the contribution of one valley by the number of valleys. Equation (3-48) becomes:

$$(\eta^2 - \kappa^2 - 1)\, \varepsilon_o = \varepsilon_o \chi = \frac{2e^2}{(2\pi)^3} \frac{\Gamma}{3} \int \frac{\tau^2}{1+(\omega\tau)^2} v^2 \frac{\partial f_o}{\partial E} d\Omega_k \qquad (3\text{-}49)$$

In which Γ represents the number of valleys. When $\omega\tau >> 1$, equation (3-49) becomes independent of scattering time. Comparison with equation (3-22) then gives:

$$\frac{N/\Gamma}{m_s} = \frac{2}{3(2\pi)^3} \int v^2 \frac{\partial f_o}{\partial E} d\Omega_k \qquad (3\text{-}50)$$

It is possible to extend the validity of equation (3-50) to smaller $\omega\tau$ values as we have done in arriving at equation (3-26a). For $\omega\tau$ large enough (say $\omega\tau > 3$), the term $\tau^2/(1 + \omega^2\tau^2)$ can be taken out of the integral in equation (3-49) and averaged over energy separately. This is a good approximation since then $\tau^2/(1 + \omega^2\tau^2)$ does not vary appreciably with energy. Comparison of equation (3-49),

approximated this way, with the corresponding equation (3-26a) (in which $\varepsilon_\infty = 1$ for free carriers) gives the same equation (3-50) as before. Thus, provided equation (3-26a) is used in the determination of m_s, the range of validity of equation (3-50) is extended to lower values of $\omega\tau$. For high degeneracy, equation (3-50) is valid with no assumption required concerning $\omega\tau$ values. Also, for high degeneracy, it is easily seen, from comparison of $\sigma = (N/\Gamma)e^2\tau/m_c$ with equation (3-47) for $\omega = 0$, that the conductivity effective mass m_c is given by equation (3-50) with m_c in the place of m_s. This confirms an earlier statement that, even for non-parabolic bands, the two masses are identical for high degeneracy.

When the constant energy surfaces are ellipsoids of revolution about the k_z axis (let it be called k_L), we have $k_x^2 + k_y^2 = k_T^2 =$ constant over a constant energy surface. We may write:

$$d\Omega_k = dS_k \frac{dE}{|\nabla_k E|} \tag{3-51}$$

and for the surface element:

$$dS_k = 2\pi k_T \, dk_L \left[\nabla_k E / |(\nabla_k E)_T|\right] \tag{3-52}$$

where the factor in brackets projects dk_L on the surface of constant energy.

Substituting equations (3-51) and (3-52) in equation (3-50) we have:

$$\frac{N_1}{m_s} = -\frac{1}{3}\frac{4}{(2\pi)^2}\int_0^\infty \frac{\partial f_o}{\partial E}\left[\int_0^{k_L\ \max.} \frac{v^2 k_T\, dk_L}{|(\nabla_k E)_T|}\right]_E dE \qquad (3\text{-}54)$$

in which $N = N_1 \Gamma$ and N_1 is the number of carriers in one ellipsoid and is given by the standard equation:

$$N_1 = \int_0^\infty \frac{\partial f_o}{\partial E}\left[\frac{2}{(2\pi)^2}\int_0^{k_L\ \max.} k_T^2\, dk_L\right]_E dE \qquad (3\text{-}55)$$

in which the term in brackets is the number of states within an ellipsoid of energy E.

Equations (3-54) and (3-55) are identical to equations 27 and 30 of Dixon and Riedl (65 D1). Experimental values of m_s determined by using equation (3-26) can now be compared to those calculated for specific energy-band models using equation (3-54). The comparison constitutes a stringent test for that energy-band model. Let us now focus our attention on the methods of analysis which allow us to extract the experimental values of m_s, τ, or ε_∞ from equations (3-26).

3.4 Methods of Analysis

It will be assumed here that free-carrier dispersion only is present, and that the correction term (equation (3-38)), due to other dispersions mechanisms, is negligible. This assumption is not restrictive since the corrections for bound carriers and lattice dispersion can be applied later. Also we assume that the free carriers are in one band only. Again, this assumption is not restrictive: when more than one band are present, equation (3-26) still holds except that m_s and τ then have different meanings. The details related to the above statements will be given at the end of this section.

From equation (3-10) and (3-26), we have the following functional relation:

$$R = f(N, \varepsilon_\infty, m_s, \tau) \qquad (3\text{-}56)$$

which does not contain ω and r^2 since ω is known and r^2 can be calculated. In the present experiment, N is determined from an independent measurement. Thus, the analysis involves the determination of the last three unknowns, in equation (3-56), from measurements of reflectivity over a relatively wide range of wavelengths. The methods described below show how this is possible.

3.4.1 ε_∞, τ and m_s Are Unknown

When all three parameters are unknown, there are two methods available depending on the value of $\omega\tau$.

a) Slope Method, $\omega^2\tau^2 >> 1$

For several high mobility materials, $\omega\tau$ is large over the wavelength range of interest. (In several cases, $\omega^2\tau^2$ is larger than 100). Equation (3-26) then becomes:

$$\eta^2 - \kappa^2 = \varepsilon_\infty - \frac{Ne^2}{m_s\varepsilon_o}\frac{1}{\omega^2} \qquad (3\text{-}57)$$

$$2\eta\kappa = \frac{Ne^2}{m_s\varepsilon_o}\frac{1}{\omega^2} \times \left(\frac{1}{\omega\langle\tau\rangle}\right)$$

For short wavelengths (large ω), $Ne^2/m_s\varepsilon_o\omega^2$ is equal to zero giving $\kappa = 0$ and $\eta = \sqrt{\varepsilon_\infty}$. As the wavelength increases, the last term on the right of the first equation (3-57) increases as λ^2 until $Ne^2/m_s\varepsilon_o\omega^2 = \varepsilon_\infty - 1$. At this point, the right-band term of the other equation (3-57) is equal to $(\varepsilon_\infty - 1)/\omega\langle\tau\rangle$. If $\omega\langle\tau\rangle$ is very large, then $\eta = 1$ and $\kappa \simeq 0$ and the reflectivity equals to zero. If the wavelength is further increased by a small amount, $Ne^2/m_s\varepsilon_o\omega^2 = \varepsilon_\infty$ and for very large $\omega\langle\tau\rangle$, η and κ are both zero, giving $R = 1$. In practice, $2\eta\kappa$ never goes to zero, (since $\varepsilon_\infty/\omega\langle\tau\rangle$ is never negligible) η and κ are never equal to zero, and R never reaches unity. However, η always goes through 1 and

there is always a minimum in the reflectivity. As seen from equation (3-57), as we move away from the reflectivity minimum (on the short wavelength side) κ becomes rapidly small as η increases. Thus, when $\omega^2\tau^2$ is reasonably large, κ can be neglected at some distance away from the minima and we have:

$$\eta^2 = \left[\frac{\sqrt{R}+1}{1-\sqrt{R}}\right]^2 \quad \text{from} \quad R = \frac{(\eta-1)^2}{(\eta+1)^2}$$
$$\eta^2 = \varepsilon_\infty\left(1 - \frac{\omega_P^2}{\omega^2}\right) \tag{3-58}$$

where ω_P is the plasma frequency defined by:

$$\omega_P^2 = \frac{Ne^2}{m_s\varepsilon_o\varepsilon_\infty} \tag{3-59}$$

η^2 can be calculated using the experimentally determined reflectivity in equation (3-58). Then, from a plot of η^2 vs $1/\omega^2$ it is possible to determine ε_∞ from the extrapolated straight line to zero wavelength and ω_P, and thereby m_s, from the slope.

b) Fitting Method

If the condition $\omega^2\tau^2 >> 1$ is not well satisfied, the reflectivity curve, covering an appreciable range of wavelengths on either side of the reflectivity minimum, can be fitted to determined ε_∞, m_s and τ. This is possible because there are large variations of reflectivity and because changes of each of the parameters separately

have rather unique effects on the reflectivity curve. This is illustrated in Figure 3 by Riedl et al. (67 R1). If only free carrier dispersion is present and the absolute reflectivity has been measured, the three parameters can be determined very accurately. In practice, however, the measured reflectivity does not represent the absolute reflectivity due to free carriers only for the following reasons:

1) Bound carrier dispersion may vary by small amounts on the short wavelength side of the minimum.

2) A small contribution from lattice dispersion may be present.

3) Surface damage or surface oxides may affect the reflectivity values specially at the long wavelengths where the penetration depth is small.

4) Deviations of the measured reflectivity from the absolute reflectivity are also present, even with good reflecting surfaces, due to experimental procedures.

Despite the presence of the above unwanted contributions, it is still possible to obtain good fits as we shall see, but because of these extra contributions, the values of the parameters corresponding tothe best fit may be inaccurate.

A program which finds the best fit to an experimental reflectivity curve was written. Its input data are the measured reflectivities (R_E) and wavelengths, and its output values are:
1) the calculated reflectivities (R_C) of the best fit which are

printed as well as plotted; 2) the values of ε_∞, m_s, and $\mu_{opt.} = e\langle\tau\rangle/m_s$ corresponding to the best fit; 3) the mean square deviation $(1/N)\sum_N[(R_C - R_E)/R_C]^2$ (where N is the number of reflectivity points) corresponding to the best fit. The best fit was obtained by letting the mean square deviation be a minimum.

To test the program and to check the effect of a deviation from absolute reflectivity, present in most experimental data, a theoretical reflectivity curve was generated using equations (3-10) and (3-26) for given values of ε_∞, m_s and μ_{opt}. To simulate a deviation from absolute reflectivity, such as the one present in the experimental data when the comparison mirror is not 100% reflecting, the theoretical reflectivities were multiplied by constant factors from .95 to 1.05. The best fit was found for all these curves. The corresponding fitting parameters and the mean square deviations are given in Figure 3.4. It is seen that the quality of the fit is highest (i.e., smallest mean square deviation) for the unchanged theoretical curve as expected, and lowest for the largest deviation from absolute reflectivity. It is important to note, however, that the lowest quality fit shown is nevertheless a good fit as seen from the small values of the mean square deviations.

The unchanged theoretical curve (x 1.00) was best fitted by the values of m_s, ε_∞ and μ_{opt} used to generate it and they are shown by arrows on the graphs. A 5% deviation from absolute reflectivity is also seen to produce values of m_s, ε_∞, and μ_{opt} 15% larger, 13%

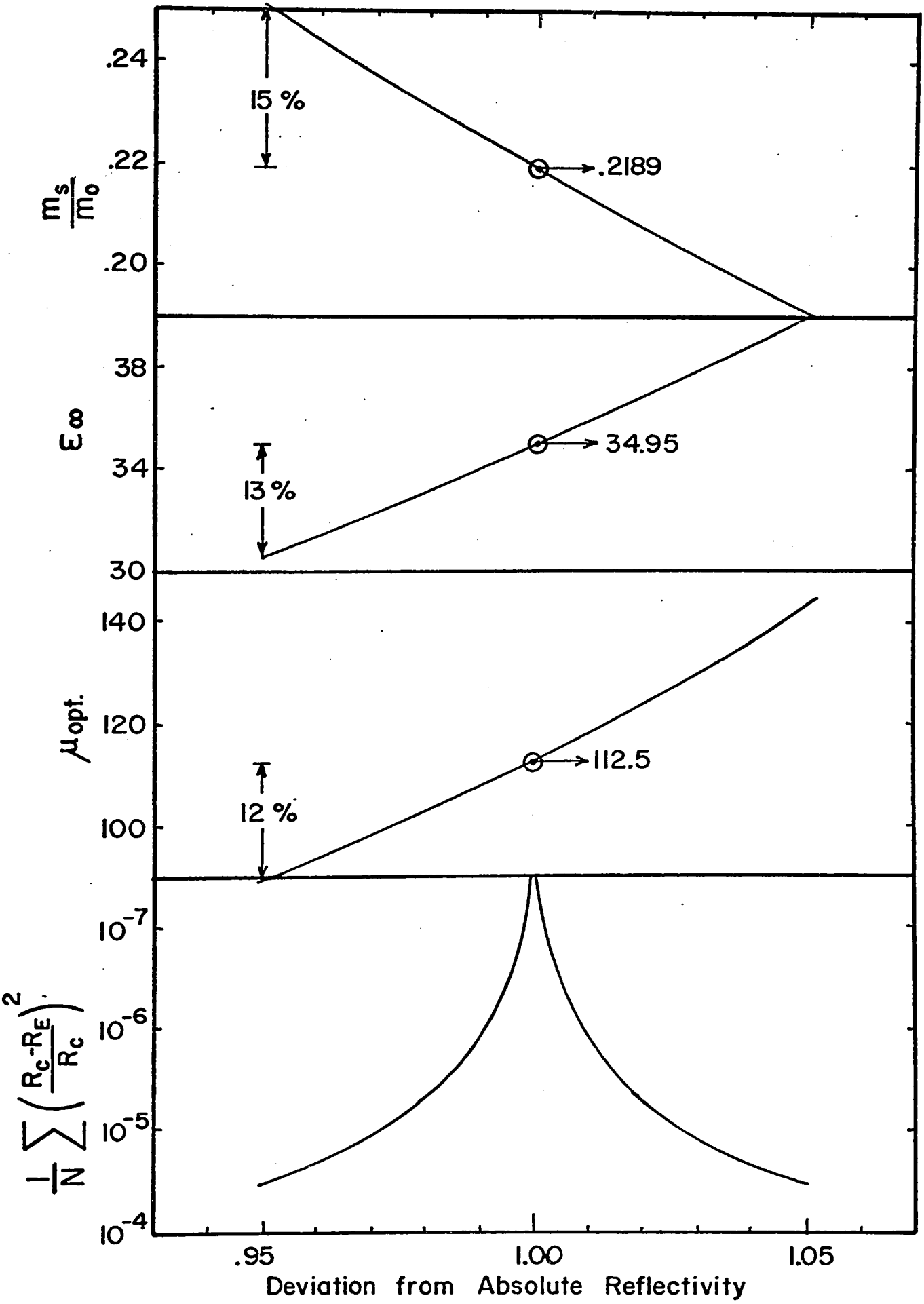

Figure 3.4 Effects of a deviation from absolute reflectivity on the fitting parameters.

smaller, and 12% smaller, respectively than the correct values. The above example therefore shows that the results obtained by curve fitting may be in error inspite of good fits. Small deviations from true free carrier reflectivity caused by any of the four items mentioned above may produce large changes in any of the fitting parameters.

A program intended to correct the systematic deviations from absolute reflectivity was written. It follows the same procedure as the one just described except that the input is the experimental curve. The quality of the fit is then seen to vary with the multiplicative factor (from .95 to 1.05). The highest quality fit, which does not necessarily occur for the multiplicative factor 1.00, then represents the best fit to the experimental data now corrected for deviations from absolute reflectivity. This program has been successful for some of our curves and has shown that the deviation from absolute reflectivity was ±3% for these curves. However, for the other reflectivity curves, the correcting program was unsuccessful. The reason for this partial success is that the average square deviations corresponding to the best fits of our experimental curves are larger than 10^{-5} due to reading and other errors. Since, as can be seen from Figure 3.4, the mean square deviation produced by a systematic error in the absolute reflectivity only is less than that, it is often undetectable.

Let us emphasize that good fits are always required if the measurements are to be analyzed with good accuracy.in terms of a free carrier dispersion model by any of the techniques described in this section. When the measurements can be well fitted then the results of curve fitting are accurate only if the absolute reflectivity due to free carriers alone has been measured or if any deviation from this ideal situation can be fully accounted for in the fitting technique.

3.4.2 ε_∞ Is Known; m_s and τ Are Unknown

The values of ε_∞ are often available or can be determined independently. A method of analysis has been developed by Moss et al. (68 M1) for this case. Their derivation is strickly applicable when the Lyden's approximation of equation (3-19) is valid. Here we intend to generalize the treatment to include the effect of the degree of degeneracy accounted for by the approximation of equation (3-21). In all cases the equations below reduce to those of Moss et al. (68 M1) when $r^2 = 1$, and we will only review the main steps. The necessary equations are:

$$R = \frac{(\eta - 1)^2 + \kappa^2}{(\eta + 1)^2 + \kappa^2} \qquad \text{or} \quad \frac{1 + R}{1 - R} = \frac{\eta^2 + \kappa^2 + 1}{2\eta} \tag{3-60}$$

$$\eta^2 - \kappa^2 - \varepsilon_\infty = \frac{-Ne^2}{m_s\varepsilon_o} \cdot \frac{1}{(\omega^2 + r^{-2}\langle\tau\rangle^{-2})} \tag{3-61}$$

$$2\eta\kappa \cdot r^2\omega\langle\tau\rangle = \frac{Ne^2}{m_s\varepsilon_o} \cdot \frac{1}{(\omega^2 + r^{-2}\langle\tau\rangle^{-2})} \tag{3-62}$$

where equation (3-60) assumes normal reflectivity in air, and equations (3-61) and (3-62) are the same as equations (3-26) re-arranged.

In what follows, we will use the fact that there is always a minimum in the reflectivity, to find an interrelation between η and κ at the minimum. For convenience, we use the reflectivity function $(1 + R)/(1 - R)$ which has a minimum for the same condition as R.

If we differentiate $(1 + R)/(1 - R)$ with respect to κ^2 on both sides we have at the minimum:

$$\frac{d\eta}{d\kappa^2} = \frac{\eta}{1 + \kappa^2 - \eta^2} \tag{3-63}$$

Manipulation of equations (3-61) and (3-62) to eliminate ω leads to:

$$(\varepsilon_\infty - \eta^2 + \kappa^2)\left[r^2 + \frac{(\varepsilon_\infty - \eta^2 + \kappa^2)^2}{4\eta^2\kappa^2}\right] = \frac{r^4 Ne^2\langle\tau\rangle^2}{m_s\varepsilon_o} = \text{constant} \tag{3-64}$$

which after differentiation with respect to κ^2 gives

$$\frac{d\eta}{d\kappa^2} = \frac{\eta}{2\kappa^2}\left[\frac{(2\kappa^2 + 3\,\varepsilon_\infty + (4r^2 - 3)\,\eta^2)\kappa^4 - (\varepsilon_\infty - \eta^2)^3}{(2\eta^2 - 3\,\varepsilon_\infty + (4r^2 - 3)\,\kappa^2)\eta^4 + (\varepsilon_\infty + \kappa^2)^3}\right] \tag{3-65}$$

From equations (3-63) and (3-65), we obtain the following interrelation between η and κ at the reflectivity minimum:

$$\kappa^2(5\eta^2 + 3\varepsilon_\infty - 2) = (\varepsilon_\infty - \eta^2)(\eta^2 - 1) - \frac{4\eta^2\kappa^4 r^2(3\eta^2-\kappa^2-1)}{(\varepsilon_\infty-\eta^2+\kappa^2)^2} \qquad (3\text{-}66)$$

in which the last term on the right is negligible for $\omega^2\tau^2 >> 1$.

Writing ω_p, defined by equation (3-59), in equations (3-61) and (3-62) we obtain:

$$\frac{\omega_p^2}{\omega^2} = \frac{(\varepsilon_\infty + \kappa^2 - \eta^2)}{\varepsilon_\infty} + \frac{4\eta^2\kappa^2 r^2}{\varepsilon_\infty(\varepsilon_\infty + \kappa^2 - \eta^2)} \qquad (3\text{-}67)$$

$$\omega\langle\tau\rangle = \frac{(\varepsilon_\infty + \kappa^2 - \eta^2)}{2\eta\kappa r^2} \qquad (3\text{-}68)$$

For given values of ε_∞ and r^2, pairs of η_{min}, κ_{min}, satisfying equation (3-66) at the minimum reflectivity, can be found and the corresponding R_{min}, ω_p/ω_{min}, and $\omega_{min}\langle\tau\rangle$ values calculated using equations (3-60), (3-67), and (3-68) respectively. From plots of ω_p/ω_{min} and $\omega_{min}\langle\tau\rangle$ versus R_{min}, for different values of ε_∞ and r^2, it is then possible to determine $\langle\tau\rangle$ and ω_p knowing the experimental values of R_{min} and ω_{min} only.

For each value of ε_∞, ranging from 16 to 50 in steps of 1, a set of η_{min}, κ_{min}, R_{min}, $\omega_{min}\langle\tau\rangle$, and ω_p/ω_{min} values, for η_{min} between 1 and 4 in steps of .05, was tabulated using an IBM-360 computer. These tables are available for values of r^2 from 1.0 to 2.0.

Figures 3.5, 3.6 and 3.7 show some very useful sets of curves extracted from the tables. ω_p/ω_{min} versus R_{min} is plotted in Figures 3.5 and 3.6 for $r^2 = 1$ and $r^2 = 2$ respectively, while $(<\tau>\omega_{min})\, r^2$ versus R_{min} is plotted in Figure 3.7. In all graphs, curves are shown for several values of ε_∞. A linear interpolation between different r^2 or ε_∞ values is sufficiently accurate.

3.4.3 ε_∞, τ Are Known; m_s Is Unknown

If ε_∞ and τ are known from an independent measurement, m_s can be determined as proposed by Lyden (64 L1). He assumes the approximation of equations (3-19) and discusses the validity of these assumptions which are shown to be accurate in most cases of interest. Rheinlander (69 R1) has generalized Lyden's equations by using approximations (3-21) to take into account lower degree of degeneracy. In the Lyden's approximation, the necessary equations are (3-60), (3-61), and (3-62) with $r^2 = 1$. The condition that $dR/d\Omega = 0$ in which $\Omega = \omega<\tau>$ leads to (64 L1):

$$M_s^3 - \frac{(3\varepsilon_\infty - 1)}{4\varepsilon_\infty\,(\varepsilon_\infty - 1)} \frac{(1/\Omega^2 + 5 + 8\Omega^2)}{(1 + 3\Omega^2)}\, C\, M_s^2 + \frac{3\varepsilon_\infty - 2}{2\varepsilon_\infty(\varepsilon_\infty - 1)^2} \times \frac{(1 + 2\Omega^2)}{(1 + 3\Omega^2)}\, C^2 M_s + \frac{C^3}{4\varepsilon_\infty(\varepsilon_\infty - 1)^2\,(1 + 3\Omega^2)} = 0 \qquad (3\text{-}69)$$

in which $C = Ne^2/m_o\varepsilon_o\omega_o^2$, ω_o is the angular frequency at the reflectivity minimum, $M_s = m_s/m_o$ where m_o is the free electron mass.

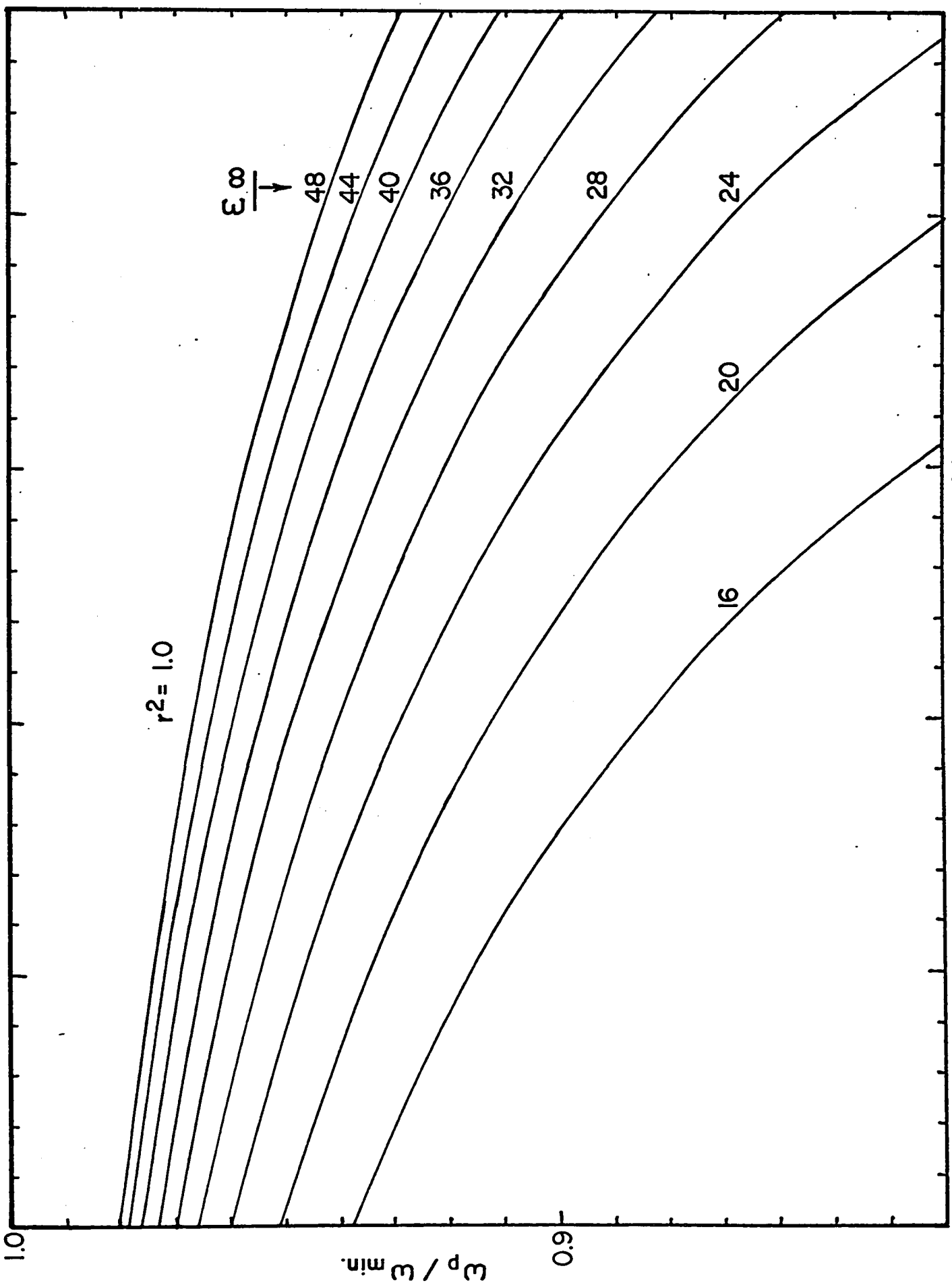

Figure 3.5 Plasma frequency vs. minimum reflectivity.

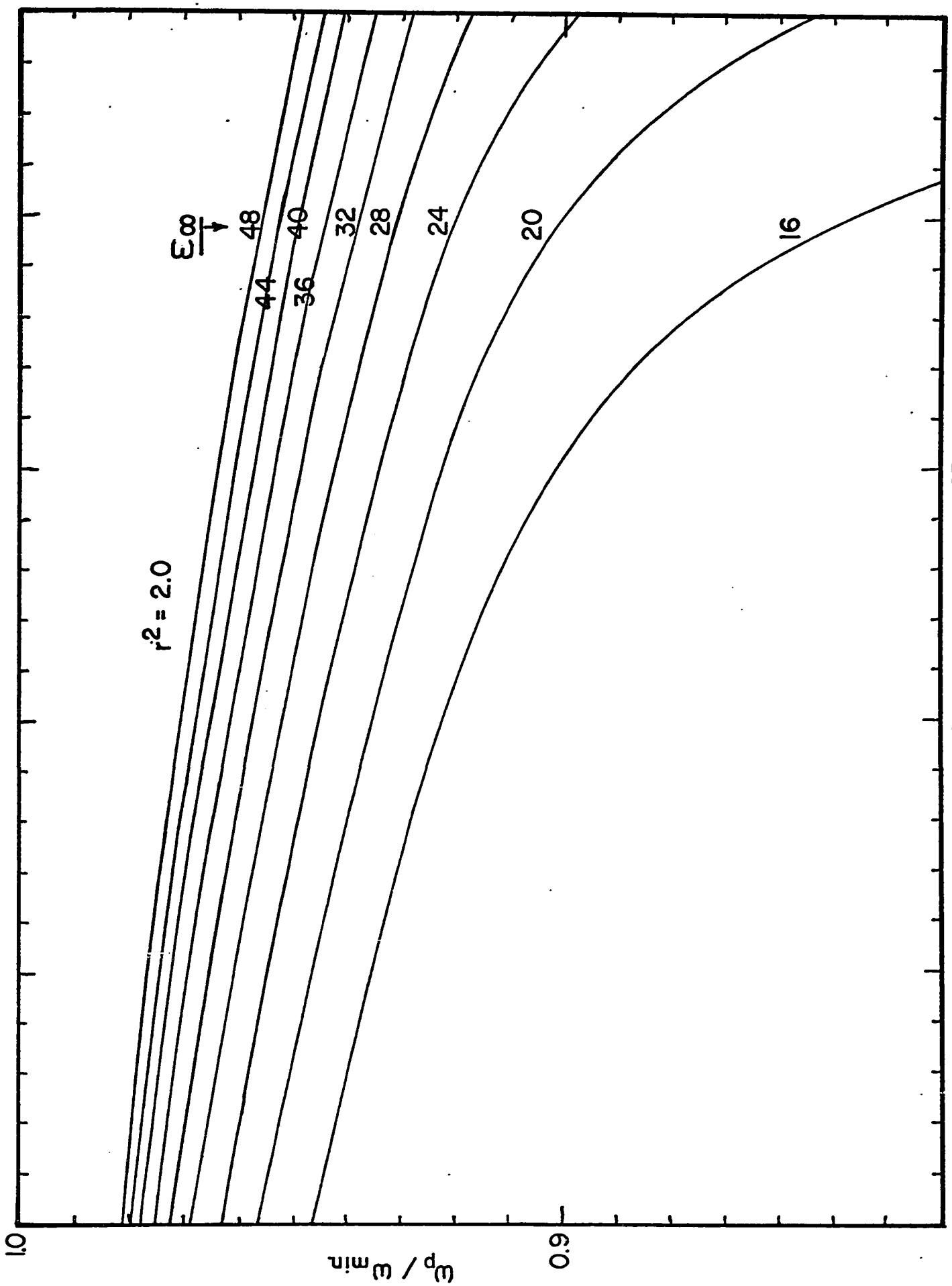

Figure 3.6 Plasma frequency vs. minimum reflectivity.

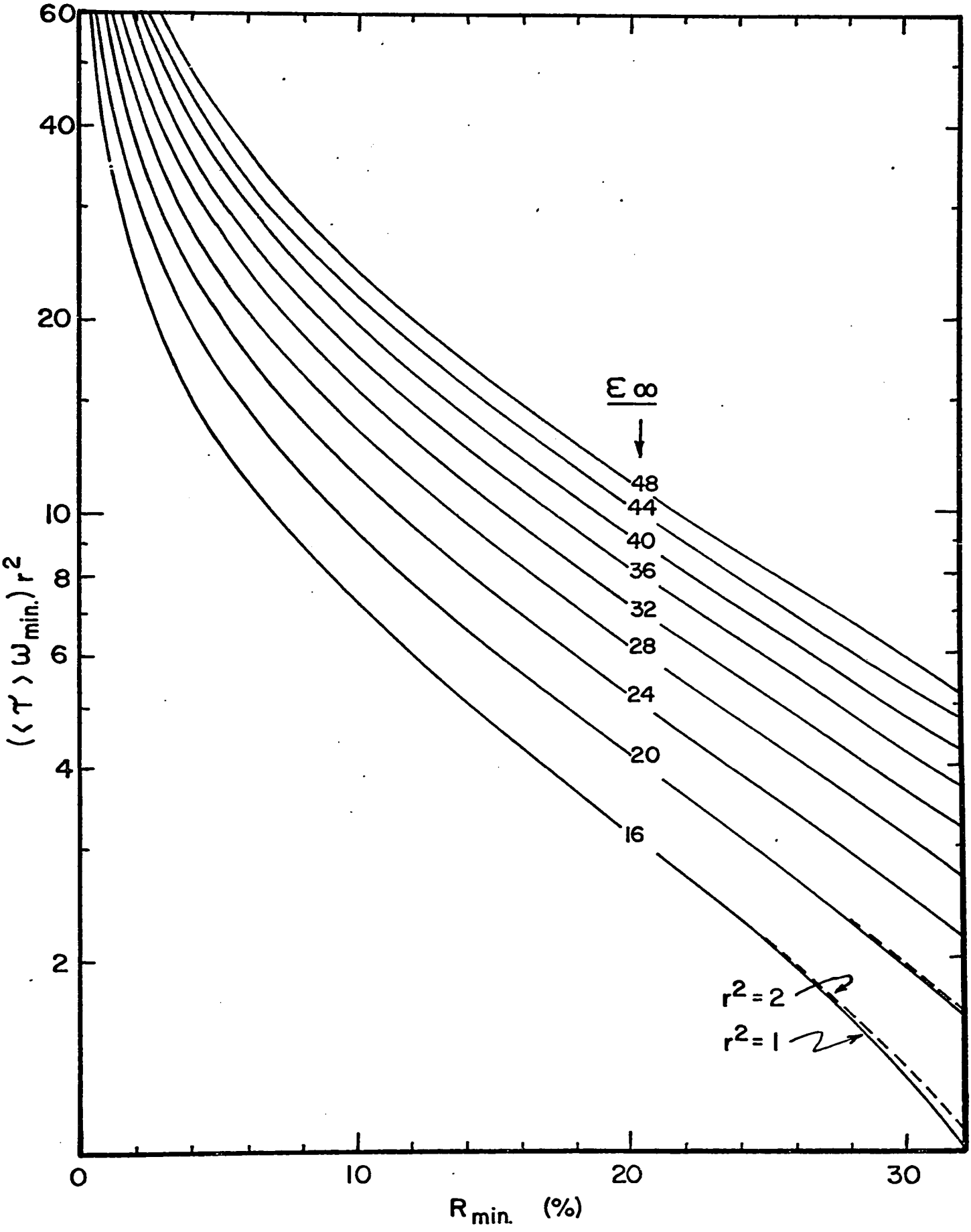

Figure 3.7 Relation between minimum reflectivity and scattering time.

If ε_∞ is known and N and $\langle\tau\rangle$ are determined from Hall and conductivity measurements, M_s can be found from equation (3-69) using the experimentally determined angular frequency of the reflectivity minimum. Some comments concerning the above procedure will now be given.

First, let us consider the equation for free carrier dispersion. For simplicity, we take the case $\omega^2\tau^2 >> 1$

$$\eta^2 - \kappa^2 - \varepsilon_\infty = - \frac{Ne^2}{m_s\varepsilon_o\omega^2} \tag{3-70}$$

$$2\eta\kappa = \frac{Ne^2}{m_s\varepsilon_o} \frac{1}{\omega^3}\left\langle\frac{1}{\tau}\right\rangle$$

in which the average over the energy has been performed. The relaxation time is proportional to $1/2\ \eta\kappa$ (equation (3-68)) so that the quantity involved in the optical mobility is $1/\langle\tau^{-1}\rangle$ as compared to $\langle\tau\rangle$ in the conductivity mobility. Thus, the Lyden approximation (i.e., $\langle\tau^{-1}\rangle = 1/\langle\tau\rangle$) should be strictly satisfied if the conductivity mobility is to be used to determine m_s in equations (3-70). Conversely, the values of optical mobilities determined if the mass is known are not expected to agree with the values of conductivity mobilities unless the assumptions used in performing the average over energy are strictly satisfied.

Secondly, in the Lyden approximation the susceptibility effective mass is the same as the conductivity effective mass as shown earlier.

Thirdly, since the conductivity mobility contains both $\langle\tau\rangle$

and M, Ω depends on M. Thus, equation (3-69) has several roots. In fact, it has 3 real roots, of which one is negative and two are positive. The two positive roots are very close to one another and much care should be exercised if the right value of M_s is to be obtained. This is illustrated in Figure 3.8 in which the left side of equation (3-69) is plotted versus effective mass. Only one of the positive roots is the correct one and it is the larger one. If the logic of the computer program, needed to solve equation (3-69), is not written correctly either of the two positive roots may be obtained.

3.4.4 Analysis For Multiband Conduction

When there are j types of carriers, each characterized by N_j, m_{sj} and τ_j, their contributions to the susceptibility add. If the contribution to the susceptibility arises from electrons (bound and free) only, we have:

$$\eta^2 - \kappa^2 = \varepsilon_\infty - \sum_j \varepsilon_j$$

$$2\eta\kappa = \sum_j \frac{\varepsilon_j}{\omega\tau_j} \qquad (3\text{-}71)$$

with

$$\varepsilon_j = \frac{e^2 N_j}{\varepsilon_o m_{sj}} \frac{\tau_j^2}{(1 + \omega^2\tau_j^2)}$$

At zero wavelength, all ε_j are zero giving $\kappa = 0$ and $\eta^2 = \varepsilon_\infty$. As the wavelength starts increasing, all $\omega\tau_j$ values are large giving a

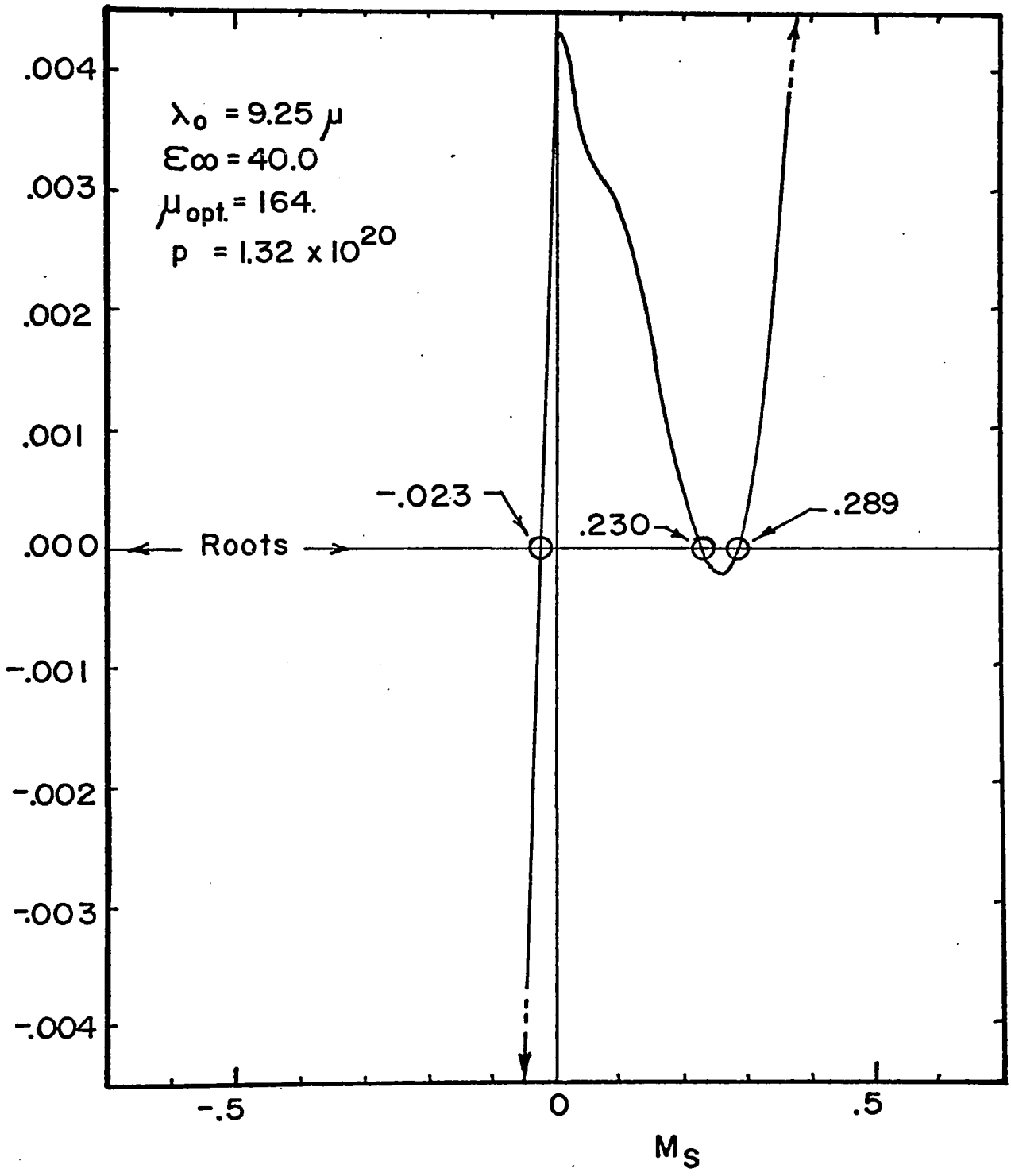

Figure 3.8 Roots of equation (3-69).

negligible value for κ and a variation of η^2 in λ^2 as for a single band. As $\sum_j \varepsilon_j$ approaches $\varepsilon_\infty - 1$, $\sum \varepsilon_j/\omega\tau_j$ remains comparatively small since in general the individual $\omega\tau_j$ are much larger than 1 in the range of wavelengths used. Thus, somewhere in that region, η^2 will be close to one while κ is not yet large giving a minimum in reflectivity as for a single band. As $\sum_j \varepsilon_j$ continues to increase by a small amount, η becomes close to zero, as κ continuous to increase, causing a large increase in reflectivity towards the value of 1.

In the last paragraph, we have somewhat repeated the earlier discussion following equation (3-57) to show that the same form of reflectivity curve is obtained when several types of carriers are present as when there is one type only. The only difference is in the meaning of the parameters m_s and τ obtained from these curves with a single band analysis*. We will now give this meaning for a simple case (69 B2).

If all $\omega^2\tau_j^2$ are much greater than one, we have:

$$\eta^2 - \kappa^2 - \varepsilon_\infty = -\frac{e^2}{\omega^2\varepsilon_o} \sum_j \frac{N_j}{m_{sj}}$$

$$2\eta\kappa = \frac{e^2}{\omega^2\varepsilon_o} \frac{1}{\omega} \sum \frac{N_j}{m_{sj}\tau_j} \qquad (3\text{-}72)$$

The meaning of m_s and τ obtained by a one-band analysis is now obvious:

$$\frac{N}{m_s} = \sum_j \frac{N_j}{m_{sj}} \qquad (3\text{-}73)$$

*This meaning can be written explicitly when $\omega^2\tau_j^2 >> 1$ and when $\omega^2\tau_j^2 << 1$ but not in the general case.

$$\frac{N}{m_s \tau} = \sum_j \frac{N_j}{m_{sj} \tau_j}$$

in which N is the total carrier concentration. It may be useful to point out here that, if the condition $\omega^2\tau^2 >> 1$ at the observed minimum is satisfied, it is safe to say that the individual $\omega^2\tau_j^2 >> 1$ are verified as well. This can be seen from the following example. Suppose that one type of carriers only is present and that we replace gradually some of them by another type of carriers. If we start with low mass, high mobility carriers and add large mass, low mobility carriers, the reflectivity minimum will shift to longer wavelengths, but shorter than that of the reflectivity minimum corresponding to total replacement. Thus, at the position of the observed minimum, the individual conditions $\omega\tau_j >> 1$ are worse and better satisfied for high and low mobility carriers, respectively. Thus, at the position of the minimum, the largest $\omega\tau_j$ is reduced and the smallest $\omega\tau_j$ is increased, providing an overall improved situation.

In conclusion, experimental reflectivity curves* can be analysed only as if there were only one type of carrier present, since there is no difference between a multiband curve and a single band curve. Equations (3-73) are the necessary equations relating the measured τ and m_s values to those of the individual bands for $\omega^2\tau_j^2 >> 1$.

* For $\omega^2\tau_j^2 >> 1$ or $\omega^2\tau_j^2 << 1$.

3.4.5 Methods of Analysis and Corrections

When corrections for bound carrier dispersion, $\Delta\varepsilon_\infty$, and for lattice dispersion, $(\varepsilon_1)_{LV}$, are not negligible, we have seen that ε_∞ in equation (3-26) must be replaced by ε_c which is given by equation (3-38) and rewritten here as $\varepsilon_c = \varepsilon_\infty + \Delta\varepsilon_\infty - (\varepsilon_1)_{LV}$. Figure 3.9 shows schematically the effect of these corrections on the reflectivity curve. In the absence of corrections, $\varepsilon_c = \varepsilon_\infty$ and the reflectivity curve is given by equation (3-26). This situation is represented by the dashed curves in Figure 3.9. The solid reflectivity curve is that for values of $\Delta\varepsilon_\infty$ and $(\varepsilon_1)_{BC}$ also shown by solid lines. The values of the corrections shown in Figure 3.9 represent well the situation in the present experiment.

From the small peak in reflectivity at short wavelengths one may be able to detect the presence of a varying bound carrier contribution $(\varepsilon_\infty + \Delta\varepsilon_\infty)$. For wavelengths longer than 5 μ, the experimental reflectivity curves look similar to those for which the corrections are negligible and $\Delta\varepsilon_\infty$ and $(\varepsilon_1)_{LV}$ are not detectable in the presence of experimental errors in reading the reflectivity. The analysis of such uncorrected curves using the fitting or the slope method would give a smaller effective mass and a larger value of ε_∞ than those taking into account the corrections. It is important to note here that the omission of either corrections reduces the effective mass.
On the other hand, in several cases and in particular for that

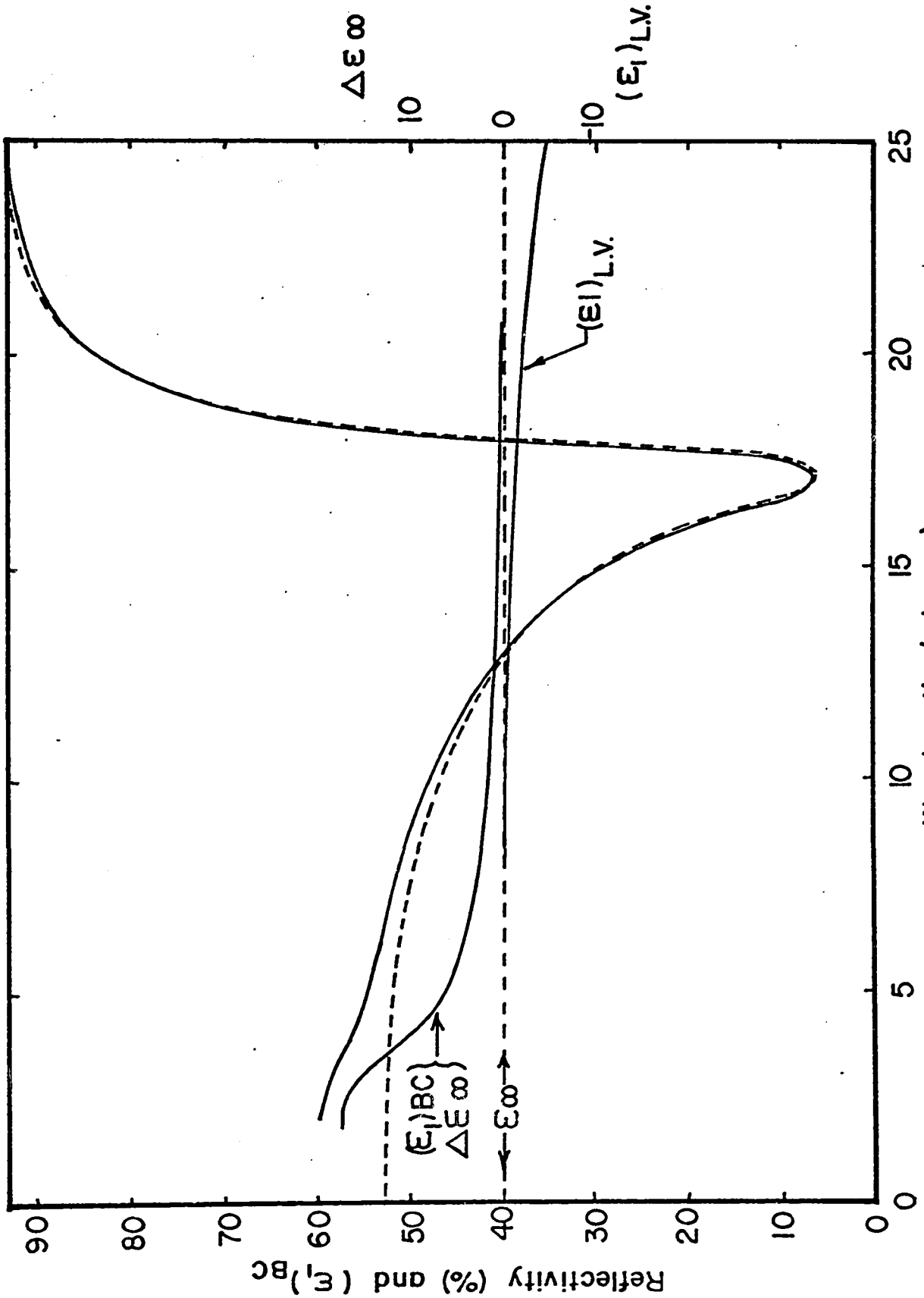

Figure 3.9 Effects of corrections on the reflectivity curve.

of Figure 3.9, the wavelength and the height of the reflectivity minimum are less affected and the Moss's or Lyden's technique gives a more correct effective mass whether or not the corrections are taken into account. This is due firstly to smaller corrections at the position of the minimum and secondly to partial cancellation of the effects due to both corrections at the position of the reflectivity minimum. Since the different methods of analysis respond differently to corrections for $\Delta\varepsilon_\infty$ and $(\varepsilon_1)_{LV}$ or deviations from the absolute reflectivity, it is desirable that the fitted reflectivity curves be analysed using the other methods as well.

When corrections are large and have to be taken into account, the inclusion of equation (3-38) in (3-26) is sufficient when using the fitting method. However, λ_o^2 must be known to avoid an undesirable fourth fitting parameter. For the other methods, the bound carrier correction has to be made for the wavelength region used before the curve is analysed (i.e., at the reflectivity minimum only for Moss's and Lyden's technique). For the lattice correction, the term $-(\varepsilon_s - \varepsilon_\infty)\lambda^2/\lambda_T^2$ can be combined with the free carrier term since both have the same wavelength dependences. If we do this, the curve uncorrected for lattice dispersion will yield a value of effective mass given by:

$$\frac{1}{m_s} = \frac{1}{m_s}\Bigg|_{\text{corrected}} + \frac{(\varepsilon_s - \varepsilon_\infty)}{\lambda_T^2}\,\frac{\varepsilon_o}{Ne^2} \qquad (3\text{-}74)$$

in which N is the free carrier concentration. However, as pointed out earlier, if $\varepsilon_c = \varepsilon_\infty$ at the position of the minimum, it is not necessary to make any correction when using Moss's or Lyden's method. Some methods of analysis therefore have marked advantages and we will now summarize them.

3.4.6 Advantages and Disadvantages of the Different Methods

The slope method is limited by the assumption that $\omega^2\tau^2 >> 1$. The advantage of the slope and fitting techniques over the technique using the minimum in reflectivity is that none of the three parameters m_s, τ and ε_∞ need to be known from an independent experiment. However, the slope and fitting techniques are accurate only when the absolute reflectivity is measured over the whole wavelength range used, when surface damage or surface oxides have no effect at any wavelength in that range, and when the presence of small deviations due to bound carriers and lattice dispersion can be accounted for. In practice, it is almost impossible to be sure that all the above conditions are reasonably satisfied. As demonstrated earlier for the fitting technique, a small deviation from absolute reflectivity (always present in such experiments) causes large errors in the fitting parameters m_s, τ and ε_∞. Errors are also introduced when small amounts of bound carrier and lattice dispersion are present as discussed in the last paragraph.

On the other hand, if it has been verified that the reflectivity spectra obtained on a particular material with given surface treatment are reasonably well fitted and if, in addition ε_∞ is known, Moss's or Lyden's

techniques have marked advantages for routine and accurate determination of the parameters:

1) Measurements need to be made near the minimun only.

2) The requirement of absolute reflectivity is not so stringent. In fact relative intensity only is required with the Lyden's method since only the wavelength of the reflectivity minimum is used. With the Moss's technique, a 5% deviation from the absolute reflectivity, for the same case as the one discussed in Figure 3.4 causes an error in m_s of 2% only as compared to an error in m_s of 15% when using the fitting technique.

3) $\Delta\varepsilon_\infty$ and the lattice contribution are in many cases small but comparable at the position of the reflectivity minimum. As discussed earlier the errors due to both contributions often cancel one another when using the Lyden's or Moss's technique, but add up, in practice, when using the other two techniques.

4) Lyden (64 L1) also points out that the method is expected to be less sensitive to surface damage when present. We will say at this point that surface damage has large effects over the whole reflectivity curve including the reflectivity minimum and postpone the discussion since this effect will be studied in some detail in Section 3.5.3.

In conclusion, good fits are always required if the reflectivity measurements are to be analyzed with good accuracy by any of the methods. The fitting technique has the important advantage that none of the three parameters need to be known from an independent

measurement. Unfortunately, the fitting technique is more sensitive to the presence of deviations from the absolute reflectivity and/or corrections due to $\Delta\varepsilon_\infty$ and $(\varepsilon_1)_{LV}$. If ε_∞ is known, it is desirable that the fitted spectra be analyzed using Moss's technique as well. Moss's technique is also advantageous, in some cases, for routine and accurate measurements of susceptibility effective masses.

3.5 Results and Analysis

3.5.1 Carrier Concentration

To determine the hole concentration in the samples studied, the high field Hall constant R_∞ was called for. Unfortunately, we did not have access to high enough fields. A high field plateau was only approached in the lowest concentration samples. This plateau is close to the high field limit from which true carrier concentrations can be determined provided there is one band only. If, for example, some carriers were in a heavier mass band, then the carrier concentration obtained from this apparent high field plateau would be more representative of the carrier concentration in the light mass band alone than of the total carrier concentration in both bands. Let us keep in mind the above complication arising when several bands are occupied, and let us assume, at this point, that all the carriers are in the <111> ellipsoids.

The carrier concentration was determined from the low field Hall constant R_o at liquid nitrogen temperature. For <111> ellipsoids only, the total carrier concentration N is:

$$N = r/R_o e \tag{3-75}$$

in which $r = R_o/R_\infty$. Our problem is now to find values of r as a function of carrier concentration.

For a parabolic band, isotropic scattering and ellipsoidal energy surfaces, r reduces to $r = \left(\langle\tau^2\rangle/\langle\tau\rangle^2\right) 3\kappa(\kappa + 2)/(2\kappa + 1)^2$ in which $\kappa = m_L/m_T$ is the ratio of the longitudinal to the transverse mass. For the Cohen non-parabolic band model (with $m_L/m_{L'} = 1$), Allgaier has shown (66 A2) that, for isotropic scattering and degenerate statistics, $r = 3\kappa'(\kappa' + 2)/(2\kappa' + 1)^2$ in which κ' is an effective anisotropy. As the number of carriers goes to zero $\kappa' = \kappa$. Such an effective anisotropy, including the effect of anisotropic scattering time, has been measured from magneto resistance experiments in PbTe with 10^{18} holes cm^{-3} at 77°K by Allgaier (60 A1); it is 4.2. Burke et al. (70 B1) found from Shubnikov de Haas studies that κ is independent of carrier concentration and alloy composition x in p-type $Pb_{1-x}Sn_xTe$ up to x = 30%; its value is 13. Allgaier calculations, for the non-ellipsoidal, non-parabolic Cohen energy surfaces (66 A2), revealed that the effective anisotropy κ' decreases with increasing carrier concentrations. Thus, the value of r increases (as κ' reduces) up to r = 1 for $\kappa' = 1$ and then decreases for κ' less than 1. Allgaier also shows that, as the Cohen surfaces become more dumbell shaped ($m_L/m_{L'} > 1$), the value of r may decrease all the way from low to high carrier concentrations. His calculation indicates that r depends primarily on the details of the band structure. Since this detailed information is not available yet, r cannot be calculated. However, we can assume that r varies in the same way in PbTe and $Pb_{1-x}Sn_xTe$ (with x = .06 and .2) on the basis that κ is the same and that the

band structure is similar.

Figure 3.10a shows the variation of the Hall constant at 77°K as a function of $\mu_H B$ where μ_H is the Hall mobility (m^2/volt-sec) at 77°K and B is the magnetic field (Webers/m^2). The two curves are for the lower carrier concentration samples 6-3 and 8-8 corresponding to alloy compositions of 6% SnTe and 20.8% SnTe respectively. A drop in the Hall constant is first observed as B increases followed by a large increase of R towards saturation. The initial drop of R, at low magnetic field, was not observed in PbTe (61 Al). We shall postpone the discussion of these results to Chapter 4. Here we only note that R_o is obtained at very low magnetic field and that extrapolation to low and high fields leads to R_o/R_∞ approximately equal to .9 for both samples. This agrees with the value .88 determined by Allgaier (60 Al) in PbTe with 10^{18} carriers cm^{-3}.

These values of R_o/R_∞ are plotted versus true carrier concentration N in Figure 3.10b together with the values determined by Allgaier for PbTe (60 Al, 66 Al). The full line represents the best curve through these points using the value of $R_o/R_\infty = .9$ at low carrier concentration. The drop in R_o/R_∞ with increasing carrier concentration for these degenerate samples is similar to that in SnTe and may be explained from the non-parabolic, non-ellipsoidal nature of the energy bands (66 A2, 68 T1).

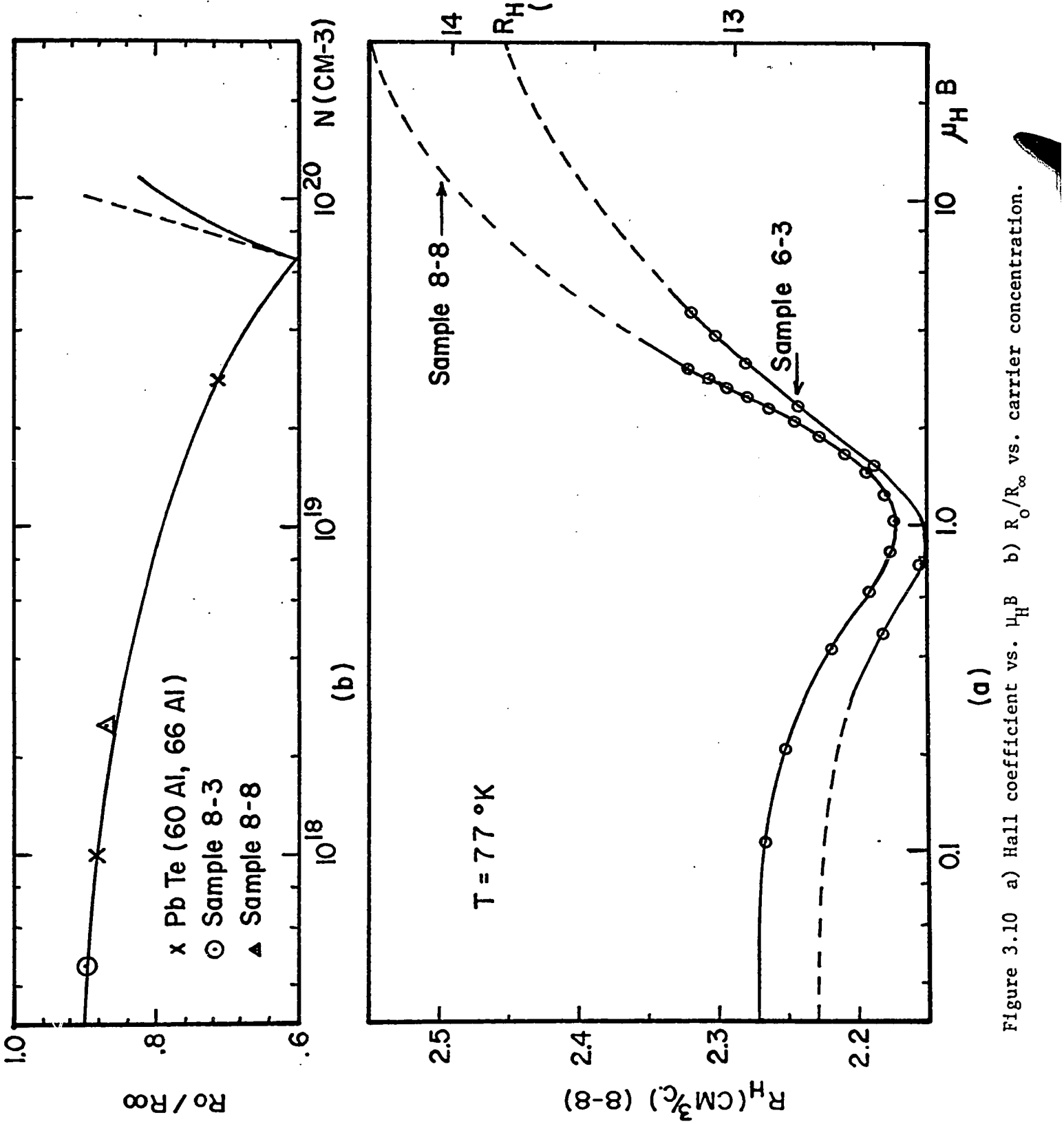

Figure 3.10 a) Hall coefficient vs. $\mu_H B$ b) R_o/R_∞ vs. carrier concentration.

At high carrier concentrations, R_o/R_∞ rises abruptly as the carriers enter a heavy mass band (see Section 3.5.4). It is not possible to measure R_o/R_∞ on the rising portion of the curve because the presence of heavy mass carriers would necessitate unattainable magnetic fields. However, very good estimates are possible. The point at which the carriers enter the heavy mass band is readily available from the kink observed in the curve of Figure 3.17b (Section 3.5.4). It occurs at $1/R_o e = 1.1 \times 10^{20}$ cm^{-3}, which converted to the scale of Figure 3.10b, $N = 6.6 \times 10^{19}$ holes cm^{-3}. For carrier concentration slightly greater than this, R_o/R_∞ rises as $.6N/N_1$ (as indicated by the dotted line in Figure 3.10b) where .6 is the value of R_o/R_∞ at the kink and N_1 is the carrier concentration in the lighter mass band at the kink. This simple relation is obtained because, past the kink, most extra carriers go in the heavy mass band due to its high density of states and do not contribute appreciably to conduction. As the numbers of heavy mass carriers is increased further R_o/R_∞ deviates more and more from the simple relation (dotted line) as indicated by the solid line in Figure 3.10b.

3.5.2 Dielectric Constant (ε_∞)

Values of ε_∞ were obtained at room temperature and at liquid nitrogen temperature on samples 8-8 and 6-3. For these lower carrier concentration samples, the free-carrier contribution to the index of refraction is negligible in the range of wavelengths used for the measurements (12-20 μ) and the reflectivity R is a direct measure of ε_∞.

The reflectivity was constant within the experimental error for the whole range of wavelengths and ε_∞ was found from $\varepsilon_\infty = \left((\sqrt{R}+1)/(1-\sqrt{R})\right)^2$. The values of ε_∞ so determined are shown in Figure 3.11a together with the values available for PbTe (65 Z1, 63 W1). The error shown on each point represents the average deviation that resulted from several measurements. The values of the energy gap E_G (67 N1, 67 T1) are shown in Figure 3.11b for the same range of alloy compositions. These values are needed for the discussion that follows.

Moss (60 M1, p.48) has discussed the relation between ε_∞ and energy gap and gives the following approximate relation.

$$\varepsilon_\infty^2 E_G = \text{constant} \qquad (3\text{-}76)$$

with the "constant" being 77. Several semiconductors, such as PbS and PbSe, obey this law quite well (60 M1, p.48). PbTe is a misfit and a "constant" equal to 325 is required to explain the room temperature data for PbTe. The above law is, however, correct qualitatively. As seen from Figure 3.11a, ε_∞ increases as the energy gap decreases. Whether the energy gap change is due to temperature or alloying similar variations in ε_∞ are produced. It is interesting to note that Figure 3.11a, together with equation (3-76), reveals a decreasing temperature variation of the energy gap with increasing SnTe content in agreement with the experimental findings of Tauber and Cadoff (67 T1).

The results in Figure 3.11 are not well fitted using equation (3-76), and another relation between ε_∞ and E_G was derived. ε_∞ is given by (60 M1, p.24):

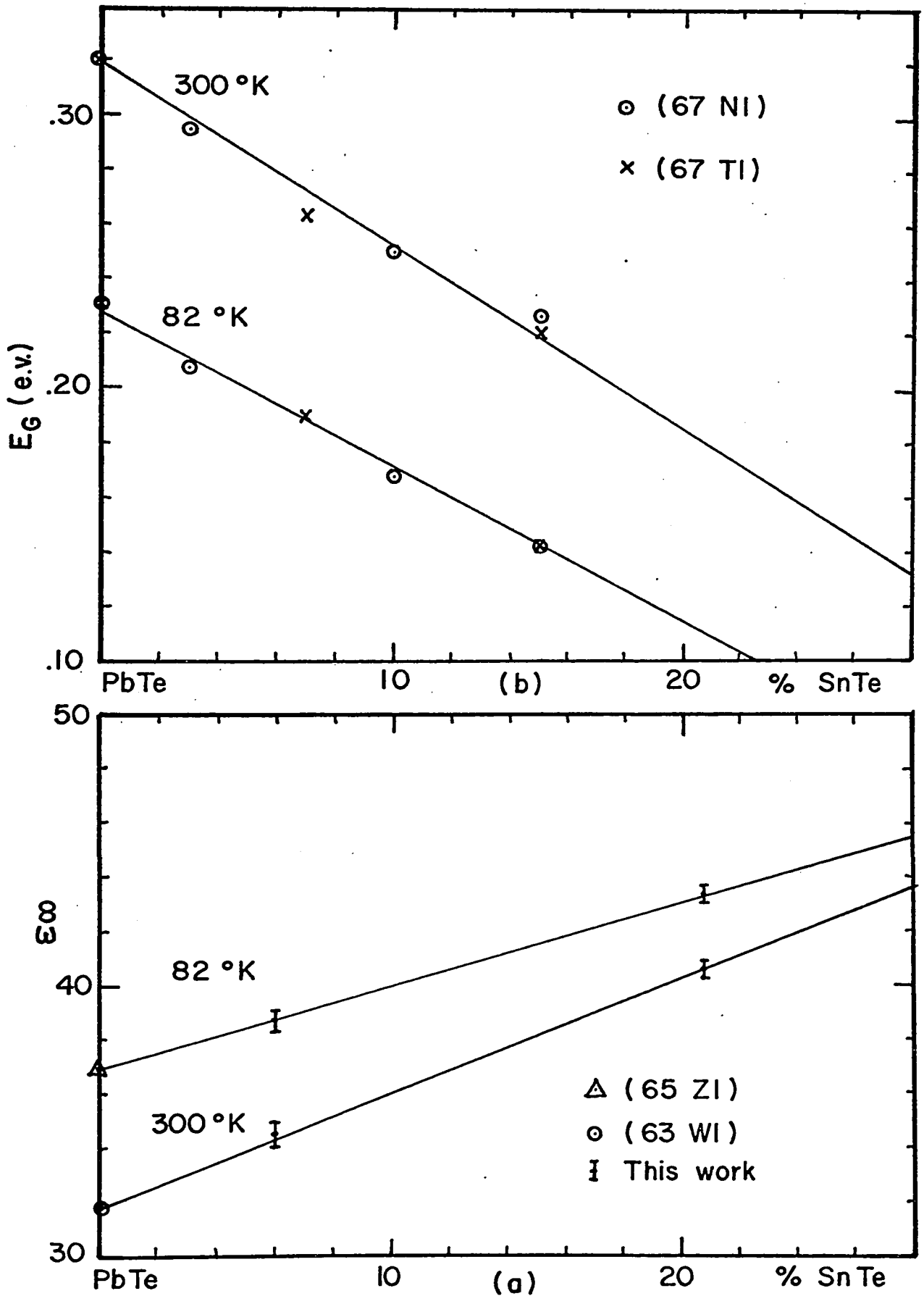

Figure 3.11 a) High frequency dielectric constant and
b) energy gap vs. alloy composition.

$$\varepsilon_\infty - 1 = \frac{2}{\pi} \int_0^\infty (2n\kappa) \frac{d\lambda}{\lambda} = \frac{-2}{\pi} \int_\infty^0 (2n\kappa) \frac{dE}{E} \qquad (3\text{-}77)$$

Thus, if $2n\kappa$ is known over all wavelengths, the value of ε_∞ can be found. Moss (60 M1, p.192) has calculated ε_∞ for p-type PbTe by graphical integration using the curve of $2n\kappa$ versus the wavelength determined by Avery and published by Moss (60 M1, p.189). He found $\varepsilon_\infty = 30.3$ in very good agreement with the experimental value of 31.8 as shown in Figure 3.11.

An important characteristic of the $2n\kappa$ curves for PbS, PbSe, and PbTe (see insert in Figure 3.12) is that the value of $2n\kappa$ is close to a constant on the short wavelength side of the absorption edge for an appreciable range of wavelengths. Let us call this value $(2n\kappa)_{PL}$ and let us assume that a change in the main gap E_G produces changes in the $2n\kappa$ curve near the absorption edge only (as shown by the dotted line in the insert) and does not affect the value $(2n\kappa)_{PL}$. In this starting model, it is also assumed that the effect of temperature or alloying on the $2n\kappa$ spectra is entirely described by the change of E_G with temperature or alloying.

With the above assumption, equation (3-77) can be integrated in two parts as follows:

$$\varepsilon_\infty - 1 = \frac{-2}{\pi} \left[\int_\infty^{E_{PL}} 2n\kappa \frac{dE}{E} + \int_{E_{PL}}^0 2n\kappa \frac{dE}{E} \right] \qquad (3\text{-}78)$$

in which E_{PL} is a convenient value of energy around which $2n\kappa$ is constant.

The first integral on the right has the same value for all temperatures and alloy compositions considered and gives a constant. For the second integral, $2\eta\kappa$ is constant except in the vicinity of the absorption edge where $2\eta\kappa$ tails down to zero. There is a negligible contribution passed the absorption edge. The tailing is taken into account by taking $2\eta\kappa$ as constant down to the value of $E = E_G$ and zero for lower energies. Equation (3-78) can now be integrated and gives

$$\varepsilon_\infty = C - (2/\pi)(2\eta\kappa)_{PL} \ln E_G \qquad (3\text{-}79)$$

in which $(2\eta\kappa)_{PL}$ is the value of $(2\eta\kappa)$ on the plateau and C is some constant. Thus from:

$$\ln E_G = \frac{-\varepsilon_\infty}{(2/\pi)(2\eta\kappa)_{PL}} + A \qquad (3\text{-}80)$$

a semi-logarithmic plot of E_G versus ε_∞ should yield the value of $(2\eta\kappa)_{PL}$ from the slope. Such a plot is shown in Figure 3.12 using the values of ε_∞ and E_G given in Figure 3.11. The insert is a reproduction of Avery data, for p-type PbTe, taken from Moss (60 M1, p.189). The dotted line (in the main graph), is equation (3-76) for which the "constant" was determined from the room temperature data on PbTe. The solid line represents the best line through the experimental points. From the slope we obtain $(2\eta\kappa)_{PL} = 18.2$ compared to 16.5 for the actual measured value. The fact that a straight line is obtained and that its slope yields a $(2\eta\kappa)_{PL}$ value close to the measured one supports the

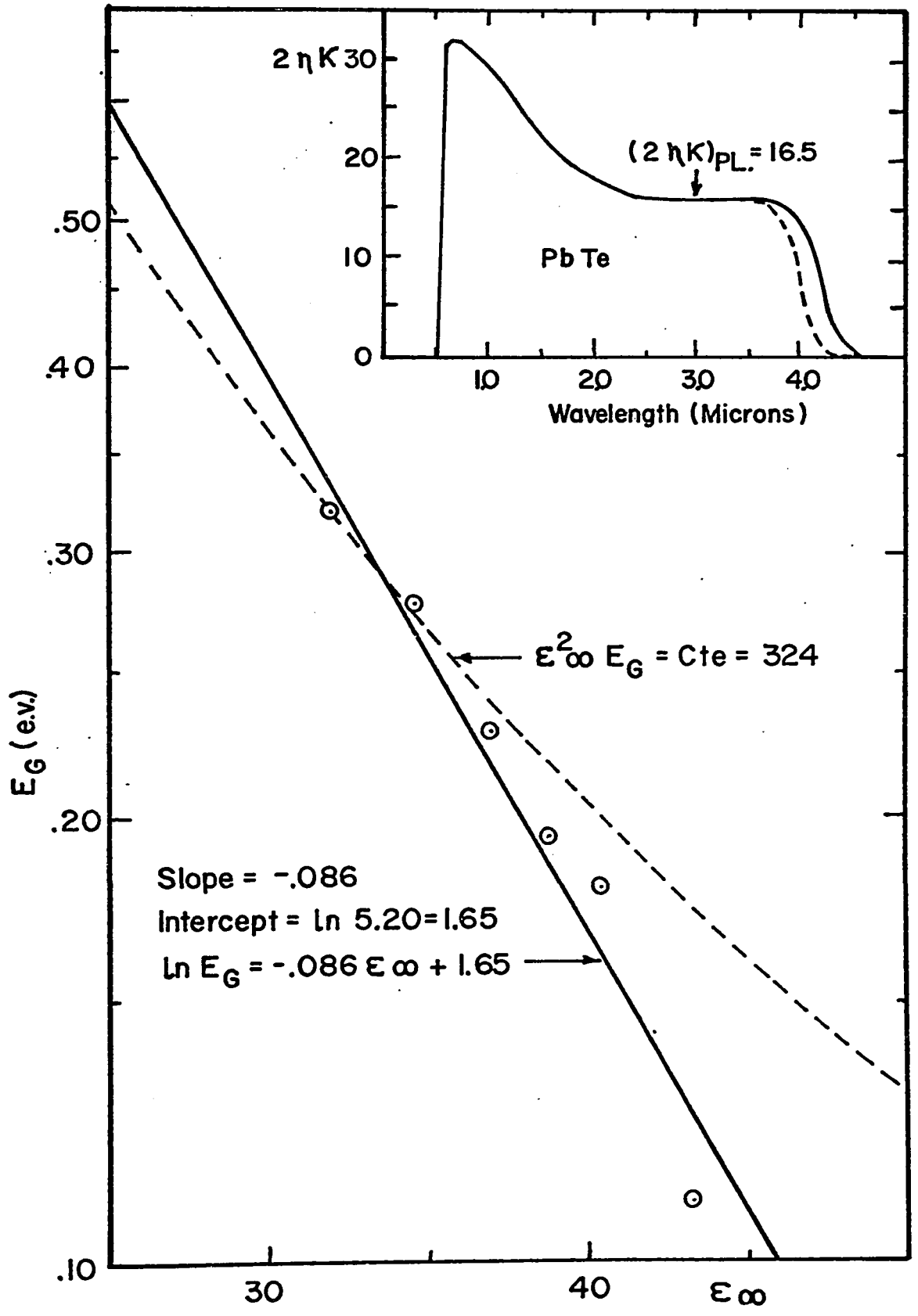

Figure 3.12 Relation between high frequency dielectric constant and energy gap.

starting model and the following equation relating E_G and ε_∞ is proposed for PbTe and the range of alloys considered.

$$\ln E_G = -.086\ \varepsilon_\infty + 1.65 \qquad (3\text{-}81)$$

This relation is for low carrier concentrations. For larger carrier concentrations, the absorption edge is Burstein shifted to higher energy E_G^*. However, replacement to E_G by E_G^* in equation (3-81) is not expected to produce correct values of ε_∞ since the shape as well as the position of the absorption edge is affected and the plateau is expected to disappear for high doping.

The values of ε_∞ versus carrier concentration ($p^* = .9/R_o e$) were obtained from the experimental reflectivity curves using the fitting technique and the slope technique. They are shown in Figure 3.13 for the two alloy compositions investigated. At the highest carrier concentration, ε_∞ increases rapidly as the carriers enter the heavy mass band.

Comparison of Figures 3.13 and 3.10b reveals that the ratio of $(R_o/R_\infty)/\varepsilon_\infty$ is close to a constant for all carrier concentrations. (Note that in Figure 3.10b the true carrier concentration N is used in abscissa while $.9/R_o e$ is used in Figure 3.13). This situation is very fortunate when using the Moss's method since the effective mass is determined through the equation:

$$\omega_P^2 = N\, e^2/m_s \varepsilon_o \varepsilon_\infty \qquad (3\text{-}82)$$

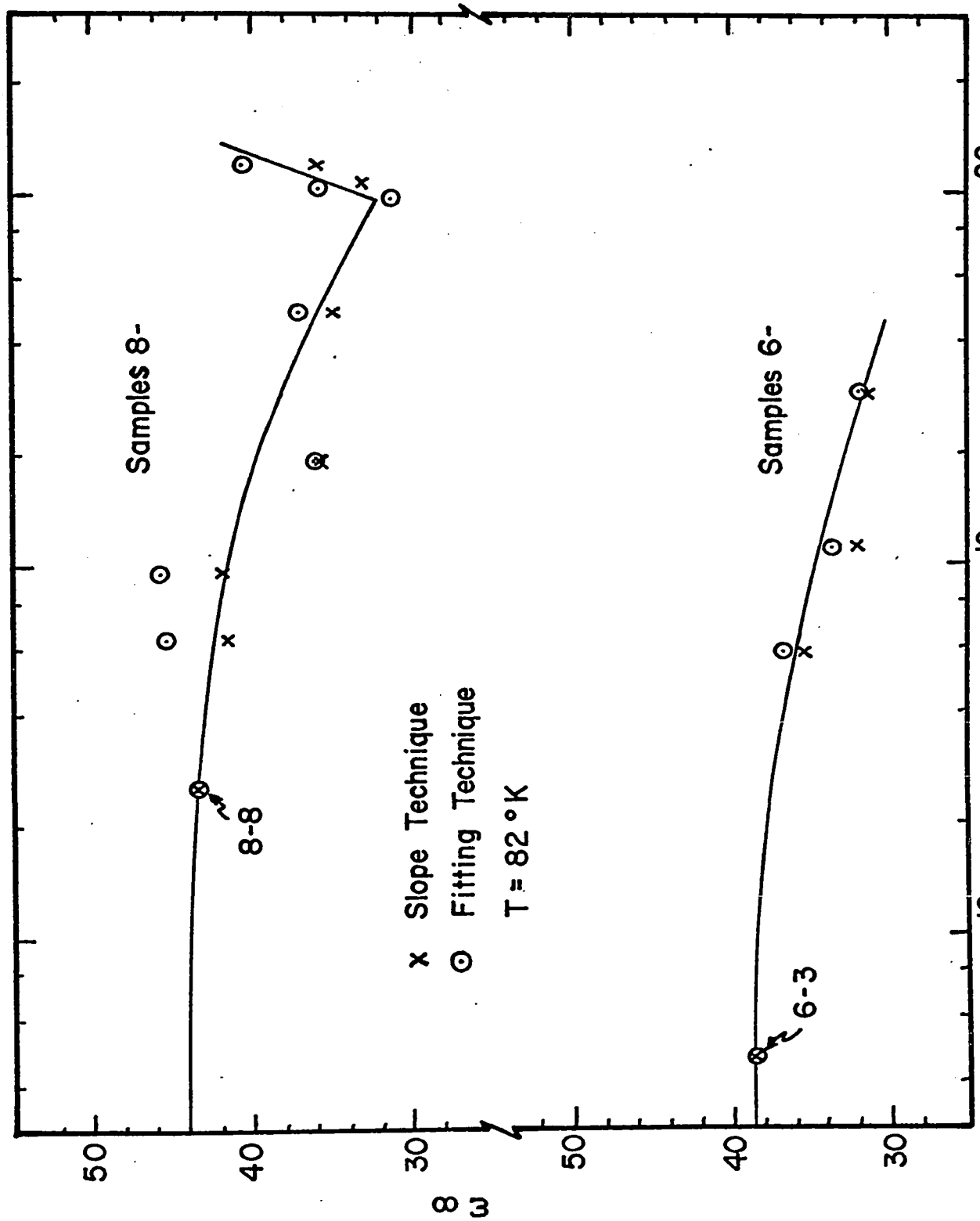

Figure 3.13 High frequency dielectric constant vs. p*.

The quantity on the right is unchanged whether we use the low carrier concentration values of (R_o/R_∞) and ε_∞ or the correct ones for a given carrier concentration if the ratio $(R_o/R_\infty)/\varepsilon_\infty$ is constant. The quantity on the left, is determined from the graphs in Figures 3.5 or 3.6 and is smaller by less than 5% when using the correct value of ε_∞ compared to the use of the low carrier concentration value. In fact, this smaller value of ω_p^2 is balanced by the small decrease of the ratio $(R_o/R_\infty)/\varepsilon_\infty$ with increasing carrier concentration. Therefore, for the variations of ε_∞ and (R_o/R_∞) shown in Figures 3.13 and 3.10b, the correct values of effective masses are obtained by using the low carrier concentration value of ε_∞ and of (R_o/R_∞) for all carrier concentrations.*

In view of the above simplification when using the Moss's method, we will use for the purpose of determing the susceptibility effective masses at all carrier concentrations:

$$p^* = (.9/R_o e)cm^{-3} \qquad (3\text{-}83)$$

together with the low carrier concentration value of ε_∞. The values of the assumed carrier concentration p* as given by equation (3-83) are given in Table 3.1. Also the true carrier concentration N using the (R_o/R_∞) values of Figure 3.10b and the conductivity mobility calculated using $(R_H\sigma/r)_{77^oK}$ are given.

*While this is supported by experiments below the kink, it is not so well justified above the kink.

Sample #	$p^* = (.9/R_o e)_{77^oK}$ cm^{-3}	$\mu_c(77^oK)$ $cm^2/V\text{-}sec$	$R_o/R_\infty(77^oK)$	$N(77^oK)$ cm^{-3}
		20.8% SnTe		
8-3	1.192×10^{20}	205	.80	1.05×10^{20}
8-5	1.055×10^{20}	258	.73	8.5×10^{19}
8-6	9.864×10^{19}	351	.60	6.6×10^{19}
8-1	4.586×10^{19}	874	.70	3.57×10^{19}
8-2	1.926×10^{19}	2184	.76	1.63×10^{19}
8-7	9.765×10^{18}	4087	.80	8.68×10^{18}
8-4	6.406×10^{18}	5740	.82	5.84×10^{18}
8-8	2.56×10^{18}	10400	.86	2.45×10^{18}
		6% SnTe		
6-1	2.882×10^{19}	1150	.73	2.34×10^{19}
6-0	1.116×10^{19}	3240	.79	9.8×10^{18}
6-6	5.805×10^{18}	5670	.82	5.3×10^{18}
6-3	4.66×10^{17}	15900	.90	4.66×10^{17}

TABLE 3.1 EXPERIMENTAL DATA FOR $Pb_{1-x}Sn_xTe$ ALLOYS

3.5.3 Surface Effects

Despite the fact that no satisfactory explanation of the surface effects observed on our specimens will be given, we nevertheless include them here in the results section to stress their importance. Of the reported infrared-plasma reflectivity measurements that the author is aware of, only those performed on chemically polished surfaces have been found to be well-fitted by equations (3.26) (for example (67 R1, 70 B2)). On the other hand, several papers deal with such measurements performed on mechanically polished surfaces (for example (70 S1, 70 R1)). The values of m_s, μ_{opt}, and ε_∞ obtained from the latter measurements are often in error as will now be seen.

Figure 3.14 illustrates the large differences in the reflectivity spectra between chemically polished surfaces and mechanically polished surfaces for some of the samples studied. Similar changes were found on all samples listed in Table 3.1 except sample 8-8 and 6-3 for which there is no free carrier dispersion in the wavelength range covered due to their low carrier concentrations. The full line in Figure 3.14 represents the best fit to the free carrier dispersion relations. In all cases, the reflectivity spectra from chemically etched surfaces were very well fitted, but none from mechanically polished surfaces could be fitted using the free carrier dispersion relations.

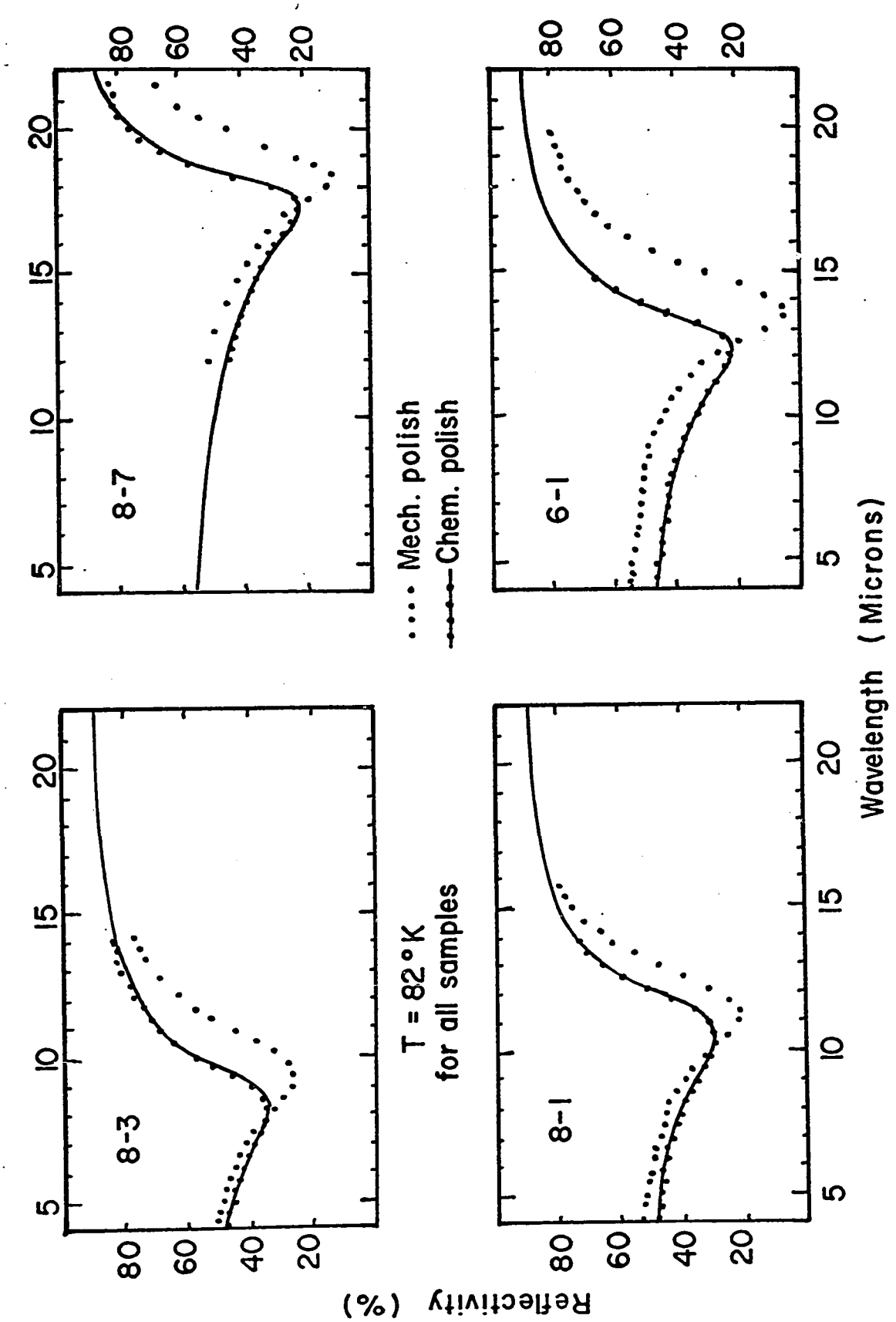

Figure 3.14 Reflectivity vs. wavelength showing the effect of surface treatment.

The results of Figure 3.14 are also reproducible. On sample 8-7 for example, the sample was mechanically polished using .05 micron aluminum oxide powder and the reflectivity spectra was taken; the sample was then chemically polished and the reflectivity spectra retaken. This procedure was repeated several times, and within experimental error the spectra obtained on mechanically and chemically polished surfaces, shown in Figure 3.14, were in turn reproduced.

At sufficiently low wavelengths not shown on the graph the reflectivity curves for both types of surface preparation merge together. In all details, the results on Figure 3.14 on $Pb_{1-x}Sn_xTe$ are similar to those reported on ZnO (66 W1) for mechanically and chemically polished surfaces. However, no explanation of this effect is given. Rheinländer (70 R1) reports infrared reflectivity measurements on mechanically polished CdSb which do not fit the classical free-carrier dispersion relations. We believe that the same distortion due to mechanical polishing as the one just described is present in his results. In addition, he found that with time the reflectivity spectra were further shifted towards longer wavelengths. He also provides no satisfactory explanation for the former deviation but gives (70 R2) a detailed explanation for the latter observed shift

with time in terms of the formation with time of a hole depletion layer at the CdSb surface. We therefore believe that the large differences between the reflectivity spectra for mechanically and chemically polished specimens is not particular to some materials only, but may be present in all materials. An explanation of this effect would be desirable since it could be used to provide extra information.

First, the possibility of a depletion layer, of the type postulated by Rheinländer (70 R2), present in mechanically polished samples was eliminated for the following reasons. The calculation of Rheinländer (70 R2) for the case where a depletion layer is present can account for an isotropic shift of the reflectivity spectra to longer wavelengths but cannot account for the large drop in reflectivity at the position of the reflectivity minimum. Also measurements, performed on mechanically as well as chemically polished surfaces after prolongated (2-5 months) storage in air or vacuum at room temperature, gave the same reflectivity spectra as the one obtained immediately after the surface treatment. This shows that there is no reduction in hole concentration near the surface and that diffusion of metal vacancies over short distances (< 1 microns) is negligible at room temperature.

Secondly, the possibility that the mechanical treatment caused the surface to be in a stressed state and was responsible for the observed distortion in the reflectivity spectra was eliminated

through two experiments. In the first experiment, it was assumed that the stress present in the surface layer was producing a change in energy band level and principally of the main gap. If these changes had caused the observed distortions in the reflectivity spectra, the nature of these distortions should have been drastically different on a $Pb_{1-x}Sn_xTe$ sample containing 50% SnTe. For the samples shown in Figure 3.14 pressure closes the gap; for 50% SnTe sample the conduction and valence have crossed over at liquid nitrogen temperature, according to Dimmock et al. (66 D1), and pressure is expected to open the gap. Experiments on both alloy compositions have shown similar distortions of the reflectivity spectra. In a second experiment, polarized light was used and produced no change in the reflectivity spectra, for the two perpendicular directions of polarization used, on either the mechanically or chemically polished surfaces. From these two experiments, it was concluded that, if stress is at all present in the surface, it does not affect the reflectivity spectra and is not responsible for the large difference in the reflectivity spectra between mechanically and chemically polished surfaces.

The reflectivity spectra in Figure 3.14 were analyzed using the slope method and the wavelength squared dependence of η^2 was verified for the chemically polished surfaces as expected and also unexpectedly for mechanically polished surfaces. These results are shown in Figure 3.15 in which only a few points for the

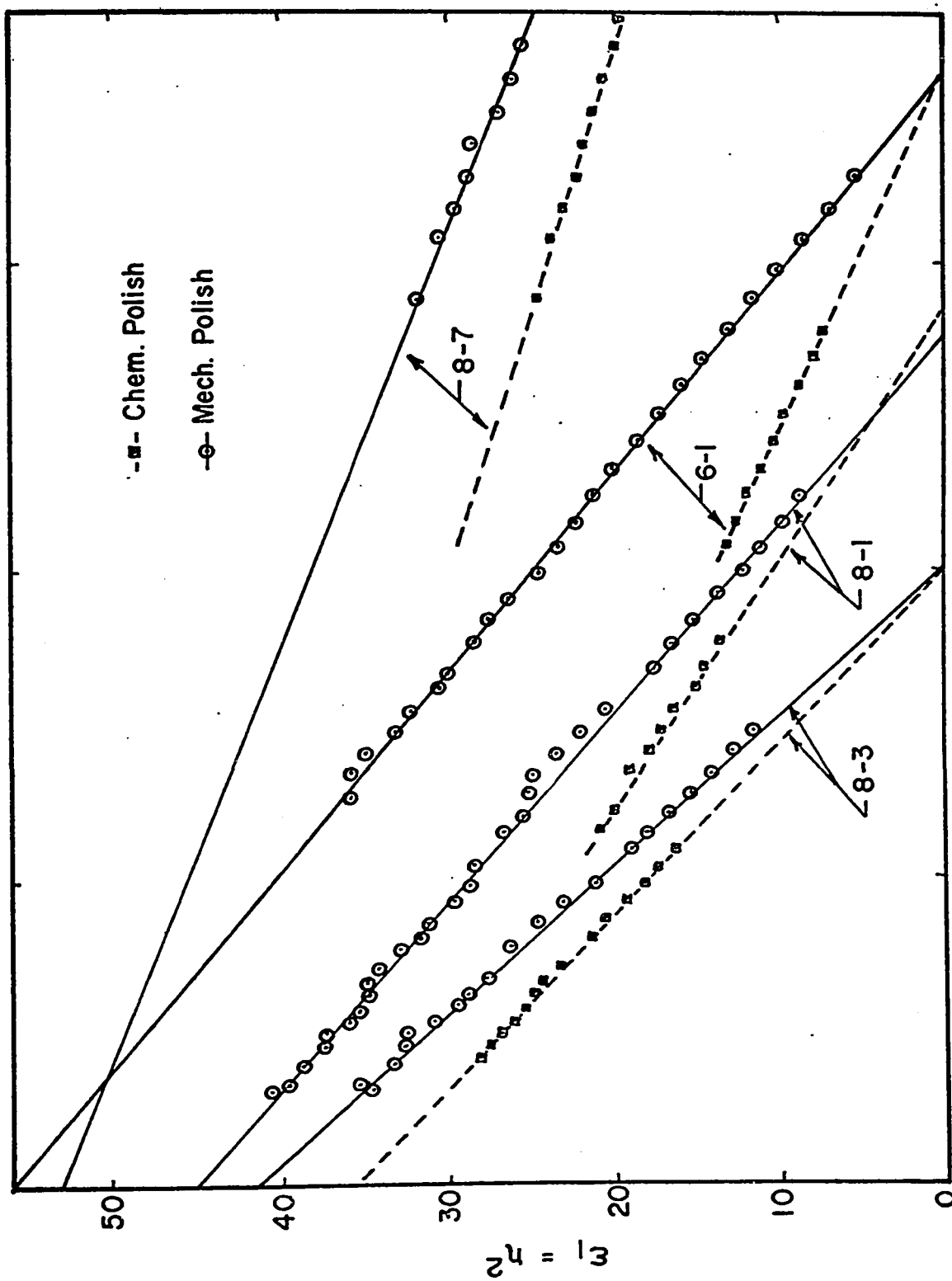

Figure 3.15 Real part of dielectric constant vs. $(\text{wavelength})^2$ showing the effect of surface preparation.

chemically etched surfaces are plotted for clarity. Also the extrapolation on the λ^2 axis gives the same value for the chemically and the mechanically polished surface within 5% in λ^2 for all samples studied. This means that:

$$\omega_p = \frac{Ne^2}{m_s \varepsilon_o \varepsilon_\infty} \qquad (3\text{-}84)$$

is approximately the same whether the sample had been mechanically or chemically polished. Since ε_∞, determined from the extrapolation to $\lambda = 0$ is as much as 80% greater (sample 6-1) for mechanically than for chemically polished surfaces, an effective mass 80% (sample 6-1) too small is obtained from mechanically polished samples. We again emphasize that the realization of the η^2 vs λ^2 linear dependence does not mean that the variation of η^2 with wavelength is due to free electrons only. It should be pointed out that the results of Rheinländer on CdSb (70 R1), obtained from mechanically polished samples, were analyzed by curve fitting using the same portion of the reflectivity spectra as that used in Figure 3.15. As it is clear from their data that the same spectral deviations as those of Figure 3.14 are present, their effective masses are too low and their optical mobilities too high.

In conclusion, no satisfactory explanation is given for the distorted reflectivity spectra observed from mechanically polished surfaces. However, it is shown that they cannot be fitted and thus analysed to yield the correct values of susceptibility effective

masses and dielectric constants. Such a guide line should be useful when facing the increasing volume of literature on the subject.

3.5.4 Effective Masses vs Carrier Concentration

To find the susceptibility masses, only the reflectivity spectra obtained from chemically polished samples were used. In all cases, good fits were obtained and the fitted curves through the experimental points are shown in Figure 3.16 together with the fitting parameters. The susceptibility masses have also been obtained from the Moss's method which, for these measurements, is expected to yield more accurate values. Table 3.2 lists the experimental values of reflectivity and wavelength at the position of the reflectivity minimum, the values of ω_p/ω_{min} and $\omega_{min}\langle\tau\rangle$ obtained from Figures 3.5, 3.6 and 3.7, the refractive index η and extinction coefficient κ at the position of the reflectivity minimum, and finally the values of $M_s = m_s/m_o$ and μ_{opt}. Figure 3.17 shows a plot of the effective mass values obtained from the fitting technique and Moss's technique for the two alloy compositions studied. The apparent discrepancies between the effective masses determined by either methods are expected from earlier discussion. Effective masses obtained by both techniques were obtained assuming $p^* = 0.9/R_o e$ for all carrier concentrations. As discussed earlier, Moss's technique gives the correct masses since we also used the low concentration value of

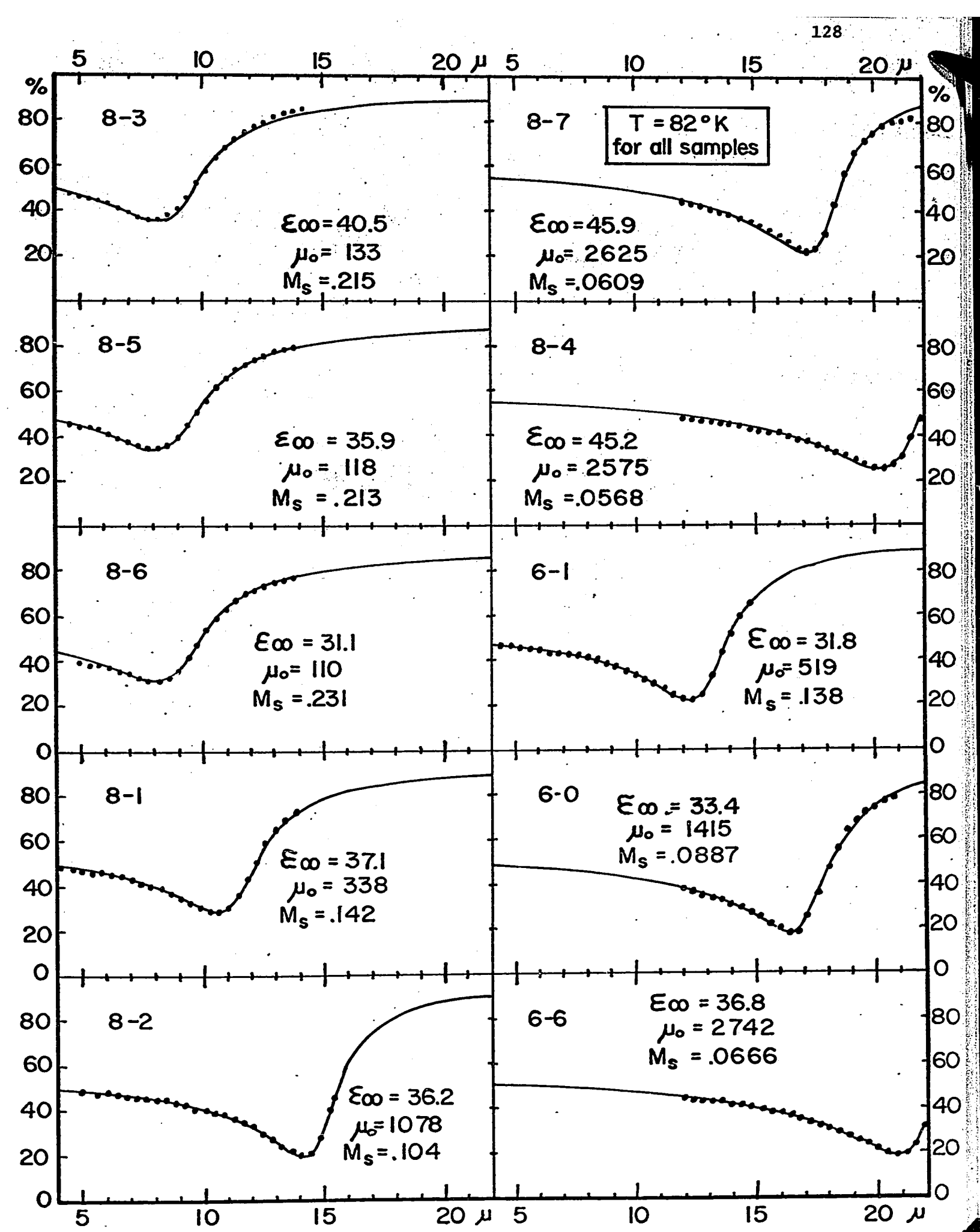

Figure 3.16 Experimental and calculated reflectivity curves

Sample #	η_{min}	κ_{min}	λ_{min} (microns)	R_{min} (%)	ω_p/ω_{min}	$\omega_{min}\langle\tau\rangle$	M_s	μ_{opt} (cm^2/V-sec)
				20.6% SnTe (T = 82°K)				
8-3	3.37	1.33	7.96	35.30	.913	3.75	.1890	134
8-5	3.23	1.30	8.02	33.95	.920	4.10	.1674	148
8-6	2.91	1.23	8.06	30.72	.933	5.04	.1537	172
8-1	2.75	1.19	10.52	28.95	.940	5.65	.1200	426
8-2	2.07	.92	14.12	19.40	.964	10.27	.0862	1452
8-7	2.18	.98	17.37	21.29	.960	9.17	.0667	2140
8-4	2.44	1.08	20.39	24.90	.952	7.30	.0614	2203
				6% SnTe (T = 82°K)				
6-1	2.22	.97	12.28	21.50	.955	8.12	.1096	680
6-0	1.92	.84	16.50	16.82	.965	11.20	.0751	1970
6-6	2.05	.90	20.92	18.95	.961	9.61	.0633	2715

TABLE 3.2 EXPERIMENTAL RESULTS FOR $Pb_{1-x}Sn_xTe$ SAMPLES

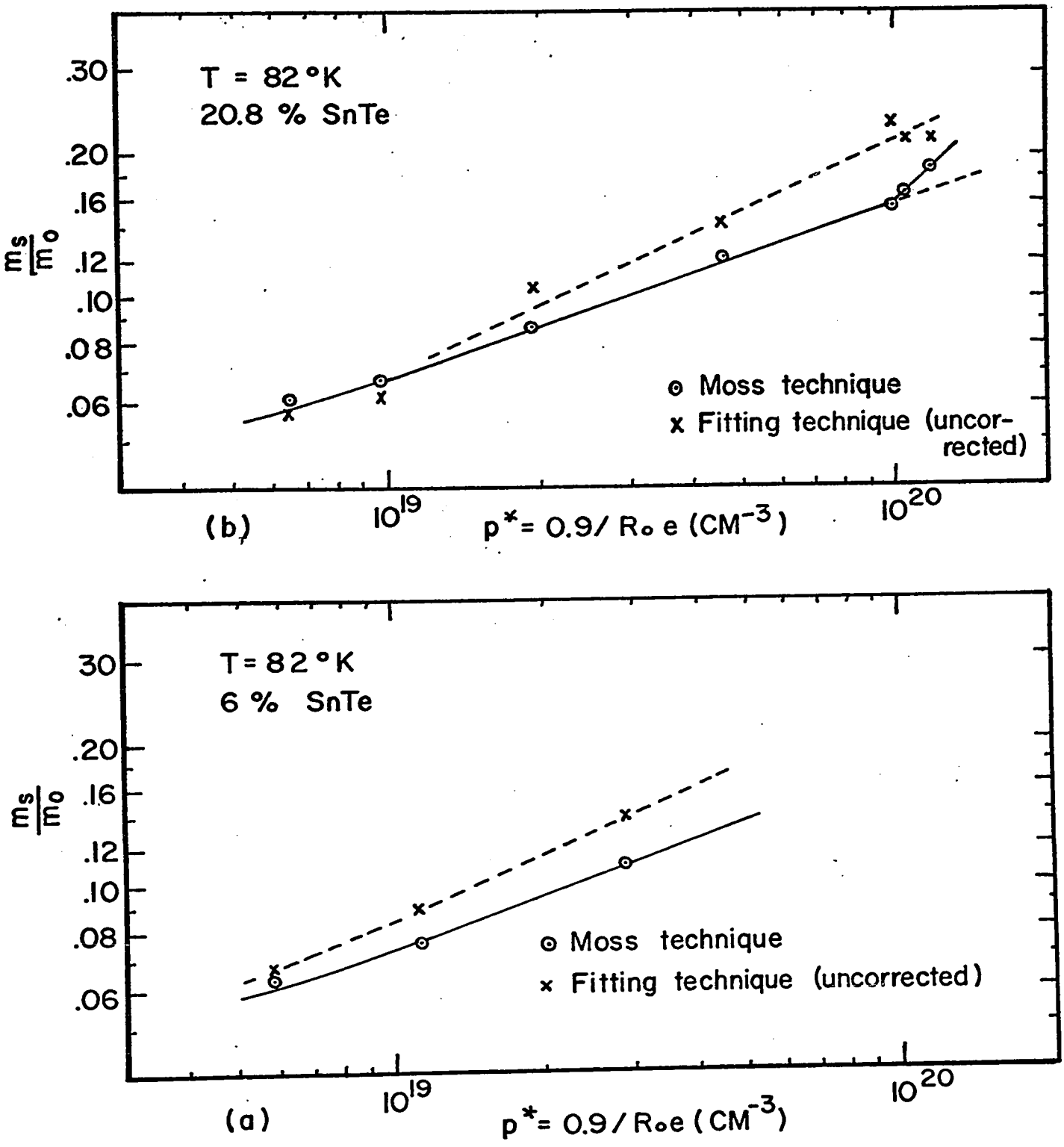

Figure 3.17 Effective mass vs. p*.

ε_∞ for all carrier concentrations. On the other hand, the variation of ε_∞ with carrier concentrations is implicitly taken into account in the fitting technique so that to obtain the correct masses it is necessary to take into account the change of R_o/R_∞ as well. When the effective mass values from fitting are corrected for the variation of R_o/R_∞ using the values of Table 3.1, good agreement results are shown in Figure 3.18.

An important point here is that it would not have been possible to detect the kink at $p^* = 10^{20}cm^{-3}$ from susceptibility masses determined using the fitting technique alone. This is because R_o/R_∞ values are required to obtain the correct susceptibility masses when the fitting method is used; but good estimates of R_o/R_∞ presuppose an accurate determination of the carrier concentration at the kink. Since, in the absence of this information, R_o/R_∞ was assumed constant when it should increase with carrier concentration (p^*) past 10^{20} carriers cm^{-3}, the values of m_s/m_o obtained using the fitting technique were more and more underestimated as the carrier concentration (p^*) increased past $10^{20}cm^{-3}$. The net effect was a smoothing out of the curve of the susceptibility mass versus p^* as shown in Figure 3.17b.

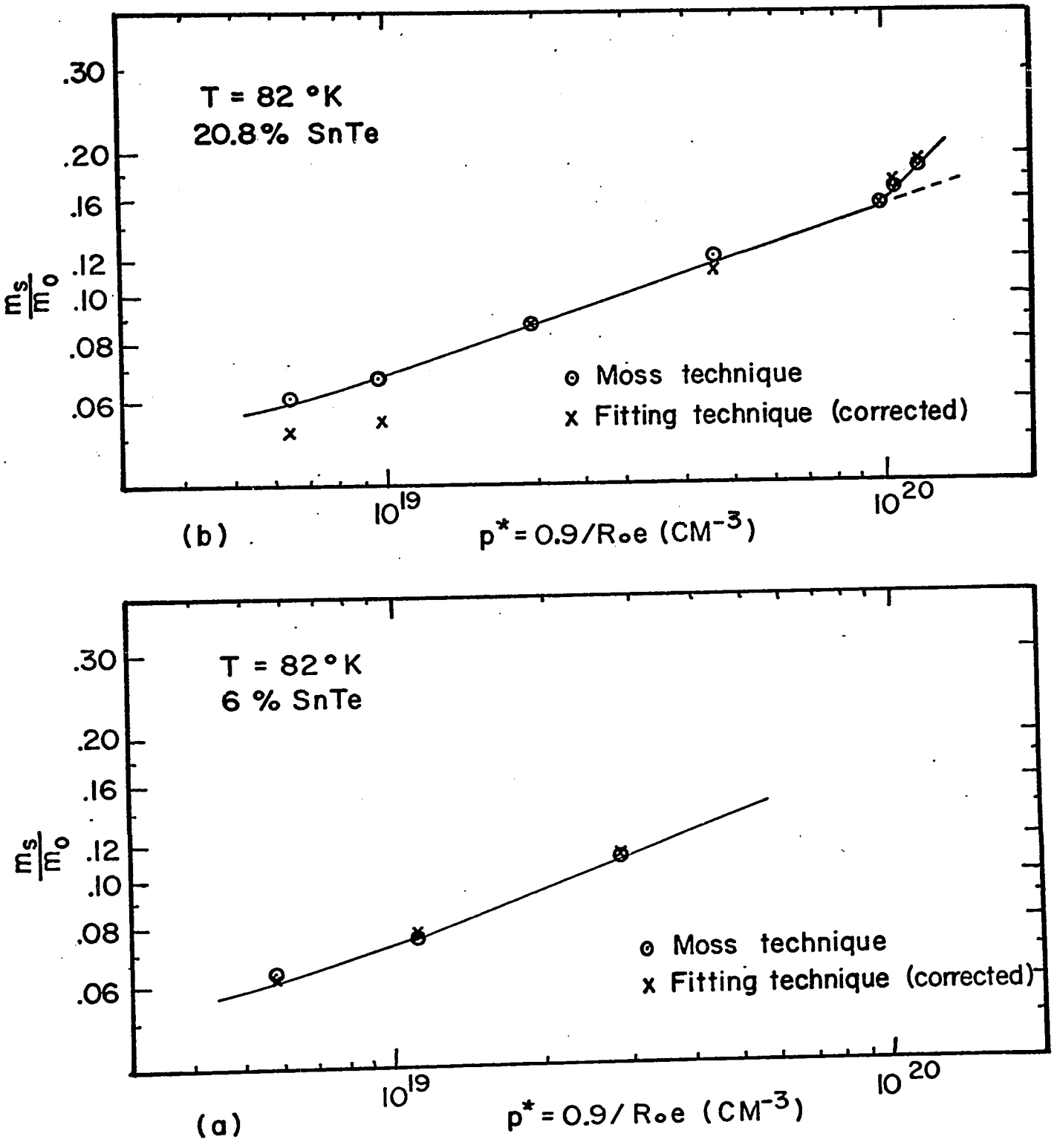

Figure 3.18 Effective mass vs. p*.

From Figure 3.18, we note that the susceptibility masses determined by the fitting technique and corrected for variation of (R_o/R_∞) are in very good agreement* with those determined using the Moss method. However, for the two lowest carrier concentrations in Figure 3.18b, the agreement is worse. We have seen earlier that both bound carrier and ionic contributions to the dielectric constant results in smaller effective masses when using the fitting technique. The above contributions turned out to be larger for these two samples on account of a longer wavelength absorption edge and the higher static dielectric constant (it varies from 400 to 1400 in going from PbTe to SnTe).

The values of R_o/R_∞ listed in Table 3.1 brought the effective mass values determined by the Moss and the fitting technique into agreement, as shown in Figure 3.18. This suggests that the R_o/R_∞ values are good estimates, and we will now use them to determine the true carrier concentration N that should appear in the abscissa. Figure 3.19 is the final plot showing the effective mass versus the true carrier concentration N. Only the values of effective mass determined by the Moss method are shown.

---

* The agreement indicates that the measurements represent closely the absolute reflectivity due to free carrier only. A good agreement between the two methods is then expected as discussed earlier. It also suggest that the R_o/R_∞ and ε_∞ values used are reasonnable.

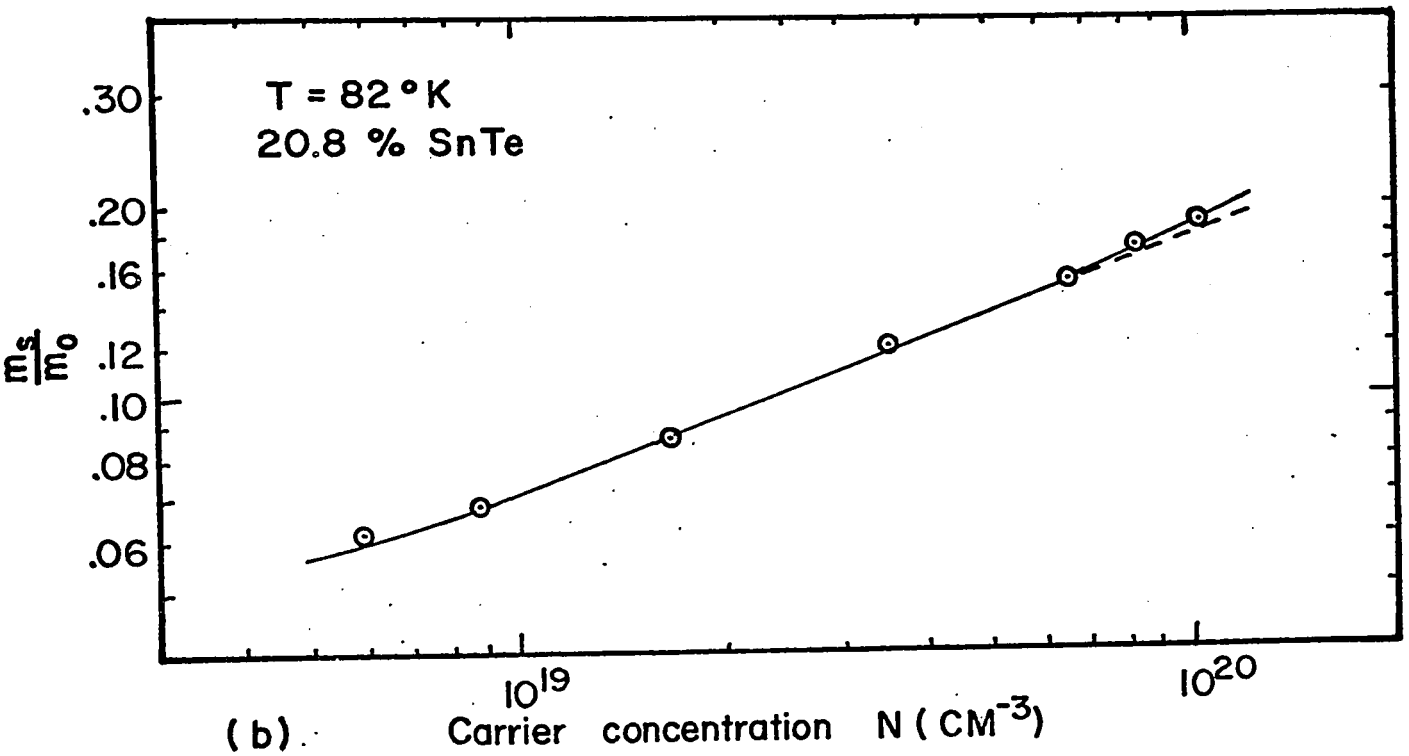

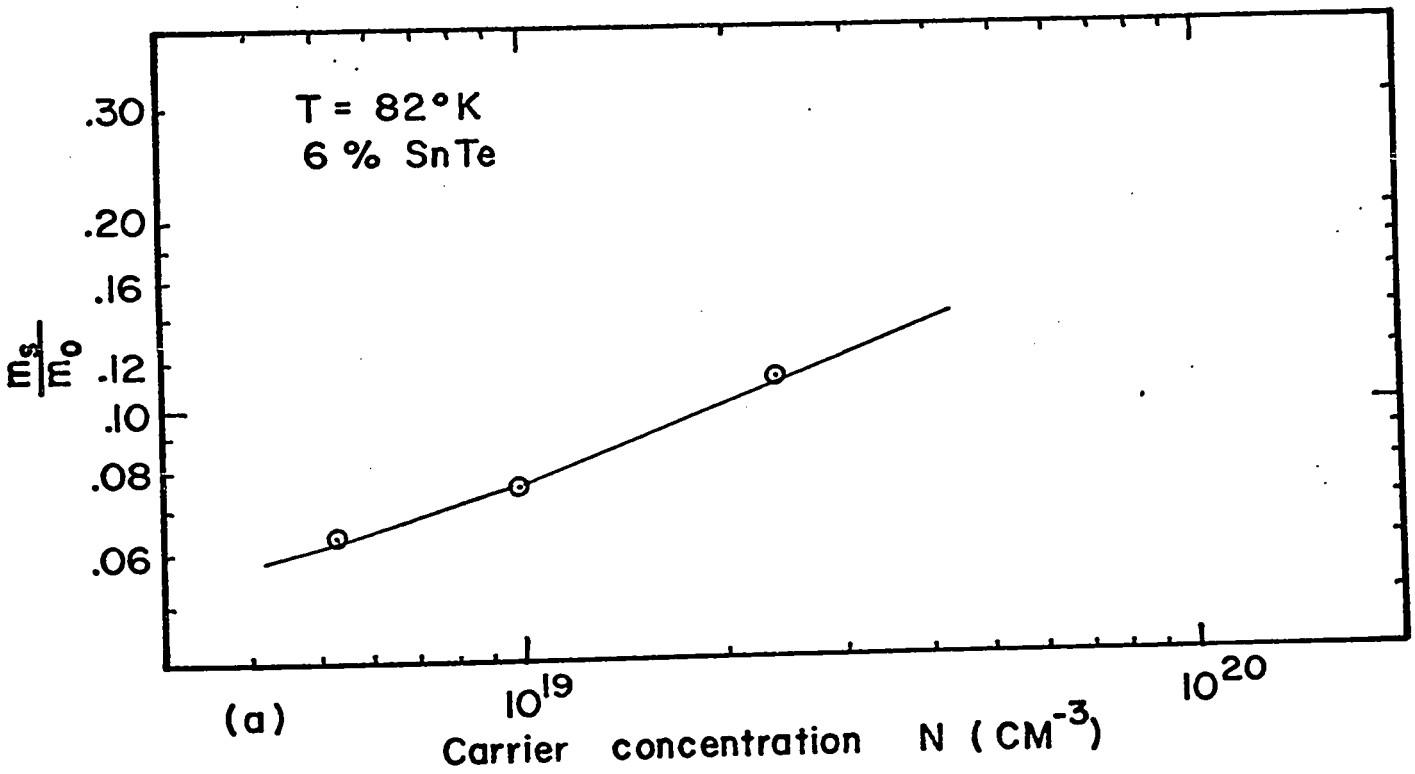

Figure 3.19 Effective mass vs. carrier concentration.

No correction for non-degeneracy was necessary for any of the samples studied at 82°K. When this effect of scattering is taken into account, as described in Section 3.3.2, it is found to change the effective mass by less than 0.2%.

3.5.5 Effective Mass vs Temperature

The reflectivity was measured as a function of wavelength in sample 8-7 for several temperatures between 82°K and room temperature. Figure 3.20 shows these reflectivity spectra in the region of the reflectivity minimum. For clarity, only a few experimental points are shown. Table 3.3 gives the values of R_{min}, λ_{min}, obtained from Figure 3.20, the values of ε_∞ obtained by linear interpolation between the experimentally determined values at room temperature and 82°K, the values of ω_p/ω_{min} and $\omega_{min} \langle\tau\rangle$ obtained from Figures 3.5 and 3.7, the values of M_s and μ_{opt} uncorrected for carrier scattering (i.e. $r^2 = 1$), and finally the values of M_s and μ_{opt} corrected for carrier scattering.

The values of r^2 (also given in Table 3.3), necessary to find these corrections, were calculated as described in Section 3.3.2. The non-parabolicity of the <111> minima was assumed to be described by $A_{\alpha\beta}\, k_\alpha k_\beta = E + E^2/E_G$ where E_G is the main gap given in Figure 3.11b (for temperatures between 82°K and 300°K, a linear interpolation was used). The Fermi level for sample 8-7 was calculated using the above model, as described in Section 3.5.7.

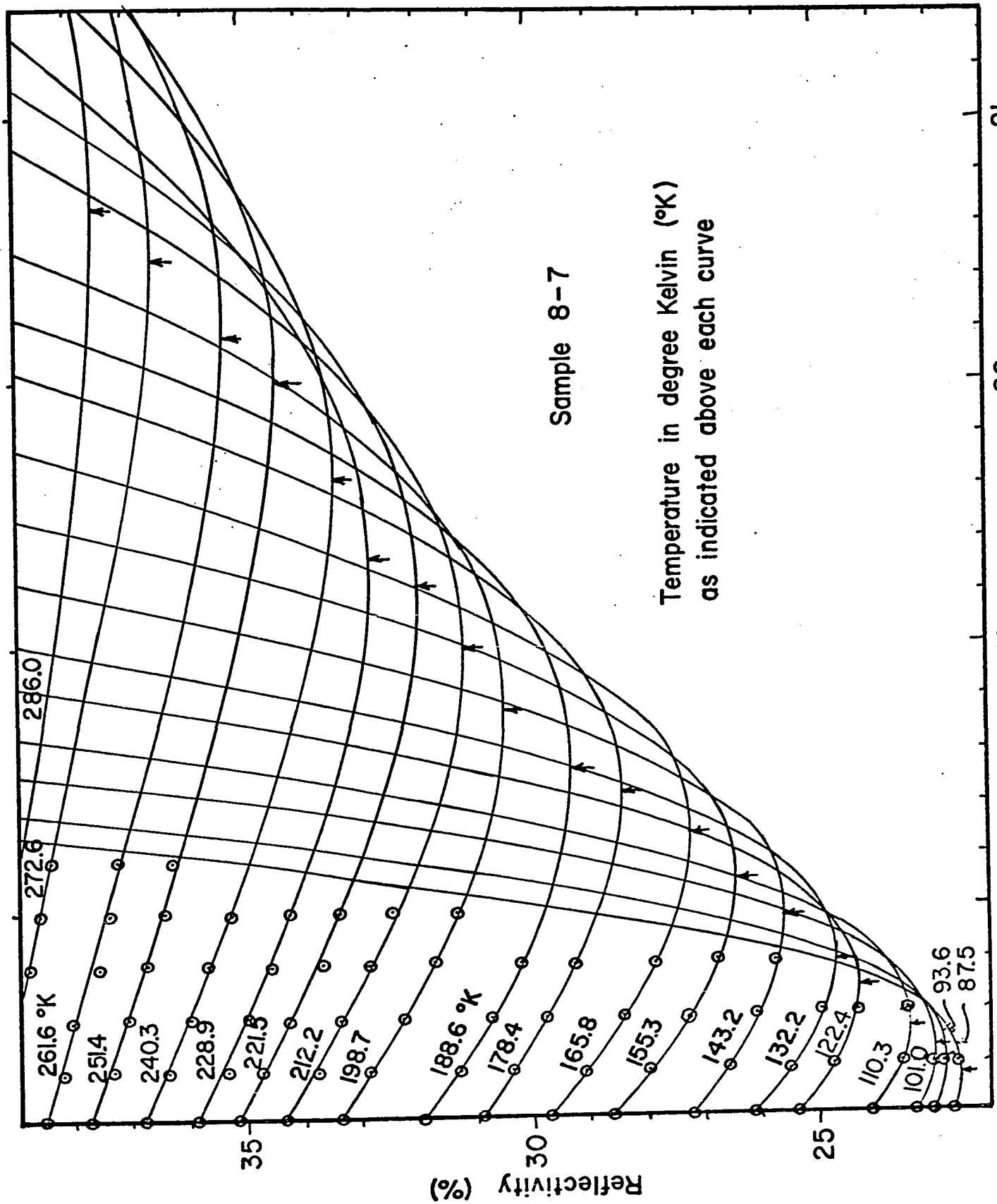

Figure 3.20 Reflectivity vs. wavelength in sample 8-7.

						Uncorrected		Corrected		
T	ε_∞	R_{min}	λ_{min}	ω_p/ω_{min}	$\omega_{min}^{<\tau>}$	M_s	μ_{opt}	M_s	μ_{opt}	r^2
°K		%	microns				cm^2/V-sec		cm^2/V-sec	
84.	43.3	22.10	17.30	.9587	8.79	.0658	2157	.0658	2074	1.04
87.5	43.3	22.53	17.36	.9578	8.55	.0664	2087	.0664	1997	1.04
93.6	43.2	22.80	17.40	.9570	8.37	.0670	2030	.0670	1933	1.05
101.0	43.0	22.98	17.46	.9564	8.22	.0678	1975	.0678	1863	1.06
110.3	42.9	23.48	17.54	.9551	7.97	.0688	1897	.0688	1773	1.07
122.4	42.8	24.30	17.69	.9530	7.52	.0705	1762	.0705	1624	1.08
132.2	42.7	24.72	17.80	.9517	7.32	.0717	1696	.0717	1542	1.10
143.2	42.5	25,65	17.97	.9491	6.85	.0738	1557	.0738	1403	1.11
155.3	42.4	26.45	18.11	.9467	6.51	.0755	1457	.0755	1289	1.13
165.8	42.2	27.30	18.29	.9440	6.14	.0779	1347	.0779	1176	1.14
178.4	42.0	28.48	18.44	.9398	5.65	.0802	1213	.0802	1041	1.16
188.6	41.9	29.30	18.54	.9367	5.33	.0818	1128	.0818	952	1.18
198.7	41.8	30.50	18.76	.9320	4.92	.0848	1016	.0848	847	1.20
212.2	41.6	31.20	19.00	.9290	4.68	.0880	943	.0880	770	1.22
221.5	41.5	31.97	19.24	.9255	4.43	.0911	873	.091	704	1.24
228.9	41.4	32.80	19.34	.9215	4.20	.0931	814	.0923	651	1.25
240.3	41.3	33.46	19.64	.9181	4.02	.0970	760	.0960	598	1.27
251.4	41.1	34.40	20.00	.9129	3.76	.1022	687	.1005	533	1.29
261.6	41.0	35.30	20.18	.9076	3.55	.1055	633	.1035	485	1.30
272.6	40.9	36.56	20.46	.8992	3.24	.1108	558	.108	423	1.32
286.0	40.7	37.54	20.65	.8915	3.01	.1154	503	.110	375	1.34
299.7	40.5	39 .20	20.87	.8785	2.67	.1217	427	.117	314	1.36

TABLE 3.3 EXPERIMENTAL RESULTS FOR SAMPLE 8-7

Figure 3.21b and 3.21c show the calculated values of $r^2 = \langle\tau^2\rangle/\langle\tau\rangle^2$ for impurity scattering and acoustical scattering, respectively. As seen, the impurity and acoustical scattering give similar values for r^2 over the temperature range for which both contributions are expected. This is fortuitous, however, and it is not expected to be true for carrier concentrations different from that of sample 8-7. Thus the r^2 values for acoustical scattering can be used for the whole range of temperature in sample 8-7.

Accurate values of r^2 are not required to correct the effective mass values since in the worst case (room temperature) a 40% increase in r^2 leads to a 4% decrease in m_s only. The correction soon becomes negligible as the temperature is lowered because the $\omega_{min}\tau$ values increase rapidly while r^2 decreases. For temperature less than 225°K, the correction is less than 1%. The correction for μ_{opt} is however large: it is 36% and 4% at room temperature and 82°K, respectively.

The corrected values of susceptibility masses are plotted in Figure 3.22b as a function of temperature. Also, in Figure 22a, the susceptibility masses calculated using an effective carrier concentration $N^* = N \frac{R_o(82^oK)}{R_o(T^oK)}$ (in which $R_o(T^oK)$ is the zero field Hall constant at the temperature of the measurement) have been plotted. The effective masses so obtained are constant over nearly the whole range of temperature. We postpone the discussion of this result to Section 3.5.7.

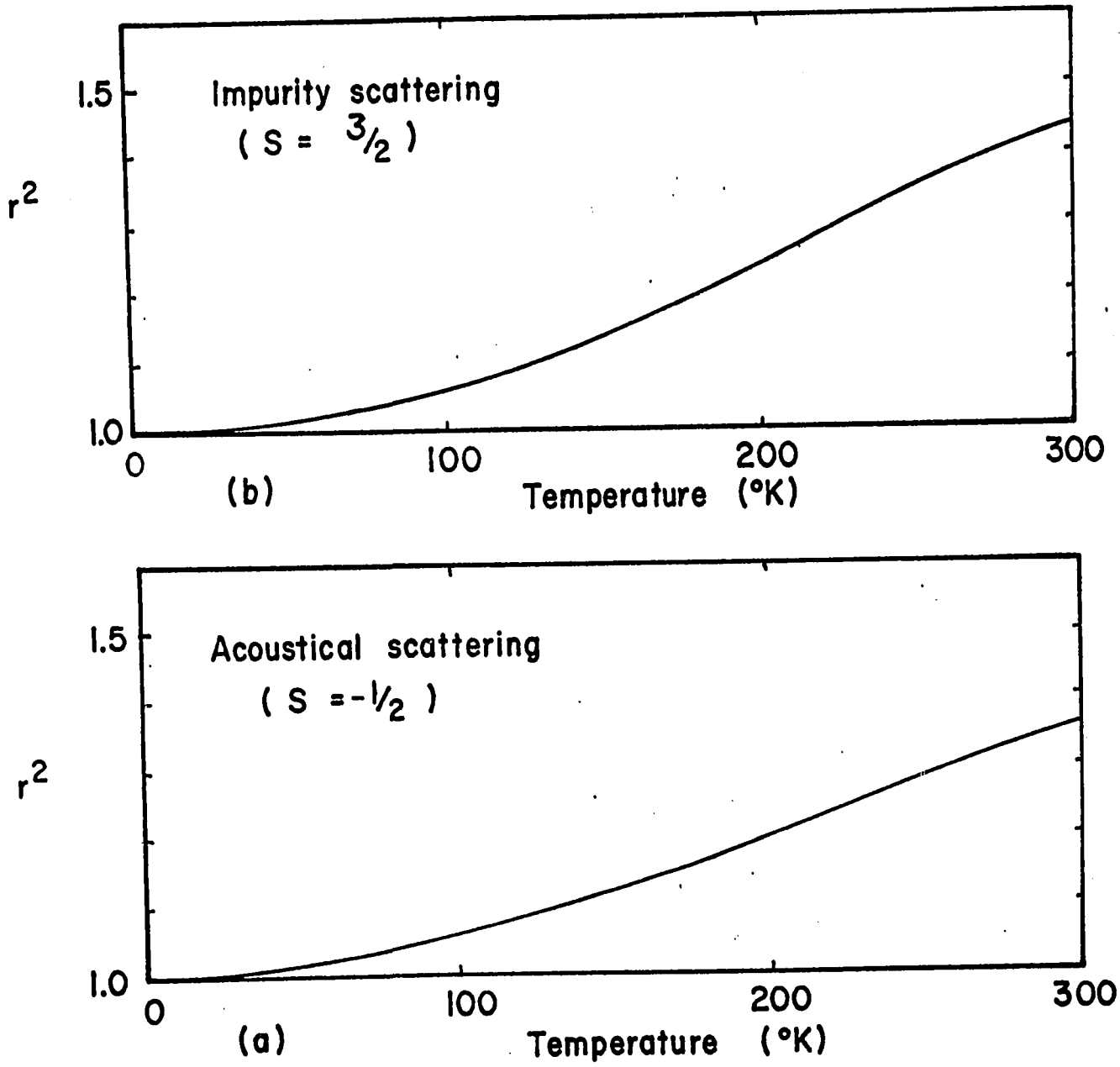

Figure 3.21 $r^2 = \langle\tau^2\rangle/\langle\tau\rangle^2$ vs. temperature in sample 8-7.

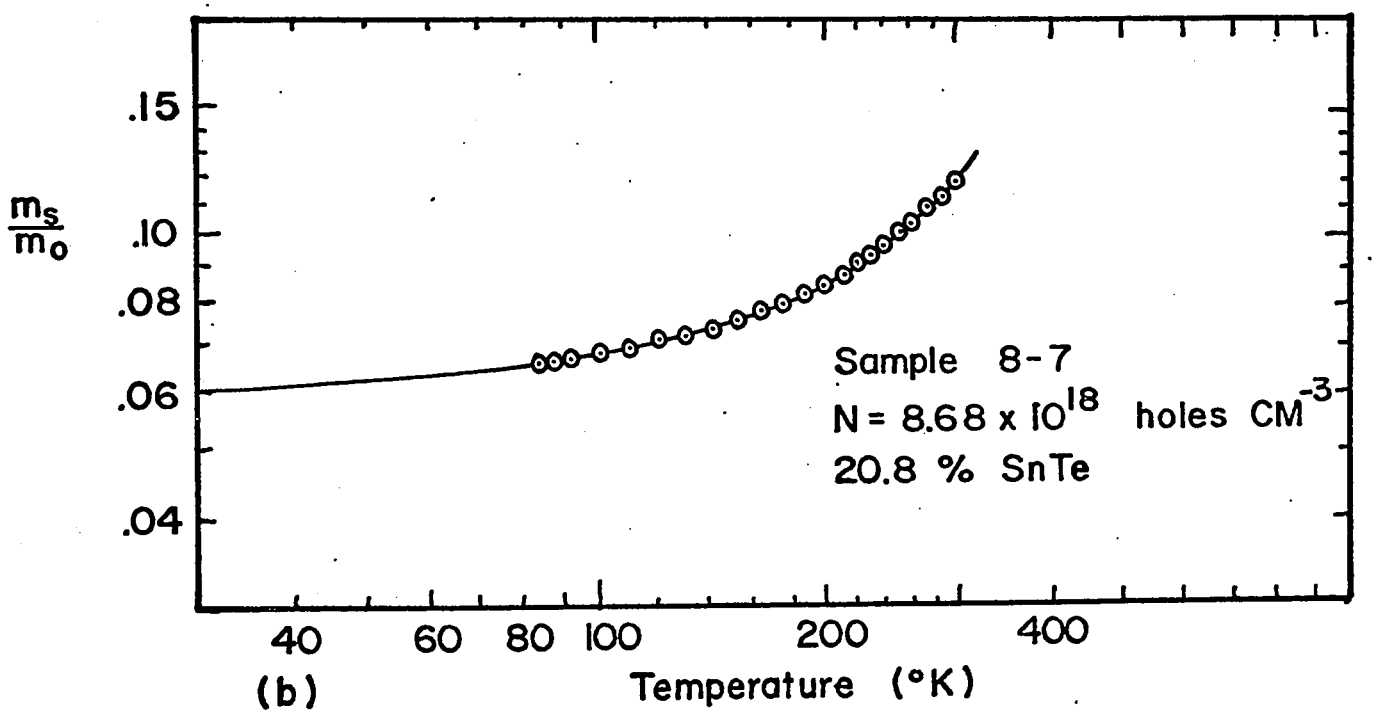

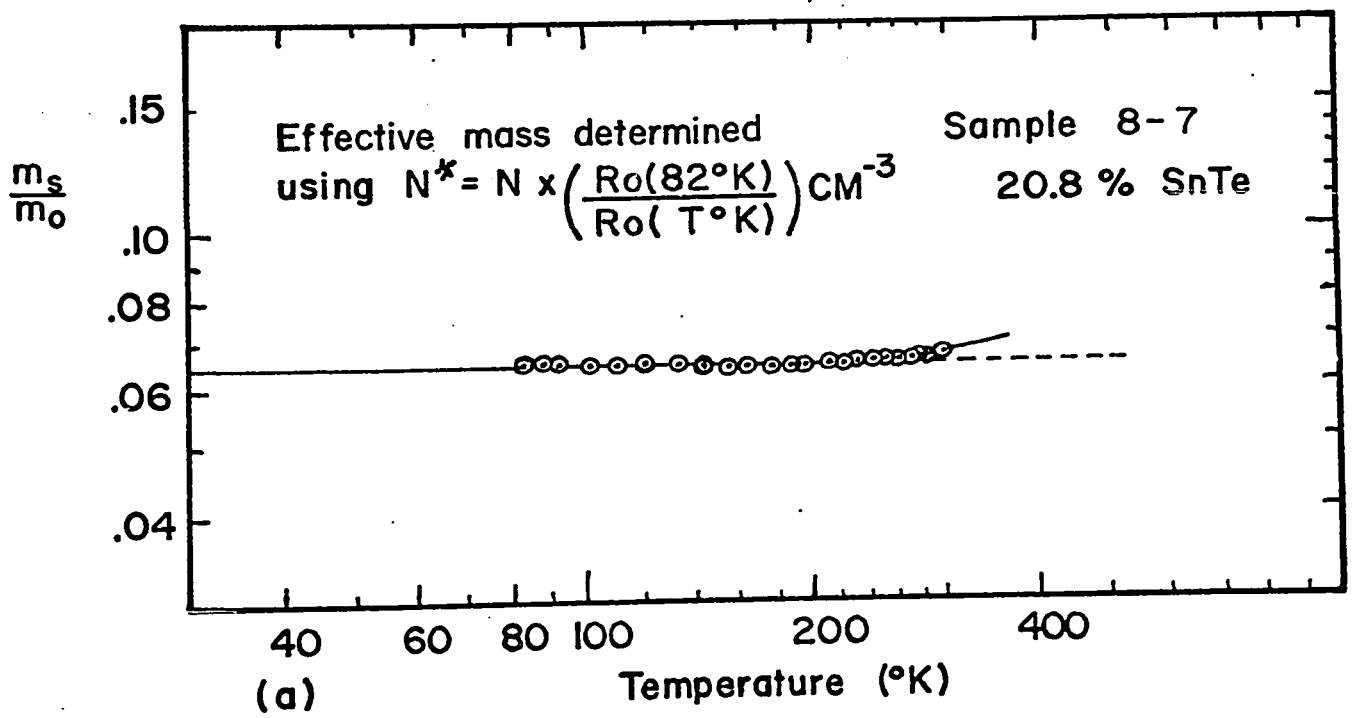

Figure 3.22 Effective mass vs. temperature in sample 8-7.

3.5.6 Optical Mobility

Optical mobilities determined using the Moss method, and given in Tables 3.2 and 3.3, are plotted in Figures 3.23 and 3.24 together with the conductivity mobilities. The conductivity mobility, assuming a one-band conduction, is given by $\mu_c = R_o(77^oK)\ \sigma(T)/r(77^o)$ in which the value of r from Table 3.1 has been used.

The optical and conductivity mobilities show a similar variation with carrier concentration and with temperature. However, the optical mobilities are always lower by approximately a factor of 2. This has been observed in PbTe (65 D1) and in SnTe (67 R1, 70 B2) but no satisfactory explanation has been given. As the thermal velocities of the electrons are hardly affected by the small electric field in either optical or conductivity experiments, this discrepancy is, in general, not expected and the scattering time should in both cases depend only on crystal properties and temperature.

However, the optical mobilities are not necessarily representive of the bulk since the light probes a very thin layer of material near the surface. If, for instance, the mean free path of the electrons becomes comparable to the penetration depth, collisions with the surface reduce the scattering time or mobility. To see if boundary scattering is important in the present experiment, we calculated the penetration depth $\delta = \lambda/4\pi\kappa$ at the minimum reflectivity using κ from Table 3.2. It ranges from .4 to 1.8 microns for the samples measured

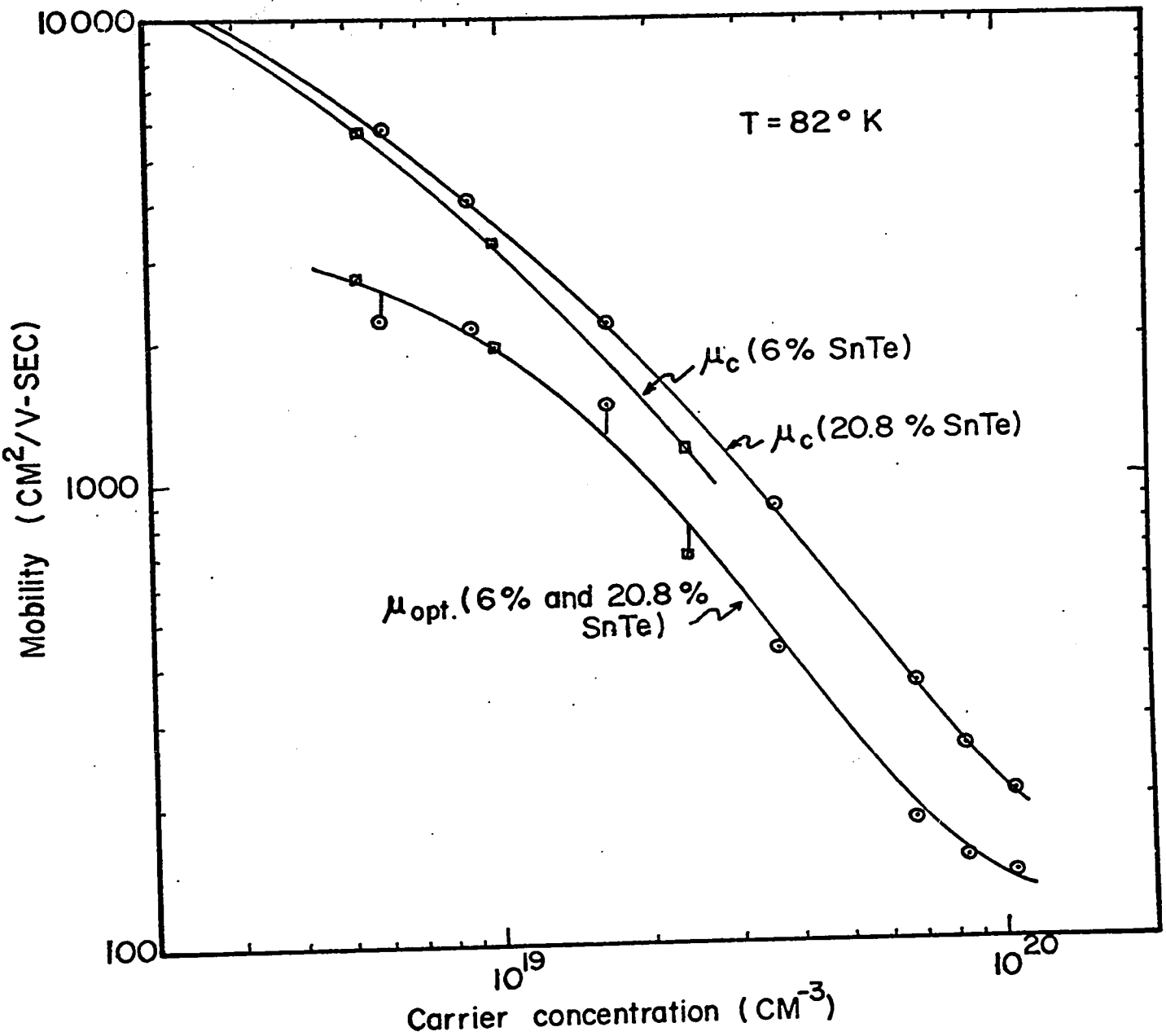

Figure 3.23 Conductivity and optical mobility vs. carrier concentration.

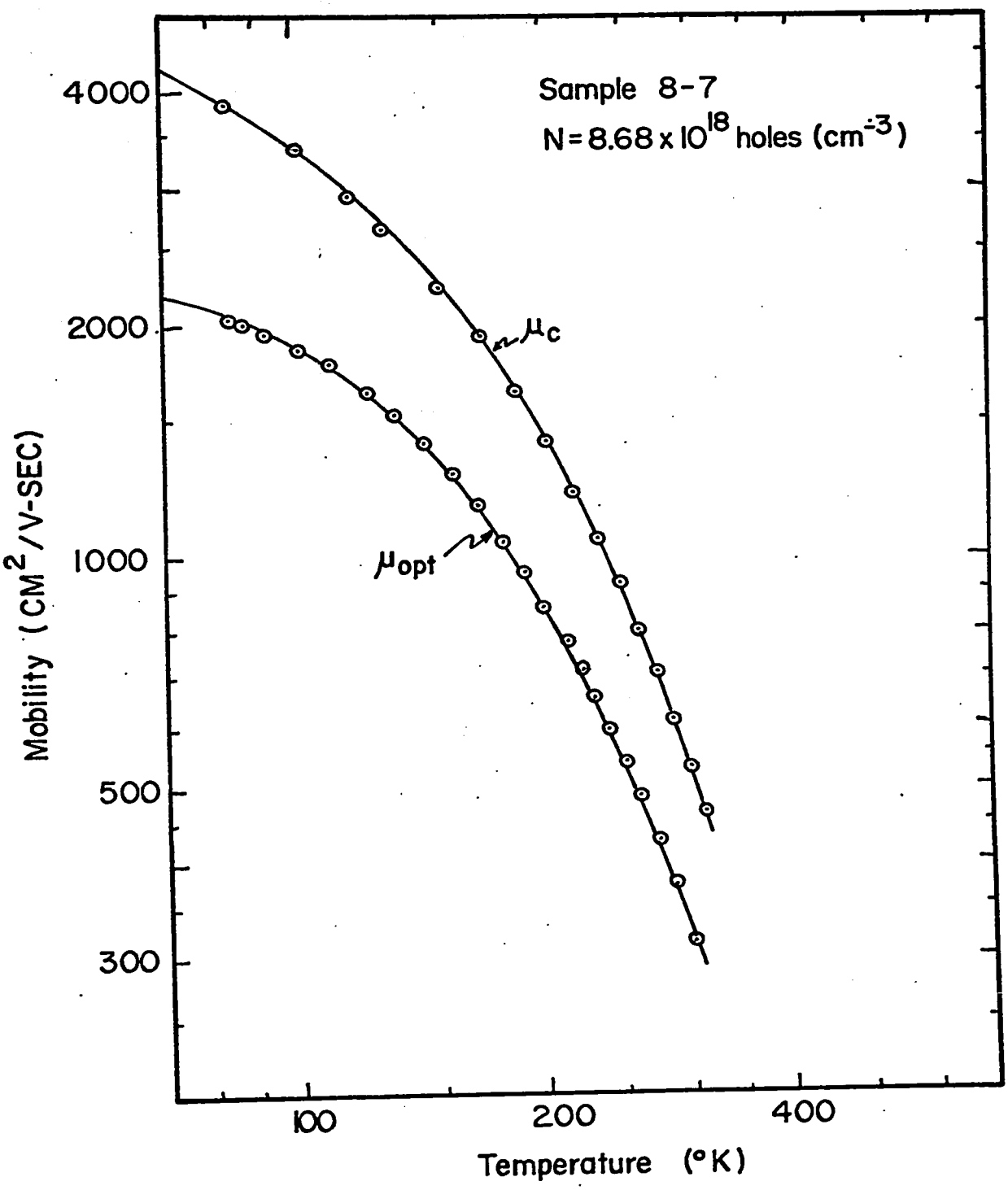

Figure 3.24 Conductivity and optical mobility vs. temperature in sample 8-7.

at 83°K. On the other hand, the velocity of the electrons can be estimated from the Fermi level and the susceptibility mass from $v_F = (2E_F/m_s)^{1/2}$. Using E_F determined from the Cohen model (Section 3.5.7) and the experimental value of m_s, v_F was calculated and the mean free path $\Lambda = v_F\tau$ was found to range from .01 to .06 microns. The mean free path of the electrons is at most 4% of the penetration depth and boundary scattering, and while non-negligible, does not account quantitatively for the observed difference between the optical and the conductivity mobility.

3.5.7 Comparison of Experiment with Theoretical Predictions

In this section, we will consider different models to describe the non-parabolicity of the 4 equivalent <111> minima. For simplicity, we will use the expression "one band model" to imply that the carriers are all in the above <111> minima.

a) One Kane Band

We refer here to the simplified Kane model for which the dispersion relation is:

$$\frac{\hbar^2 k_T^2}{2\, m_T} + \frac{\hbar^2 k_L^2}{2\, m_L} = E(1 + E/E_G) \qquad (3\text{-}85)$$

in which k_T and k_L are the transverse and longitudinal wave numbers; m_T and m_L are the transverse and longitudinal band-edge masses; and E_G is the interaction gap. This model has been used to explain the

non-parabolicity of the valence band in PbTe by Dubrovskaya et al. (70 D1). They explained the dependence of the density-of-states (determined from thermoelectric power in a strong magnetic field) on the energy, for carrier concentration ranging from 5.7×10^{17} to 4×10^{19} holes cm^{-3}, using $E_G = .12$ e.v. and a density-of-states band-edge mass $m_d = 0.13\ m_o$. Our results of susceptibility effective masses could not be explained on the basis of equation (3-85) for carrier concentration ranging from 5×10^{18} to 10^{20} holes cm^{-3}. We will now substantiate this statement.

The susceptibility effective mass is given by equation (3-54). If we use $v = (1/\hbar)|\nabla_k E|$, it becomes:

$$\frac{N_1}{m_s} = \frac{-4}{3\hbar^2(2\pi)^2} \int_o^\infty \frac{\partial f_o}{\partial E} \left(\int_o^{k_L max} \frac{|\nabla_k E|^2 k_T}{|(\nabla_k E)_T|} \, dk_L \right)_E dE \qquad (3\text{-}86)$$

in which N_1 is the carrier concentration in one valley and is given by:

$$N_1 = N/4 = \int_o^\infty - \frac{\partial f_o}{\partial E} \, H_K(E) \, dE \qquad (3\text{-}87)$$

in which $H_K(E)$ is the number of states within a Kane surface (equation (3-85)) of energy E and is:

$$H_K(E) = \frac{2}{(2\pi)^2} \int_0^{k_L\,max} k_T^2 \, dk_L \tag{3-88}$$

From equation (3-85), since we have $k_L max$ for $k_T = 0$, we have:

$$k_L max = E(1 + E/E_G)\ 2\ m_L/\hbar^2 \tag{3-89}$$

Equation (3-88) can be integrated using the expression for k_T^2 from equation (3-85) to give:

$$H_K(E) = H_P(E)\ \left(1 + E/E_G\right)^{3/2} \tag{3-90}$$

in which $H_P(E) = 2^{3/2} m_d^{3/2} E^{3/2}/3\pi^2\hbar^3$ is the number of states within a parabolic band of energy E and with mass parameters m_L and m_T (m_d is the corresponding bottom of the band density-of-states mass).

The integrand in equation (3-86) is easily obtained from equation (3-85). It is:

$$\frac{|\nabla_k E|^2}{|(\nabla_k E)_T|}\ k_T dk_L = \left[\frac{2E(1+E/E_G)}{(1+2E/E_G)} + \frac{\hbar^2 k_L^2 (m_T - m_L)}{m_L^2 (1+2E/E_G)} \right] dk_L \tag{3-91}$$

Substitution in equation (3-86) and integration over k_L leads to:

$$\frac{N_1}{m_s} = \int_0^\infty \frac{\partial f_o}{\partial E}\ H_P(E)\ I_K(E)\ dE \tag{3-92}$$

in which $I_K(E) = (1 + E/E_G)^{3/2}/m_c(1 + 2E/E_G)$ and m_c is the bottom of

the band conductivity effective mass. At the temperature of the measurement, 82°K, all samples are strongly degenerate and the integration over energy is readily obtained. From equations (3-92), (3-87) and (3-90) we have

$$m_s = m_c (1 + 2E_F/E_G) \tag{3-93}$$

This is exactly the same expression as for the conductivity effective mass.

Furthermore, from $N = 4H_K(E)$ the Fermi level can be expressed in terms of N as follows:

$$E_F = -E_G/2 + \left[\left(\frac{E_G}{2}\right)^2 + \frac{E_G}{M_d} \left(\frac{N}{C}\right)^{2/3} \right]^{1/2} \tag{3-94}$$

in which $M_d = m_d/m_o$ and $C = \frac{64x2^{1/2}\pi}{3h^3} m_o^{3/2} = 18.17 \times 10^{21}$ cm^{-3}. Writing equation (3-94) in equation (3-93) we have:

$$M_s^2 = M_c^2 + \frac{4 M_c^2}{E_G M_d} \left(\frac{N}{C}\right)^{2/3} \tag{3-95}$$

Thus, a plot of the susceptibility effective mass squared vs. $N^{2/3}$ should be a straight line with slope $(4 M_c^2/E_G M_d C^{2/3})$ and intercept M_c^2. Such a plot is shown in Figure 3.25 for the two alloy compositions measured. As seen, equation (3-95) is not obeyed; the curves deviate more and more from straight lines as the carrier concentration is increased.

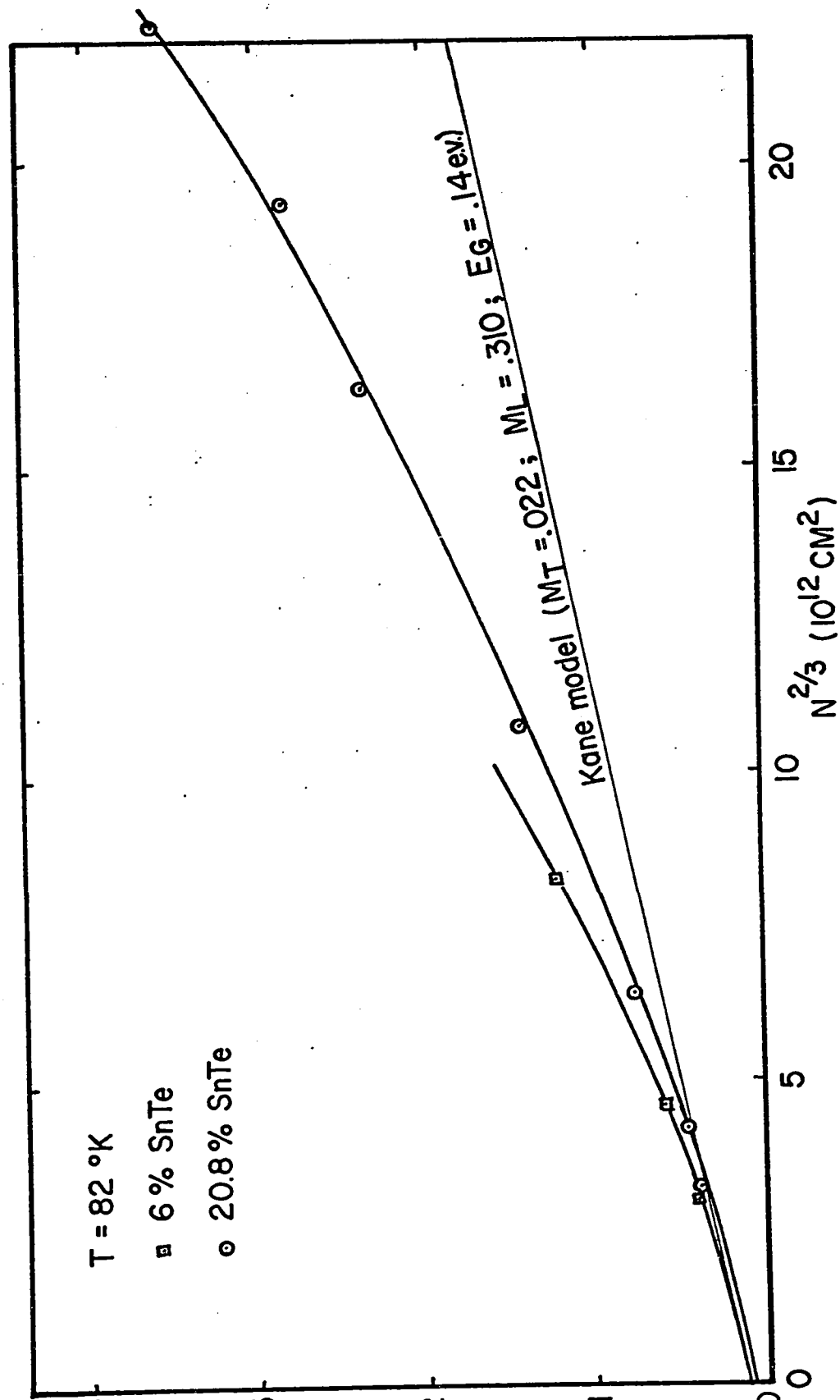

Figure 3.25 $(m_s/m_o)^2$ vs. $N^{2/3}$. The Kane model is used for the calculated curve.

For comparison, we have plotted a theoretical curve using $M_T = .022$, $M_L = .310$ and $E_G = .14$. These bottom of the band parameters were determined for PbTe at 4.2°K by Cuff et al. (64 C1). Since the energy gap for 6% SnTe alloy is about the same at 82°K as it is for PbTe at 4.2°K, the above parameters should apply to the 6% SnTe alloy. We have assumed also that changes in the other energy bands at <111> produce negligible effects on the above parameters. This is valid if M_T is determined by the interaction of the nearest bands only. Cuff et al. (64 C1) pointed out that the mass components in the valence band and the conduction band are determined principally by the momentum matrix elements across the small intrinsic gap.

As seen from Figure 3.25, the low carrier extrapolation of the experimental curve for 6% SnTe alloy coincides with the theoretical curve, but the experimental curve deviates more and more from the calculated curve as the carrier concentration increases above 10^{18} carriers cm^{-3}. Also the experimental curve for 20.8% SnTe alloy extrapolates at a lower M_c value than that for 6% SnTe alloy as expected, and the same deviation is present as the carrier concentration increases. The reasons for the disagreement are that the non-parabolicity of the valence band is larger than that predicted by the Kane model of equation (3-85) or that a heavier mass band is becoming populated past 10^{18} carriers cm^{-3} or a combination of both.

In conclusion, it can be said, that the simplified Kane model is a good representation of the valence band for carrier concentrations not in excess of 10^{18} cm^{-3}.

b) One Cohen Band

The use of the Cohen model in the case of PbTe, and the alloys considered here, is suggested by the results of Shubnikov-de Haas measurements (64 C1). The Cohen model has also been used with some success for PbTe by Dixon and Riedl (65 D1). They report that the susceptibility effective mass variations with temperature and carrier concentration are partially explained in terms of a single Cohen band. The dispersion relation describing the Cohen energy surface is:

$$E = \frac{\hbar^2}{2}\left\{ \frac{k_T^2}{m_T} \frac{1}{\left(1 + (1/E_G)(E + \hbar^2 k_L^2/2m_L^1)\right)} + \frac{k_L^2}{m_L} \right\} \qquad (3\text{-}96)$$

in which k_T and k_L are the transverse and longitudinal wave numbers; E_G is the interaction gap; m_T and m_L are the transverse and longitudinal band-edge masses; and m_L^1 is the longitudinal band-edge mass of the interacting band (i.e. the conduction band). Equation (3-96) contains several parameters besides the interaction gap E_G. We will assume that they are given by:

$$\begin{aligned} & m_L/m_L^1 = 1.3 \\ & M_T = E_G/(E_P - E_G) \quad \text{with } E_P = 6.4 \text{ e.v.} \\ & m_L = K\, m_T \qquad \text{with } K = 13 \end{aligned} \qquad (3\text{-}97)$$

The first assumption states that the ratio of the transverse band-edge mass of the valence band to that of the conduction band is

constant for the alloys considered and equal to that determined from Shubnikov-de Haas measurements in PbTe (64 C1). This is suggested by the results of Cuff et al. (64 C1) which disclose the similarity of the conduction and valence band and the predominance of their interaction. Moreover, this assumption is not restrictive: calculations using values of either m_L or m_L^1 differing by a factor of 2 showed that the calculated values of m_s were not changed by more than 5%.

Secondly, we assumed that the experimentally determined relation for PbTe, i.e., $_T = E_G/(E_P - E_G)$ with $E_P = 6.4$ e.v. is applicable to the alloys measured. As mentioned earlier, Cuff et al. (64 C1) point out that the interaction with the most remote energy levels at <111> is of secondary importance and that the mass components are determined principally by the small gap between the valence and conduction bands. This situation is expected to be more valid in 6% SnTe and 20% SnTe alloys due to the small energy gap.

Thirdly, Burke et al. (70 B1) found from Shubnikov-de Haas studies that K is independent of carrier concentration and alloy composition in $Pb_{1-x}Sn_xTe$ up to x = 30%. We will use their averaged value of 13 for all samples. Again, this assumption is not restrictive since the calculated values of M_s are not very sensitive to changes in K.

The expression for M_s is obtained as before from equation (3-86). We will not go through the different steps of the calculation since this has been done in detail by Dixon and Riedl (65 D1). The effective mass was calculated for the Cohen model with the relations

(3-97). The integrations over energy were performed by numerical integration.

Figures 3.26 and 3.27 give the final result of the calculation together with the experimental results. In Figure 3.26a (20% SnTe) the calculated susceptibility masses are given for the interaction gap E_G = .20, .12, and .08 e.v. The curve for E_G = .12 e.v. shown in full is the one that gives the best agreement with the experimental values. Up to 10^{19} holes cm^{-3}, the experimental points coincide with the calculated curve. As the carrier concentration increases past 10^{19} hole cm^{-3}, the deviation of the experimental points from the calculated curve increases. As pointed out before, experimental results suggest that a heavy mass band becomes populated at around 6.6×10^{19} holes cm^{-3}. This may explain the discrepancies between measurements and calculations past 6.6×10^{19} holes cm^{-3} but not those from 10^{19} to 6.6×10^{19} cm^{-3}. On the whole, the Cohen model appears to be the appropriate one in the alloys measured at least for carrier concentrations up to 10^{19} holes cm^{-3}. The effective gap E_G = .12 e.v. used is in very good agreement with the optical gap (.11 e.v.). This suggests that the influence of the far removed bands at <111> on the non-parabolicity is negligible at least for the lowest carrier concentrations.

In Figure 3.27a (6% SnTe), the effective gap E_G = .16 e.v. gives the best agreement up to 10^{19} holes cm^{-3}. This again is not much different from the optical gap (.19 e.v.). The corresponding

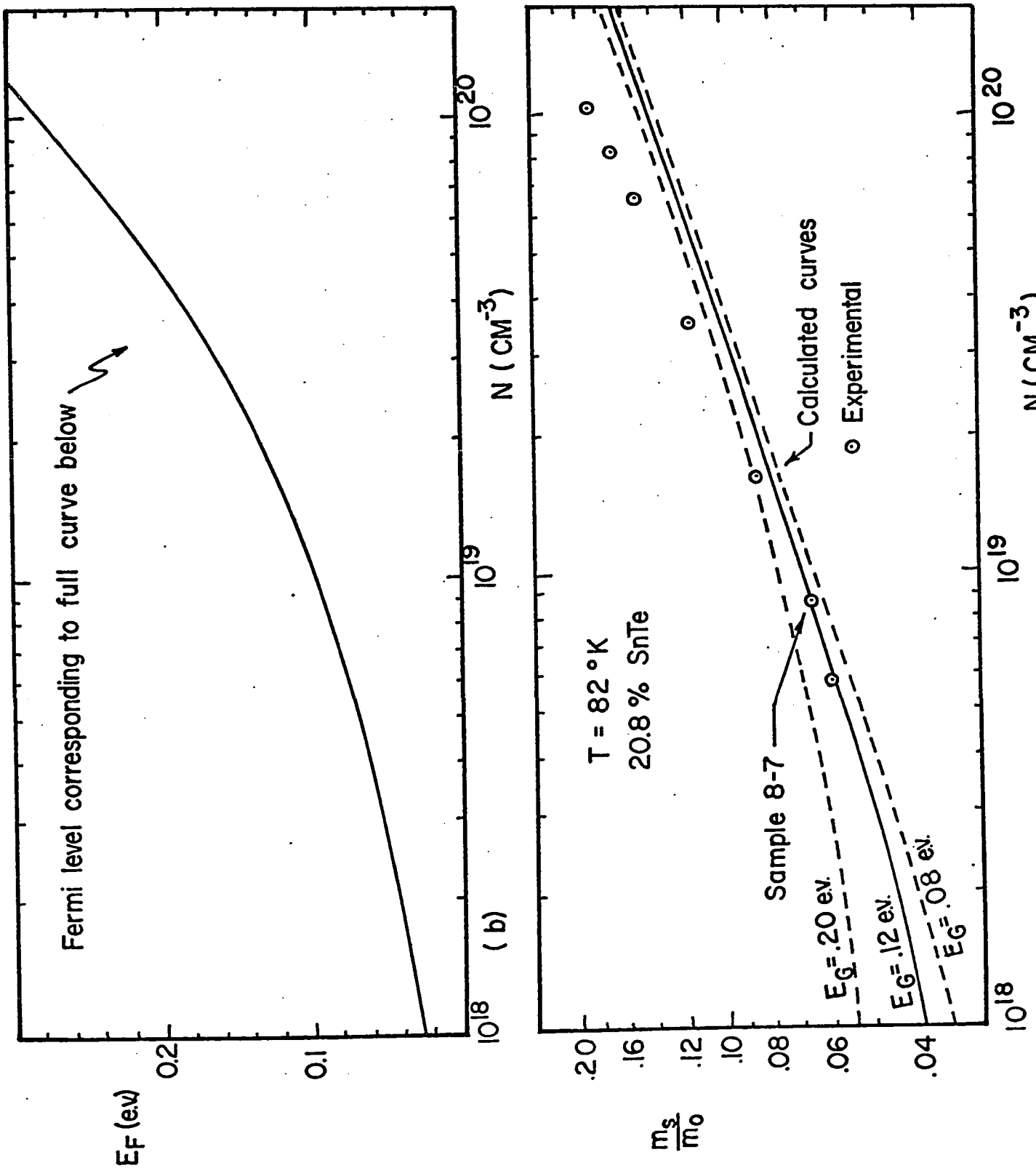

Figure 3.26 a) m_s/m_o and b) Fermi level vs. N.
The Cohen model is used for calculated curves.

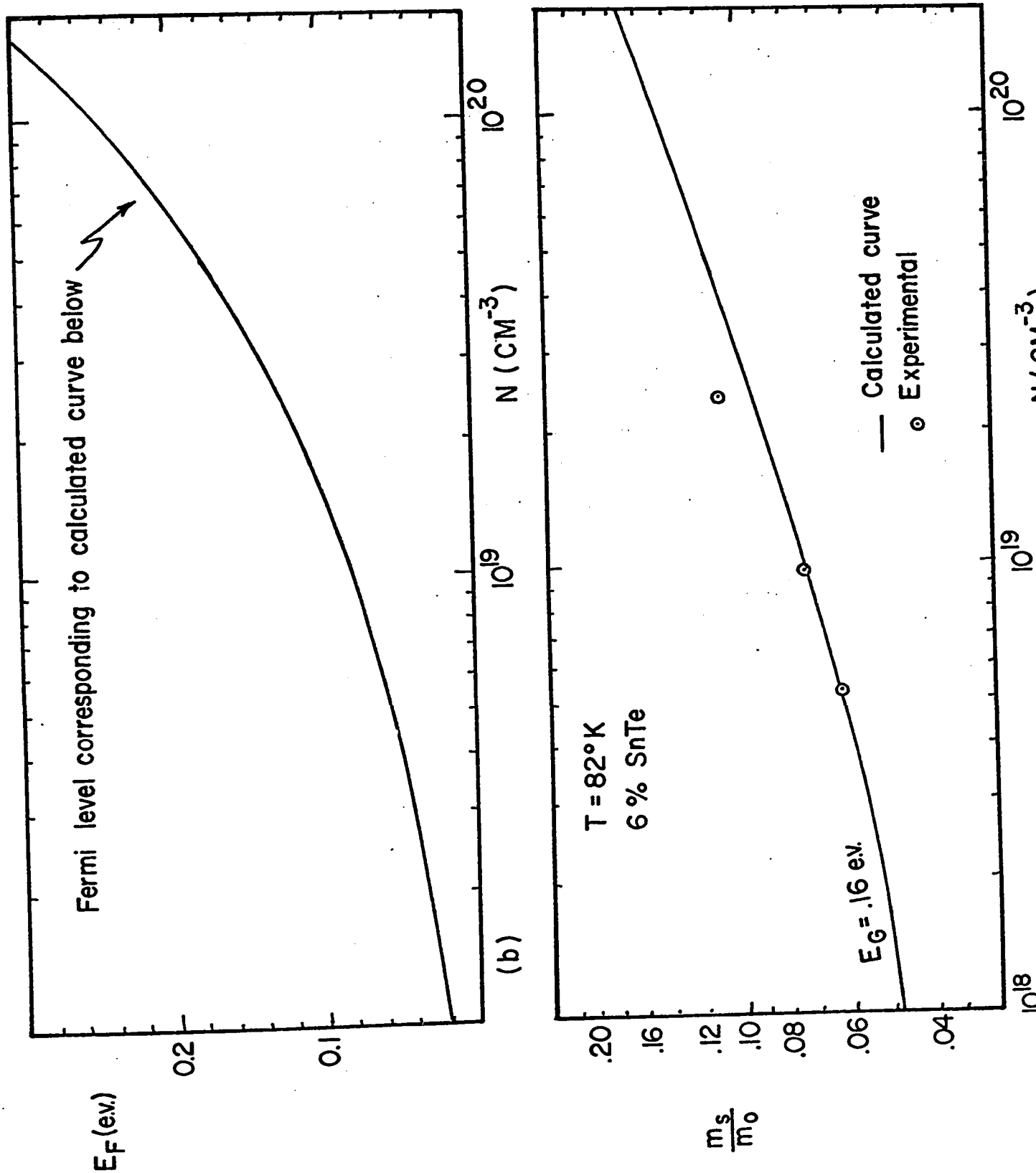

Figure 3.27 a) m_s/m_o and b) Fermi level vs. N.
The Cohen model is used for calculated curves.

values of the Fermi level were calculated and are shown in Figures 3.26b and 3.27b.

The Cohen model gives a good fit for sample 8-7 in Figure 3.26a. It is therefore in line to check whether or not the increase of effective mass in sample 8-7 from 82°K to 300°K is due to the non-parabolicity only. Figure 3.28b compares the experimentally determined m_s to the calculated one using the Cohen model with $E_G(T) = E_G(82^oK) + \alpha\ (T - 82^oK)$ in which $E_G(82^oK) = .12$ e.v. and α is the linear variation coefficient of E_G with temperature in e.v./°K. As seen, the increase of susceptibility effective mass with temperature is not accounted for by the Cohen model for reasonable values of α. The experimentally determined value for α is close to 3×10^{-4} as obtained from Figure 3.11b and measured by Tauber and Cadoff (67 T1). For this value of α, less than half the increase of m_s from 82°K to 300°K is accounted for. For $\alpha = 7.0 \times 10^{-4}$ the discrepancies are smaller, but there are no justifications for the use of such a large value of α. The use of different values of $E_G(82^oK)$ from .08 to .18 does not change appreciably the calculated curve and the above conclusions are unchanged. The values of the Fermi level corresponding to the calculated curve are given in Figure 3.28a.

In conclusion, we must say that either the Cohen model is inadequate for the alloys considered even for the low concentration sample 8-7 despite the apparent agreement of Figure 3.26a or that there are extra heavy mass bands becoming populated as the temperature

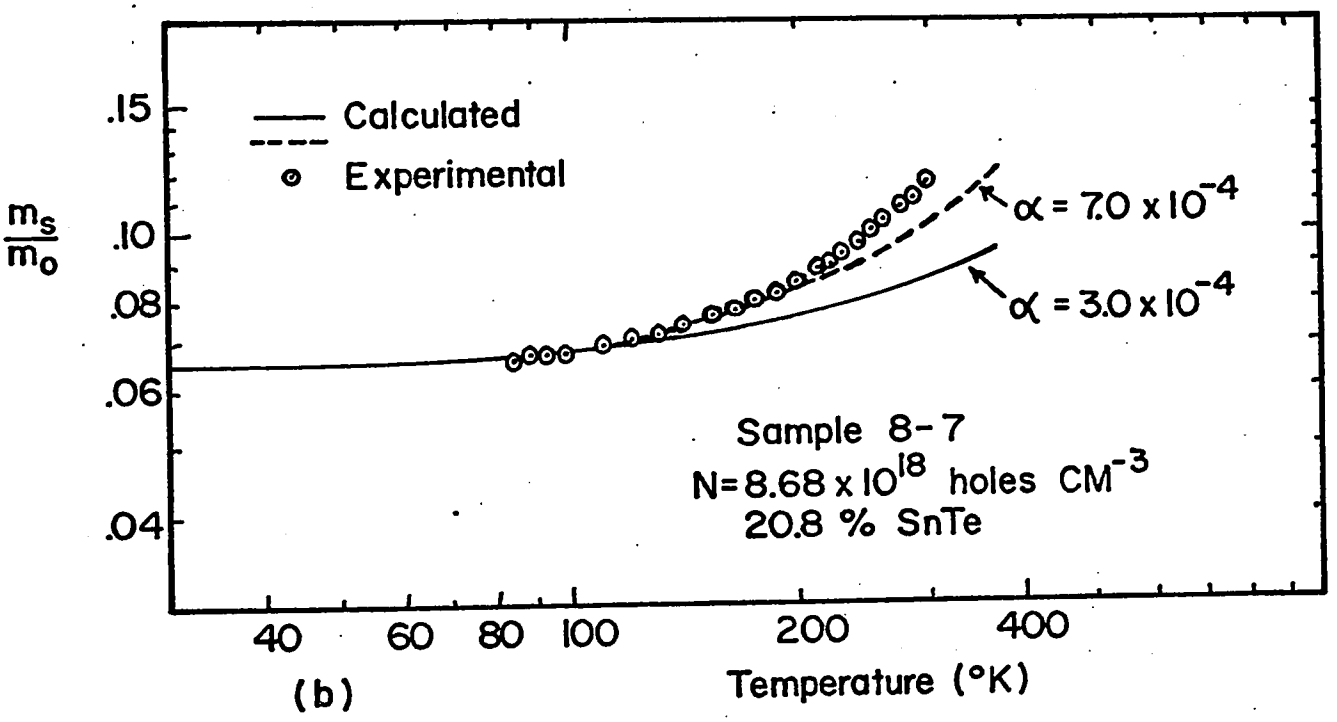

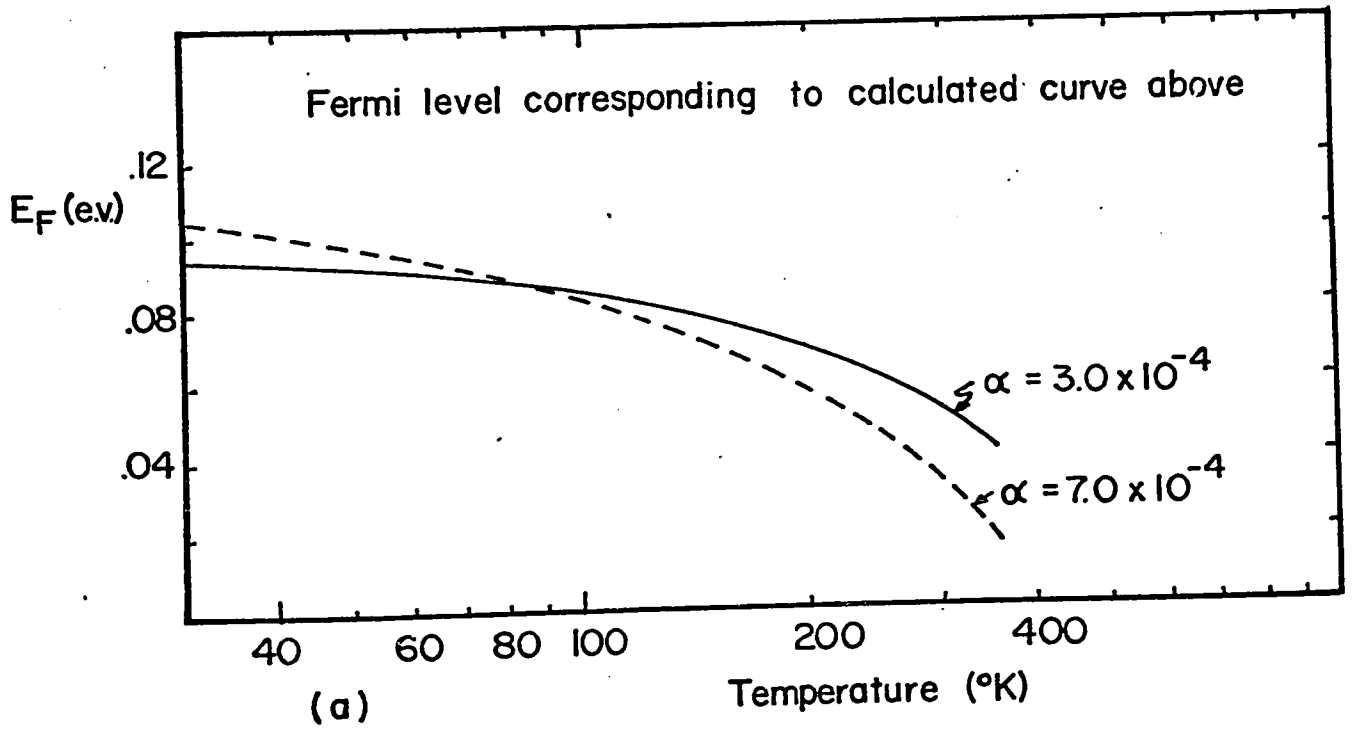

Figure 3.28 a) Fermi level and b) m_s/m_o vs. temperature. The Cohen model is used for calculated curves.

increases toward 300°K in sample 8-7. As mentioned earlier, there is experimental evidence that a heavy mass band becomes populated for approximately 6.6×10^{19} holes cm^{-3} at 82°K. From the value of the Fermi level at this carrier concentration (Figure 3.26b), we can estimate that the heavy mass band should be separated from the <111> minima by at least .23 e.v. at 82°K. On the other hand, from Figure 3.28a, we have that E_F is approximately .05 e.v. at 300°K. Thus for this heavy mass band to account for the large increase of m_s at room temperature, the temperature variation of the energy separation between the light and heavy mass band would have to be much larger than -3×10^{-4} e.v./°K. If it was the case, a much steeper increase of effective mass than that shown in Figure 3.28b would be observed when the heavy mass band becomes populated.

c) One Dimmock Band

Dimmock (70 D2) has derived a dispersion relation for $Pb_{1-x}Sn_xTe$. In doing so, he has treated the interaction between the valence and conduction band at <111> exactly, and included the interaction of the far removed bands at <111> as a second order perturbation.

Thus, the Dimmock model is better founded in that it takes into account the interaction of 6 bands at <111>. The values he used for the intrinsic gap are in agreement with experiment at least in the alloy range considered. However, the positioning of the far removed band is based on theoretical calculations for PbTe (66 L1) and SnTe (69 T1) and the assumption of a linear variation across the alloy range. In view of the privileged interaction of the conduction and valence bands the Dimmock model appears reasonable provided the errors in positioning the far removed levels are not too large.

His specific model for the valence and conduction bands of $Pb_{1-x}Sn_xTe$ uses the observation that the relative positions of the above six energy bands at the L-point do not change greatly across the alloy system. This allows a semi-empirical determination of the four effective masses and two momentum parameters based on the results of Cuff et al. (64 C1) and the matrix elements of Lin and Kleinman (66 L1) for PbTe. The only variable left is the energy gap E_G. The model equation is:

$$(\tfrac{1}{2}E_G+1.81\,k_L^2+3.38\,k_T^2-E)(-\tfrac{1}{2}E_G-0.87\,k_L^2-7.23\,k_T^2-E)=0.033\,k_L^2+.536\,k_T^2 \qquad (3\text{-}98)$$

in which E and E_G are in Rydbergs and k in atomic units. The zero of energy is taken at the center of the energy gap; E_G is positive for PbTe and negative for SnTe (the change in sign occurring at the cross-over at around 40% SnTe); E is positive for the conduction band and negative for the valence band.

The equation necessary to calculate the effective mass is:

$$\frac{N_1}{M_s} = \frac{-2}{3(2\pi)^2} \int_o^\infty \frac{\partial f_o}{\partial E} \left[\int_o^{k_L max} \frac{|\nabla_k E|^2}{|(\nabla_k E)_T|} k_T dk_L \right]_E dE \qquad (3\text{-}99)$$

where

$$N_1 = N/4 = \int_o^\infty - \frac{\partial f_o}{\partial E} H_D(E)\, dE \qquad (3\text{-}100)$$

in which $H_D(E)$ is the number of states within a Dimmock surface of energy E and is

$$H_D(E) = \frac{2}{(2\pi)^2} \int_o^{k_L max} k_T^2 \, dk_L \qquad (3\text{-}101)$$

Equation (3-99) is the same as equation (3-86) except that E is expressed in Rydbergs (2Rd = 1 a.u.) and k in atomic units. For these units, $\hbar^2$ is equal to 1 and M_s is in units of free electron mass.

In order to calculate the susceptibility effective mass, expressions for $k_L max$, k_T^2, and $|\nabla_k E|^2/|(\nabla_k E)_T| \times k_T$ must be obtained from the dispersion relation of equation (3-98). To avoid carrying numbers through the long algebraic manipulations necessary to arrive at these expressions, equation (3-98) is rewritten as follows:

$$(G + a\, k_L^2 + b\, k_T^2 - E)(G + c\, k_L^2 + e\, k_T^2 + E) + p\, k_L^2 + q\, k_T^2 = 0 \qquad (3\text{-}102)$$

with $G = (1/2)E_G$ etc.

The limit of integration $k_L max$ is obtained by writing $k_T^2 = 0$ in equation (3-102). After a few algebraic manipulations we have:

$$k_L max = \left[\frac{-A_1}{2ac} \pm \frac{1}{2ac}\left(A_1^2 - 4ac(G+E)(G-E)\right)^{1/2}\right]^{1/2} \qquad (3\text{-}103)$$

with

$$A_1 = (c+a)\,G + (a-c)\,E + p$$

For the alloys considered here the valence band extrema ($E = -G$) occur at the L point ($k_L = 0$) and only the positive sign is to be retained in equation (3-103). This is not true for $Pb_{1-x}Sn_xTe$ with $x > .9$ since then the extrema occur at $k_L \neq 0$ (70 D2).

The expression for k_T^2 is also obtained from equation (3-102) and is:

$$k_T^2 = -\frac{1}{2be} A_2 + \frac{1}{2be}\left[A_2^2 - 4be\left((G+ak_L^2-E)(G+ck_L^2+E) + pk_L^2\right)\right]^{1/2} \qquad (3\text{-}104)$$

with

$$A_2 = \left((e+b)G - (e-b)E + (ae+bc)\,k_L^2 + q\right)$$

The expression for $|\nabla_k E|^2/|(\nabla_k E)_T| \times k_T$ is most easily arrived at by implicit partial differentiation of equation (3-102). The final result is:

$$\frac{|\nabla_k E|^2}{|(\nabla_k E)_T|}\, k_T = \frac{2k_L^2\left(A_3 + (bc+ae)\,k_T^2\right)^2 + 2k_T^2\left(A_2 + 2be\,k_T^2\right)^2}{\left|\left(A_4 + (e-b)\,k_T^2\right)\left(A_2 + 2be\,k_T^2\right)\right|} \qquad (3\text{-}105)$$

in which

$$A_3 = \left((a + c)G + 2ac\, k_L^2 + (a - c)\, E + p\right)$$

$$A_4 = \left(2E - (a - c)\, k_L^2\right)$$

and A_2 is given above.

Now with equations (3-102), (3-104) and (3-105) substituted in equations (3-99), (3-100) and (3-101), the effective mass and the Fermi level were calculated. All integrations were performed numerically. These lengthly calculations were performed using two programs. The first program calculated the susceptibility masses for several input values of the Fermi level and gave curves of susceptibility mass versus carrier concentration. The second program calculated the susceptibility mass versus temperature in a sample of known carrier concentration by solving equation (3-100) for the Fermi level and then calculating M_s from equation (3-99). The accuracy of the numerical integrations was better than 1 part in 10,000.

The calculated values of the susceptibility effective mass are shown in Figure 3-29a together with the experimental values. The three calculated curves shown are for E_G equals to .23, .19 and .11 e.v. Since E_G is not an effective gap in the Dimmock model but the actual gap, or the optical gap, these values correspond to PbTe, 6% SnTe and 20.8% SnTe respectively. The corresponding values of the Fermi level are shown in Figure 3.29b.

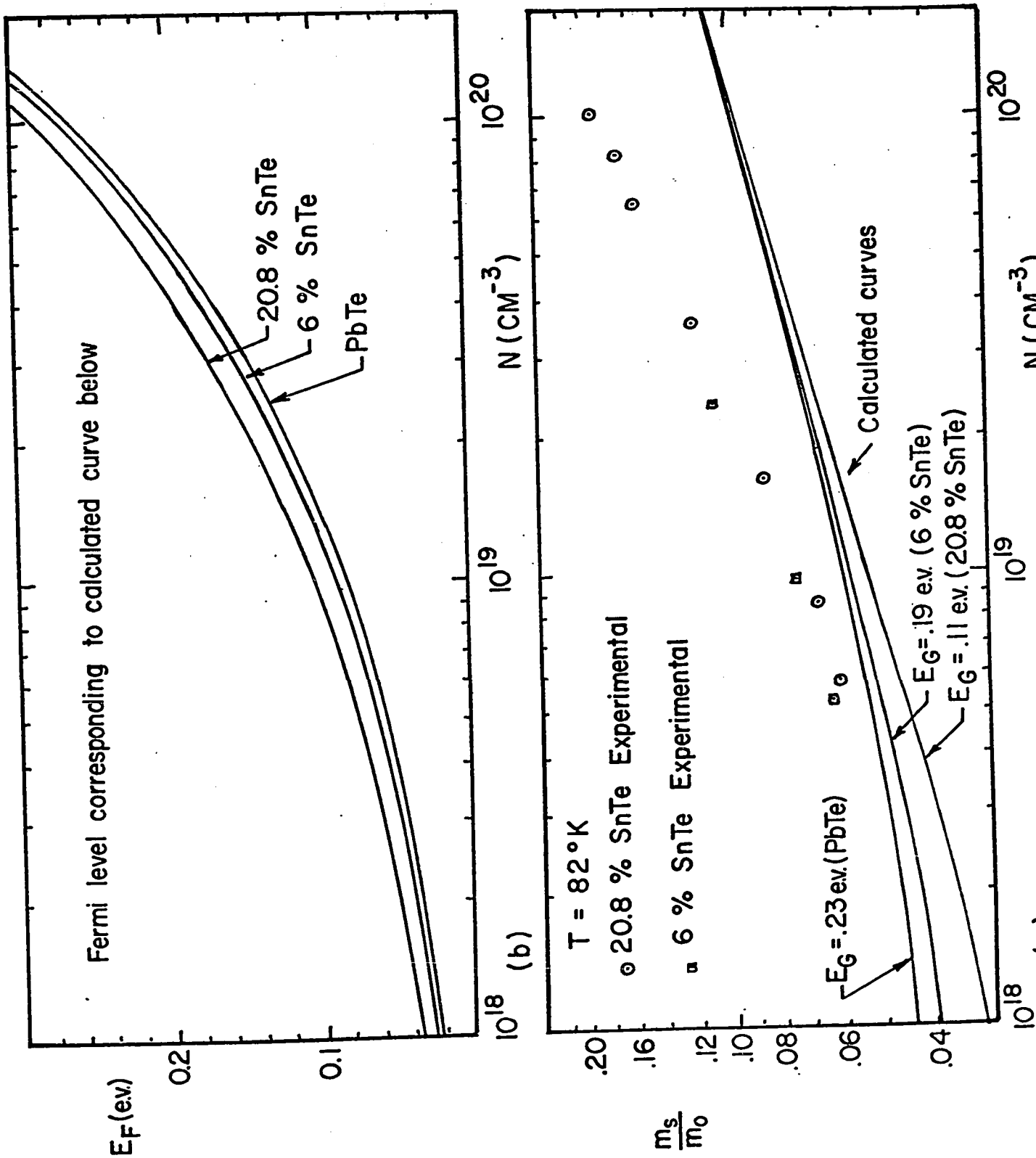

Figure 3.29 a) m_s/m_o and b) Fermi level vs. N. The Dimmock model is used for calculated curves.

Comparison with Figure 3.26, shows that the non-parabolicity of the <111> valence band extrema is less pronounced for the Dimmock model than for the Cohen model. The Cohen model was in agreement with experimental values at least for the lowest carrier concentration samples; on the other hand, the Dimmock model predicts a much lower effective mass than the experimentally determined one for all carrier concentrations measured. Figure 3.30 also shows that the Dimmock model failed to explain the temperature variation of the susceptibility effective mass.

Therefore, the discrepancy suggests that there are carriers in two bands even at the lowest carrier concentrations. However, we pointed out earlier that the positioning of the far removed energy level at the L point was based on theoretical calculations by Lin and Kleinman for PbTe (66 L1). In a recent paper, Overhof and Rössler (70 O1) recommended caution with the Lin and Kleinman band models. They have found very different values of energy spacing for the far removed level at <111>. In fact, if their values are correct, the assumptions leading to the Dimmock model equation (3-98) are incorrect. Also Dubrovskaya et al. (70 D1) pointed out that as the far removed bands at <111> are brought closer to the lowest conduction band or the uppermost valence band, the non-parabolicity is reduced. The results of Overhof and Rössler (70 O1) disagree with those of Lin and Kleinman (66 L1) in that the far removed bands (all 4 of them) are situated farther away from the interaction gap. Thus it appears that the

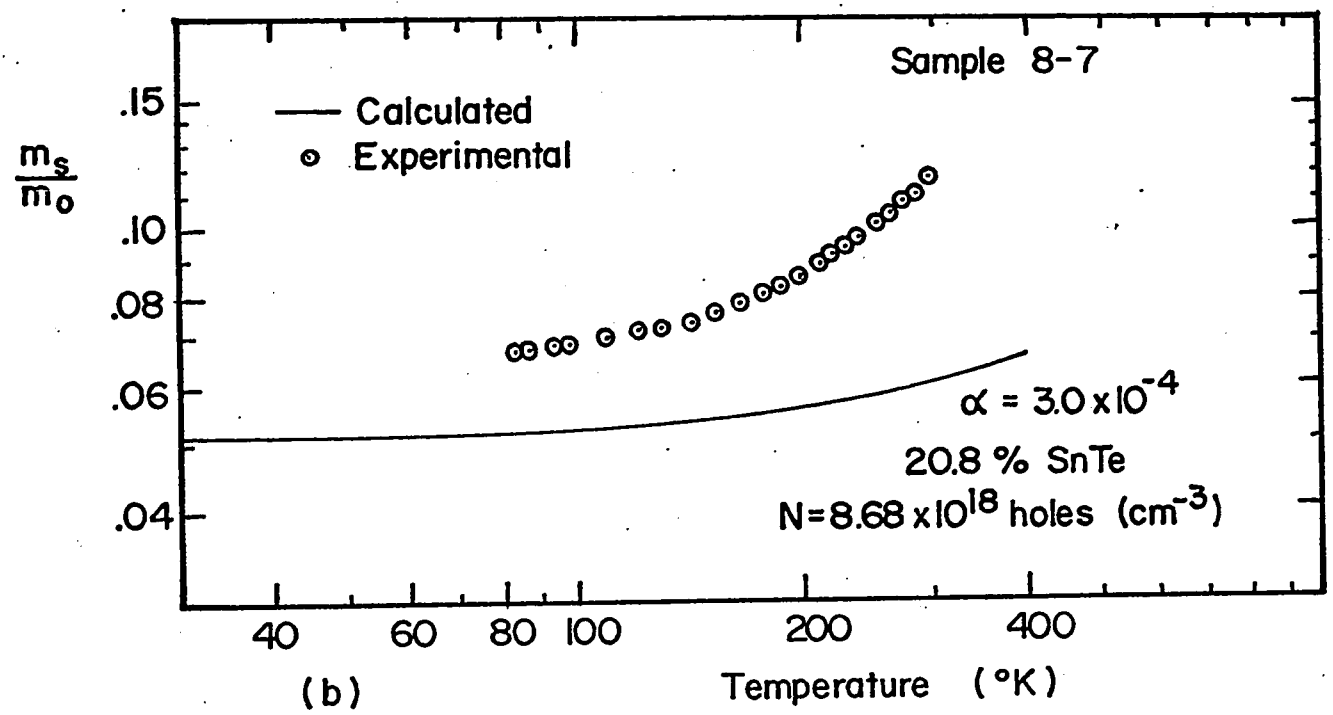

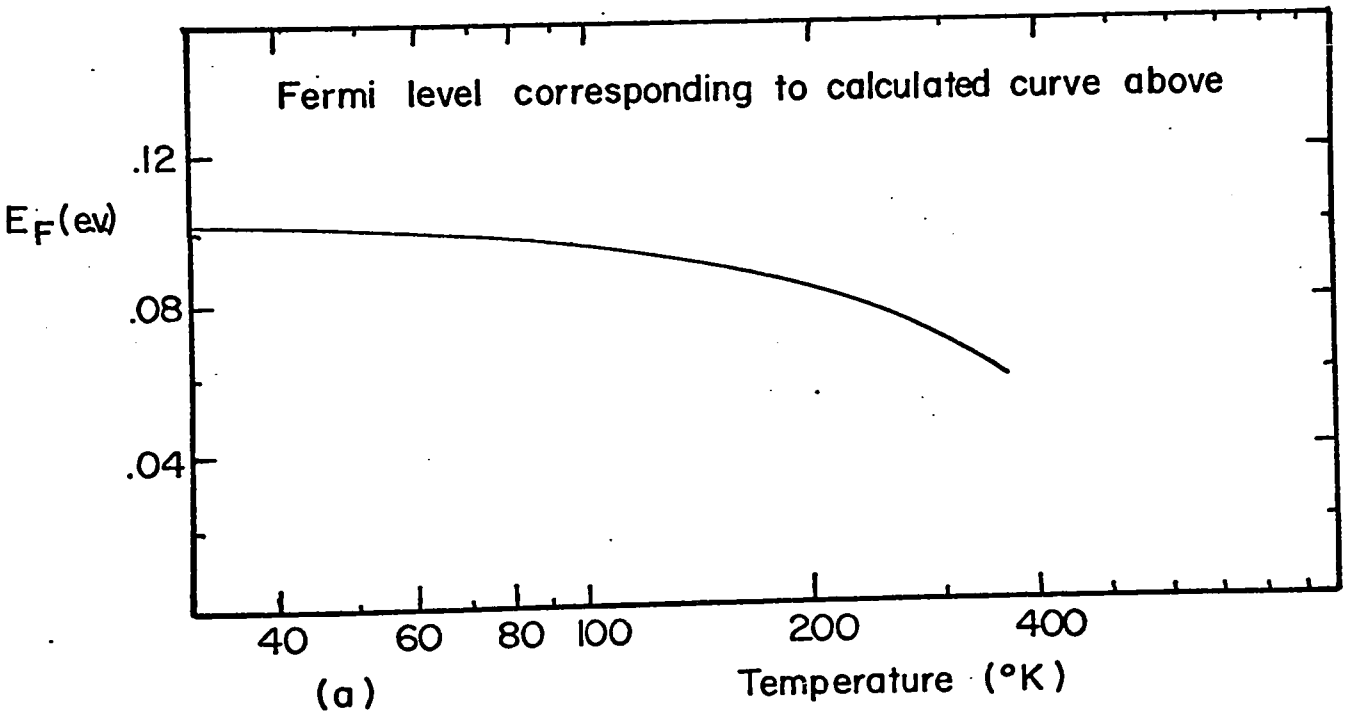

Figure 3.30 a) Fermi level and b) m_s/m_o vs. temperature. The Dimmock model is used for calculated curves.

Dimmock model underestimates the non-parabolicity. For these reasons it may be that the Cohen model is closer to reality in neglecting the far removed band interactions. The fact that the interaction gap in the Cohen model is close to the optical gap, also tends to support the above assertion. On the other hand, the validity of the Dimmock model cannot be ruled out on experimental grounds.

d) Multiband Models

1) One Cohen plus One Spherical Band

We have seen that at $1/R_o e = 1.1 \times 10^{20}$ cm^{-3} there is a kink in the m_s/m_o curve for the 20.8% SnTe samples at low temperature (see Figure 3.17b) indicating a heavy mass band. For carrier concentrations less than 6.6×10^{19} cm^{-3}, the Cohen model gave the best fit to the experimental data. Let us ask the question: Is the Cohen band plus one heavy mass band adequate to explain the experimental data?

A determination of $1/R_o e$ at which the Fermi level enters the heavy mass band at liquid nitrogen temperature was also obtained from the Hall ratio (see Chapter 4). It is $1/R_o e = 8.4 \times 10^{19}$ cm^{-3}. Let us use the average value of the two determinations, i.e. $1/R_o e = 9.5 \times 10^{19}$ cm^{-3}. From Figure 3.10b we estimate that R_o/R_∞ is equal to .6. For this value of R_o/R_∞, the carrier concentration N is 5.7×10^{19} cm^{-3} and the corresponding Fermi level (from Figure 3.26b) is .22 e.v. at 82^{o}K. Referring to Figure 3.26a, we see that the susceptibility effective mass versus carrier concentration is adequately explained

provided the non-parabolicity is slightly more than predicted by the Cohen model for carrier concentrations in excess of 2×10^{19} and that there is a heavy mass band situated .22 e.v. below the Cohen model. A heavy mass approximately equal to that determined by Smirnov and Ukhanov (70 S1) when most of the carriers are in the heavy mass band for PbTe would then be adequate to describe the increase of effective mass past 5.7×10^{19} cm^{-3} carriers. Its value is $m_{c2} = 0.32\ m_o$.

The above model applied to sample 8-7 predicts, for a temperature variation of the inter-valence band gap of -3.0×10^{-4} e.v./^oK, that 10% of the carriers are in the heavy mass band at 300^oK. We have assumed here that the heavy mass band-conduction band separation does not change with temperature and hence that the temperature variation of the inter-valence gap is the negative of that determined by Tauber and Cadoff for the main gap (67 T1). Also we distributed the heavy holes in 8 equivalent minima* (70 S1), i.e. $m_{d2} = 1.28\ m_o$. Thus for the model to be consistent, the increase of the susceptibility effective mass with temperature in Figure 3.28b should be entirely due to the non-parabolicity of the light mass band except for a very small percentage (~ 5%) near room temperature. However, this situation is realized using the Cohen model only if we assume a temperature variation of the effective gap: $\alpha \sim 8.0 \times 10^{-4}$ e.v./^oK (see Figure 3.28b). The temperature variation of the optical gap is about one half of this value.

*Smirnov et al (70 S1) have positioned the heavy mass maxima along the <111> axis near the Brillouin zone boundary. Other more likely locations are situated along the <110> and <100> axis.

We conclude here that a Cohen band plus a heavy mass band is adequate qualitatively. Quantitative agreement with experiment would be obtained if the non-parabolicity vs carrier concentration was to be slightly more pronounced for carrier concentrations in excess of 2×10^{19} cm^{-3}, and if a temperature variation of the interaction gap twice that of the optical gap is assumed.

2) Possibility of a Three Band Model

Let us now consider the susceptibility effective mass versus temperature in sample 8-7 (Figure 3.22). For this carrier concentration, 8.68×10^{18} cm^{-3}, we expect the carriers to be in the <111> minima only, at least up to 200°K, according to the discussion of the last paragraph. If this is true we would expect the increase in the Hall constant and the increase of the susceptibility mass to be entirely due to non-parabolicity. By using $N^* = N \times \frac{R_o\ (82^oK)}{R_o\ (T^oK)}$ as we have done to determine m_s in Figure 3.22a, we obtain a constant value of susceptibility mass to better than 1% up to 240°K, and equal to $m_s\ (82^oK)$. Since N* only neglects the variation of $r = R_o/R_\infty$ with temperature as compared to N, we have the result that the increase of susceptibility mass with temperature is equal (to better than 1%) to the increase of the Hall factor with temperature, i.e., $m_s(T)/m_s(82^oK) = r(T)/r(82^oK)$. The probability that this result is correct for sample 8-7 over such a large range of temperatures is almost negligible since in general the two increases should be different. The Hall factor depends on the

scattering while the susceptibility effective mass is independent of scattering. Unless the result is entirely fortuitous, it argues against a single band interpretation at low carrier concentrations and low temperatures up to 240°K.

A more general explanation of Figure 3.22a can be obtained in terms of two valence bands which are both occupied even at low temperatures in sample 8-7. As temperature is increased, carriers are transferred in a heavier mass band. The Hall constant at a given temperature is then a measure of the number of carriers left in the light hole band. Also, using R(T), the susceptibility effective mass measured is that of the light hole band since $p/m_s = p_1/m_{s1} + p_2/m_{s2}$ and the contribution of p_2/m_{s2} is negligible for not too large a number of heavy holes.

For the above model, to explain Figure 3.22a, we must have:

1. The light hole band is close to parabolic, or the increase of effective mass in that band due to non-parabolicity, is exactly balanced by the loss of carriers in that band as temperature increases.
2. The heavier mass band is no more than .08 e.v. below the light hole band. This value corresponds to the Fermi level at 82°K of one Cohen band acting alone.
3. The number of carriers that have left the light hole band must be at least 45% to explain the increase of m_s up to 240°K.

Adding the heavy mass band, which becomes populated at $1/R_o e = 9.5 \times 10^{19}$ holes cm^{-3}, we cannot eliminate the possibility of a three band model consisting of: One light hole band of the Cohen type or the Dimmock type; one heavy mass band no more than .08 e.v. below the light hole band; one heavy mass band not far below the first heavy mass band. The position of this last band would depend on the density-of-states of the former heavy mass band and is less than .22 e.v. below the light hole band, as determined from the Fermi level of one Cohen band acting alone.

We will not try to fit our results with this model since the necessary parameters, to calculate R_o/R_∞ and the susceptibility effective mass, are not available. First attempts, however, using one Dimmock band, a mass for the first heavy mass band of .15 m_o as reported by Stiles et al.* (61 S1), and a mass of .32 m_o (70 S1) for the second heavy mass band suggest that good fits are possible by adjusting the number of valleys, the energy gaps and their temperature variations.

*The "Stiles band" has been discredited.

3.6 Discussion

3.6.1 Accuracy of the Experimental Results

The experimental errors in the determination of the effective masses using the Moss method are of two types.

The first type of errors is that inherent to the method and the measurement itself. We estimate that the errors in the measurement of absolute intensity is less than 5% in the worst cases. The wavelength position of the reflectivity minimum was also determined to better than 0.5%. Repeated measurements involving remounting, repolishing (chemical), etc., as described earlier gave values of R_{min} and λ_{min} within the above precision. In the worst cases, these errors in R_{min} and λ_{min} led to less than 2% error in effective masses. For most of the measurements, and specially all those at 82°K, the error in effective mass was less than 1%.

The second type of error is a systematic one, such as the error on ε_∞ and on R_o/R_∞ that enters in the equation used to determine the effective mass. This error can be completely eliminated at a later date if accurate values of these parameters are found. Using Moss's method, the systematic error in m_s is related to the deviation of $(R_o/R_\infty)/\varepsilon_\infty$ from the constant value

determined experimentally at low carrier concentration. In order to find the real carrier concentration and be able to plot the results we were also led to use R_o/R_∞ values over the whole concentration range. These values were obtained from extrapolation between experimentally determined R_o/R_∞ values according to the presupposed model of Section 3.5.7 d-1. One argument in favor of the use of these R_o/R_∞ values was that they brought the effective masses determined by the Moss and fitting techniques into agreement. We believe that this procedure was to be preferred to the alternative of using a $1/R_o e$ scale because R_o/R_∞ is very much different from one in $Pb_{1-x}Sn_xTe$ alloys.

3.6.2 The Valence Band Structure

The presence of a heavy mass band at $1/R_o e \simeq 9.5 \times 10^{19}$ cm^{-3} has been confirmed from the measurement of susceptibility effective mass versus carrier concentration. Attempts to explain the lower carrier concentration data using one non-parabolic band have not been successful for neither a Kane nor a Dimmock band. The best fit to our experimental data was obtained using a Cohen band. The susceptibility effective mass versus carrier concentration could be fitted using one Cohen band plus one heavy mass band .22 e.v. below the light hole Cohen band except for small discrepancies at intermediate carrier concentrations. However, we were not able to explain the suscpetibility effective mass versus temperature unless the temperature variation of the main energy gap is assumed to be twice that of the optical gap.

It should be pointed out here that the situation is in all respect similar to that described by Dixon and Riedl for PbTe (65 D1).

The Dimmock model which is better founded in that it takes into account the interaction of 6 bands at <111>, was in marked disagreement with the experimental results. We have pointed out earlier that the main assumptions leading to the Dimmock dispersion law for $Pb_{1-x}Sn_xTe$ are questionable and that there is evidence that it underestimates the non-parabolicity of the light hole band. However, the lack of experimental data concerning the position of the energy levels at <111>, does not allow any firm conclusions to be made about the validity of the Dimmock model. With these considerations in mind, we conclude that a heavy mass band is necessary to explain the experimental results together with a Dimmock band even at the lowest carrier concentrations measured.

That one non-parabolic band (Dimmock band) plus two heavy mass bands be necessary to account for all the experimental results of this chapter could not be ruled out. Perhaps one of the important results is that of Figure 3.22a. It could not be explained using one Cohen band only unless fortuitous. It could only be explained if by some mechanism (such as the transfer to a heavy mass band) carriers in the light mass band were lost to conduction as the temperature increased from $82^{o}K$ to $240^{o}K$.

CHAPTER IV

ELECTRICAL PROPERTIES OF $Pb_{1-x}Sn_xTe$

4.1 Introduction

In the last Chapter, we investigated specific models of the non-parabolicity of the <111> minima in $Pb_{1-x}Sn_xTe$. The Cohen model plus one heavy mass band gave the best fit to the experimental values of the effective mass versus carrier concentration. To account for the effective mass variation with temperature, it was necessary to modify one parameter of the Cohen model by using a larger temperature variation of the main gap than that measured experimentally. Literal use of the Cohen (or Dimmock) model would necessitate the presence of two extra valence bands* (besides the <111> maxima) to explain the experimental results.

Since there is evidence for the presence of only one heavy mass band*, we believe that the literal use of the models investigated in Chapter 3 should be abandoned. On the other hand, we may modify the Cohen model, for example, to explain one set of data, but the same modifications are often inadequate to explain other data. To illustrate this, let us first recall that we were able to explain the temperature variation of the effective mass, in 21% SnTe alloys, by using a larger temperature variation of the main gap than that determined experimentally. Also, Allgaier's calculations (66 A2) suggest that parameter values (again in disagreement with experimental measurements), which make the energy surfaces more dumbbell-shaped, need to be used to account for the variation of the low temperature Hall

*Subsidiary maxima of the same valence band as the main one at L.

factor of the <111> minima in $Pb_{1-x}Sn_xTe$. Perhaps the most severe test of models of non-parabolicity and energy surfaces is the attempt (70 E1) to explain the weak-field magnetoresistance in SnTe. Despite the numerous changes made in all the parameters of the Cohen model, it was not possible to explain the experimental results. The authors suggested the presence of highly distorted energy surfaces which could not be described by usual models such as the Cohen model. Recently, Allgaier (68 A1, 70 A1, 70 A2) proposed an alternative approach to the method of introducing many parameters in standard models to account for the distorted energy surfaces.

In this chapter, we will study the electrical properties of $Pb_{1-x}Sn_xTe$. To explain quantitatively the experimental results, a model describing the non-parabolicity and the energy surfaces of the <111> minima is needed. While the Cohen model may account for quantities such as the density of states at low temperatures, as shown in Capter 3, it cannot be used when the shape of the energy surfaces is expected to have an effect. Such effects resemble multi-band effects (70 A1), and are important when measuring electrical properties. Thus, we believe that the use of the Cohen model (or other standard models) cannot be expected to yield quantitative

explanations for most of the electrical results. Detailed quantitative analysis of electrical data in $Pb_{1-x}Sn_xTe$ still awaits an adequate model of the <111> minima.

4.2 Experimental

4.2.1 Apparatus Design

a) Low Temperature Cryostat

The cryostat used for the following experiments is described in detail elsewhere (69 A1). Its temperature range of operation was from 4.2°K to a few degrees above room temperature. The specimen chamber was a cylindrical silver capsule of controllable temperature which was measured from a thermocouple or a Cu-resistance thermometer.

b) High Temperature Apparatus

A furnace was designed to perform measurements between room temperature and 800°K. A schematic drawing of the section near the sample holder is shown in Figure 4.1. The main features of this apparatus are:

1) There are no measurable temperature gradients near the specimen due to the use of a well insulated copper capsule.

2) No cooling is required other than ambiant air. At the maximum operating temperature (800°K) the temperature of the outside walls is less than 70°C. Heat losses are minimized by putting the heated copper capsule in a thin quartz tube which is insulated from room temperature by two vacuum spaces. The power input at 700°K is less than 15 watts.

3) It has a small size. This is an advantage that allows a 1 cm. long sample to be mounted perpendicular to the long axis of

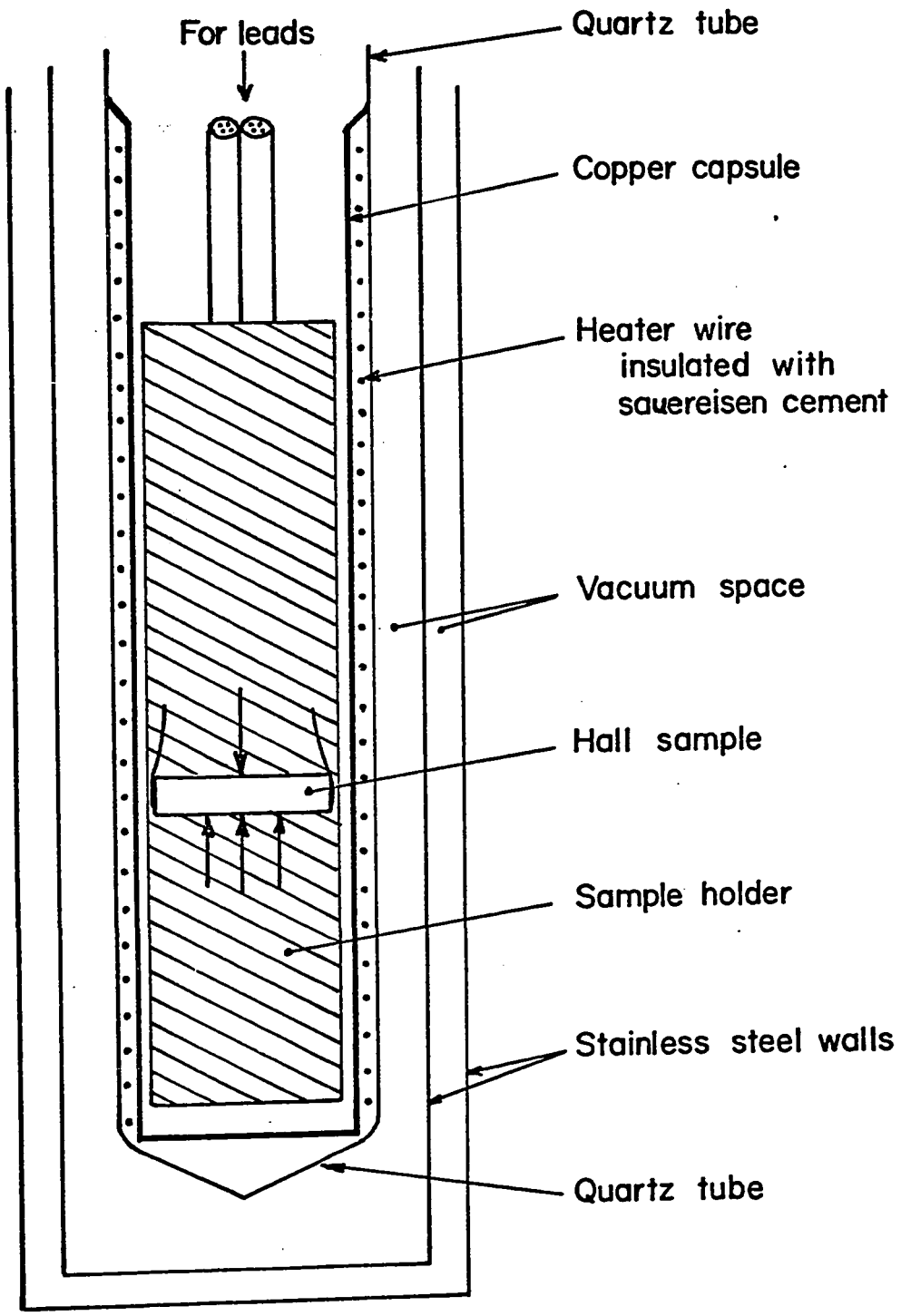

Figure 4.1 Schematic of apparatus for high temperature electrical measurements.

the capsule, as shown in Figure 4.1, and still permits the use of the apparatus in a $1\frac{1}{4}$ inch magnet gap.

4) Measurements at liquid nitrogen temperature are possible by introducing liquid nitrogen in the vacuum space around the quartz tube.

c) Temperature Control

The temperature of the silver capsule, in the low temperature cryostat, and of the copper capsule, in the high temperature apparatus, was controlled using the temperature control described in Figure 4.2. The temperature signal from a copper-constantan thermocouple was fed to a standard potentiometer, and the difference between the thermocouple voltage and the potentiometer voltage (that correspoding to the temperature of the measurement) produced a deviation of the light spot on the galvanometer scale. A photoelectric cell situated in the galvanometer scale, as shown in Figure 4.2, changed its resistance according to the position of the light spot as shown in Figure 4.2. The plate current (i.e. that in the heater) was made to increase, with increasing resistance of the cell, using the circuit of Figure 4.2. When the temperature of the capsule changed slightly, the current adjusted itself continuously to compensate the change. The temperature was stabilized this way to better than $.01^{o}C$ at all temperatures between liquid nitrogen temperature and $800^{o}K$.

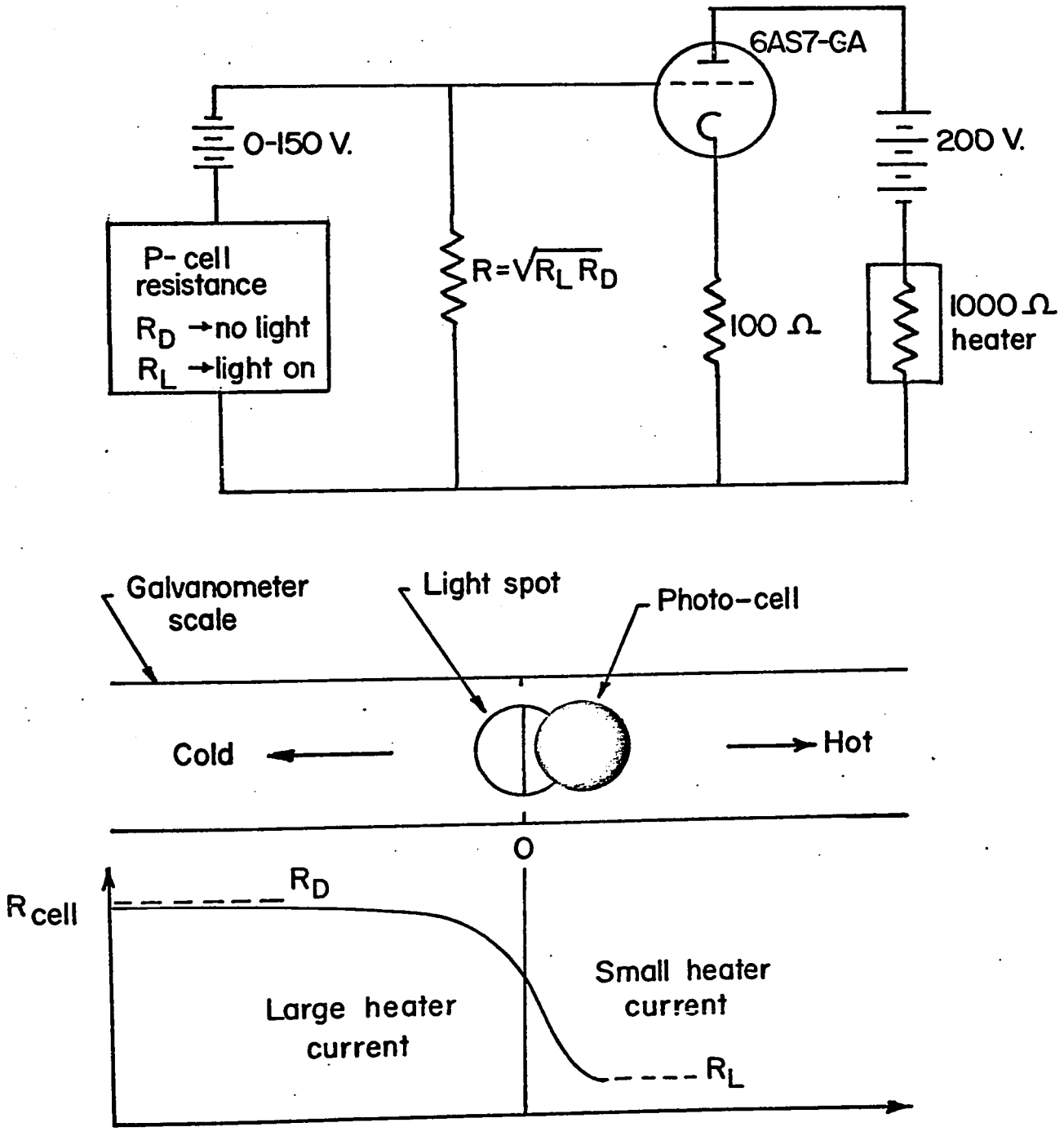

Figure 4.2 Temperature control.

d) Sample Holder

The sample holder is shown in Figure 4.3. The electrodes used for pressure contacts were made of 2% thoriated tungsten rods, .020" in diameter. The contact end of the rods, were made by electrolytic etching in a KOH solution. After the etching, the end of the rod was conical with a tip highly polished and rounded (radius of curvature of less than .001"). The springs were made of .003" diameter tungsten wire. To avoid any temperature gradients along the specimen due to the Peltier effect the specimen was mounted so that the two ends of the sample (with as massive current contacts as possible), the two current leads, and the two screws to which they were attached, were as close as possible ($\sim$ .5 mm) to the capsule walls in the cryostat.

4.2.2 Measurements

a) Temperature

The temperature was measured using both a copper-constantan thermocouple (also used for the control of temperature) and a copper resistance thermometer. The copper resistance thermometer was calibrated by measuring its resistance at 4.2°K and ice point. The published (54 D1) resistance ratios $R/R_{273.16}$ were then corrected, as described in (54 D1), and a table of resistance versus temperature was made. Usual precautions, such as the use of separate leads for current and voltage measurements, were taken. The temperature measured using the thermocouple and the Cu-resistance agreed within 0.1°K.

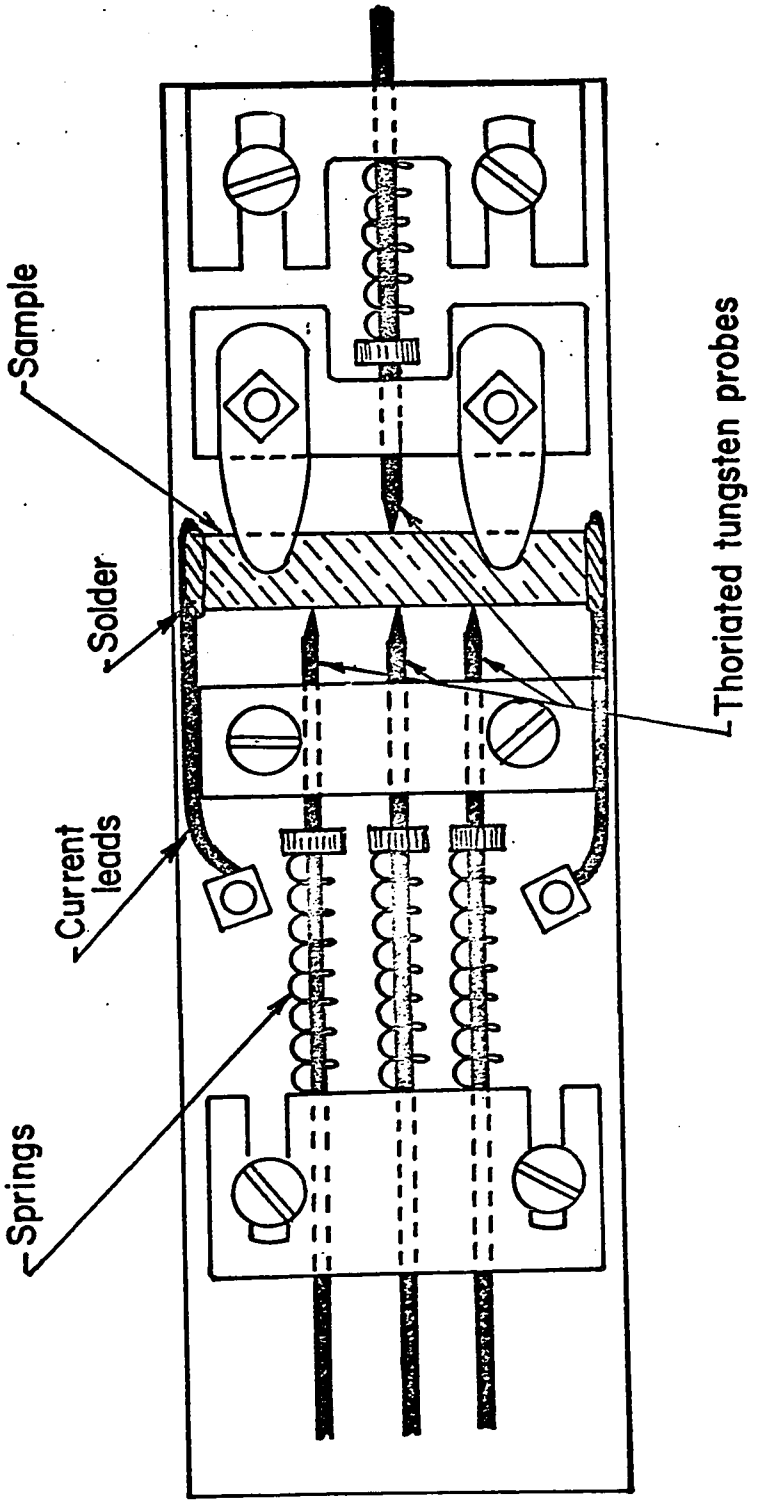

Figure 4.3 Sample holder.

b) Magnetic Field

The magnet used was a Magnion-Harvey-Wells 15 inch model. The pole gap was $1\frac{1}{4}$" and the maximum field, 3.2 Webers/m^2. The field was accurate to five parts in 10^5, and stable to one part in 10^6. The uniformity over the specimen, placed in the center of the pole gap, was one part in 10^5. A calibration table, relating the field measured at the position of the gaussmeter probe to the field at the position of the specimen, was made to the above quoted accuracy. The procedure is described in (69 A1).

c) Electrical Measurements

The direct current technique was chosen for the measurements of resistivity, magnetoresistance, and Hall voltages. All voltages were measured using a nanovolt amplifier and a digital voltmeter. Resistivity voltages were measured at two positions along the specimens for each direction of current. Hall voltages were measured for both directions of current and magnetic field. For magnetoresistance, the zero field resistivity was backed off using the variable zero of the nanovolt amplifier which is stable to better than .05 μ.V. In addition, the temperature and resistivity voltages were measured both before and after the measurements performed at fixed temperatures. In all cases, they agreed to better than one part in 10^4.

The samples were in the form of rectangular parallelepiped of typical dimensions 9 x 2 x 1 mm. All faces were lapped using 5μ.

powder. The dimensions were measured to an accuracy of .005 mm. The distance between the tungsten probes was measured to .01 mm. The area of contact of the tungsten probe with the specimen was estimated to be about 100 $\mu.^2$. No noise, due to the pressure contacts with the specimen, was observed.

For current contacts, at room temperature and below, indium was first electro-plated over the ends of the samples and then covered with low melting point solder ($\sim 40^{\circ}C$). The copper wire current leads could then be easily embedded in the solder after the specimen was mounted in the holder. For measurements at higher temperatures, pressure contacts were used for current.

In $Pb_{1-x}Sn_xTe$ the thermoelectric figure of merit $z = \alpha^2 T/\kappa\rho$ (where α is the thermoelectric power; T, the temperature; ρ, the resistivity; and κ, the thermal conductivity) is large and consequently the sample current will cause absorption of heat at one current contact and generation of heat at the other current contact. When this Peltier effect is present wrong Hall and resistivity voltages are measured even when the measurements are averaged over both directions of current and field (63 B1). In fact, the resistivity ρ_a, measured in adiabatic conditions, is related to the resistivity ρ_i, measured in isothermal conditions, by $\rho_a = \rho_i(1+z)$. Since z may be as large as one in $Pb_{1-x}Sn_xTe$, the resistivity of a well insulated sample can be as much as two times as large as that of a sample of constant temperature. The sample holder, as described

earlier, was designed to eliminate the temperature gradients due to the Peltier effect. For this arrangement the Peltier heat was supplied or removed by the massive current contact, situated at about .5 mm from the metal capsule, through the helium exchange gas. To check that the Peltier effect was unimportant, we measured the resistivity immediately after the current was reversed and looked for variations with time. We observed variations of less than 1%. Thus it can be assumed that our measurements were made in isothermal conditions.

4.3 Results and Analysis

This section will mainly be concerned with some of the Hall, magnetoresistance and mobility results obtained from two series of samples with compositions 6% SnTe and 21% SnTe respectively. The growth, the annealing procedures, and the preparation of these samples for electrical measurements have been described in Chapter 2. Let us recall here that these samples have been found to be homogeneous in their alloy compositions and in their carrier concentrations. The homogeneity in carrier concentration resulted from the absence of temperature gradients across the specimens during the annealing. It was confirmed by measurements of resistivity at two positions along all specimens and for all temperatures measured. However, there were a few exceptions in the lowest carrier concentration samples. At temperatures between 4.2 and 77^{o}K drastic changes in Hall coefficient (change from p-type to n-type) and resistivity were observed. These measurements were rejected. We will start this section with a brief discussion of the anomalies observed.

4.3.1 Anomalous Effect

a) Low Temperature Anomalies

A change from p-type to n-type was observed in two of our 6% SnTe alloys as the temperature was decreased below liquid nitrogen temperature. In these samples with $(1/R_o e)_{77}$ equal to 1.56×10^{17} and 5.0×10^{17} holes cm^{-3}, the Hall zero occurred at 55^{o}K and 35^{o}K,

respectively. Besides the change in type, there was a large increase in resistivity near the change over. This exceptional behavior has been observed by other in PbTe (66 Al). The following observations were made:

1) The samples were homogeneous, as determined from resistivity measurements at two positions along the length of the samples, for all temperatures except in the vicinity of the change over to n-type.

2) The increase of resistivity, near the cross over to n-type, was not localized. It occurred in one half of the sample for one polarity of the current and in the other half, for the other polarity. All changes observed appeared to have their origin at the current contacts.

Because 1) much care was taken to anneal these samples for long periods of time at constant temperature (± 1°C over the length of the specimens), 2) the samples were quenched fast at the end of the annealing, 3) 100 microns of material was removed on all six faces of the samples prior to the measurements, and also because of the above observations, we do not believe that the anomalies are due to bulk crystal inhomogeneities. We were not able to detect any internal precipitates from metallographic observations. The possibility of submicroscopic metal precipitates, forming during quenching due to retrograde solubility (see Section 2.3.3), is not ruled out. However, we would like to point out that all samples were lapped with 5 μ powder and that important surface effects were found (3.5.3) due to

less severe mechanical treatments. Also minority carrier diffusion lengths of the order of 1 mm are possible in low dislocation density $Pb_{1-x}Sn_xTe$ (68 M2) at low temperatures. That associated with surface effects and rectifying contacts may lead to unpredictable effects. It could even be that the above anomalous change to n-type is associated with the high degree of perfection of the bulk material in that low dislocation densities and high mobilities are associated with long minority carrier diffusion lengths. We end the discussion by recalling that these anomalous measurements were rejected.

b) High Temperature Effects

Measurements of the Hall constant were reproducible, in the $Pb_{1-x}Sn_xTe$ samples investigated, with temperature cycling from liquid helium temperature to about 500°K. When the cycling included higher temperatures than about 500°K the measurements were not reproducible. This effect is due to the irreversible diffusion which occurs in $Pb_{1-x}Sn_xTe$ at elevated temperatures.

Figure 4.4 is a plot of the Hall constant versus temperature showing the effect of diffusion at high temperatures. The Hall constant was measured while the furnace temperature was stable, but the successive points were taken from low to high temperatures and also in the reversed direction as indicated by the arrows. The reason for the large differences between the two curves, especially at high temperatures near the n-type Hall maximum, is that the excess tellurium

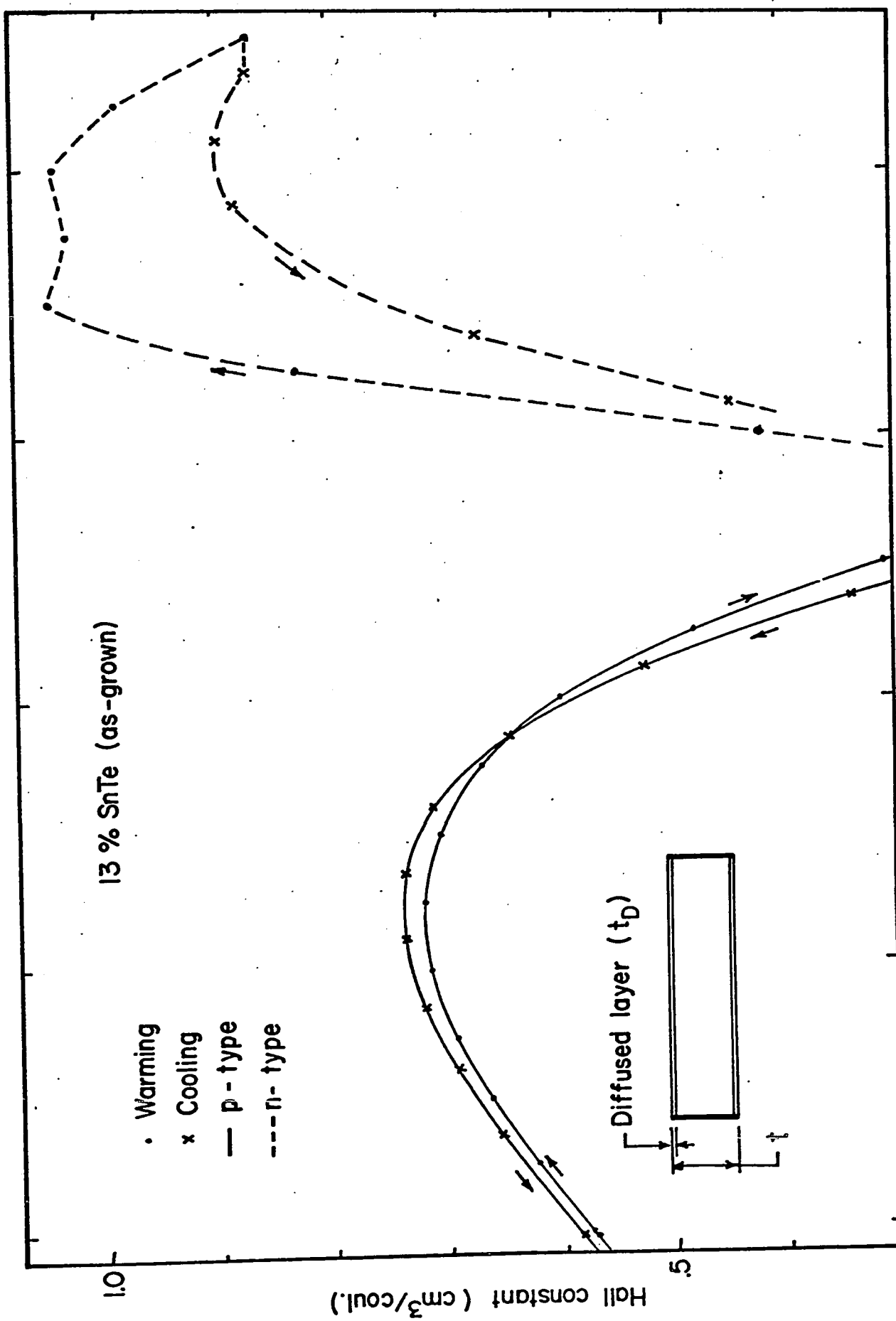

Figure 4.4 Hall constant vs. temperature showing the effect of diffusion at high temperature in $Pb_{1-x}Sn_xTe$.

diffused out of the specimens. At these high temperatures the Hall constant continuously diminished with time. Since the time between successive points varied between 10 and 20 minutes, the resulting Hall curve is highly distorted.

As seen from the results of Chapter 2, the annealing at around 700°K in 13% SnTe alloys converts it to n-type with approximately 10^{17} to 10^{18} carriers cm^{-3}. Since the sample of Figure 4.4 contains approximately 10^{19} extrinsic holes cm^{-3}, it can be shown that the diffused layer, that forms with time, is of lower resistivity than the bulk at high temperature, and of higher resistivity than the bulk when the sample is brought back to room temperature. To a first approximation, when the sample is brought back to room temperature after the temperature cycling, the Hall constant is larger by a factor $2t_D/t$ (in which t_D is the depth of the diffused layer and t is the thickness of the sample). This is due to the much higher resistivity of the diffused layer which carry no current and does not affect appreciably the Hall voltage from the now reduced bulk material.

The above discussion suggests a rapid technique by which diffusion constant may be measured in $Pb_{1-x}Sn_xTe$. The starting hole concentration and the annealing temperature could be chosen to satisfy the requirement that after annealing the diffused layer have a much higher resistivity than that of the bulk. The Hall constant R_I is measured at room temperature after which the sample is rapidly heated to the annealing temperature. When the annealing period is over, the

sample is rapidly cooled to room temperature and the Hall constant R_F remeasured. From these measurements the concentration of excess tellurium in the sample can be deduced, the annealing time is known, and the diffusion depth can be calculated from $2t_D/t = (R_F - R_I)/R_I$. Thus, the diffusion constant can be determined.

4.3.2 Hall Constant

Two groups of samples will be mainly considered in the following. The groups are identified by their first number 6 and 8 and have alloy compositions of 6% SnTe and 21% SnTe respectively. All samples are single crystals. The samples 8 all have the same orientation, and were measured with the magnetic field and the current directions parallel to the (011) and $(31\bar{1})$ direction, respectively. The samples 6 all have the same orientation except samples 6-0 and 6-4. For the other samples, the magnetic field and current directions were parallel to (143) and $(21\bar{2})$ respectively. One of the reasons for this somewhat arbitrary orientation was that the samples were obtained from a circular disk cut perpendicular to the axis of the ingot to minimize the alloy gradient.

a) Hall Constant versus Temperature

1. Hall Ratio below Room Temperature

Figures 4-5 and 4-6 show the variation of the Hall ratio $(R_T - R_{77})/R_{77}$ as a function of temperature for 6% SnTe and 21% SnTe samples respectively. The Hall constants were measured in a magnetic

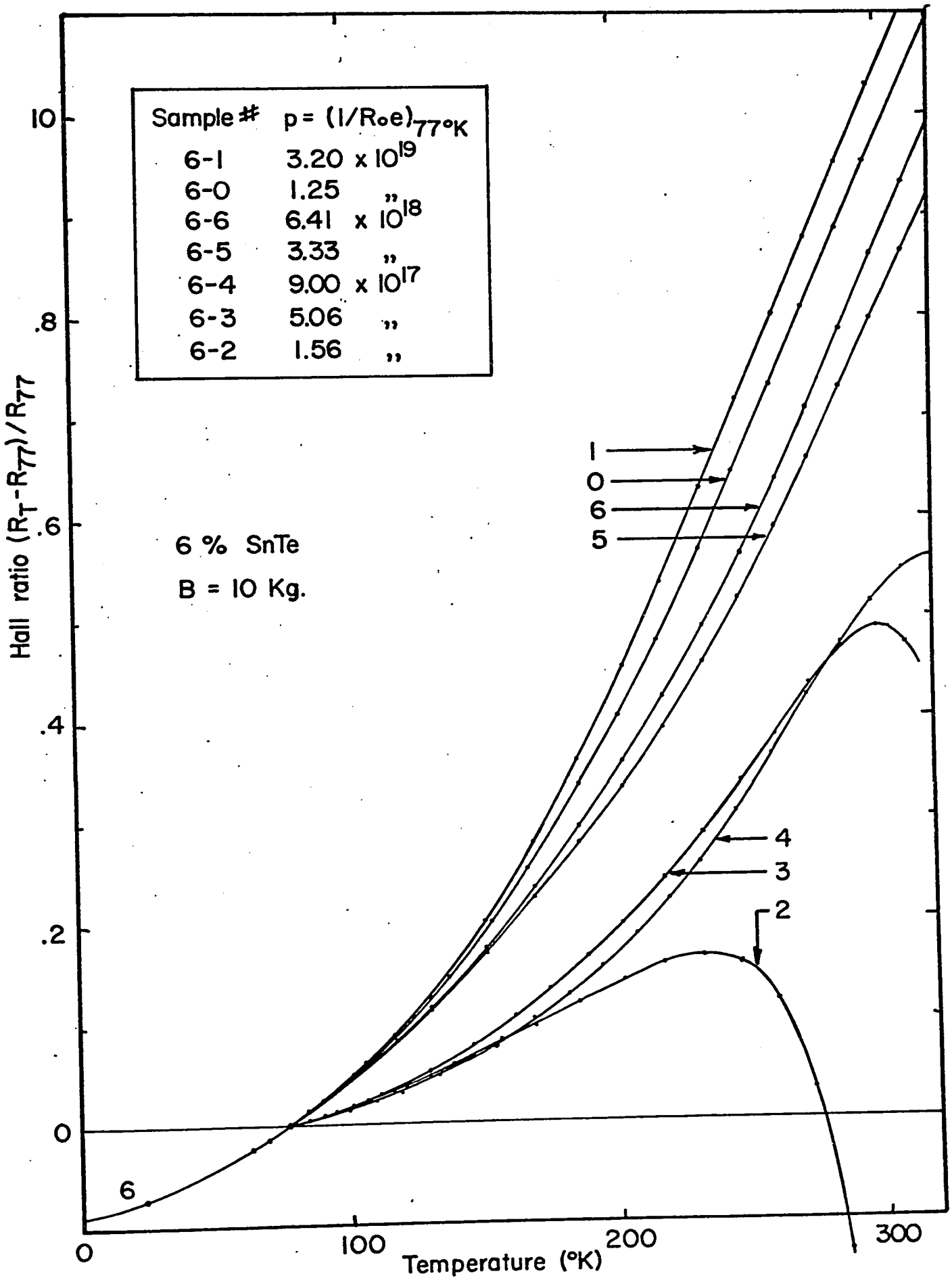

Figure 4.5 Hall ratio vs. temperature.

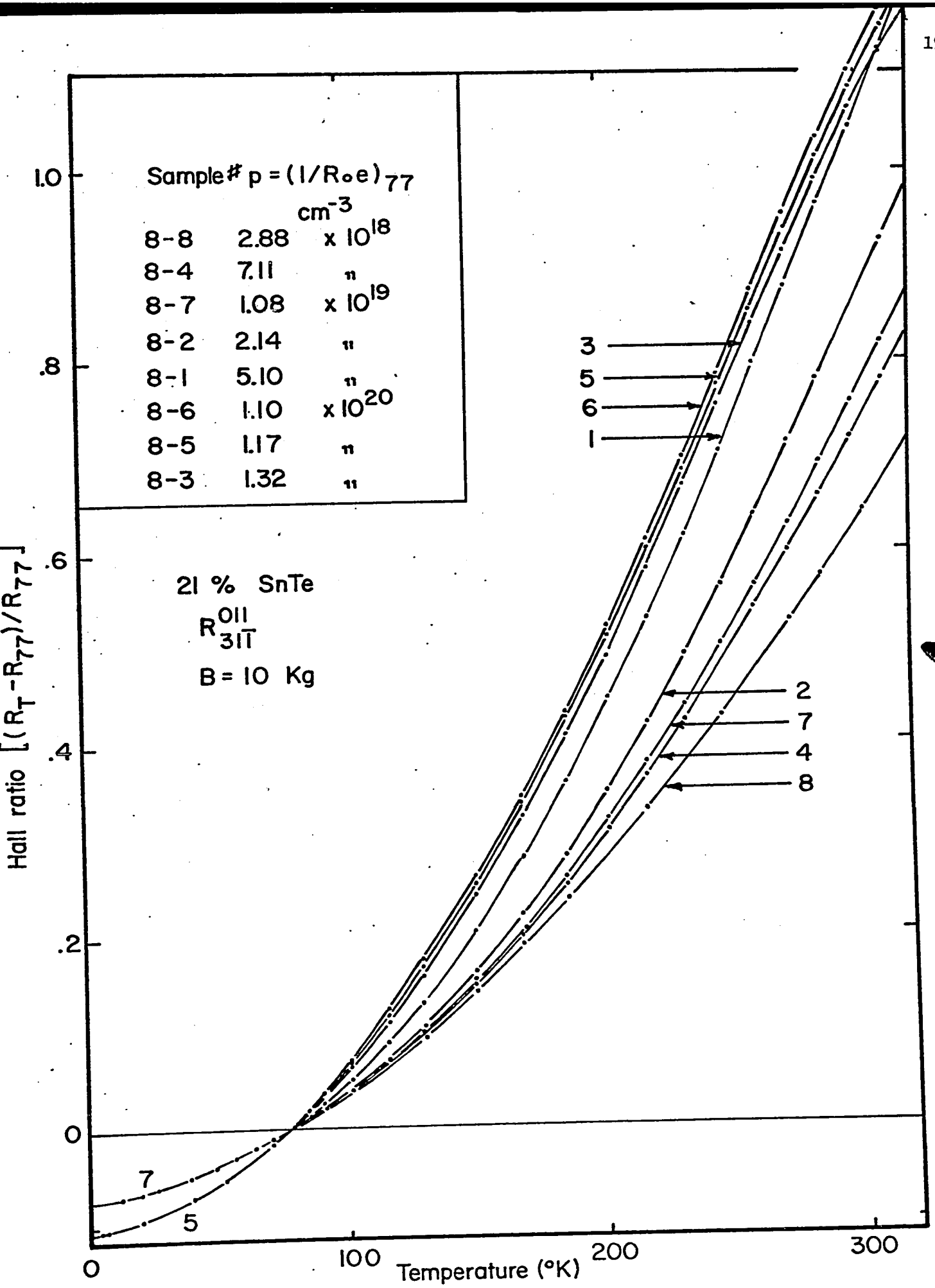

Figure 4.6 Hall ratio vs. temperature.

field of 10 kilogauss; the subscript of R is the temperature in degress Kelvin. The temperature variation of the Hall ratio in Figures 4.5 and 4.6 is very similar to that reported for PbTe (67 C1). The large increase of the Hall ratio with temperature in PbTe has been interpreted by Allgaier and Houston (66 A1) in terms of two valence bands. For this model all carriers are in the <111> minima (band 1) at low temperature. For increased temperature some of the carriers are transferred to a heavy mass band (band 2) situated .14 e.v. below the <111> minima at $0^{\circ}K$. As a result, the Hall constant increases toward a maximum corresponding to equal conductivities in both valence bands. However, because of the small energy gap between the valence and conduction bands, and of the small electron mass, the contribution from the conduction electrons becomes important at relatively low temperature and there is conduction in three bands. As a result, a maximum in the Hall ratio is usually observed as the temperature increases (because of the increasing contribution from the conduction electrons), before the conductivities in both valence bands are equal. When the maximum is due to bipolar conduction (electrons and holes), it occurs at lower values of the Hall ratio than the largest values of the Hall ratio measured.

In Figure 4.5, the Hall maximum in the low carrier concentration samples is due to bipolar conduction. In Figure 4.6, the Hall ratio for the three highest carrier concentration samples

shows a tendency towards the maximum resulting from equal conductivities in both valence bands. The main differences between the results of Figures 4.5 and 4.6 and those obtained on PbTe (67 C1) are the following:

1) The maximum in Hall ratio due to bipolar conduction occurs at an appreciably lower temperature in the alloys. For example, in PbTe with $(1/R_o e)_{77} = 4.33 \times 10^{17}$ cm^{-3}, it occurs at 340°K (67 C1) while, in 6% SnTe alloy, it occurs at 230°K and 300°K for $(1/R_o e)_{77}$ equal to 1.56×10^{17} cm^{-3} and 5.06×10^{17} cm^{-3}, respectively. This is simply explained by the reduction in energy gap between the conduction and valence bands with increasing SnTe content.

2) The Hall ratio, at a fixed temperature, does not increase monotonically with carrier concentration, in Figure 4.6, as it was the case in PbTe up to $(1/R_o e)_{77} = 10^{20}$ cm^{-3}. The curves for samples 8-3 and 8-5 are below the curve for sample 8-6. Moreover, the curve for sample 8-1 crosses over the curves for samples 8-3, 8-5 and 8-6 at temperatures higher than 300°K. As we will see (4.3.2b) this is due to the entrance of the Fermi level in the higher mass band at low temperature. A similar crossing over the curves is observed, in Figure 4.5, for sample 6-4. However, this may not be a two-band effect. At this low carrier concentration (9×10^{17} cm^{-3}), the effect of scattering upon change of statistics (from degenerate at low temperature to classical at high temperature) may be important

in the light hole band. Moreover, as mentioned earlier, sample 6-4 was not measured in the same condition of orientation as the other samples. At magnetic field of 10 kg, as we will see later, the Hall coefficient is anisotropic. If we add to this the possible effects of anisotropic scattering in band 1, we have several reasons to believe that the Hall ratio, due to band 1 only, is important at low carrier concentrations and that it explains the cross over of the curves for sample 6-4.

3) At low carrier concentrations the Hall ratio is not constant between 77°K and 150°K in the alloys (see sample 6-2) as it is in PbTe for similar carrier concentrations. Using the two-band model, and assuming that the heavy mass band is situated as far below the <111> minima in 6% SnTe alloys as in PbTe, all carriers are in the <111> minima, for temperatures lower than 150°K, and thus, the increase in Hall ratio, at low temperatures, is a single band effect.

Before we proceed with the discussion of the two-valence band model, it is useful to recall the most generally accepted band model for PbTe. Figure 4.7a, taken from Andreev (68 A2), shows the temperature variation of the bands. A similar model will be used to explain the results in $Pb_{1-x}Sn_xTe$. Figure 4.7b, taken from Dimmock et al (66 D1), shows the proposed variation of the main gap (E_{G_o} at 0°K) with alloy compositions. Let us keep in mind Figure 4.7 and specially Figure 4.7a as we go to the next section.

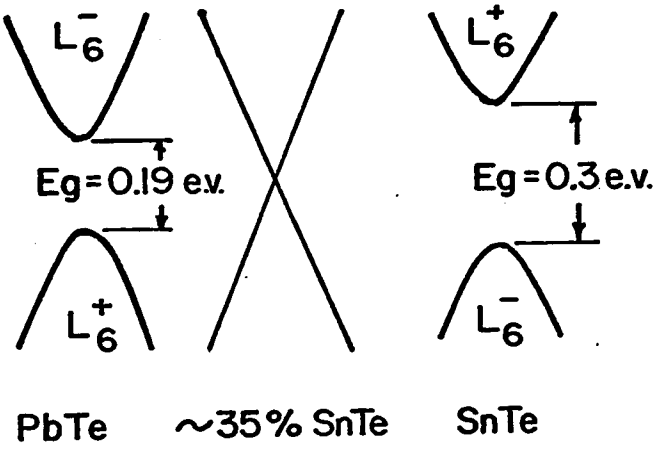

(b)

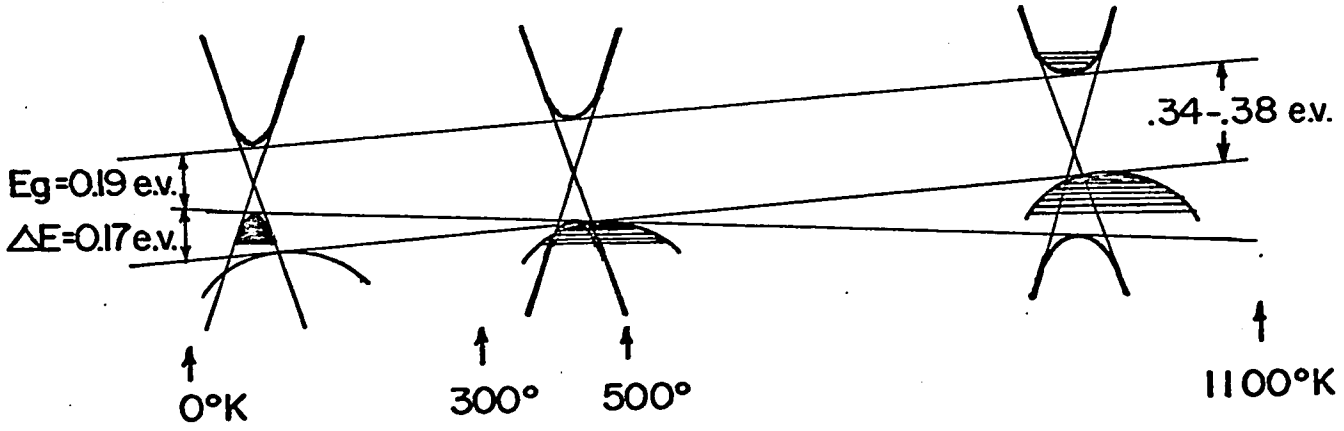

(a)

Figure 4.7 Displacement of band edges a) with temperature in PbTe b) with alloy composition in $Pb_{1-x}Sn_xTe$.

2. Simple Two-band Model. - Singular Points

The temperature dependence of the Hall ratio for a simple two-band model has been studied in detail by Allgaier (65 A1). The Hall ratio is given by:

$$\frac{R - R_o}{R_o} = \frac{(1 - b)^2 t}{(1 + bt)^2} \qquad (4\text{-}1)$$

In which R_o is the low temperature Hall constant $b = \mu_2/\mu_1$ is the ratio of the mobilities, (subscript 2 refers to the heavy mass band and subscript 1, to the light mass band) and $t = p_2/p_1$ is the carrier concentration ratio. In arriving at equation (4-1), it has been assumed that the Hall factors r_1 and r_2 are independent of temperature. Furthermore, b has been assumed to be small. The carrier concentration ratio is given by:

$$t = P \frac{F_{1/2}(\eta_F - \eta_V)}{F_{1/2}(\eta_F)} \qquad (4\text{-}2)$$

In which $P = (N_{v_1}/N_{v_2})(m_2/m_1)^{3/2}$ where the N_v's are the number of valleys and the m's are the density of states effective masses. The functions $F_{1/2}$ are standard Fermi integrals defined by:

$$F_{1/2}(\eta) = \int_o^\infty \frac{x^{1/2}}{1 + e^{x-\eta}}\, dx \qquad (4\text{-}3)$$

The symbols η_F and η_V represent E_F/kT and $\Delta E/kT$, respectively.

Some comments related to the use of the above model for $Pb_{1-x}Sn_xTe$ should be made here:

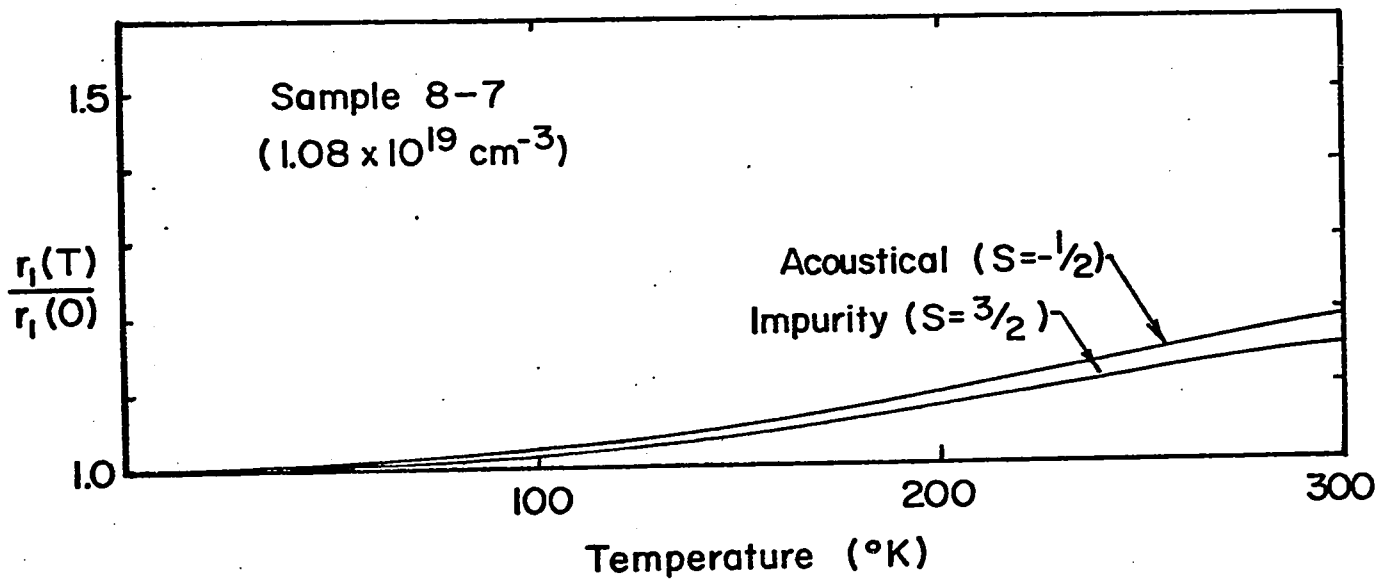

Figure 4.8 Normalized Hall factor for the <111> ellipsoids described by the Cohen model vs. temperature.

The following were used in the calculation:

1) Isotropic scattering given by $\tau = \tau_o E^s$.

2) Equation 19 (corrected) given by Allgaier (66 A2). $\mu = 1$ was assumed.

3) All other parameters are given by equation (3.97). E_G, the main gap, was taken from Figure 3.11, and linearly interpolated for other temperatures.

1) As shown by Allgaier for PbTe (66 A1) and as will be seen shortly for the alloys there is a heavy mass band in $Pb_{1-x}Sn_xTe$ in addition to the <111> minima, and b is small.

2) The assumption that $r_1(T)/r_1(0)$ is independent of temperature is not valid even for a parabolic band. For example, it goes from 1 to 1.18 when the statistics change from degenerate to classical for acoustical scattering. For a non-parabolic band, the increase of r_1 due to changing statistics is expected to be larger. The results of a calculation of $r_1(T)/r_1(0)$ for sample 8-7 using Allgaier's equation 19 (66 A2) derived for the Cohen model are shown in Figure 4.8. It is seen that, for this sample, the effect of the non-parabolicity is not important. The increase of r_1 from 0^oK to room temperature is not much different than that for a parabolic band.

Therefore, equation (4-1) is not strictly applicable to our results because it neglects the increase in Hall ratio due to the <111> minima alone. However, the increase in the Hall ratio due to the <111> minima only is, in many cases, small compared to the increase in the Hall ratio due to the transfer of carriers from the <111> minima to the heavy mass band. The main consequence of this assumption is that we cannot hope to explain the results in detail. Since there exists no satisfactory model to describe the <111> minima at present (Chapter 3), let us find out what can or cannot be explained by the two-band model.

The predictions of equation (4-1), as the temperature increases, are well described in reference (66 A2). Let us summarize briefly:

1) At low temperatures, all carriers are in band 1 (unless the inter-valence gap ΔE is small or the carrier concentration is large) and the Hall ratio is equal to zero.

2) With increasing temperatures, carriers are transferred from band 1 to the heavy mass band 2, and the Hall ratio increases until it reaches a maximum corresponding to equal conductivities in both bands at the maximum:

$$\left(\frac{R - R_o}{R_o}\right)_{max} = (1 - b)^2/4b \qquad (4\text{-}4)$$

This maximum may not be attainable for two reasons. Firstly, the largest value of t is P, as seen from equation (4-2), and the condition for equal conductivities in both bands is $bt = 1$ which will never be satisfied for $P < 1/b$. Secondly, bipolar conduction often takes over before the condition $bt = 1$ is reached. In both cases, the value of b determined using equation (4-4) is an upper limit.

3) When the statistics are classical, equation (4-2) becomes $t = P\, e^{-\Delta E/kT}$, and equation (4-1) reduces to the well known Aukerman-Willardson (hereafter called A.W.) equation for $b \ll 1$:

$$\frac{R - R_o}{R_o} \simeq P\, e^{-\frac{\Delta E}{kT}} \qquad (4\text{-}5)$$

Because, in several cases, bipolar conduction occurs at relatively low temperatures, other singular points are of interest. Since $b' = \mu_e/\mu_{h1}$ is larger than 1, a change from p-type to n-type is

observed with increasing temperature. For a single conduction band and a single valence band, it can be shown (68 P1) that at the cross-over, when the Hall coefficient R = 0, we have:

$$\sigma = \sigma_i = \eta_i e(\mu_h + \mu_e) \tag{4-6}$$

in which σ_i is the intrinsic conductivity. For further increase of temperature, past the cross over, the Hall constant goes through a negative maximum and we have (68 P1):

$$\frac{R_{max}}{R_{ex}} = \frac{(b' - 1)^2}{4b'} \tag{4-7}$$

in which R_{ex} is the Hall constant in the extrinsic region.

Table 4.1 summarizes the results obtained from the singular points in $Pb_{1-x}Sn_xTe$ with different alloy compositions and carrier concentrations. The temperature T_{max} is the temperature of the p-type Hall maximum, which is due to bipolar conduction (one or two valence bands plus one conduction band) for all samples except perhaps the last two in Table 4.1. The higher the carrier concentration, the larger T_{max} is; the larger the alloy fraction x, the smaller T_{max} is. The former is due to increased degeneracy with increasing carrier concentration; the latter to a decreasing main energy gap with increasing alloy fraction. The former is evidenced for sample with x =.13; the latter, for the two samples with x = .13 and .17 and with carrier concentrations 2.0×10^{19} cm^{-3} and 3.5×10^{19} cm^{-3} respectively. For these two samples, T_{max} decreases with

x	$1/R_{77}e$ cm^{-3}	$\left(\frac{R-R_{77}}{R_{77}}\right)_{max}$	T_{max} ^oK	$\frac{\mu_{h_2}}{\mu_{h_1}}$ Upper Limit	$\frac{\mu_e}{\mu_h}$	σ_i $\Omega^{-1}cm^{-1}$	T(R=0) ^oK	$(E_G)_0$ ^oK e.v.
.06	1.6×10^{17}	-	230	-	-	9.2	317	
.13	7.9×10^{16}	-	160	-	3.7	14.4	271.5	.14
.13	5.6×10^{17}	-	280	-	6.1	25.3	354	
.13	2.0×10^{19}	1.57	420	1/8.1	8.4	68	578	
.17	3.5×10^{19}	1.57	400	1/8.1				
.37	1.1×10^{20}	1.93	500	1/9.6				
.48	1.3×10^{20}	1.93	540	1/9.6				

TABLE 4.1 RESULTS FROM SINGULAR POINTS IN THE HALL CURVES VERSUS TEMPERATURE.

increasing x despite the increase in carrier concentration. The upper limit to the value of b determined according to equation (4-4), shows that b is indeed small.

From equation (4-7) $b' = \mu_e/\mu_h$ has been estimated in 13% SnTe alloys. Because the <111> conduction and the <111> valence bands are very similar b' is not expected to vary with carrier concentrations if only those two bands participate in the conduction. Thus, the values of b' in Table 4.1 show that, at the temperature of the negative Hall maximum, the holes are distributed between valence band 1 and valence band 2 for the highest carrier concentration samples. In the sample with carrier concentration 7.9×10^{16} holes cm^{-3}, the temperature of the Hall maximum is $340^{o}K$ only, and it is expected (see Figure 4.7a) that the heavy mass band is still appreciably below the light hole band. Consequently, most of the holes, if not all, are in the low mass band. Thus, the correct value of μ_e/μ_{h_1} is equal to or smaller than 3.7. As the carrier concentration increases, for $x = .13$, the temperature of the negative Hall maximum increases, and if ΔE decreses linearly with increasing temperature, there will be more and more heavy holes present at the Hall maximum. This explains the increase of b' with increasing carrier concentrations. Conversely, the increase of b' with increasing carrier concentrations is evidence that ΔE decreases with increasing temperatures.

The values of the intrinsic conductivities determined at the cross over when R = 0 are also shown in Table 4.1 together with the temperatures T(R = 0) of the Hall zero. From the values of the intrinsic conductivities in the lowest concentration samples with x = .13, the main gap between the conductivition band and valence band 1 has been determined to be $(E_G)_{0^oK}$ = .14 e.v., in good agreement with the optical determination (67 T1). Since only two samples were used in this determination, the accuracy is about 10% as determined from the absolute accuracy (∿3%) of the individual σ_i values. The method used was as follows.

The intrinsic electron concentration is given by (68 P1) $n_i = C\,T^{3/2}(m_e m_h)^{3/4}\ \exp-(E_{G_o}/2kT)$ in which all quantities not varying with temperature have been included in C. Writing this expression in equation (4-6) we have:

$$\sigma_i \propto (\mu_h + \mu_e)\ (m_e m_h)^{3/4}\ T^{3/2}\ e^{-\frac{E_{G_o}}{2kT}} \qquad (4\text{-}8)$$

Two limiting cases are of interest in $Pb_{1-x}Sn_xTe$:

1) All holes are in the <111> minima and the heavy mass band is empty. For this case, we have that μ_h and μ_e are proportional to $m_e^{-5/2}T^{-3/2}$ for lattice scattering and also that m_e and m_h are proportional to $T^{1/2}$ (64 L2). Thus, equation (4-8) becomes: $\sigma_i \propto T^{-1/2}\ \exp.(-E_{G_o}/2kT)$.

2) All holes are in the heavy mass band. For this case, it can be assumed that the effective mass in the heavy mass band does not vary with temperature and we have (remembering that $\mu_e >> \mu_h$ and and that $m_e \propto T^{1/2}$): $\sigma_i \propto T^{-7/8}\ \exp.(-E_{G_o}/2kT)$.

In case 1, E_{G_o} represents the gap between the light mass band and the conduction band extrapolated to zero temperature. In case 2 it represents the gap between the heavy mass band and the conduction band extrapolated to zero temperature. We thus expect, from Figure 4.7a, a much larger gap in case 2. In fact, both gaps have been measured optically and are, for 13% SnTe alloy (67 Tl), .12 and .25 e.v. for case 1 and case 2, respectively. For the intermediate cases, the holes are distributed in both valance bands and intermediate values of the energy gaps are expected.

As evidenced by the small T(R = 0) values, in Table 4.1, the two samples with carrier concentration 7.9×10^{16} cm^{-3} and 5.6×10^{17} cm^{-3} approach case 1. Calculation, using the expression of σ_i for case 1, gave for these two samples $E_{G_o} = .14$ e.v. in good agreement with the optical gap (67 Tl). On the other hand, the two samples with carrier concentrations 5.6×10^{17} cm^{-3} and 2.0×10^{19} cm^{-3} are intermediate cases. Calculation using the expression of σ_i given for case 1 (in case 2, the expression for σ_i differ only by the factor $T^{-3/8}$) gave for the gap .194 e.v. in agreement with the above discussion. Only the value of the first determination is of interest since it represents case 1. Case 2 would be obtained for higher carrier concentrations, i.e., higher T(R = 0), but, at high temperatures, diffusion as described earlier invalidates the results.

b) Hall Ratio versus Carrier Concentration

We mentioned earlier that the Hall ratio, at a fixed temperature, does not increase monotonically with increasing carrier concentration in 21% SnTe samples (see Figure 4.6). Let us point out that, in Figure 4.6, the Hall maximum corresponding to equal conductivities in both valence bands ($bt = 1$) has not been reached for any of the curves. Thus, we limit the discussion to points on the low temperature plateau (T_L) and to point of the ascending portion (T_H) of the Hall ratio curves versus temperature. In considering the variation of the Hall ratio between T_L and T_H as a function of carrier concentration, two cases must be distinguished (65 Al). Let us call E_{FL} and ΔE_L the Fermi energy and the inter-valence energy gap at T_L.

1) For $E_{FL} < \Delta E_L$, all carriers are in band 1, at the low temperature T_L, and equation (4-1) may be used to describe the behavior of $(R_H - R_L)/R_L$ versus carrier concentration. At low carrier concentration, where the statistics are classical, the Hall ratio is given by equation (4-5) and is constant. As the carrier concentration increases, $(R_H - R_L)/R_L$ increases continuously as shown by Allgaier who also produced quantitative curves (65 Al, 66 Al).

2) For $E_{FL} > \Delta E_L$, then even for $T_L = 0^{\circ}K$ there are carriers in band 1. And because the transfer of carriers to the heavy mass band have already started at T_L so much less transfer is detected by the Hall ratio as compared to the situation of case 1).

Allgaier calculation (65 A1) shows that the Hall ratio $(R_H - R_L)/R_L$ becomes a decreasing function of carrier concentration as soon as the Fermi level enters the heavy mass band at the temperature T_L. In this case, the Hall ratio may be calculated using (65 A1):

$$\frac{R_H}{R_L} = \frac{1 + \dfrac{(1-b)^2 t_H}{(1+bt_H)^2}}{1 + \dfrac{(1-b)^2 t_L}{(1+bt_L)^2}} \qquad (4\text{-}9)$$

which reduces to equation (4-1) when $t_L = 0$.

To summarize, at low carrier concentrations, the Hall ratio $(R_H - R_L)/R_L$ is constant. As the carrier concentration increases, for $E_{FL} < \Delta E_L$, the Hall ratio increases. Then, the Hall ratio decreases with increasing carrier concentration for $E_{FL} > \Delta E_L$. Allgaier has shown that a sharp kink near $E_{FL} = \Delta E_L$ is observed. It is important to note that this kink is due to the entrance of the Fermi level in the heavy mass band at the low temperature T_L. Therefore, the observation in Figure 4.6 that $(R_H - R_L)/R_L$ increases with increasing carrier concentrations and then decreases for the two highest carrier concentrations is another strong evidence for the presence of the heavy mass band in 21% SnTe alloy. It indicated that the Fermi level enters the heavy mass band, at $T_L = 77^{\circ}K$, in the vicinity of $(1/R_o e)_{77} = 10^{20}\ cm^{-3}$.

Figure 4.9 is a plot of $(R_T - R_{77})/R_{77}$ for several values of the temperature $T > 77^oK$ (indicated above the curves) as a function of the carrier concentration $(1/R_o e)_{77}$. As discussed earlier, the detailed shape of the curves cannot be explained by the simple two-band model because there is an increase of the Hall ratio due to the band 1 only. For example, at low carrier concentrations, an appreciable increase in Hall ratio may be attributed to the change in statistics and the effect of non-parabolicity. At higher carrier concentrations, an appreciable contribution to the Hall ratio is expected from the non-ellipsoidal nature of the energy surfaces (65 A1). Detailed fits would be possible if an accurate energy band model was available for the <111> minima, but, as shown in Chapter 3, no such model exists at present. However, the general prediction of the simple two-band model are obvious in Figure 4.9. Since T_L is kept fixed, i.e., 77^oK for all the curves, the kink appears when the Fermi level enters the heavy mass band at 77^oK for all curves. It occurs at $(1/R_o e)_{77} = 8.4 \times 10^{19}$ cm^{-3}.

In Figure 4.10, we show a plot of $(R_{295} - R_T)/R_T$ versus $(1/R_o e)_{77}$ for several values of the temperature $T < 295^oK$ (indicated above the curves). The kink, which now appears at T, as predicted by the simple two-band model, is shown to occur at lower $(1/R_o e)_{77}$ values as the temperature T increases. This effect cannot be attributed to the decreasing degree of degeneracy as the temperature T is increased since at high carrier concentration E_F/kT is always

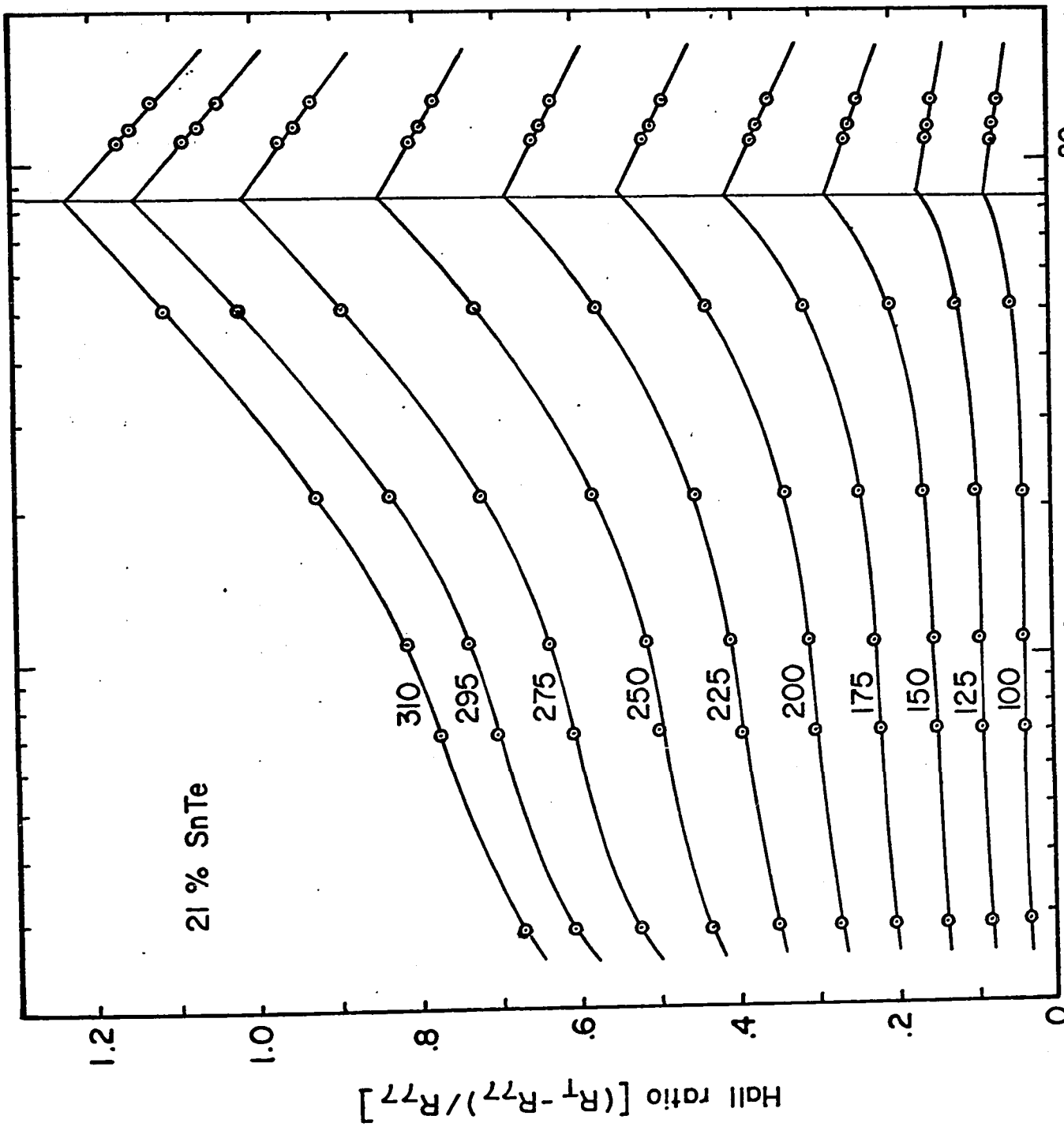

Figure 4.9 Hall ratio $(R_T - R_{77})/R_{77}$ vs. $(1/R_oe)_{77}$.

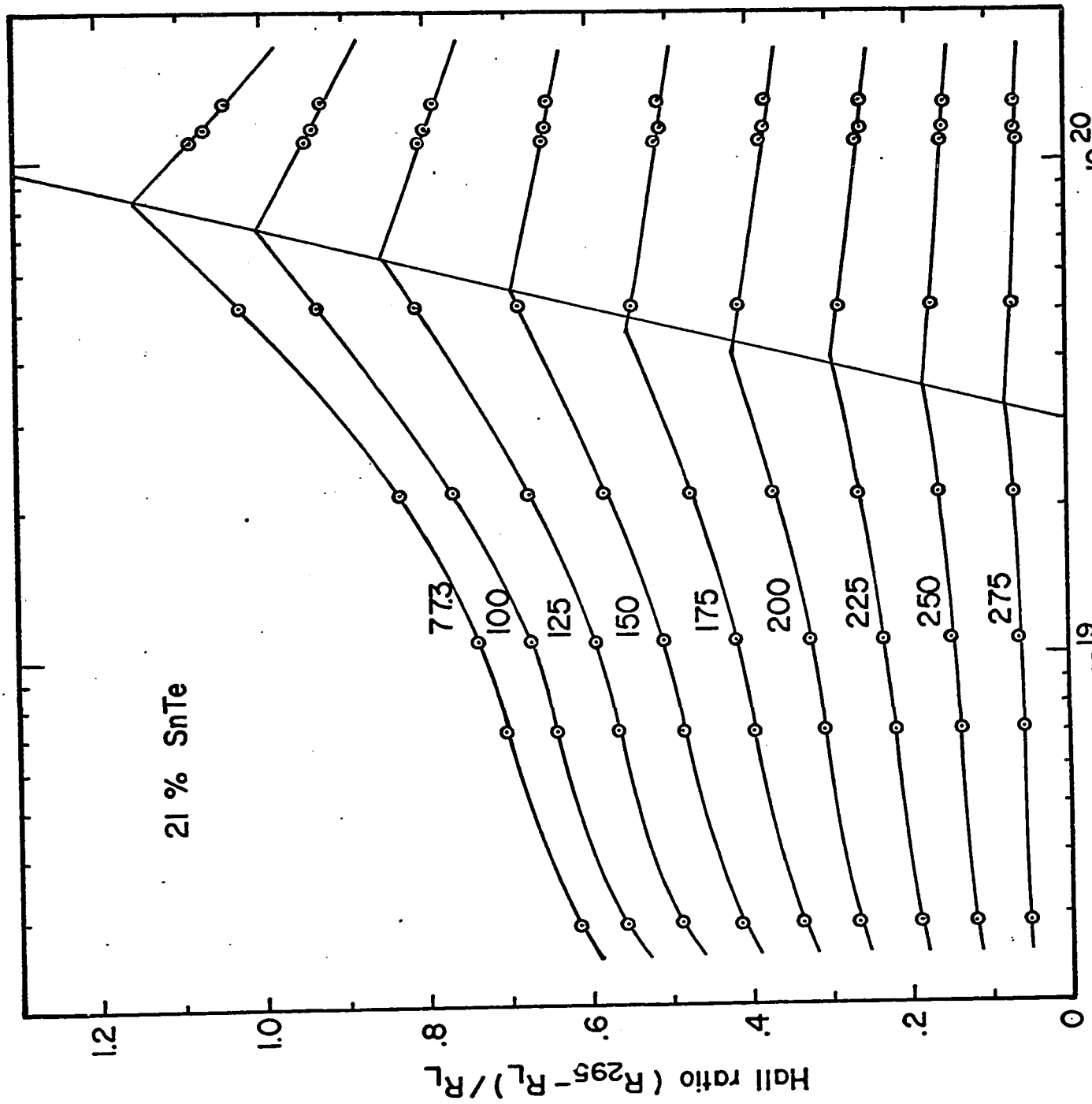

Figure 4.10 Hall ratio $(R_{295} - R_L)/R_L$ vs. $(1/R_oe)_{77}$.

much greater than 1, even at room temperature, and a negligible contribution to the Hall ratio is expected from band 1. Also the earlier entrance of the carriers in the heavy mass band due to the increasing kT cannot account for the effect observed. It can produce a rounding off but no appreciable shift of the kink. The only other possibility is the decrease of ΔE with increasing temperature.

We believe that Figure 4.10 constitutes one of the strongest pieces of evidence for the presence of the heavy mass band and that ΔE decreases with increasing temperature. At $T = 77.3^{o}K$ and $150^{o}K$ the kink occurs at $(1/R_o e)_{77}$ equal to 8.4×10^{19} cm^{-3} and 5.5×10^{19} cm^{-3} respectively. Using the values given in Figure 3.10b for the Hall factor r_1 in band 1 (i.e. .64 and .68 respectively) we find that the carrier concentrations N at the kink, for $T = 77.3^{o}K$ and $150^{o}K$, are 5.37×10^{19} cm^{-3} and 3.74×10^{19} cm^{-3}, respectively. Using the values of the Fermi energy calculated using the Cohen model (see Figures 3.26b) we find that the difference in Fermi energy between these two carrier concentrations is .032 e.v. This corresponds to $\frac{d\Delta E}{dT} = 4.4 \times 10^{-4}$ e.v./degree. For the value of $(\Delta E)_{77^{o}K}$, we obtain .21 e.v. using the Cohen model as described in Chapter 3 (see Figure 3.26b). Our value of $(\Delta E)_{0^{o}K}$ is thus .25 e.v. The errors involved in the above values of $(\Delta E)_{0^{o}K}$ and its temperature variation depend on our assumed values of the Hall factor r_1 in band 1. An error of 10% in r_1 lead to an error of about 8% in ΔE. For $\frac{d\Delta E}{dT}$ we could assume that r_1 is the same for both carrier concentrations and

assume it to be equal to 1 or .5 and still be within 20% of the values quoted above. An error is also involved in the determination of the Hall ratio kink which is obtained from extrapolation. The use of different models for the non-parabolicity of band 1 (i.e., the Cohen, Kane, or the Dimmock model) does not change the results appreciably. We estimate that $(\Delta E)_{0^oK}$ and $\frac{d\Delta E}{dT}$ are within 10-15% of the correct values.

From the position of the kink in the Hall ratio versus carrier concentration reported for PbTe (68 C1) i.e., $(1/R_o e)_{77} = 1.5 \times 10^{20}$ cm^{-3} and assuming $r_1 = .5$ (66 A1) we can find as above the value of $(\Delta E)_{77}$ in PbTe. We find $(\Delta E)_{77} = .23$ e.v., i.e., approximately the same value as in the 21% SnTe alloys. The Cohen model, which we have used for the determination, has been shown to account for the effective mass variation with carrier concentration at low temperature by Dixon and Rield (65 D1) and thus gives reasonably accurate values of Fermi level.

The value of about .25 e.v. for $(\Delta E)_{0^oK}$ in PbTe and 21% SnTe alloy bring out a serious disagreement* with the value of 0.14 e.v. often quoted and reported by Allgaier for PbTe (66 A1). As discussed above, we do not believe that our value is more than 10-15% in error.

c) Hall Ratio at Low Carrier Concentration

We repeated the experiment, originally performed by Allgaier (66 A1) on a PbTe sample for which the A.W. analysis, equation (4-5), was appropriate. We used a PbTe sample with

*$E_G + \Delta E = .19 + .25 = .44$ e.v. at 0^oK in PbTe. This is also in disagreement with the value quoted in Figure 4.7 taken from Andreev (68 A2).

$(1/R_o e)_{77} = 6.15 \times 10^{17}$ cm^{-3}. A temperature independent baseline (i.e., a temperature independent Hall factor r_1) was assumed to exist and was determined from the experimental Hall data at low temperatures. The values of $(1 - b)^2 P$ and $(\Delta E)_{0^oK}$ determined from the intercept at $1/T = 0$ and the slope, respectively, were 23 and .127 e.v. respectively. The results are shown in Figure 4.11. Both values are slightly lower than Allgaier's values. The difference is insignificant and could be attributed to the error involved in the determination of the R_L baseline. Thus our determination of $(\Delta E)_{0^oK}$ using A.W. equation (4-5) also conflicts with the previous determination from the kink in the Hall ratio versus carrier concentration.

Similar determinations of $(\Delta E)_{0^oK}$ for other alloy compositions, ranging from 6% to 25% SnTe, using A.W. analysis gave values of $(\Delta E)_{0^oK}$ ranging from .03 to .06 e.v. The results for sample 6-2 are plotted in Figure 4.12. Since no temperature independent baseline was observed, R_L was taken as the value of the Hall constant at 0^oK. As seen, the A.W. equation is obeyed accurately, and we conclude that either a third valence band situated about .03 e.v. below the <111> minima has been detected or that the A.W. analysis is not valid.

We favor the second alternative because no temperature independent baseline was observed and a Hall ratio increase is expected due to the light mass band only (see for example Figure 4.8). Thus, the result of Figure 4.12 appears to be fortuitous. Perhaps the

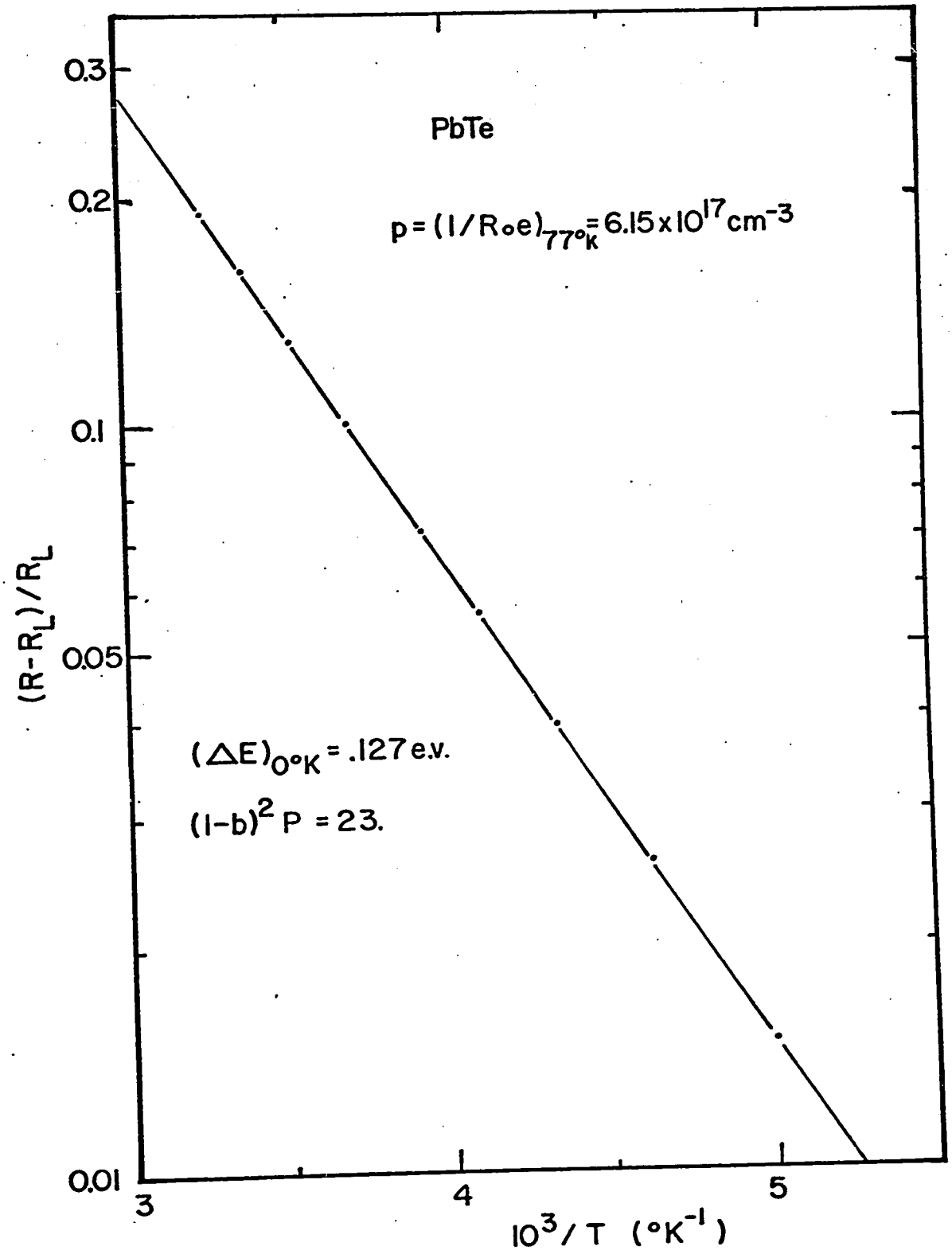

Figure 4.11 Hall ratio vs. reciprocal temperature in PbTe.

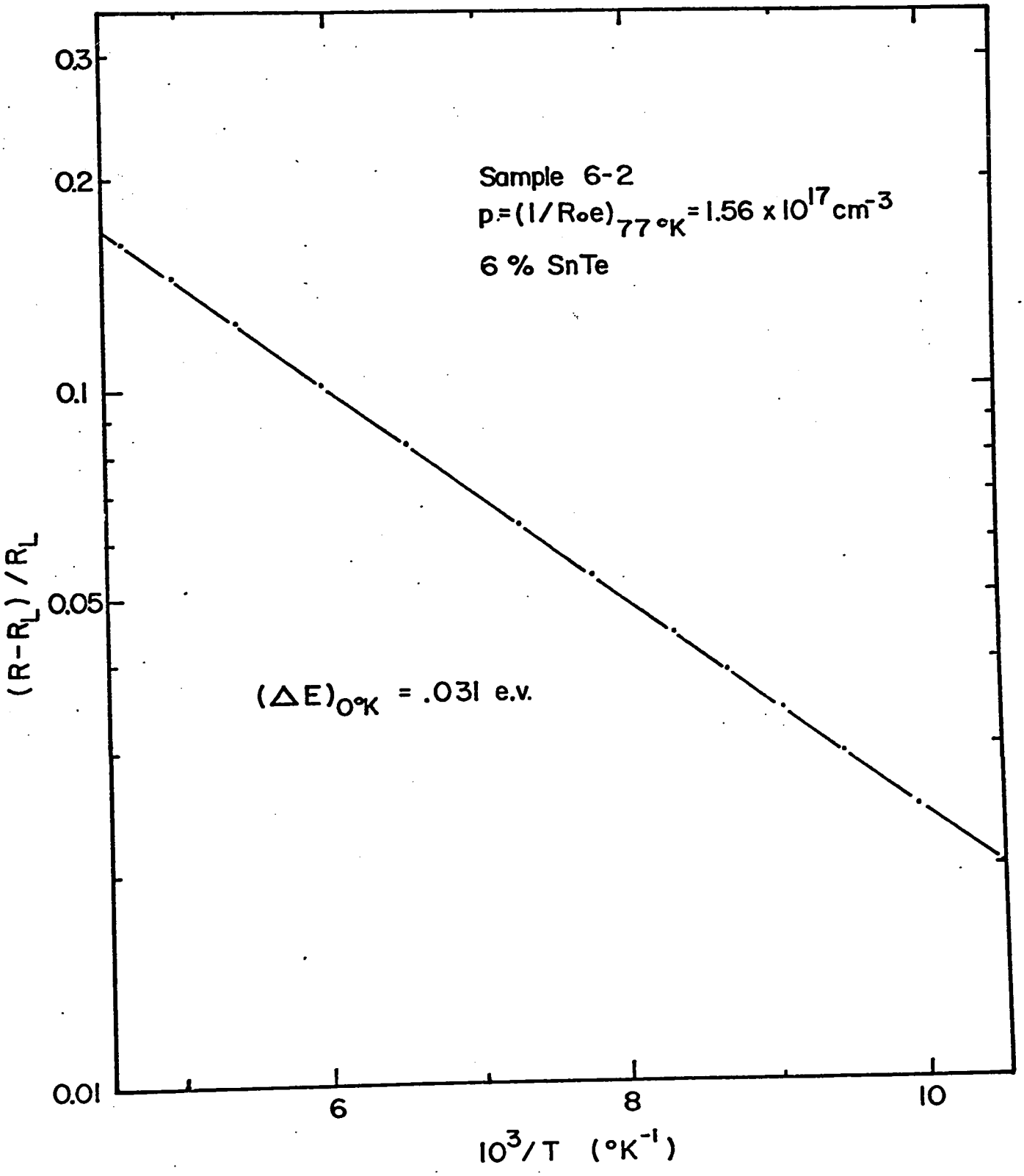

Figure 4.12 Hall ratio vs. reciprocal temperature in $Pb_{1-x}Sn_xTe$.

manifestations of the non-ellipsoidal energy surfaces and of the non-parabolicity in band 1 are analogous to those of a simple two-band model in sample 6-2.

Assuming $(\Delta E)_{0^oK} \sim .25$ e.v. for sample 6-2 and $\frac{d\Delta E}{dT} = 4 \times 10^{-4}$ e.v./^oK we expect no carrier in the heavy mass band even at the highest temperature in Figure 4.12. Therefore, the total increase of the Hall ratio with increasing temperature in Figure 4.12 represents the variation of r_1 with temperature. For higher carrier concentrations, the two-band effect should become apparent. Figure 4.13 illustrates this for sample 6-3. If the low temperature portion of the curve is taken to be the contribution of r_1 and is extrapolated to higher temperatures, we see that the two-band contribution is indeed small. To determine $(\Delta E)_{0^oK}$ from the A.W. analysis the contribution of r_1 should be subtracted. Extrapolation of the r_1 contribution to higher temperature, and the subtraction of r_1 gives for $(\Delta E)_{0^oK} \sim .15$ e.v. as illustrated in Figure 4.13. The important point we want to bring out here is that one cannot obtain $(\Delta E)_{0^oK}$ from A.W. analysis due to the non-existence of a temperature independent baseline. In Figure 4.13 we showed that an estimate of $(\Delta E)_{0^oK}$ is possible only if a temperature dependent baseline is assumed.

In conclusion, we suggest that the A.W. analysis in $Pb_{1-x}Sn_xTe$ is invalid because r_1 varies with temperature. The effect of r_1 has been shown to be very important in the alloys. In PbTe the effect of r_1 was not apparent* at low temperatures but we believe that it was nevertheless present at higher temperature and has caused the determination of $(\Delta E)_{0^oK}$ to be underestimated by a factor of about 2.

*Undetectable increase in r_1 may be present at higher temperatures than the low temperature plateau.

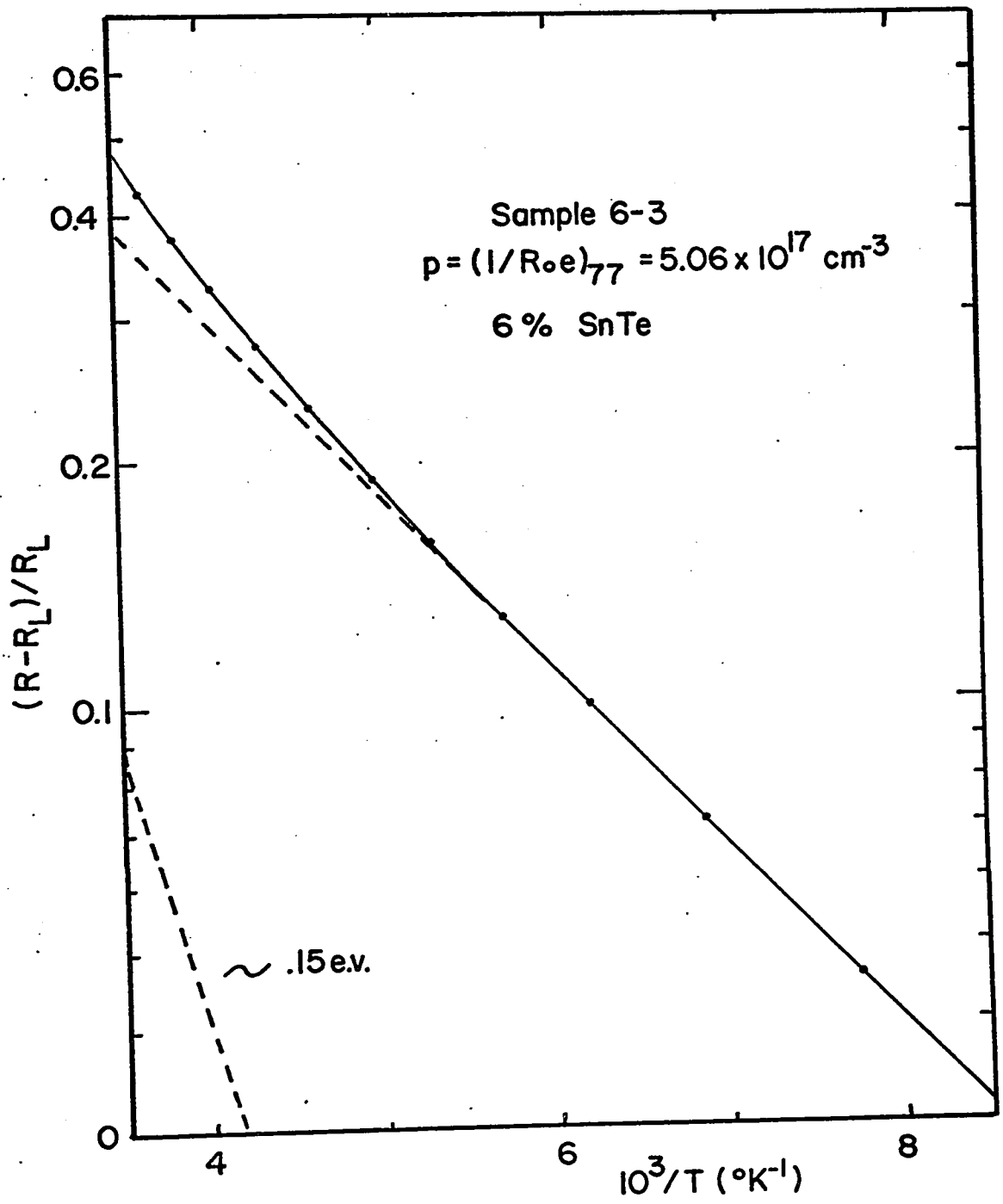

Figure 4.13 Hall ratio vs. reciprocal temperature in $Pb_{1-x}Sn_xTe$.

d) Hall Constant versus Magnetic Field

In Figure 3.10a, we reported that the Hall constant first decreases and then increases with increasing magnetic field. This was not the case in PbTe (61 A1). The increase in Hall constant at high field is expected from the ellipsoidal energy surface. The initial decrease in Hall constant was originally taken to be a two-band effect. In that case, for a simple two-band model with degenerate statistics, the ratio of the weak to strong field Hall coefficient is (61 A1):

$$\frac{R_o}{R_\infty} = \frac{f_a\mu_a^2 + f_b\mu_b^2}{(f_a\mu_a + f_b\mu_b)^2} \qquad (4\text{-}10)$$

where the f's and μ's are the fractions of the total carrier concentration and the mobilities in bands a and b. This expression can be much larger than unity and the Hall coefficient R_B is expected to decrease in going from weak to strong fields. Thus, the apparent explanation of the behaviour of R_B versus magnetic field in Figure 3.10a, was that R_B initially decreases due to the two-band effect until the effect of anisotropic energy surfaces takes over with increasing magnetic field following which R_B increases. Such an interpretation would appear to be consistent with the low values of $(\Delta E)_{0^oK}$ found in the same alloy using A.W. analysis (Figure 4.12). However, further investigations showed that this agreement is fortuitous.

Figure 4.14 is a plot of R_B/R_o versus $\mu_H^o B$, where R_o is the zero field Hall constant, μ_H^o is the zero field Hall mobility

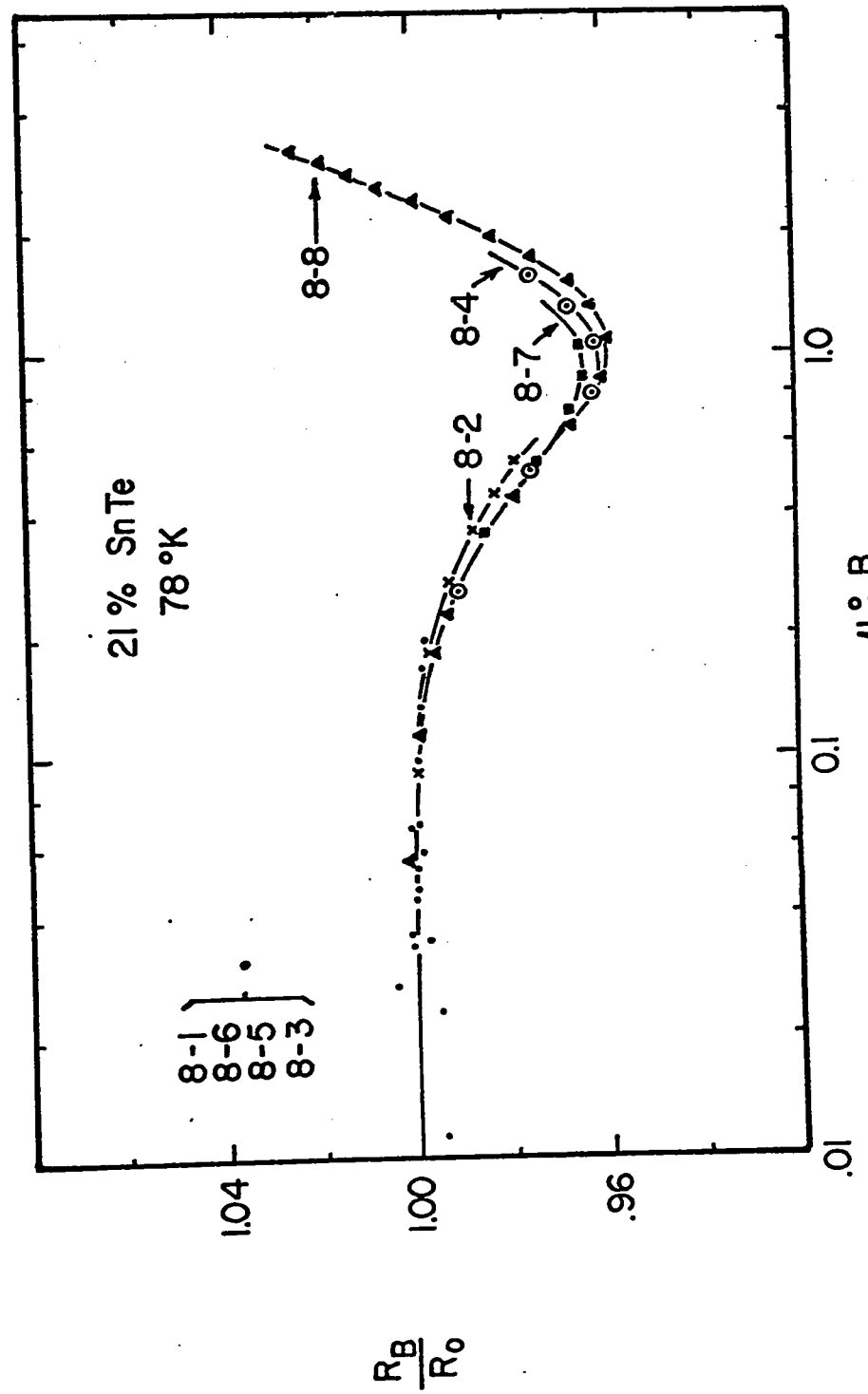

Figure 4.14 R_B/R_o vs. $\mu_H^o B$ for several carrier concentrations in $Pb_{1-x}Sn_xTe$.

(calculated using the zero field Hall constant) in $m^2/v.sec$ and B is the magnetic field in Webers/m^2. The carrier concentration values are given in Figure 4.6. The results of Figure 4.14 show that the interpretation of the low-field Hall constant data in terms of two bands is incorrect. The initial decrease of R_B/R_o is the same within experimental errors for all samples measured at 78°K. From sample 8-2 to sample 8-8 the carrier concentrations change by about a factor of 10. If two bands were present at 78°K, the inevitable changes in the f's and μ's in equation (4-10) would predict appreciable changes in the low field portion of the curves (i.e. for μ_H^o B < 1.0).

The possibility that the minimum observed be due to the particular orientation of the Hall sample, as predicted by calculations (63 B1, p.90), was taken as improbable because the depth of the minimum changed with temperature in degenerate samples. It diminishes by a factor of 2 from liquid nitrogen to liquid helium temperature. Also the same behavior was observed for other directions of the current and magnetic field.

We believe that the initial decrease of R_B/R_o is due to a distorted Fermi surface. The effect on galvanomagnetic properties of the shape of Fermi surface has been described by Allgaier and Perl (70 A1). For electrons moving on a flat portion of the Fermi surface the low field condition ($\mu B \ll 1$) is easily realized. For the electrons moving around a highly curved portion of the Fermi surface large Hall angles (or large μB values) are possible and the low field condition

is not so easily realized. The electrons when moving on a highly curved portion of the Fermi surface have smaller effective masses and higher mobilities than when they move on flatter sections of the Fermi surface (70 Al). When the magnetic field is high enough to allow the electrons on the highly curved portion of the Fermi surface to make the turn before they collide, then the Hall factor (which is always smaller than 1 when arising from Fermi surface distortion) takes its minimum value (70 Al). Therefore, as the magnetic field increases the Hall constant goes through a minimum and then increase towards R_∞.

The apparent two-band effect, described at the beginning of this section, is expected, as pointed out by Allgaier et al (70 Al). In equation (4-10), the band-a characteristics apply to the carriers on the highly curved portions of the Fermi surface. There is a small number of high mobility carriers which, as described before, explains the curves of Figure 4.14.

In Figure 4.15, R_B/R_o is plotted versus $\mu_H^o B$ for several temperatures in 6% SnTe and 21% SnTe samples. Again the behavior of R_B/R_o at low magnetic field resembles a two-bands effect. However, it is not the case for the lowest temperature as explained earlier. For $(\Delta E)_{0^oK} = .25$ e.v. there are no carriers in the heavy mass band for temperature lower than 150^oK. At room temperature, an appreciable two-band contribution to the decrease in Hall constant is present. In fact the B^2 dependence of the low field Hall constant was realized at

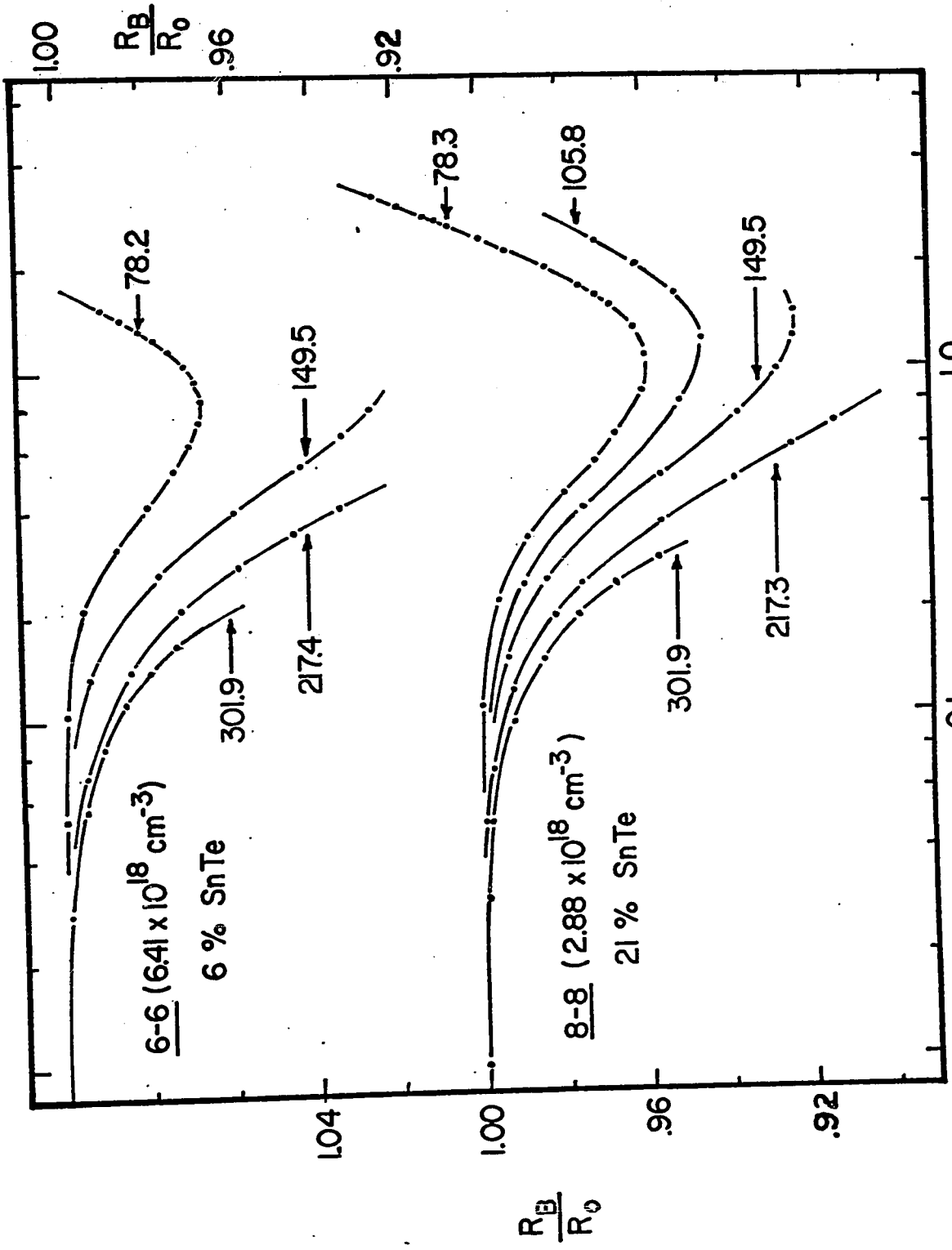

Figure 4.15 R_B/R_o vs. $\mu_H^o B$ for several temperatures in $Pb_{1-x}Sn_xTe$.

room temperature but not at the other temperatures showing that the two-band effect was dominant at room temperature only.

4.3.3 Transverse Magnetoresistance

The dimensionless weak-field magnetoresistance $M_{\alpha\beta\gamma}^{\delta\varepsilon\zeta}$ is defined by (60 A1):

$$\frac{\Delta\rho}{\rho_o} = M_{\alpha\beta\gamma}^{\delta\varepsilon\zeta} \left(\mu_H^o H/C\right)^2 \qquad (4\text{-}11)$$

where $\Delta\rho/\rho_o$ is the fractional change in zero-field resistivity, $\alpha\beta\gamma$ and $\delta\varepsilon\zeta$ identify the current and magnetic field directions relative to the cubic axes of the crystal, μ_H^o is the zero-field Hall mobility, C is a factor which depends on the system of unit used (60 A1). In this section we will use μ_H^o B, in the place of μ_H^o H/C, with μ_H^o and B expressed in m^2/v.sec and Webers/m^2 respectively. The dimensionless Seitz coefficients a, b, and c are related to equation (4-11) by (60 A1, 70 E1, 70 A1):

$$M_{\alpha\beta\gamma}^{\delta\varepsilon\zeta} = b + c\left(\Sigma_s i_s \eta_s\right)^2 + d\Sigma i_s^2 \eta_s^2 \qquad (4\text{-}12)$$

where i_s and η_s are the direction cosines of the current and magnetic field directions in the cubic-axis system.

For the transverse magnetoresistance the magnetic field and the current directions are perpendicular to one another. For the cubic system, we then have $(\sum_s i_s \eta_s^2) = 0$ and equation (4-12) reduces to:

$$M_{\alpha\beta\gamma}^{\delta\varepsilon\zeta} = b + d \sum_s i_s^2 \eta_s^2 \qquad (4\text{-}13)$$

For the particular orientation used here, we have:

$$M_{31\bar{1}}^{011} = b + .09d \qquad (4\text{-}14)$$

$$M_{21\bar{2}}^{143} = b + .24d \qquad (4\text{-}15)$$

The dimensionless Seitz coefficient b, c, and d have been determined in PbTe and are given in reference (60 A1). Substitution of these coefficients in equations (4-14) and (4-15) gives the $M_{31\bar{1}}^{011}$ and $M_{21\bar{2}}^{143}$ values for PbTe. These values will be needed later to compare the results from $Pb_{1-x}Sn_xTe$ alloys with those of PbTe.

In Figures 4.16 and 4.17, $\Delta\rho/\rho_o$ versus $\mu_H^o B$ is plotted on a log-log scale for several carrier concentrations and temperatures in 21% SnTe alloys (similar curves were obtained in 6% SnTe alloys). It can be seen that the weak-field theory is precisely obeyed (i.e., $M_{\alpha\beta\gamma}^{\delta\varepsilon\zeta}$ is constant) up to $\mu_H^o B = 0.1$. As predicted by equation (4-11), the slope is exactly 2. For $\mu_H^o B > 0.1$ the slope gradually decreases and there is a tendency towards saturation. To obtain the correct values of $M_{\alpha\beta\gamma}^{\delta\varepsilon\zeta}$ it is important that $\Delta\rho/\rho_o$ and R_H be measured at low enough magnetic field. As shown in Figures 4.14 and 4.15, the low field Hall constant is obtained for $\mu_H^o B = .1$ at 77°K and for values as low as $\mu_H^o B = .02$ at 300°K. For the determination of all $M_{\alpha\beta\gamma}^{\delta\varepsilon\zeta}$ values, we used the low field Hall constant to calculate $\mu_H^o B$, and the values of $\Delta\rho/\rho_o$ at $\mu_H^o B = .1$. In a few cases, it was necessary to extrapolate the data, but as seen in Figure 4.16 this extrapolation was straight forward and involved negligible errors.

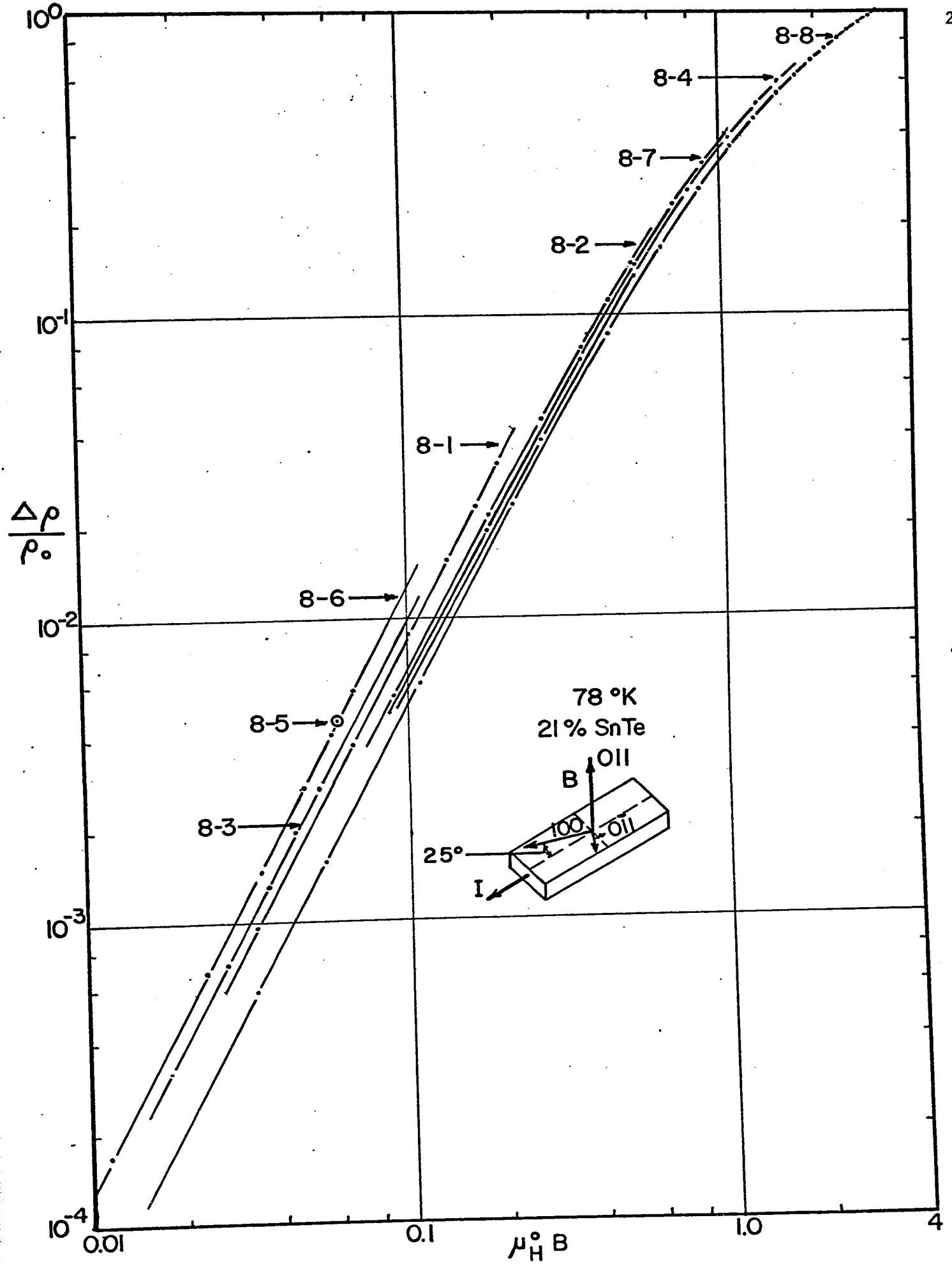

Figure 4.16 $\Delta\rho/\rho_o$ vs. $\mu_H^o B$ in $Pb_{1-x}Sn_xTe$.

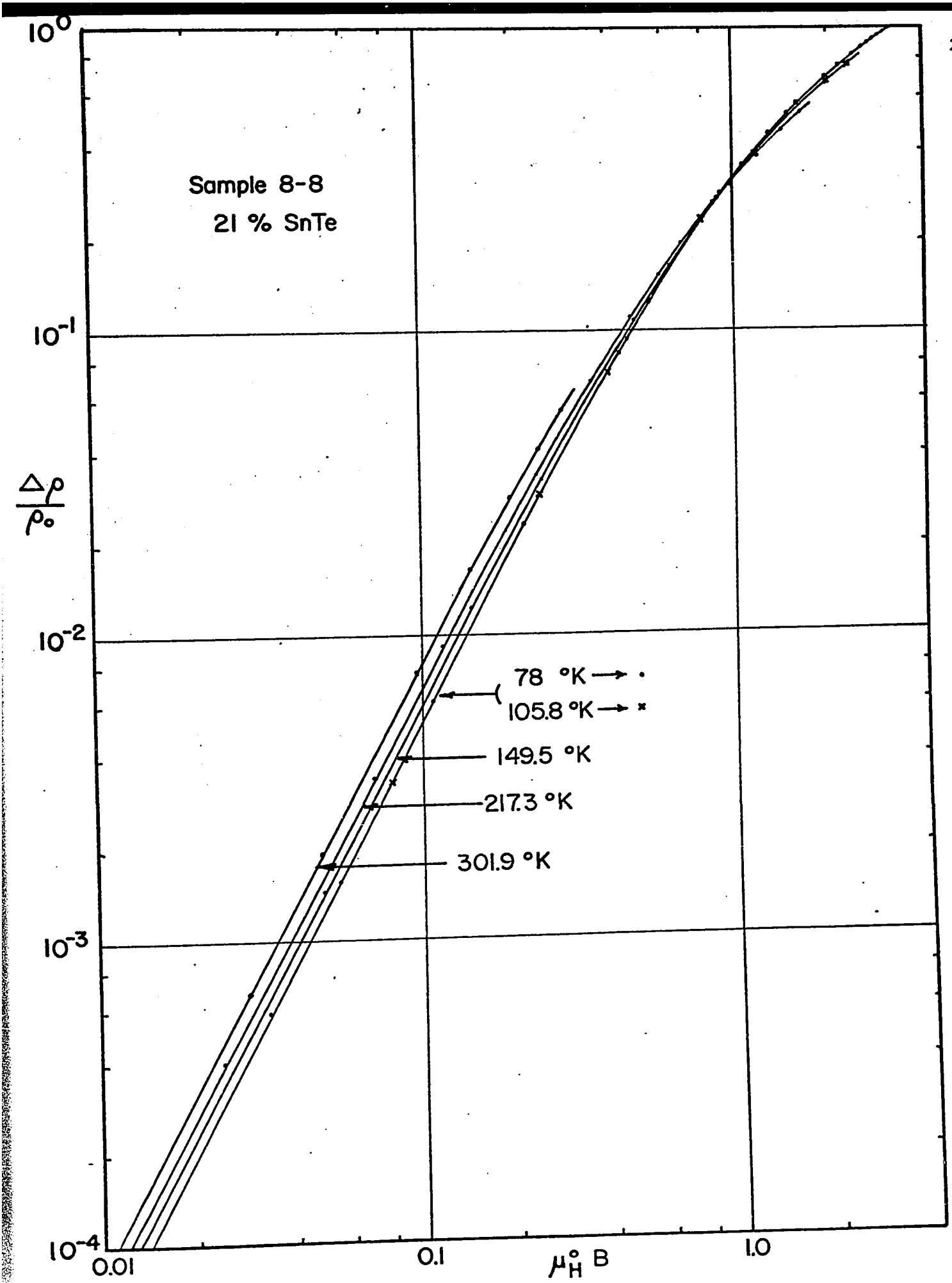

Figure 4.17 $\Delta\rho/\rho_o$ vs. $\mu_H^o B$ in $Pb_{1-x}Sn_xTe$.

In Figure 4.18, $M_{21\bar{2}}^{143}$ and $M_{31\bar{1}}^{011}$ values, obtained in 6% SnTe and 21% SnTe respectively, are shown versus $(1/R_o e)_{77}$. For comparison, the corresponding values for PbTe are also shown. These last values were obtained, as described earlier, from equations (4-14) and (4-15) using the dimensionless Seitz coefficient which were determined experimentally by Allgaier (60 A1). In Figure 4.19, $M_{21\bar{2}}^{143}$ and $M_{31\bar{1}}^{011}$ values for samples 6-6 (6% SnTe) and 8-8 (21% SnTe), respectively, are shown versus temperature. The corresponding values for PbTe at 77°K and room temperature are also shown.

In $Pb_{1-x}Sn_xTe$ with $x = 0$, $0.16 < x < .32$, (60 A1, 71 M1) it is well established that the energy surfaces consist of <111> prolate ellipsoids oriented along the <111> axis at the L point. If we assume that the ellipsoid is of revolution about the <111> axis and that the <111> band is parabolic (EORP model), then the dimensionless Seitz coefficients are (58 A1):

$$b = A\left[\frac{(2K+1)^2}{3K(K+2)}\right] - 1$$

$$c = -\left[A\left[\frac{(2K+1)^2}{3K(K+2)}\right] - 1\right] \qquad (4\text{-}16)$$

$$d = A\left[\frac{2(2K+1)(K-1)^2}{3K(K+2)^2}\right]$$

in which $K = m_L/m_T$ and $A = G_1G_3/G_2^2$ with G_p given by (58 A1):

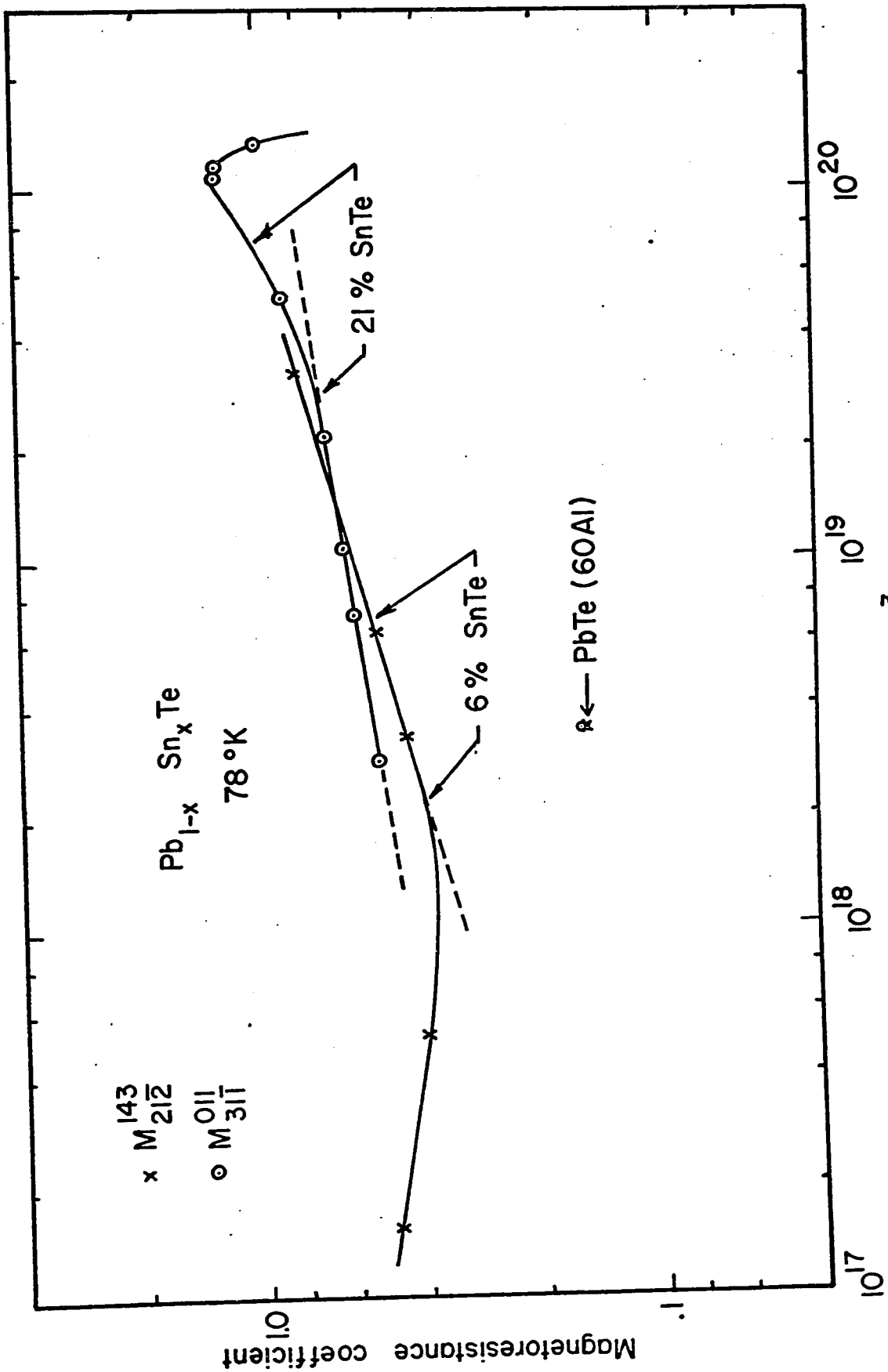

Figure 4.18 Magnetoresistance coefficient vs. $(1/R_o e)_{77}$ in $Pb_{1-x}Sn_xTe$.

$$G_P = \int E^{3/2} \tau^P \frac{\partial f_o}{\partial E} dE \qquad (4\text{-}17)$$

For constant τ (or for full degeneracy) $A = 1$; for classical statistics and isotropic scattering given by $\tau = \ell E^n$ we have $A = 4/\pi$ and $A = 32768/6615\pi$ for acoustical ($n = -1/2$) and impurity ($n = 3/2$) scattering, respectively. To include the effect of anisotropic scattering time $K = (m_L/m_T)/(\tau_L/\tau_T)$ is used in equation (4-16). m_L and τ_L, and m_T and τ_T are, respectively, the effective masses and scattering times parallel and perpendicular to the <111> symmetry axis of the ellipsoid.

Allgaier (60 A1) found that the EORP model was appropriate for PbTe. In addition Allgaier determined $K = (m_L/m_T)/(\tau_L/\tau_T)$ and G at 77°K and room temperature for the EORP model. At 77°K, K and G were 4.2 and 1.016 respectively; at room temperature, they were 4.7 and 1.17 respectively. The values of $M_{21\bar{2}}^{143}$ and $M_{31\bar{1}}^{011}$ calculated for PbTe using Allgaier results (60 A1) are shown in Figures 4.18 and 4.19. The prediction of the EORP model for $Pb_{1-x}Sn_xTe$ alloys with $x = .06$ and .21 are not expected to be much different from that for PbTe because m_L/m_T is the same (71 M1) for the alloys studied as for PbTe. The highest value of $M_{31\bar{1}}^{011}$ that can be obtained at 78°K ($G \sim 1$) for prolate ellipsoids in the EORP model is when $K = \infty$; it is from equations (4-14) and (4-16) $M_{31\bar{1}}^{011} = .453$. While values of K larger than 10 are very improbable, it can be seen from Figure 4.18 that the highest possible value of $M_{31\bar{1}}^{011}$ for the EORP model is still lower than

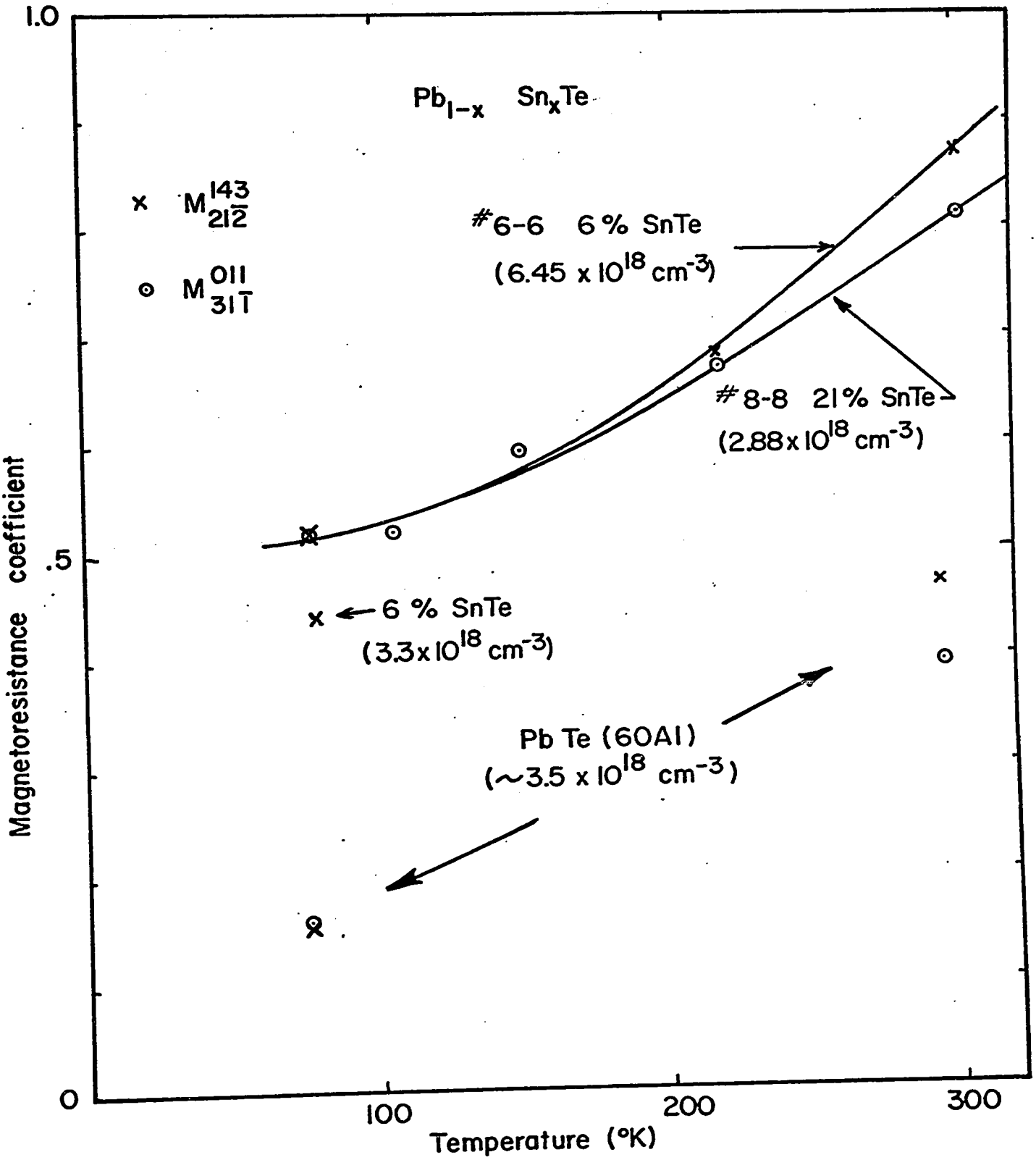

Figure 4.19 Magnetoresistance coefficient vs. temperature in $Pb_{1-x}Sn_xTe$.

the experimental values measured in the alloy. Thus, the EORP model cannot account for the high values of magnetoresistance found in $Pb_{1-x}Sn_xTe$ alloys investigated.

In Figure 4.19 the temperature variation of the magnetoresistance coefficients is the same in the alloys as in PbTe provided a temperature invariant contribution to the magnetoresistance coefficient is subtracted in the alloys. The temperature dependence is mainly due to the change in statistics which increases G. In Figure 4.18, it is seen that the magnetoresistance coefficients increase with increasing carrier concentration in the alloys measured. We disregarded the two lowest carrier concentration samples because they do not satisfy the condition of degeneracy as is the case for the other samples, and an appreciable magnetoresistance is expected from the relatively large values of G in these two samples. As expected from earlier results, the carriers are distributed between the <111> minima and a heavy mass band at the highest carrier concentration shown in Figure 4.18 and a large two-band magnetoresistance is observed. The increase above the dotted line at high carrier concentration (see Figure 4.18) can thus be ascribed to the two-band magnetoresistance. As the conductivity in the heavy mass band become appreciable both the two-band and the <111> minima contributions to the magnetoresistance decreases, and, if the heavy mass band contribute negligible magnetoresistance, a sharp decrease is expected as shown in Figure 4.18. Finally low carrier extrapolation in Figure 4.18 suggest that the

bottom of the band magnetoresistance coefficients in the alloys are similar to those in PbTe and that they can be accounted for by the EORP model.

To account for the high magnetoresistance observed in $Pb_{1-x}Sn_xTe$ alloys it appears that highly distorted Fermi surfaces are necessary. For $(1/R_oe)_{77} < 3 \times 10^{19}$ cm^{-3} in Figure 4.18 the carriers are all in the <111> minima as evidenced by earlier results and there is no two-band contribution to the magnetoresistance. The effect of non-parabolicity at 78°K is also expected to be negligible. The only other important source of magnetoresistance is energy surface distortion (70 A1). If it is the case in $Pb_{1-x}Sn_xTe$ alloys, the Fermi surface is more and more distorted as the carrier concentration increases. Examples of permissible distortions have been suggested* for SnTe (70 E1) which also shows large magnetoresistance. It is mentioned (70 E1) that the cross sections of the Fermi surface perpendicular to the <111> symmetry axis of the valleys could develop three- or sixfold symmetry. It is shown by Allgaier and Perl (70 A1) that sharp bends on the Fermi surface produce large magnetoresistance analogous to that arising from the isotropic two-band model.

In conclusion, the magnetoresistance in $Pb_{1-x}Sn_xTe$ is anomalous in that it cannot be described by the EORP model. The results suggest that at low carrier concentration ($\sim 10^{17}$ cm^{-3}) the EORP model may be adequate. However, at higher carrier concentration, it appears that the Fermi surface becomes highly distorted and caused the magnetoresistance to be anomalously high as is the case in SnTe (70 E1).

*A specific kind of 3-fold distortion was proposed by Allgaier at the Dallas A.P.S. meeting (1970)

4.3.4 Hall Mobility

The Hall mobility in 6% SnTe and 21% SnTe alloys was measured as a function of temperature for all samples listed in Figures 4.5 and 4.6. Figure 4.20 shows the results for the 21% SnTe alloys. Similar curves were obtained in 6% SnTe alloys. The variation of the Hall mobility with temperature resembles that observed in PbTe (67 C1) suggesting that the same scattering mechanisms are operative in both PbTe and the alloys measured. However, the Hall mobility is smaller in magnitude except near room temperature for $(1/R_o e)_{77} < 10^{19}$ cm^{-3} where the Hall mobility is about the same in PbTe as in the alloys.

The scattering mechanisms operative in this temperature range are not well specified yet (68 R1). The scattering by long wavelength acoustical vibrations is believed to be dominant in the temperature range investigated, for not too low carrier concentrations (62 A1, 67 C1, 70 R3). For classical and degenerate statistics, respectively, we have for acoustical scattering only (70 R3):

$$\mu_{cl} \propto m^{*-5/2} T^{-3/2}$$
$$\mu_{deg} \propto m^{*-2} T^{-1} \qquad (4\text{-}18)$$

The stronger temperature dependence of the effective mass m*, as the temperature increases, coupled with the change from degenerate to classical statistics is believed to cause the increasing dropping rate of the Hall mobility as the temperature increases. Finally, let us mention that the transfer of holes to the heavy mass band (in which

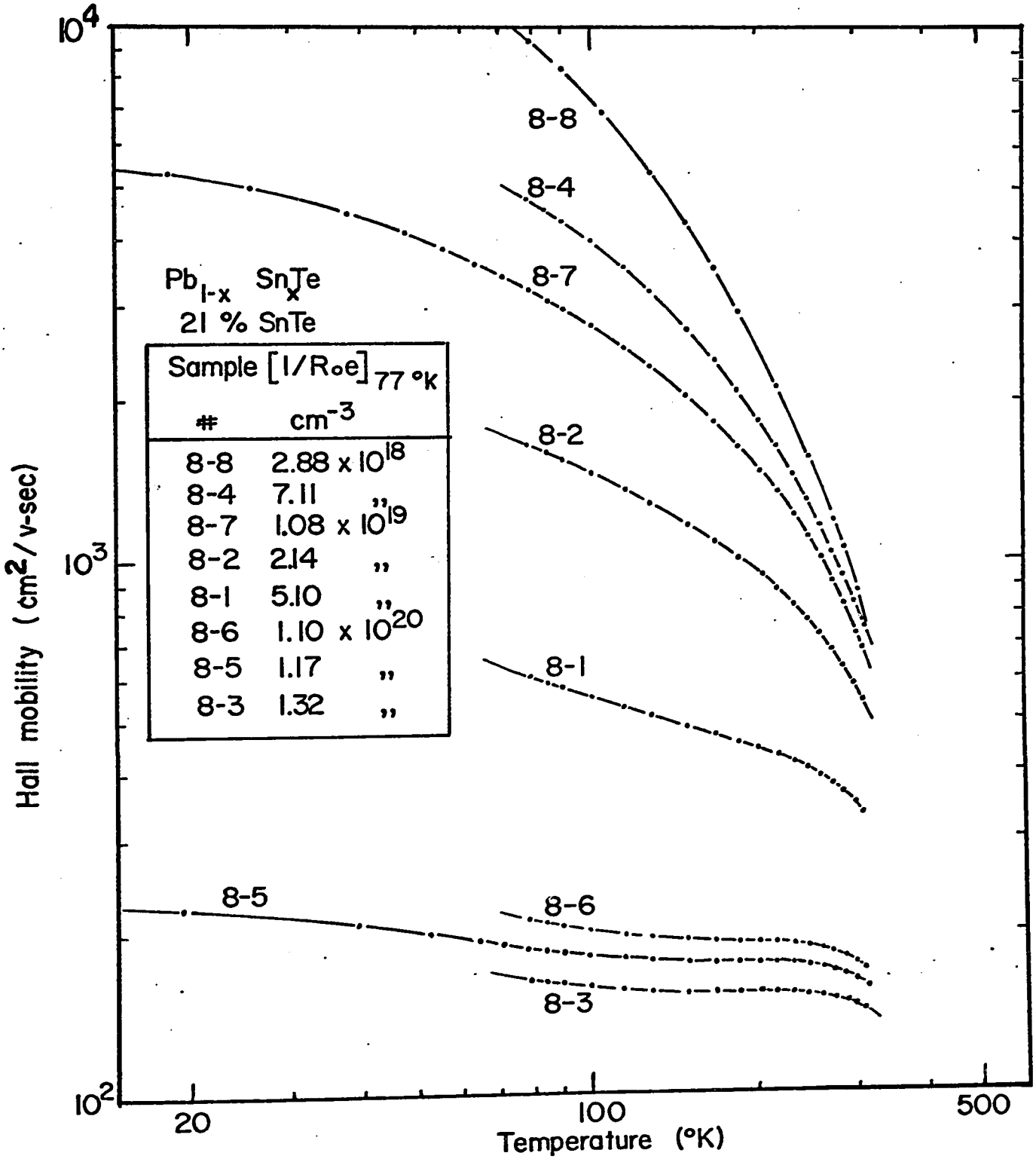

Figure 4.20 Hall mobility vs. temperature for several carrier concentrations in p-type $Pb_{1-x}Sn_xTe$ with x = .21.

the mobility is very small), as the temperature increases, is expected to reduce the Hall mobility. However, this reduction in the average Hall mobility due to the transfer of holes to the heavy mass band is partly compensated by an increase in Hall coefficient (70 R3). Ravich (70 R3) also points out the importance of polar scattering at low carrier concentrations, and discusses the possibility of other scattering mechanisms in $Pb_{1-x}Sn_xTe$.

In Figure 4.21 we show the Hall mobility at 77.3 and 4.2°K versus carrier concentration $(1/R_o e)_{77}$. The full lines represent the 6% SnTe and 21% alloys (as indicated on the graph), and the dotted lines are the results for PbTe published by Allgaier and Houston (62 A1). The Hall mobility in the alloys at 77°K shows approximately the same $(1/R_o e)_{77}$ dependence as in PbTe. However, there is a large difference in the magnitude of the Hall mobility at high carrier concentrations. At lower carrier concentrations, where acoustical and polar scattering are dominant (70 R3), the difference tends to disappear.

In PbTe the 4.2°K curve which shows $p^{-1.4}$ $(p = 1/R_{77}e)$ dependence has been ascribed to impurity scattering which predicts a $p^{-4/3}$ dependence for degenerate statistics (62 A1). In the alloys measured, the Hall mobility at 4.2°K is 10 times smaller than in PbTe but shows a $p^{-4/3}$ dependence characteristic of impurity scattering. Dixon and Bis (68 D1) found that the Hall mobility, $R_H(4^oK)/\rho$, in $Pb_{1-x}Sn_xTe$ is dependent upon carrier-related imperfections in agreement with our results. In addition, they found that for p

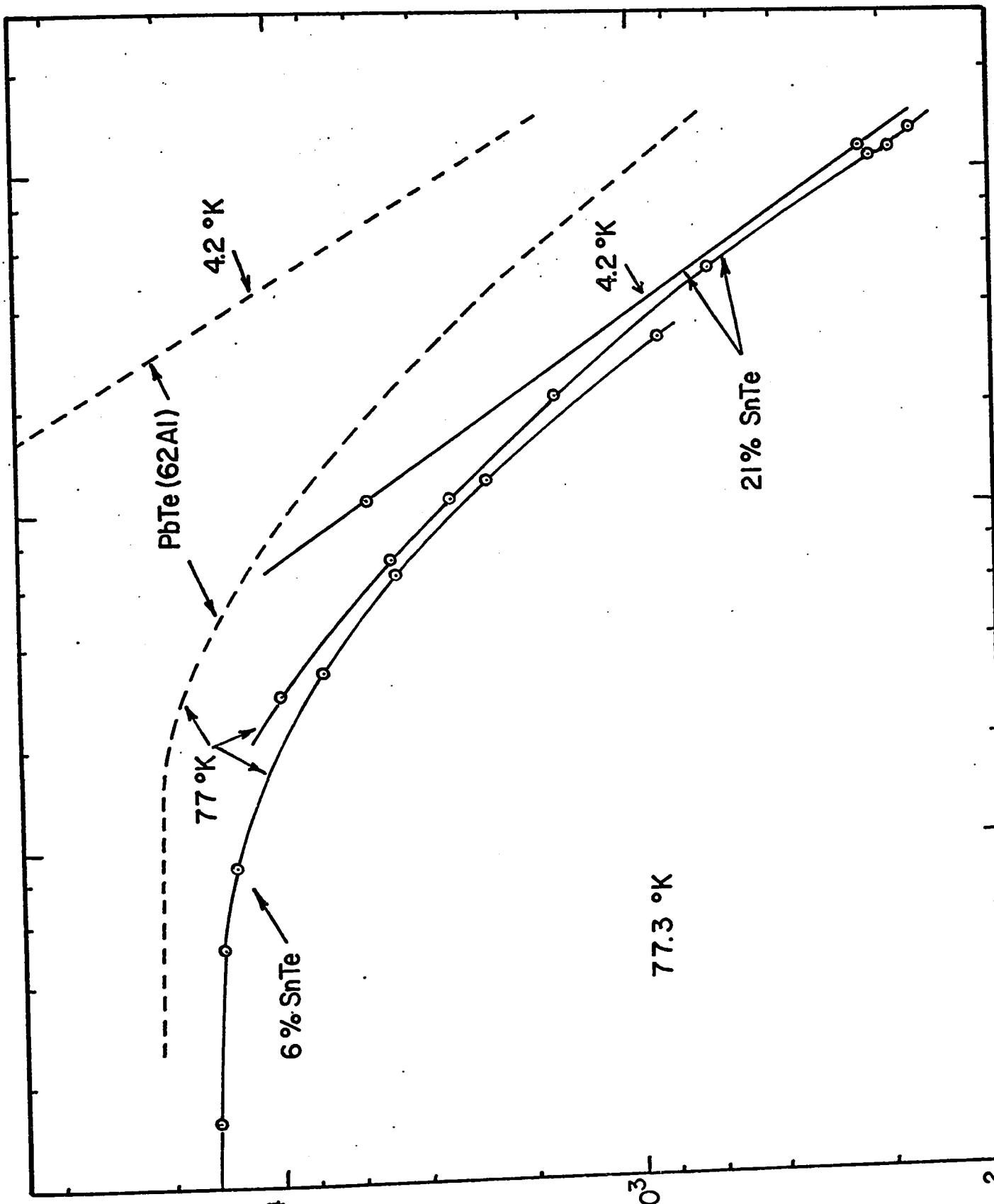

Figure 4.21 Hall mobility vs. carrier concentration in p-type $Pb_{1-x}Sn_xTe$.

varying from 1 to 5 x 10^{20} cm^{-3} the Hall mobility, $R_H(4^oK)/\rho$, in the alloys could be represented by $\mu \propto \frac{1}{x(1-x)}$, where x is the alloy fraction, indicating that the degree of alloying is also significant in determining the low temperature Hall mobility.

We would like to suggest that the dependence of the Hall mobility on the degree of alloying, reported by Dixon and Bis at very high carrier concentrations, can be explained, entirely or in part, in terms of the heavy mass band which becomes more or less populated depending on the carrier concentration and alloy composition. They used samples with carrier concentrations in the vicinity of the Hall ratio kink. As discussed earlier, the Fermi level is in the heavy mass band at low temperature for carrier concentrations larger than that at the kink. From our results and those of Albany and Ocio (68 A3), the Hall ratio kinks occur at carrier concentrations $(1/R_{77}e)$ less than 10^{20} cm^{-3} for alloy compositions between 20% SnTe and 60% SnTe. The low Hall mobilities observed by Dixon and Bis (68 D1) for these alloy compositions, with $(1/R_oe)_{77}$ ranging from approximately 2 to 5 x 10^{20} cm^{-3}, may well be due to the large population of heavy holes which have very low mobilities and which are expected to reduce the average Hall mobility.*

The flatness of the mobility curves at low temperatures (Figure 4.20, 68 D1), and the $p^{-4/3}$ dependence of the Hall mobility at 4.2°K suggest that impurity scattering is dominant in the alloys measured. However, the large decrease (10 times) from PbTe to the alloys could not be explained.

*This alternative explanation assumes that past the kink the mobility in band 1, which decreases rapidly with increasing p, is still higher than that in band 2. However, this may not be the case.

4.4 Discussion

Despite the fact that no adequate model for the <111> band was available for a detailed quantitative analysis of the electrical data, several important results were obtained. The main ones are:

1) The ratio of the mobilities in the heavy mass band to that of the light mass band is smaller than 1/8.1 in 13% and 17% SnTe alloys and smaller than 1/9.6 in 37% and 48% SnTe alloys.

2) The ratio of the mobilities in the light hole band to that of the conduction band was found to be smaller than 3.7 in 13% SnTe alloys.

3) The thermal energy gap between the light hole band and the conduction band was found to be .14 e.v. in 13% SnTe alloys in good agreement with the optical gap.

4) The energy separation between the light hole band and the heavy hole band at $77^{o}K$ was found to be .21 e.v. in 21% SnTe alloys and .23 e.v. in PbTe, is disagreement with the generally accepted value of .14 e.v.

5) The temperature variation of the energy gap in 4) was found to be 4.4×10^{-4} e.v./^{o}K in 21% SnTe alloys which yields for this energy gap at $0^{o}K$ a value of .25 e.v.

In addition, several new observations were reported and discussed concerning the variation of the Hall constant with magnetic field, the magnetoresistance versus carrier concentration and

temperature, and the Hall mobility. Perhaps one of the most significant results is that several experimental data suggest that the Fermi surface are highly distorted in $Pb_{1-x}Sn_xTe$. These distortions appeared to be more severe at large carrier energies.

CHAPTER V

SUMMARY

A study of the metallurgical, optical, and electrical properties of p-type $Pb_{1-x}Sn_xTe$ alloys has been carried out. This study contains original contributions in apparatus design, experimental techniques, methods of analysis, as well as in experimental results and their interpretations. They are in order of appearance:

1. The design of a constant temperature furnace for annealing studies (2.2.2).
2. A new method for the determination of alloy compositions (2.3.2b).
3. New techniques to control the carrier concentration by heat treatment (2.4.2).
4. The results of metal and tellurium saturation annealing experiments for several alloy compositions (2.4.2).
5. A systematic, comparative, and critical study of the methods of analysis to obtain the susceptibility effective mass, the high frequency dielectric constant, and the optical mobility from plasma resonance reflectivity data (3.4).
6. The inaccuracy of the slope and fitting methods of analysis when small contributions to the dielectric constant other than that of free carriers are present and when small, often unavoidable, deviations from the absolute reflectivity, are present (3.4.1b).

7. New graphs from which susceptibility effective masses and optical mobilities can be determined routinely and accurately, even for non-degenerate materials, from the experimental measurement of the wavelength and the value of reflectivity of the reflectivity minimum only (3.4.2).

8. The determination of the high frequency dielectric constant for several carrier concentrations and alloy compositions (3.5.2).

9. A new relation between the high frequency dielectric constant and the energy gap in PbTe rich alloys (3.5.2).

10. An investigation of the effects of the surface preparation showing that the analysis of reflectivity spectra from samples with mechanically polished surfaces leads to erroneous results (3.5.3).

11. The results of effective mass versus carrier concentration and temperature in PbTe rich alloys (3.5.4, 3.5.5).

12. Critical tests of the Kane, Cohen, and Dimmock models of the <111> minima and the inadequacy of the above models to explain all our experimental results of effective mass versus carrier concentration and temperature (3.5.7).

13. The design of a new high temperature apparatus for electrical measurements (4.2.1b).

14. A rapid technique to determine the interdiffusion constant of the alloys (4.3.1b).

15. A thermal energy gap (main gap) in good agreement with optical determination and mobility ratios obtained from singular points in the Hall curves vs. temperature (4.3.2a-2).

16. The determination of the energy separation between the light and heavy mass band and its temperature variation in 21% SnTe alloys (4.3.2b).

17. The non-validity of the A.W. analysis in determining the energy separation between the light and heavy mass band from the low carrier concentration Hall data in $Pb_{1-x}Sn_xTe$ alloys and compounds (4.3.2c).

18. The highly distorted energy surfaces suggested by the experimental results of Hall constant and magnetoresistance versus magnetic field for several carrier concentrations, temperatures, and alloy compositions (4.3.2d, 4.3.3).

19. An alternative explanation for the apparent evidence of alloy scattering reported elsewhere in $Pb_{1-x}Sn_xTe$ alloys (4.3.4).

More details related to the above original contributions may be found in the corresponding sections.

SELECTED BIBLIOGRAPHY

71 M1 John Melngailis, T. C. Harman, J. G. Mavroides, and J. O. Dimmock, Phys. Rev. 3B, 370 (1971).

70 A1 R. S. Allgaier and Robert Perl, Phys. Rev. B2, 877 (1970).

70 A2 R. S. Allgaier, Phys. Rev. 2B, 3869 (1970).

70 B1 J. R. Burke, J. D. Jensen, and B. Houston, Phys. Rev. B2, 1977 (1970).

70 B2 R. F. Bis and J. R. Dixon, Phys. Rev. B2, 1004 (1970).

70 D1 I. N. Dubrovskaya, Yu. I. Ravich, and O. S. Gryaznov, Soviet Phys.-Semiconductors 3, 1500 (1970).

70 D2 J. O. Dimmock, Conference on the Physics of Semimetals and Narrow Gap Semiconductors, Dallas, Texas, 20-21 March (1970).

70 E1 C. C. Evans, and T. A. Reglein, and R. S. Allgaier, Phys. Rev. B2, 980 (1970).

70 F1 E. Fortin, Rev. Sci. Instr. 41, 1252 (1970).

70 O1 H. Overhof and U. Rõssler, Phys. Stat. Sol. 37, 691 (1970).

70 R1 B. Rheinländer, Phys. Stat. Sol. 38, 193 (1970).

70 R2 B. Rheinländer, Surface Science 19, 29 (1970).

70 R3 Yu. I. Ravich, B. A. Efimova, and I. A. Smirnov, Semiconducting Lead Chalcogenides. Ed: Soviet Physics-Semiconductors, Plenum Press New York (1970).

70 S1 I. K. Smirnov and Yu. I. Ukhanov, Soviet Phys.-Semiconductors 3, 1553 (1970).

69 A1 M. Aubin, Ph.D. Thesis, University of Ottawa (1969).

69 B2 R. F. Bis, Ph.D. Thesis, University of Maryland (1969).

69 B1 R. F. Bis and J. R. Dixon, J. Appl. Phys. 40, 1918 (1969).

69 D1 R. Dalven, Infrared Physics, 9, 141 (1969).

69 R1 B. Rheinländer, Phys. Letters (Netherlands) 29A, 420 (1969).

69 T1 Y. W. Tung and M. L. Cohen, Phys. Rev. 180, 823 (1969).

68 A1 R. S. Allgaier, Phys. Rev. 165, 775 (1968).

68 A2 A. A. Andreev, Journal de Physique, Colloque C-4, Suppl. 29, 50 (1968).

68 A3 H. J. Albany and M. Ocio, Journal de Physique, Colloque C-4, Suppl. 29, 125 (1968).

68 B1 J. F. Butler and T. C. Harman, J. Electrochem. Soc. 115, 67C (1968).

68 C1 I. A. Chernik, V. I. Kaidanov, M. I. Vinogradova, and N. V. Kolomoets, Soviet Phys.-Semiconductors 2, 645 (1968).

68 C2 A. R. Calawa, T. C. Harman, M. Finn, and P. Youtz, Trans. TMS-AIME 242,374 (1968).

68 D1 J. R. Dixon and R. F. Bis, Phys. Rev. 176, 942 (1968).

68 M1 T. S. Moss, T. D. F. Hawkins, and G. J. Burrell, J. Phys. C (Proc. Phys. Soc.), 1, 1435 (1968).

68 M2 I. Melngailis and T. C. Harman, Applied Physics Letters 13, 180 (1968).

68 P1 E. H. Putley, The Hall Effect and Semiconductors Physics (Dover Publications, Inc., New York 1968).

68 R1 Yu. I. Ravich, Journal de Physique, Colloque C-4, Suppl. 29, 114 (1968).

68 W1 John W. Wagner and Robert K. Willardson, Trans. TMS-AIME, 242, 366 (1968).

68 S1 A. J. Strauss and R. F. Brebrick, Journal de Physique, Colloque C-4, Suppl. 29, 21 (1968).

68 T1 R. Tsu, W. E. Howard, and L. Esaki, Phys. Rev. 172, 779 (1968).

67 C1 A. J. Crocker and L. M. Rogers, Brit. J. Appl. Phys. 18, 563 (1967).

67 N1 P. M. Nikolic, Brit. J. Appl. Phys. 18, 897 (1967).

67 R1 H. R. Riedl, J. R. Dixon, and R. B. Schoolar, Phys. Rev. 162, 692 (1967).

67 T1 R. N. Tauber and I. B. Cadoff, J. Appl. Phys. 38, 3714 (1967).

67 W1 J. W. Wagner and J. C. Woolley, Mat. Res. Bull. 2, 1055 (1967).

66 A1 R. S. Allgaier and B. B. Houston, Jr., J. Appl. Phys. 37, 302 (1966).

66 A2 R. S. Allgaier, Phys. Rev. 152, 808 (1966).

66 D1 J. O. Dimmock, I. Melngailis, and A. J. Strauss, Phys. Rev. Letters 16, 1193 (1966).

66 L1 P. J. Lin and L. Kleinman, Phys. Rev. 142, 478 (1966).

66 W1 R. L. Weiker, Phys. Rev. 152, 736 (1966).

65 A1 R. S. Allgaier, J. Appl. Phys. 36, 2429 (1965).

65 D1 J. R. Dixon and H. R. Riedl, Phys. Rev. 138, A873 (1965).

65 Z1 J. N. Zemel, J. D. Jensen, and R. B. Schoolar, Phys. Rev. 140, A330 (1965).

64 B1 R. F. Brebrick, J. Phys. Chem. Solids 24, 27 (1963).

64 C1 K. F. Cuff, M. R. Ellett, C. D. Kuglin, and L. R. Williams, Proc. Seventh Inter. Conf. on Physics of Semiconductors, Paris, 1964 (Academic Press Inc., New York, 1965) p.667.

64 K1 J. Kolodziejczak and S. Zukotynski, Phys. Stat. Solidi 5, 145 (1964).

64 L1 H. A. Lyden, Phys. Rev. 134, A1106 (1964).

64 L2 H. A. Lyden, Phys. Rev. 135, A514 (1964).

64 S1 R. A. Smith, Semiconductors (Cambridge University Press, London, 1964).

63 B1 A. C. Beer, Galvanomagnetic Effects in Semiconductors; Solid State Physics, Suppl. 4 (Academic Press, Inc., N.Y., 1963).

63 B2 R. F. Brebrick, J. Phys. Chem. Solids 24, 27 (1963).

63 S1 F. Stern, Solid State Physics, Edited by F. Seitz and D. Turnbull (Academic Press, Inc., New York, 1963), Vol. 15, pp.229-408.

63 W1 A. K. Walton and T. S. Moss, Proc. Phys. Soc. (London), B81, 509 (1963).

62 A1 R. S. Allgaier and B. B. Houston, Jr., Proc. Int. Conf. Semiconductors Physics, Exeter pp.172-78 (1962).

61 A1 R. S. Allgaier, J. Appl. Phys. 32, 2185 (1961).

61 C1 D. G. Coates, W. D. Lawson, and A. C. Prior, J. Electrochem. Soc. 108, 1038 (1961).

61 S1 P. J. Stiles, E. Burstein, and D. N. Langenburg, J. Appl. Phys. 32, 2179 (1961).

60 A1 R. S. Allgaier, Phys. Rev. 119, 554 (1960).

60 B1 R. F. Brebrick and R. S. Allgaier, J. Chem. Phys. 32, 1826 (1960).

60 M1 T. Moss, Optical Properties of Semiconductors; A Semiconductor Monograph (Butterworths Scientific Publications, London, 1959).

59 S1 W. W. Scanlon, Solid State Physics, Academic Press, New York V.9, 83 (1959).

58 A1 R. S. Allgaier, Phys. Rev. 112, 828 (1958).

58 S1 M. J. Sinnott, The Solid State for Engineers (John Wiley & Sons, Inc., New York) p.62.

57 S1 W. G. Spitzer and H. Y. Fan, Phys. Rev. 106, 882 (1957).

56 K1 C. Kittel, Introduction to Solid State Physics (John Wiley & Sons, Inc., New York, 1956).

54 D1 T. M. Dauphinee and H. Preston-Thomas, Rev. Sci. Inst. 25, 884 (1954).

52 T1 International Tables for X-ray Crystallography (The Kynock Press, Birmingham, England, 1952).

43 D1 C. G. Darwin, Proc. Roy. Soc. 152, A182 (1943).

36 W1 A. H. Wilson, The Theory of Metal (Cambridge Univ. Press, New York, 1936) p.124.

ABSTRACT

Seven ingots of $Pb_{1-x}Sn_xTe$ alloys totalling 492 grams of material were prepared by the step-freeze technique. The as-grown material covering all alloy compositions $0 < x < .8$ was found to be single crystals with a high degree of perfection, to be free of metal precipitates and cellular structure, and to be homogeneous in carrier concentration as well as in alloy composition. In addition, the alloys grown by the step-freeze technique in our laboratory were found to be purer and to have higher mobilities than other alloys grown elsewhere. It was shown that the alloy composition, usually determined from lattice constant measurements using Vegard's law, can also be determined from measurements of the integrated intensity ratio I_{311}/I_{222} of only two lines in the X-ray powder diffraction pattern. Twenty samples of six different alloy compositions $0 < x < .5$ were heat treated for periods of 2 to 30 days, at temperatures of 570 to 869°C, to produce samples of different carrier concentrations ($1/R_{77}e$) ranging from 7.9×10^{16} to 1.32×10^{20} holes cm^{-3}. To obtain homogeneous heat treated samples, a constant temperature annealing furnace was designed which eliminated temperature gradients ($\pm 1^{\circ}C$) over the sample and its container at all annealing temperatures. Two new annealing techniques were developed and found to have several advantages over already known techniques.

Reflectivity measurements were made* in the 2-23 microns region of the infrared spectrum on four 6% SnTe and eight 21% SnTe alloy samples with carrier concentrations ($1/R_{77}e$) ranging from

*at 82°K

5.06 to 10^{17} to 3.20 x 10^{19} holes cm^{-3} and from 2.88 x 10^{18} to 1.32 x 10^{20} holes cm^{-3}, respectively. In addition, reflectivity measurements were made at 22 different temperatures between 84°K and 300°K on a 21% SnTe alloy sample with a carrier concentration of 8.7 x 10^{18} holes cm^{-3}. These measurements were analysed in terms of a free carrier dispersion model. All known methods of analysis were used to extract the values of the model parameters namely the susceptibility effective mass m_s, the high frequency dielectric constant ε_∞, and the optical mobility μ_{opt}. It was found that the different methods gave inconsistent results. A systematic, comparative, and critical study of the methods of analysis was made for the first time and all the inconsistencies explained. In particular, it was found that the slope and the fitting method of analysis were inaccurate when small contributions to the dielectric constant other than that of the free carriers were present and when small, often unavoidable, deviations from the absolute reflectivity were present in the experimental reflectivity spectra. The most reliable and also the simplest method of analysis was found to be that proposed by Moss et al. His method of analysis was generalized to include the case of non-degeneracy. New graphs were produced which permit a routine and accurate measurement of m_s and μ_{opt} from the experimental measurement of the wavelength and the value of the reflectivity of the minimum in reflectivity. To obtain accurate values of m_s, the Hall factor must be known for all carrier concentrations, in addition, using the Moss et al method, ε_∞ vs carrier

concentration is required. In the present experiment it was found that the ratio of the Hall factor to ε_∞ was close to a constant for all carrier concentrations measured. Because of this, m_s was obtained with good absolute accuracy when using the Moss et al method, and it was possible to detect the presence of a heavy mass band situated (at 82°K) .22 e.v. below the light mass band in p-type $Pb_{1-x}Sn_xTe$ alloys with 21% SnTe. The low carrier concentration value of ε_∞ was determined in 6% and 21% SnTe alloys at 300°K and 82°K and a new relation between ε_∞ and the energy gap E_G was derived and fitted to our results and those obtained elsewhere. It is: $\text{Ln } E_G = -.086\ \varepsilon_\infty + 1.65$. An investigation of the effects of the surface preparation showed that the analysis of reflectivity spectra of samples with mechanically polished surfaces leads to erroneous results. The results of effective mass versus carrier concentration and temperature in 6% SnTe and 21% SnTe alloys were compared with those expected on the basis of the Kane, Cohen and Dimmock models of the <111> valence band minima in $Pb_{1-x}Sn_xTe$. The results of these comparisons indicate that none of these models explains adequately all of our experimental results of susceptibility effective mass. Finally, the optical mobility was found to be about two times smaller than the conductivity mobility in all samples measured.

The Hall coefficient, the transverse magnetoresistance and the Hall mobility were measured from 4.2°K to 800°K for several hole concentrations and alloy compositions. The ratio of the mobilities in the heavy mass band to that of the light mass band* was found to be smaller than 1/8.1 in 13% and 17% SnTe alloy and smaller than 1/9.6 in

*Measured at the temperature of the positive Hall coefficient maximum: $400°K < T_{max} < 540°K$

37% and 48% SnTe alloys. The ratio of the mobilities in the light hole band to that of the conduction band* was found to be smaller than 3.7 in 13% SnTe alloys. The thermal energy gap** between the light hole band and the conduction band was found to be .14 e.v. in 13% SnTe alloy in good agreement with the optical determination. The energy separation between the light hole band and the heavy hole band at 77°K was found to be .21 e.v. in 21% SnTe alloys and .23 e.v. in PbTe in disagreement with the generally accepted value of .14 e.v. determined from the A.W.† analysis on low carrier concentration Hall data. In addition, the temperature variation of the inter-valence band gap was found to be 4.4×10^{-4} e.v./°K in 21% SnTe alloys. It was also found that the A.W. analysis is not appropriate to determine the inter-valence energy gap from low carrier concentration Hall data in $Pb_{1-x}Sn_xTe$ because of a temperature dependent Hall factor. Finally, the Hall coefficient and the magnetoresistance were measured as a function of magnetic field for several carrier concentrations, temperatures and alloy compositions. The results suggest that the energy surface in p-type $Pb_{1-x}Sn_xTe$ are highly distorted.

---

* Measured at the temperature of the Hall zero, i.e., 271°K

** Extrapolated at 0°K

† Aukerman-Willardson